Fall 2013

Aerosol predictions and their links to weather forecasts through online interactive atmospheric modeling and data assimilation

Pablo Enrique Saide Peralta
University of Iowa

AEROSOL PREDICTIONS AND THEIR LINKS TO WEATHER FORECASTS THROUGH ONLINE INTERACTIVE ATMOSPHERIC MODELING AND DATA ASSIMILATION

by

Pablo Enrique Saide Peralta

A thesis submitted in partial fulfillment
of the requirements for the Doctor of
Philosophy degree in Civil and Environmental Engineering
in the Graduate College of
The University of Iowa

December 2013

Thesis Supervisor: Professor Gregory R. Carmichael

Graduate College
The University of Iowa
Iowa City, Iowa

CERTIFICATE OF APPROVAL

_____

PH.D. THESIS

_____

This is to certify that the Ph.D. thesis of

Pablo Enrique Saide Peralta

has been approved by the Examining Committee
for the thesis requirement for the Doctor of Philosophy
degree in Civil and Environmental Engineering at the December 2013
graduation.

Thesis Committee: _____
Gregory R. Carmichael, Thesis Supervisor

_____
Scott N. Spak

_____
Jerald L. Schnoor

_____
Keri C. Hornbuckle

_____
Patrick O'Shaughnessy

To my wife Paula for her support through all these years

ACKNOWLEDGMENTS

There is a countless list of people that have contributed their share in different aspects which have resulted in this dissertation. First, I would like to acknowledge my Thesis adviser Professor Gregory Carmichael for taking me as his student and for his continuous encouragement, guidance and support in every project or idea that I wanted to develop. Prof. Scott Spak also played an important role providing guidance for most of the studies in this thesis. Special thanks to Professors Jerry Schnoor, Keri Hornbuckle and Patrick O'Shaughnessy for being part of the thesis committee and for providing important feedback.

I would like to thank people at the CGRER where I developed all my research. My colleagues throughout all years were important providing good feedback and also their friendship. Special thanks to Ada, Pallavi, Yafang, Jaemeen and Ashish. Thanks to CGRER staff Jeremie and Jane for all their help and good will. Thanks also to all the Environmental Engineering department, professors and students, as it was a great positive place to develop my studies.

Thanks to my friends I made outside the school, especially to Gabriel and the soccer team, for reminding that not everything is studying. Thanks to my family back in Chile, especially to my parents, as they provided me with the education necessary to be successful in the US. Finally but most importantly, thanks to my wife Paula who joined me in this journey out of our country, leaving everything behind so I can accomplish my dreams. I hope you are accomplishing your dreams now too.

ABSTRACT

Atmospheric particles represent a component of air pollution that has been identified as a major contributor to adverse health effects and mortality. Aerosols also interact with solar radiation and clouds perturbing the atmosphere and generating responses in a wide range of scales, such as changes to severe weather and climate. Thus, being able to accurately predict aerosols and its effects on atmospheric properties is of upmost importance.

This thesis presents a collection of studies with the global objective to advance in science and operations the use of WRF-Chem, a regional model able to provide weather and atmospheric chemistry predictions and simultaneously representing aerosol effects on climate. Different strategies are used to obtain accurate predictions, including finding an adequate model configuration for each application (e.g., grid resolution, parameterizations choices, processes modeled), using accurate forcing elements (e.g., weather and chemical boundary conditions, emissions), and developing and applying data assimilation techniques for different observational sources. Several environments and scales are simulated, including complex terrain at a city scale, meso-scale over the southeast US for severe weather applications, and regional simulations over the three subtropical persistent stratocumulus decks (off shore California and southeast Pacific and Atlantic) and over North America. Model performance is evaluated against a large spectrum of observations, including field experiments and ground based and satellite measurements.

Overall, very positive results were obtained with the WRF-Chem system once it had been configured properly and the inputs chosen. Also, data assimilation of aerosol and cloud satellite observations contributed to improve model performance even further. The model is proven to be an excellent tool for forecasting applications, both for local and long range transported pollution. Also, advances are made to better understand

aerosol effects on climate and its uncertainties. Aerosols are found to generate important perturbations, ranging from changes in cloud properties over extensive regions, up to playing a role in increasing the likelihood of tornado occurrence and intensity. Future directions are outline to keep advancing in better predictions of aerosols and its feedbacks.

TABLE OF CONTENTS

LIST OF TABLES

LIST OF FIGURES

CHAPTER 1 GENERAL INTRODUCTION

Aerosols are defined as a collection of liquid or solid particles suspended in a gaseous medium (Hinds, 2012). In the atmosphere, aerosols play multiple roles, where perhaps the most important and most studied are the health impacts. Particulate air pollution is associated with a broad spectrum of acute and chronic health effects, with the most serious including lung cancer and cardiopulmonary mortality, and estimated to contribute 2.1 million deaths globally and annually (Silva *et al.*, 2013). Due to these effects, several countries perform forecasts to warn the population (e.g. http://www.airnow.gov/). In other places, like the case of Santiago, Chile, pollutant concentrations have become such a problem that the government is required by law to perform forecasts and to take measures to try to avoid episodes if dangerous air quality is forecasted. These facts require air quality forecasting tools that have good skill and are reliability, which is often a challenge for current models (Koch *et al.*, 2009; McKeen *et al.*, 2007).

Another important role of aerosol is their impact on climate (Solomon *et al.*, 2007). Aerosols can absorb and scatter solar radiation and act as a cloud condensation nuclei (CCN) or ice nuclei. These effects have a great variety of consequences such as partially heating the atmosphere (Ramanathan and Carmichael, 2008), reducing visibility (Ramanathan *et al.*, 2008) and even invigorate convective systems (Andreae *et al.*, 2004). Current weather forecasts do not include these aerosol feedbacks as including them in models is in a research stage where their current reliability is low, and because of the additional computational expenses that such systems require. Thus, there is a need to advance in the use of models with aerosol feedbacks, reducing their uncertainties, proving their skill and feasibility, and showing the impact obtained when aerosol interactions are included.

Due to the importance of aerosol impacts in health and climate, a variety of tools have been developed to predict aerosols and their effects (Baklanov, 2011). This thesis is focused on developments, evaluation and use of the Weather Research and Forecasting/Chemistry (WRF-Chem) model (Skamarock *et al.*, 2008; Grell *et al.*, 2005), a regional scale fully coupled online model. WRF-Chem is able to simultaneously perform forecasts of weather and aerosol distributions incorporating the aerosol feedbacks to meteorology. The uncoupled part of this model (WRF) is extensively used in operational centers around the globe (http://wrf-model.org/plots/wrfrealtime.php), so by using WRF-Chem the future transition to operations would be smoother. The main premise of this thesis is that WRF-Chem allows obtaining accurate predictions of aerosols and its effects, which can help improve air quality and weather forecasts. The model is configured in a variety of domains with different applications to demonstrate its usefulness for advancing science, research and operations.

Chapter 2 is focused on the development and evaluation of an air quality forecast system specially for the city of Santiago, Chile. Here, the ability of WRF-Chem to reach high resolution simulations is necessary to resolve the conditions of complex topography found in the domain of study. Also, the operational nature of WRF are important to transfer this model to the Chilean meteorological service to be used as a forecasting tool. This chapter is based on the results published on Saide *et al.* (2011).

Chapter 3 consists of analyzing WRF-Chem simulations performed over the South-East Pacific, in an area where a persistent stratocumulus deck is found and a field campaign was performed to assess aerosol and cloud interactions. The focus is on studying the ability of WRF-Chem to represent meteorology and atmospheric composition in the area and on examining the aerosol effects on clouds as modeled by WRF-Chem. This chapter is based on the results published on Saide *et al.* (2012b)

Chapter 4 and 5 describe the development and evaluation of data assimilation techniques that use satellite data to improve aerosol estimates predicted by WRF-Chem.

Chapter 4 deals with a new technique that uses cloud retrievals, and chapter 5 focuses on a technique using aerosol optical properties retrievals. These chapters are based on the results published on Saide *et al.* (2012a) and Saide *et al.* (2013).

Chapter 6 presents an application of WRF-Chem to study the influence of Central American biomass burning smoke on an historical US severe weather outbreak. Using simulations where the fire emissions are included and excluded, WRF-Chem generates different meteorological conditions as aerosol feedbacks to radiation and to clouds are included in the model. By analyzing the differences between the conditions generated, the impact of the smoke is assessed.

Chapter 7 focuses on WRF-Chem simulations and analysis for a field experiment performed over the US. The experiment tries to accomplish a wide variety of objectives, such as measurement for hurricanes, convection, wild fires, atmospheric chemistry and others, thus the simulations need to incorporate all these aspects and provide weather and chemical forecasts for flight planning. The model is also used to put measured data in context during the experiment and to provide post-campaign analyses.

Finally, chapter 8 also analyses the effects of biomass burning smoke on weather, but in a completely different environment. The impacts of smoke generated in Africa over the south-east Atlantic stratocumulus deck are assessed. This is done in the framework of supporting the planning of a field campaign that plans to measure the smoke and cloud interactions, to generate input on the expected variability and effects of smoke.

All these applications point towards reducing uncertainties for aerosol estimates and interactions, which increase the reliability on the model and encourage its development and use in research and operations.

CHAPTER 2 FORECASTING URBAN PM10 AND PM2.5 POLLUTION EPISODES IN VERY STABLE NOCTURNAL CONDITIONS AND COMPLEX TERRAIN USING WRF-CHEM CO TRACER MODEL

Abstract

This study presents a system to predict high pollution events that develop in connection with enhanced subsidence due to coastal lows, particularly in winter over Santiago de Chile. An accurate forecast of these episodes is of interest since the local government is entitled by law to take actions in advance to prevent public exposure to PM10 concentrations in excess of 150 $\mu g/m^3$ (24 h running averages). The forecasting system is based on accurately simulating carbon monoxide (CO) as a PM10/PM2.5 surrogate, since during episodes and within the city there is a high correlation (over 0.95) among these pollutants. Thus, by accurately forecasting CO, which behaves closely to a tracer on this scale, a PM estimate can be made without involving aerosol-chemistry modeling. Nevertheless, the very stable nocturnal conditions over steep topography associated with maxima in concentrations are hard to represent in models. Here we propose a forecast system based on the WRF-Chem model with optimum settings, determined through extensive testing, that best describe both meteorological and air quality available measurements. Some of the important configurations choices involve the planetary boundary layer (PBL) scheme, model grid resolution (both vertical and horizontal), meteorological initial and boundary conditions and spatial and temporal distribution of the emissions. A forecast for the 2008 winter is performed showing that this forecasting system is able to perform similarly to the authority decision for PM10 and better than persistence when forecasting PM10 and PM2.5 high pollution episodes. Problems regarding false alarm predictions could be related to different uncertainties in the model such as day to day emission variability, inability of the model to completely

resolve the complex topography and inaccuracy in meteorological initial and boundary conditions. Finally, according to our simulations, emissions from previous days dominate episode concentrations, which highlights the need for 48 h forecasts that can be achieved by the system presented here. This is in fact the largest advantage of the proposed system.

Introduction

Santiago de Chile (33.5S, 70.5W, 500 m.a.s.l.) is a city with 6 million inhabitants located in a basin by the high central Andes. The city regularly faces severe air pollution related to particulate matter (PM) in winter due to emissions of particles and precursor gases, complex terrain and poor ventilation and vertical mixing (Rutllant and Garreaud, 1995; Rutllant and Garreaud, 2004; Garreaud *et al.*, 2002; Gallardo *et al.*, 2002). These conditions result in high PM concentrations (>300 $\mu g/m^3$ hourly PM10 sometimes reaching 600 $\mu g/m^3$) known as "episodes". Maximum PM concentrations occur mainly during the night, and in the western parts of the Santiago basin (e.g., Gramsch *et al.*, 2006).

The first air quality attainment plan was implemented in 1997, and it has been subject to revisions, the latest in 2009. Measures targeting large sources of emissions due to heating, transportation and industry resulted in reduced emissions and some improving in air quality. The plan includes a stipulation that a forecast model must be used to predict air pollution episodes in advance (MINSEGPRES, 2010). Three kinds of PM10 pollution episodes are defined based on Chile's 24 h mean PM10 standard of 150 $\mu g/m^3$, inspired by the former USEPA Air Quality Index for PM10, with the intention to limit acute exposure to air pollution. Alert is declared for 24-h average PM10 concentrations between 195 $\mu g/m^3$ (30% over standard) and 240 $\mu g/m^3$ (60% over standard), for which wood burning stoves are banned from operating. Pre-emergency is declared for concentrations between 240 $\mu g/m^3$ and 330 $\mu g/m^3$ (120% over standard) for which emissions are further reduced by restricting private transport use in the city by up to 40%,

alongside with restricting operation of ~500 industries that do not meet a strict emissions standard of 30 $\mu g/m^3$ of PM; and finally, an emergency is declared for concentrations over 330 $\mu g/m^3$ and this triggers even stricter pollution reduction measures (60% ban on private transportation, and up to 900 industries are banned from operating). However, the percentage of compliance with these regulations and the effective emission reduction during episodes is unknown. Measures must be announced at 8 pm to be applied from 7:30 am the next day.

The forecast model currently used by the authorities is the so called "Cassmassi model", which is a multivariate regression tool that weight tendencies on PM10 concentrations and 24 h forecasts of five discrete meteorological categories associated with synoptical and subsynoptical features linked to atmospheric stability (i.e., PMCA, Meteorological Potential of Atmospheric Pollution index) (Cassmassi, 1999). The decision on declaring episodes is not completely based on the results from the Casmassi model; it also involves a decision made by experienced air quality forecasters followed by a final political decision. For the moment, the focus is on PM10 and there is no prediction or measures taken for PM2.5 or any other pollutant.

Several approaches have been developed to predict air pollution episodes in the Santiago basin. Rutllant and Garreaud (1995) first showed that meteorological indexes for the Santiago basin could be computed using measured variables such as temperatures at different altitudes that correlate with PM measurements, and these could be used to predict episodes 12 h in advance. Neural networks, linear algorithms and clustering algorithms have been developed to forecast PM10 (Perez and Reyes, 2002, 2006) and PM2.5 (Perez and Salini, 2008) episodes. These models use measured variables (Temperature, PM) and prediction factors such as maximum temperature or the PMCA index for the next day to provide 30 h forecasts of air pollution episodes. To the knowledge of the authors, PM forecasts using deterministic air pollution models have not been performed for the city of Santiago, at least on an operational basis.

Predicting air quality using deterministic air pollution models is not an easy task and several initiatives have addressed its challenges (e.g., Baklanov, 2006). These studies point out the importance of an accurate representation of meteorology conditions at the city scale (e.g., Fay and Neunhäuserer, 2006), the importance of the meteorological scales (e.g., Palau *et al.*, 2005), the influences of terrain resolution on complex topography scenarios (e.g., Schroeder *et al.*, 2006; Finardi *et al.*, 2008; Shrestha *et al.*, 2009), the PBL scheme (e.g. Pérez et al., 2006) and urban PBL representation (e.g., Hamdi and Schayes, 2007), accurate surface fluxes description (e.g., Baklanov *et al.*, 2008), the use of meteorological and chemical data assimilation (Kim *et al.*, 2010; Pagowski *et al.*, 2010), and the need for integration with health exposure models (e.g., Baklanov *et al.*, 2007). Regardless of the type of model used to predict air quality, whether it is statistical or deterministic, most of them need an accurate forecast of meteorological variables.

In the case of Santiago, the key-meteorological condition to forecast is the establishment of coastal lows (CLs), which are disturbances that propagate along the coast such as the warm low-level lows. Rutllant and Garreaud (1995) identified two main patterns for the CLs: type A and type BPF. Type A corresponds to the onset of a CL in Central Chile moving southward along the coast. This coastal trough appears between an enhanced Pacific high to the west of the Andes and a migratory cold high east of the Andes. Type BPF is a prefrontal condition ahead of a weak and often occluded front, which slows down or becomes stationary when reaching Central Chile. Typically, CLs of type A produce more intensive air pollution episodes than those of type BPF. The start of the high concentration episodes associated with type A coastal lows coincides with a sharp decrease in boundary layer height due to the establishment of easterly winds in connection with the subsynoptic disturbance. The easterly winds are forced to subside by the high Andes giving rise to adiabatic compression and therefore to an enhancement of the subsidence inversion and clear sky conditions, possibly accelerating secondary

aerosol formation due to intense photochemistry (Gallardo *et al.*, 2002). The end of the episodes typically occurs in connection with humid air advection from the coast along the east-west valleys and the appearance in the Central Valley of Chile of fog conditions, which follows from the reestablishment of westerly winds near the surface and a weakening of the subsidence inversion, which in turn diminishes rapidly the pollutant concentrations in the basin. The intensity and duration of CLs varies depending on the overall synoptic configuration, the intensity of the weather systems involved and both the largeand local-scale topography. Regional scale models capture these features but they have difficulties ascertaining the rapid changes associated with the onset and end of coastal lows (Garreaud *et al.*, 2002; Gallardo *et al.*, 2002).

There is a strong correlation between carbon monoxide (CO) and PM measurements in the Santiago monitoring network (Perez *et al.*, 2004), especially for the high values (>4 ppm of CO). Hence, in principle, by predicting CO one can also forecast PM levels. In terms of air quality modeling, CO might be easier to forecast than PM for several reasons: 1) Santiago CO emissions are better constrained than PM emissions (Jorquera and Castro, 2010; Saide *et al.*, 2009a); and 2) At the city scale CO behaves as an inert gas phase tracer only subject to atmospheric transport and mixing (e.g., Saide *et al.*, 2009a) while PM responds to complex heterogeneous chemistry, aerosol dynamics and wet and dry removal processes (e.g., Seinfeld and Pandis, 2006).

In this paper we present a forecast system for CO for Santiago using the WRF-Chem platform (Skamarock *et al.*, 2008; Grell *et al.*, 2005). We evaluate the predictions of CO and meteorological data against local observations for different settings of the model trying to find an optimum configuration. We then explore the use of CO predictions to produce PM10 and PM2.5 forecasts by applying a linear conversion. The PM forecast is tested for a whole winter period and results are compared to the authority decisions. Finally, the need for two days or more forecast is discussed and the settings for the operational simulation are established.

Methodology

Observations

Air quality data

Data for 2008 were obtained over the internet from the Ministry of Environment (http://sinca.mma.gob.cl/). The official monitoring network MACAM2 consisted in 2008 of eight monitoring stations that reported different criteria pollutants on an hourly basis. All stations had CO and PM10 monitors and five had PM2.5 monitors for the period analyzed. These stations were also equipped with temperature, wind and relative humidity monitors. This network was recently expanded by including three new sites: one on the northwestern part of Santiago, one in the South and one in the Maipo Valley entrance, all with CO, PM10 and PM2.5 monitors.

Meteorological data

MACAM2 stations measure temperature, wind and relative humidity. We also use data collected by the National Center for the Environment (http://aire.cenma.cl/) which consists of 10 surface stations that measure additional meteorological information, such as incoming radiation, pressure and precipitation. Their locations are more spread out over the domain, providing information not only in the basin, but also in the surrounding mountains. Daytime mixed layer for cloud free days were provided from a ceilometer located in the Department of Geophysics of the University of Chile (DGF) in downtown Santiago (Muñoz and Undurraga, 2010). For this study, none of these observations are assimilated; rather they are used to evaluate the predicted fields. Locations and names for stations from both networks and DGF station in the domain of study can be found in Fig. 2.1.

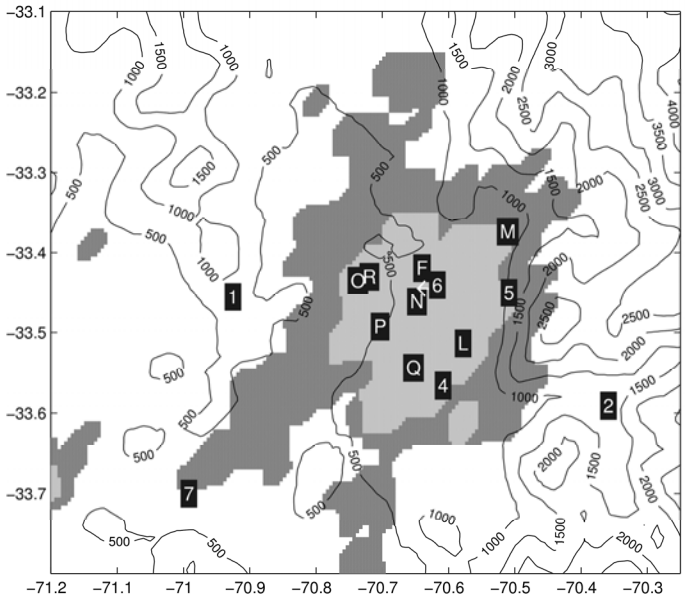

Figure 2.1. Map showing locations of MACAM2 (letters) and CENMA (numbers) stations, topography (m.a.s.l) and the existence of urban land cover for USGS (light gray) and MODIS (light plus dark grey) data. MACAM2: F: Independencia, L: La Florida, M: Las Condes, N: Parque O'Higgins, O: Pudahuel, P: Cerrillos, Q: El Bosque, R: Cerro Navia. CENMA stations: 1: Lo Prado, 2: El Manzano, 3 and 4: La Platina, 5: La Reina, 6: Entel (note this station is moved, original location pointed by white arrow), 7: El Paico. DGF ceilometer station is 600m north from Parque O'Higgins station.

General model settings and emissions

In this study we use the WRF-Chem model, with the objective to produce CO forecasts during the winter in Santiago. The present system uses WRF-CHEM v3.1.1 and v3.2 meteorological and air quality simulations (Skamarock *et al.*, 2008; Grell *et al.*, 2005). This is a fully coupled online model that enables air quality simulations at the same time as the meteorological model runs, improving its potential for operational forecasts. For the city scale studied here, CO can be considered as a passive tracer (Saide *et al.*, 2009a; Jorquera and Castro, 2010). The tracer assumption is reasonable due to the relatively long life time of CO (order of months, Seinfeld and Pandis, 2006) together with the fact that the residence time of pollutants in the basin is usually not more than 2 days for the worse episodes (see Results and discussion section). A background value of 0.08

ppm is used as CO initial and boundary conditions since no relevant sources are found up-wind from the Santiago.

Two sets of CO emissions were used. The first one is an emission inventory updated by the environmental agency based on the 2000 inventory, which has been used in previous works (Schmitz, 2005; Saide *et al.*, 2009a; Saide *et al.*, 2009b). Emissions due to mobile sources, which contribute ~90% of total CO emitted for this year, are based on the approach by Corvalán *et al.* (2002). The emission inventory is available spatially (2 km resolution) and temporary distributed (1 h resolution for a representative day of the year).

The second set of emissions is a CO emission inventory developed for this study. It uses the same total amount of CO as the first inventory (200,000 ton/yr), but it has a different temporal and spatial distribution. It has been shown that population density is a good proxy for road density which can be used to distribute traffic emissions (Saide *et al.*, 2009b). In this inventory emissions are spatially distributed using Landscan 2008 population data at 30'' (Dobson *et al.*, 2000), as proposed by Mena (2007). Saide *et al.* (2009a) and Jorquera and Castro (2010), which use different total emissions but same methodology to spatially distribute them, found an overestimation of emissions in the downtown area where the 2000 emission inventory shows the highest values. Thus, by using population as a proxy for distributing emissions (and thus the complete road network), these emissions are more spread out over the city and less concentrated downtown. Another feature of using Landscan data is the representation of the growth of the city in the last years, not represented by the 2000 official emission inventory. The temporal resolution used corresponds to average traffic counts over the city distinguishing each day of the week (Corvalán *et al.*, 2002).

Temporal and spatial distribution of wood burning (W.B.) emissions is not considered in the 2000 official emission inventory, but it is thought to be an important factor influencing episodes (Jorquera and Castro, 2010), since these emissions occur

mainly during evening and nighttime periods. In the 2005 official emission inventory CO W.B. emissions are estimated as 3.5% of the total CO emissions. However, considering that these emissions occur only during four months of the year, the percentage contribution of W.B. to CO emissions increases to 9.8% for these months. For PM10 and PM2.5 these percentages were estimated to be 7.8% and 25.8%, respectively. These estimates are very uncertain since W.B. emission factors have a broad variation, illegal burning is not taken in account, and fugitive dust sources, that contribute with 80% of PM10 emissions, are thought to be largely overestimated (Jorquera and Castro, 2010). Thus the contribution of W. B. stated before is possibly underestimated. As a first estimation, W.B. emissions are considered to be 30% of the total which were obtained by model simulations using different trials. For the spatial distribution the amount of stoves per municipality is used, extracted from the official 2005 emission inventory, and weighted by population to avoid placing emissions in uninhabited regions. The diurnal profile is assumed to be a step pattern starting at 6 pm and finishing at 1 am with half steps at these extremes, making a total of 7 h of use a day.

The final model configuration and emissions used were determined by extensive testing and are discussed in the Results and discussion section.

PM10 and PM2.5 forecast model

During high pollution episodes in the city of Santiago, CO and PM hourly observations show a high correlation (Perez *et al.*, 2004) as shown in Fig. 2.2a. This linear behavior is not accurate for low concentrations, but it is clear for high concentrations (>4 ppm of CO), indicating the close relationship between CO and PM during episodes. Moreover, the correlation increases when the 24-h means are applied over the hourly data (from 0.93 to 0.98 for the period and station analyzed shown in Fig. 2.2) and the linear model is also valid for the low 24-h mean concentrations. The time series for four months of winter 2008 was investigated, not finding any peak where both

PM and CO were not correlated, showing that episodes are related to cases where both CO and PM are co-emitted. This behavior is not only shown when comparing observations, but also when comparing model predictions of CO and PM. The full chemistry model CBMZ-MOSAIC (Zaveri *et al.*, 2008) was run for the eight day period simulated on section 3.1. Hourly data comparison between modeled CO and PM2.5 shows a correlation of 0.98 for critical stations (not shown), which is even higher than the observed correlation. Thus, when predicting episodes for the case of study, there is not much that can be improved by using the full chemistry-aerosol compared to the CO tracer in terms of the type of episode forecasted. However, there is a great savings in computing time when running the tracer model, which allows for faster forecast cycles, use of more updated meteorological analysis and observations, and the dedication of computing time to more important aspects of the forecast like model resolution (see Results and discussion section).

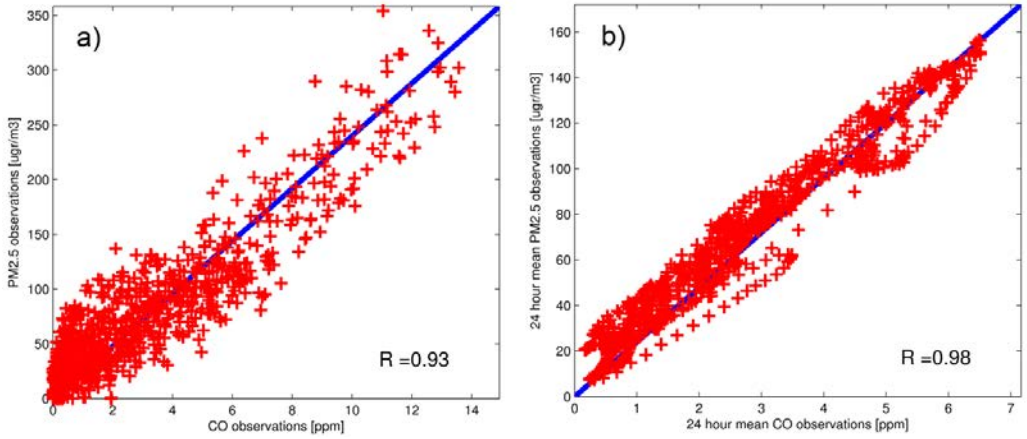

Figure 2.2. Dispersion plots between CO observations converted to PM2.5 and PM2.5 observations for Cerro-Navia monitor. a) Hourly data. b) 24-hour moving mean. Units in µgr/m^3.

Thus, by accurately predicting CO, a good estimation of PM10 and PM2.5 24 h mean can be made using a linear conversion. This linear model corresponds to a

multiplication by a constant that changes the units from modeled CO to predicted PM10 or PM2.5, which can be estimated by different techniques. One way is to estimate it by using the mass ratio of the emissions inventory for each species. However, official PM10 and PM2.5 emission inventories for Santiago might be greatly overestimated (Jorquera and Castro, 2010) making this option unreliable. A second way is to calibrate the model comparing modeled CO with PM10 and PM2.5 observations and computing the factors for each station. This option is also used to remove biases between model and observations that could be station dependent. Another aspect to consider is the fact that episodes tend to concentrate on weekends as observed by Rutllant and Garreaud (1995). Considering observed episodes from years 2002-2009, 40% of the alerts and 44% of the pre-emergencies happened on weekends, where if there were no accumulation on weekends this number would be 29% (2 weekend days for every 7 days that a week has, 2/7 = 0.29). This behavior is directly related to emissions on Friday night and Saturday night that accumulate after the PBL collapses (see Results and discussion section). These additional emissions could be related to traffic activity (traffic counts show increase for these periods), wood burning (2005 emission inventory shows one additional hour of W.B. for weekends,CONAMA, 2007) or other activities (e.g. increased activity in restaurants or private barbecues, illegal industrial activity). Due to the high uncertainty in these emissions it remains difficult to produce an emission inventory for these days. Therefore, we adopt the solution of making the factors weekend-week day dependent. Finally, the CO to PM conversion can be written as the following:

$$P\text{M\_MOD}(\text{station}, \text{time}) = \text{F}(\text{station}, \text{weekend flag}) * \text{CO\_MOD}(\text{station}, \text{time}) \quad (1)$$

where MOD indicates model values. We choose a simple calibration for the conversion factor F:

$$\text{F}(\text{station}, \text{weekend flag}) = \frac{\sum_{\text{t} \in \text{ weekend flag}} \text{PM\_OBS}(\text{station}, \text{t})}{\sum_{\text{t} \in \text{ weekend flag}} \text{CO\_MOD}(\text{station}, \text{t})} \quad (2)$$

where OBS indicates observation values. For calibration, a representative period must be chosen that contains episodes for both weekend and week days. In order to fit the factor to high concentrations (where CO and PM hourly concentrations are linear) we calibrated the model with values of days where hourly CO observations greater than 4 ppm were measured. After calibration, the conversion factor is not changed for further analysis. Once the hourly PM has been computed with Eq. (1), the 24 hour moving average is calculated and the forecast is produced. The decision to declare episodes is typically taken at 8pm the day before, thus observations until 8pm are available to be used in the forecast. The 24h average is computed using observations until 8pm and the PM model further on. The following analysis is focused on the two critical stations (Pudahuel and Cerro Navia) located on the west-north side of the city, as they are the ones that usually reach alert or pre-emergency values triggering the declaration of PM10 episodes. However, to declare episodes, all stations are taken into consideration. The period analyzed goes from May 1st to August 31th of 2008, covering the whole period of episodes of that year.

Results and discussion

Finding WRF-Chem optimal settings for forecasting episodes

Several simulations were performed in order to find the optimum WRF-Chem configuration to represent meteorology and CO observations occurring for high pollution episodes. A period of 8 days was selected for testing, from May 26th to June 2nd of 2008. This was a period with high PM concentrations and with three episodes declared by the authorities (2 of them corresponding to Pre-emergencies). A coastal low of type A was observed during May 29th and 30th followed by a BPF episode on May 31st and June 1st evolving to a rapid advection of cold and humid air on June 2nd that generated cleaner conditions.

Land Use data

WRFv3.1.1 allows the use of USGS (U.S. Geological Survey) and MODIS (Moderate Resolution Imaging Spectroradiometer) land use (Skamarock *et al.*, 2008). WRF-Chem currently allows the use of USGS data. In Figure 2.1 the difference in urban land use between the data sets are plotted showing an underestimation of urban land cover by the USGS data, probably due to the use of old maps. In order to use an updated urban land cover with WRF-Chem the USGS WRF input files were modified by replacing the urban land cover by the MODIS data. The rest of the USGS categories remained the same, and are only modified to account for the change in urban land cover. This modification allows a more realistic and updated representation of the urban conditions.

Meteorological Initial and Boundary conditions

Three types of meteorological initial and boundary conditions were tested: FNL (GFS final analysis, Wu *et al.*, 2002); NCEP-NCAR reanalysis (Kistler *et al.*, 2001); and NCEP-DOE reanalysis (Kanamitsu *et al.*, 2002). Similar results were found running with either NCEP-NCAR or the NCEP-DOE reanalysis. The use of FNL improved the representation of the coastal low developed during this period, producing a higher temperature increase in the middle troposphere (see temperature in station Lo Prado, Fig. 2.3), which further lowered the base of the inversion and increased CO concentrations. Other characteristics of coastal lows (Garreaud *et al.*, 2002; Garreaud and Rutllant, 2003) such as abrupt decrease in relative humidity, and a shift in the wind direction and clear sky conditions are also obtained in agreement with observations (not shown). This shows the importance of initial and boundary conditions in order to accurately represent the meteorological conditions.

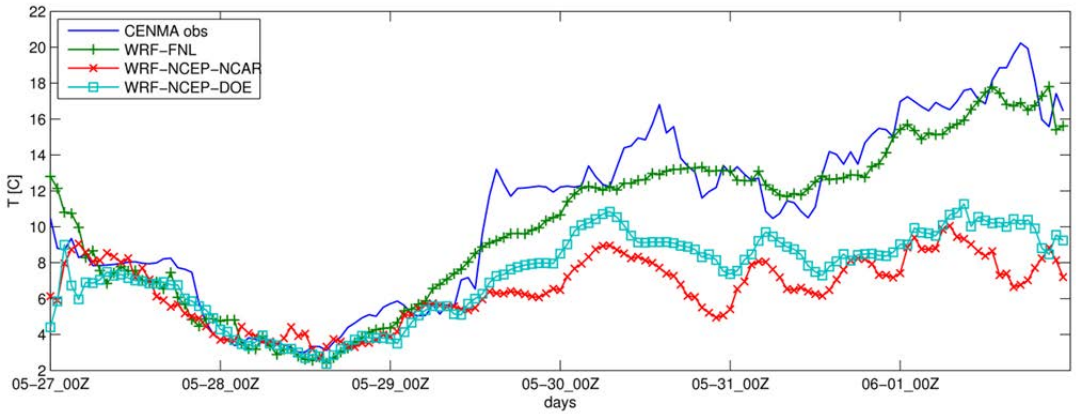

Figure 2.3. Observed and modeled temperature evolution on high altitude station Lo Prado during an episode using different meteorological initial and boundary conditions. Time in UTC (local = UTC – 4 for winter in Santiago).

PBL parameterization

The choice of the PBL scheme is a key aspect in predicting pollution levels in Santiago and elsewhere. WRF allows the choice of ~10 PBL schemes which support urban canopy models (which are not used in this case due to unavailability of detailed urban land cover). Seaman *et al.* (2009) showed sensitivity runs over night and steep terrain conditions and found that really high resolution in the vertical (2 m close to the surface) and in the horizontal (~0.44 km) are both needed to accurately represent the low magnitude winds found under stable conditions. These resolutions cannot be achieved by all PBL schemes since they are not designed to work with really fine vertical resolution. Four schemes that work under these conditions were tested: MYJ (Janjić, 2002); QNSE (Sukoriansky *et al.*, 2005); MYNN (Nakanishi and Niino, 2004); and YSU from WRFv3.2 (Hong, 2010). CO correlations at critical stations (Pudahuel and Cerro Navia) were used to check the stability behavior during night, since correlation is more sensitive to higher values and it gives a measure of whether the meteorological patterns needed to transport nighttime plumes are being represented or not. Table 2.1 presents statistics showing that all schemes behave similarly in terms of wind and temperature agreement

with observations, but the CO correlation is clearly better represented by the MYNN PBL scheme, probably due to a better representation of the vertical profiles. Figure 2.4.a shows big differences within diagnosed PBL height for different schemes and overestimation by all schemes of the observed diurnal PBL height. However, the MYNN scheme shows the closest agreement in terms of magnitude (presents the lowest error), shape (captures the growing of the PBL height) and tendency of the maximum values over the days (MYNN scheme shows the minimum PBL on May 30th, same as the observations) which might be some of the reasons why CO correlations are better when using this scheme. The MYJ scheme, that does a fare job on PBL height and showed the best predictions of temperature and wind, presents problems by not mixing enough in the vertical, resulting in the accumulation of fresh emissions in the first layer creating unrealistic high peak concentrations when the plume passes over a station (see Fig. 2.4.b). The choice of PBL scheme can also change the way the plume's movement through the basin is represented. For instance, for July 1st almost all the schemes showed similar drainage of the plume through the Maipo river basin, but the MYNN scheme showed the least, resulting in higher nighttime concentrations (see Fig. 2.4.b). A typical basin flow pattern that produces episodes in the stations located in the NW is shown in Fig. 2.5 when using the MYNN scheme. When the PBL collapses, emissions start to accumulate (Fig 2.5.a) and the plume moves slowly towards the NW stations peaking around 0 to 2 am (Fig 2.5.b). Different days can have different patterns. For instance, for the one shown in Fig. 2.4, the plume partially leaks through the Maipo river basin and also stays meandering around these stations during the whole night (Fig. 2.5.c) and adds to fresh morning emissions on the next day (Fig 2.5.d). Even though PBL schemes show differences, sometimes over a factor of four within each other on diurnal PBL height (Fig. 2.4.a), all schemes show similar CO concentrations magnitudes during the night (Fig 2.4.b), showing that accumulation probably relates to fresh emissions emitted after

the PBL collapses. However, an accurate diurnal PBL height representation is critical for pollutants showing diurnal peaks such as ozone and must be included in these analyses.

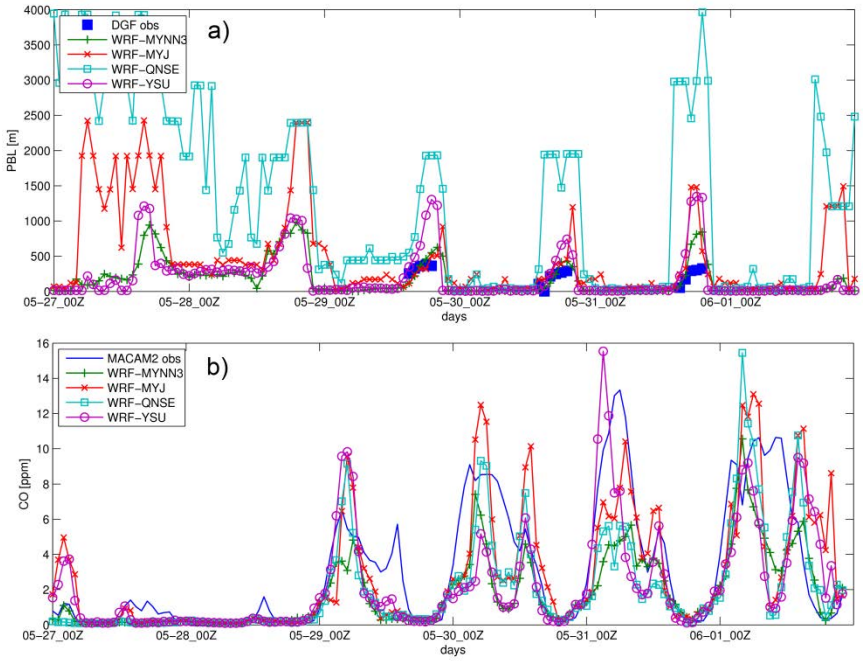

Figure 2.4. Observation versus model time series using different PBL schemes. a) PBL for DGF station. b) CO for averaged Pudahuel and Cerro Navia stations.

For these reasons the MYNN scheme is chosen as the PBL scheme in subsequent model simulations. Two levels of closure for this scheme are available and were tested: 2.5 and 3. Even though the level 3 closure shows slightly improved results (Table 2.2), level 2.5 is chosen since it was found to be numerically more stable. Table 2.2 also shows that using gravitational settling of fog, slope radiative effects and topography shading does not improve the results for the period analyzed; thus they were not used in further simulations. In the WRF-Chem model, vertical diffusion coefficients are computed in the meteorological module and then passed to the Chem routines where sometimes they are filtered by applying minimum value thresholds. For the present study no thresholds were

applied, which enables the model to go to high stability conditions and produce the observed night-time maximum concentrations.

Table 2.1. Correlation coefficient (R), Root mean square error (RMSE, in ppm), Mean absolute error (MAE) and Index of Agreement (IOA) for carbon monoxide (CO, ppm units) at Pudahuel and Cerro Navia stations and for temperature (T, Celsius units) and wind speed (WS, m/s units) for all MACAM2 stations combined using different PBL schemes.

		MYNN3	MYJ	QNSE	YSU
CO	R	0.78	0.66	0.70	0.59
	RMSE	2.75	2.94	2.85	3.17
T	MAE	1.37	1.29	1.43	1.48
	IOA	0.96	0.96	0.95	0.95
WS	MAE	0.66	0.57	0.62	0.60
	IOA	0.45	0.48	0.44	0.42

Notes: MYNN3, MYJ and QNSE are for WRFv3.1.1 and YSU for WRFv3.2. All runs use the same configuration: WSM3 microphysics, RRTM long wave radiation, Dudhia short wave radiation, thermal diffusion scheme for surface model, 39 vertical levels and 2km horizontal resolution.

Horizontal diffusion

In steep terrain simulations the use of diffusion in physical space is recommended rather than on coordinates surfaces (Skamarock *et al.*, 2008). When diffusion on coordinate surfaces was used we found that pollutants tended to diffuse out through the mountains surrounding the basin, not allowing the night accumulation shown by observations. This problem is supposed to be fixed when using diffusion on the physical space. However, we found that the model was very unstable when this option was used. The best option was to use no horizontal diffusion on the inner domain and allow diffusion on the coarser domains by means of the 6th order horizontal filter (Skamarock

et al., 2008). This option generates the desired effect of accumulation in the basin during nighttime. Even though no horizontal diffusion scheme is used on the most inner domain, numerical diffusion and diffusion due to changes in wind direction from one time step to the next one due to the fully coupled model used still occur.

Table 2.2. Statistics as in Table 2.1 for sensitivity studies changing model configuration

		MYNN2.5	MYNN3	MYNN3 g.s.	MYNN3 s.s.
CO	R	0.72	0.78	0.77	0.74
	RMSE	2.86	2.75	2.82	2.75
T	MAE	1.42	1.37	1.36	1.47
	IOA	0.96	0.96	0.96	0.95
WS	MAE	0.66	0.66	0.65	0.71
	IOA	0.47	0.45	0.48	0.44

Notes: Different cases are using the MYNN2.5 and MYNN3 PBL schemes and using MYNN3 with additional options as gravitational settling of fog (g.s.) and topography shading and slope radiative effects (s.s). WRF settings are the same for all cases and as described in Table 2.1.

Vertical grid resolution

Garreaud and Rutllant (2003) proposed high resolution vertical layers in the PBL in order to better represent fluxes and vertical mixing (mean layer thickness equal to 70 m below 1 km), which produces a better representation of coastal lows. This configuration was refined by Rahn and Garreaud (2010) especially on the levels close to the ground. Seaman *et al.* (2009) showed improvements in performance in steep terrain and stable conditions during night by using 11 vertical levels in the first 68 m (first 10 m with 2 m level thickness). Combinations of these settings were tested (see Table 2.3) imitating Seaman et al. (2009) configuration (44 levels), another with 39 levels with the

first layer at 10m and six levels below 100 m (closer to Rahn and Garreaud, 2010), and another using the standard GFS configuration (28 levels). Results show that the finer resolution runs considerably improved results for CO, temperature and wind speed. In order to run with 44 levels (5 levels below 10 m) the time step must be reduced making it less feasible for operational forecasts. Furthermore, the differences between using 44 vertical levels or 39 levels were small. Thus the 39 vertical levels resolution is chosen for subsequent runs.

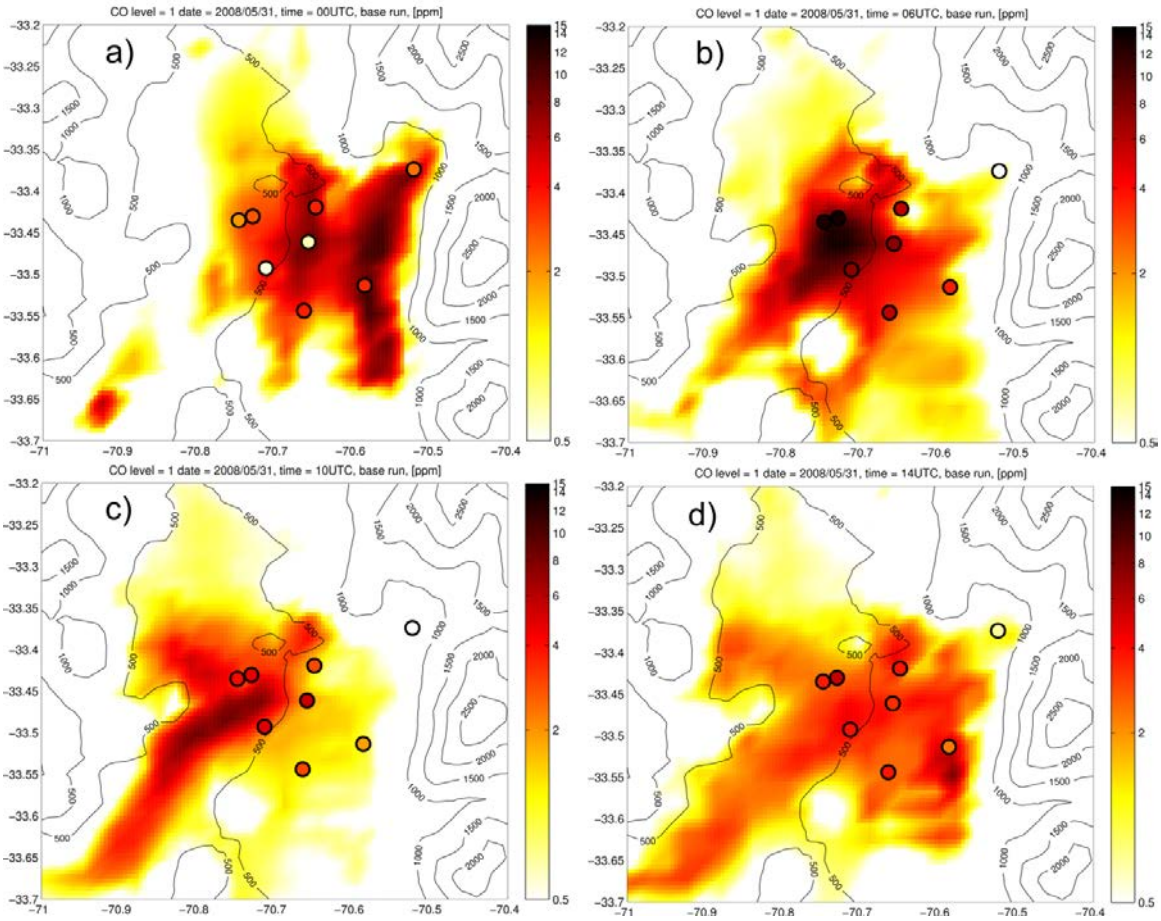

Figure 2.5. CO maps for the first model level for different times. “a” is for 9pm, “b” for 2am, “c” for 6am and “d” for 10am local time. Model configuration is the same as described in table 2.1 using the MYNN3 PBL scheme. For station names see Fig. 2.1. Units in ppm.

Table 2.3. Statistics as in Table 2.1 where different cases are using different vertical resolution.

		44 VL	39 VL	28 VL
CO	R	0.72	0.72	0.68
	RMSE	2.81	2.86	3.77
T	MAE	1.59	1.42	2.04
	IOA	0.95	0.96	0.90
WS	MAE	0.80	0.66	1.25
	IOA	0.43	0.47	0.26

Notes: WRF settings are the same for all cases and as described in Table 2.2 using MYNN2.5 PBL scheme. See text for details on vertical levels.

Horizontal grid resolution

Previous studies for the same area and similar objectives found that 2 km resolution in the inner domain produced good results (Jorquera and Castro, 2010). Other studies for different areas that tried to represent stable conditions in steep terrain found that using 1km (Shrestha *et al.*, 2009) and ~400m (Seaman *et al.*, 2009) increased performance. In this study three different grid sizes were analyzed: 6 km, 2km and 667m, using nesting from the coarser one to the finer ones and starting from an 18km coarser grid spanning from -44º to -24º on latitude and -88º to -63º on longitude. Results were extracted from different simulations in order to use 2-way nesting except for the 667m domain run, where 2-way nesting was not used due to instability issues. All the runs were performed with the MYNN3 PBL parameterization. When going from 6km to 2km horizontal resolution there is a sharp increase in accuracy in CO and wind speed model performance, probably due better terrain representation, but not so in temperature which is barely changed (see Table 2.4). However temperature, winds and CO predictions did not improve much when going from 2 km to 667m. This feature could be related to the MYNN PBL scheme and/or not using 2-way nesting (e.g., Palau *et al.*, 2005).

Table 2.4. Statistics as in Table 2.1 where different cases are using different horizontal resolution.

		667m	2km	6km
CO	R	0.73	0.78	0.51
	RMSE	2.74	2.75	3.97
T	MAE	1.49	1.37	1.38
	IOA	0.95	0.96	0.95
WS	MAE	0.80	0.66	0.83
	IOA	0.35	0.45	0.42

Notes: WRF settings are the same for all cases and as described in Table 2.2 using MYNN3 PBL scheme.

Other options

Radiative feedbacks generated by clouds play an important role on CO nighttime concentrations. The RRTM long wave radiation and Dudhia short wave radiation schemes (Mlawer *et al.*, 1997; Dudhia, 1989) were chosen in order to correctly capture the cloud optical depth effects on solar radiation effects (Skamarock *et al.*, 2008). Many microphysics schemes were tested and only the WSM 3-class (Hong *et al.*, 2004) was successful in representing cloud coverage. All the other schemes largely underestimated cloud coverage for all PBL schemes tested (not shown). The reasons for this behavior are being explored and could be related to the specific configuration, such as resolution, low time step or not using horizontal diffusion. The new Grell Scheme is used for Cumulus parameterization and a thermal diffusion scheme for surface physics (Skamarock *et al.*, 2008).

Emission inventory

All the previous sensitivity simulations were performed using the official 2000 emission inventory mentioned earlier. However, since these emissions have been shown to be over-estimated in the downtown area, the modified emissions were tested using the

same WRF configuration. Table 2.5 shows that the use of the modified emissions inventory outperforms the old 2000 emission inventory, as shown by the increase in the correlations at all stations. This increase in performance is also reflected in the correlation with PM10 and PM2.5. When using the new emission inventory with W.B. emissions the correlation improved for CO, PM10 and PM2.5 for most stations compared to the results with the new emissions but without W.B, indicating a substantial contribution from wood burning to the episodes. The improvements in accuracy when using the new emissions is clearer when comparing modeled and observed CO time series for the critical stations (Fig. 2.6). It is important to note that when using the W.B. inventory, emissions are extended to 1AM based on surveys on wood burning hours of use, but even with this extension the concentrations tend to decay at the same time as those results that did not consider W.B (see Fig. 2.6). This decay appears to be due to advection and not to a wrong temporal resolution of emissions, which seems to be a modeling inaccuracy because observations do not show this fast decay, moreover they sometimes show a second peak of PM that is relevant to triggering episodes.

PM10 and PM2.5 forecast model performance

A summary of the calibration factors used for this study is shown in table 2.6. On average, conversion factors are over 10% higher in week days than in weekends and can go over 30% for specific stations, showing the effect discussed in section 2.3. For PM10, there is not much variability for factors in between stations, while for PM2.5 the variability is greater due to station “Independencia” that has double the factor than the rest of the stations where the factors are similar. The behavior on this station is also observed in CO to PM10 factors but to a lesser extent. As shown by Table 2.5, this station is also the one with the lowest CO and PM observation correlations, so there are probably local sources of emission that create these differences and change the behavior for this station.

Table 2.5. Correlation coefficient computed using observations and model simulations for different emission inventories.

		F	L	M	N	O	P	Q	R
Obs CO	Inv2002	0.31	0.38	0.60	0.44	0.73	0.65	0.71	0.78
	New Inv	0.43	0.60	0.64	0.68	0.84	0.80	0.74	0.83
	New Inv+W.B.	0.61	0.69	0.63	0.79	0.87	0.84	0.82	0.86
Obs PM10	Inv2002	0.62	0.54	0.67	0.66	0.65	0.75	0.71	0.74
	New Inv	0.63	0.72	0.69	0.79	0.75	0.85	0.75	0.79
	New Inv+W.B.	0.68	0.73	0.56	0.80	0.76	0.85	0.79	0.80
	Obs CO	*0.69*	*0.81*	*0.80*	*0.78*	*0.92*	*0.91*	*0.90*	*0.93*
Obs PM2.5	Inv2002	0.53	-	-	0.37	-	0.63	0.66	0.81
	New Inv	0.61	-	-	0.57	-	0.75	0.73	0.87
	New Inv+W.B.	0.72	-	-	0.70	-	0.79	0.82	0.89
	Obs CO	*0.80*	-	-	*0.85*	-	*0.92*	*0.92*	*0.96*

Notes: First column are CO, PM10 and PM2.5 observations and second column WRF simulations using the official 2000 emission inventory (Inv2000), using the emissions developed with Landscan (New Inv) and adding a 30% of wood burning for heating emissions (New Inv +W.B.). Also Correlation between PM and CO observation is computed (in italic). For station names refer to Fig. 2.1.

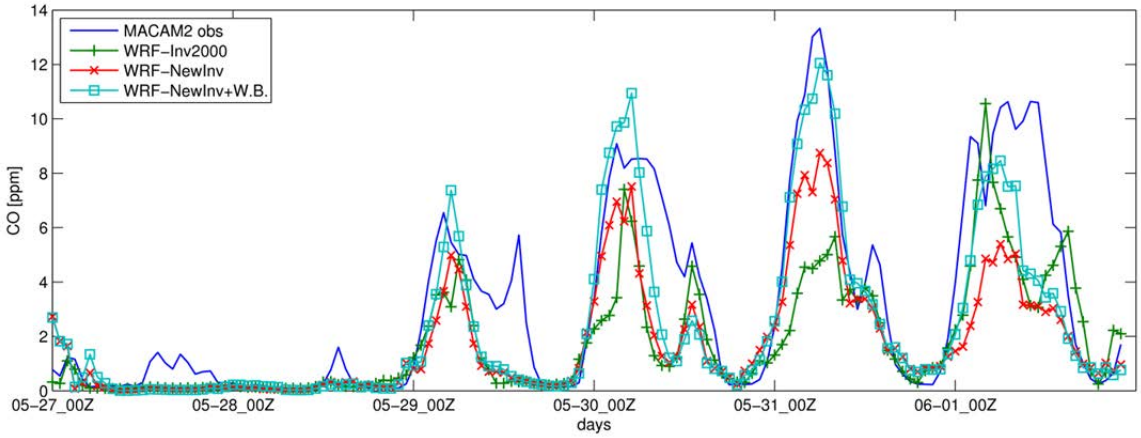

Figure 2.6. Observation versus model time series using different emission inventories for averaged Pudahuel and Cerro Navia stations. Refer to table 2.6 caption for legend explanation.

Figure 2.7 shows time series of the 24-hour moving mean for PM10 and PM2.5 observations and predictions for one station. Horizontal lines in these figures represent the thresholds for classifying the different episode types. The PM10 thresholds are the same as stated before. Currently there are no official thresholds for PM2.5 in Santiago, so we use the values recommended by Perez and Salini (2008) based on US-EPA present and previous standards, i.e. Air quality index for PM2.5 (http://www.airnow.gov/). The thresholds are: 35 $\mu g/m^3$; 65 $\mu g/m^3$; and 100 $\mu g/m^3$. The forecasts results are also shown in terms of contingency tables in tables 2.7 and 2.8. These are generated using observed and modeled data for all stations. For PM10, since there have not been emergency episodes since 1998, this kind of episode is not taken into account in the forecast contingency table. Using the record of the episodes declared by the authority and the observational data, a contingency table can be built for the Authority decision. A table with persistence (episode observed the day before is forecasted) is added as a reference, since observations from 9 to 11 pm are not available by 8pm, which is the time when the forecast must be issued, making this type of forecast unavailable.

Table 2.6. Statistics for CO to PM10/PM2.5 conversion factors.

		Week day	Week end
PM10	Mean	51.1	57
	Std. Dev.	8.4	9.4
PM2.5	Mean	26.7	31.5
	Std. Dev.	8.5	7.5

Note: Units in $\mu gr/m^3$/ppm.

When comparing the authority decision table with the one from the forecast model (Table 2.7) it can be seen that our simulations produce statistics similar to the expert and politically mediated decision made by the authority. The forecast model has

the tendency to predict false alarms on pre-emergencies and alerts, which is analyzed further in the text. Overall, our model does similar as persistence, but is able to correctly forecast almost twice as many episodes (persistence does a better job for non-episode days). The contingency table for PM2.5 (Table 2.8) shows a similar trend as for PM10, again overestimating episodes and behaving better than persistence for the higher concentration episodes.

Table 2.7. Comparison of contingency tables for the expert and politically mediated authority decision (a), the PM10 model developed (b) and persistence (c) (see text for details).

a)Authority 2008		Forecasted A	B	C	Tot	%O
Observed	A	88	13	1	102	86%
	B	5	7	3	15	47%
	C	1	1	4	6	67%
	Tot	94	21	8	123	
	%F	94%	33%	50%		**80%**

b)CO PM10 2008		Forecasted A	B	C	Tot	%O
Observed	A	85	12	7	104	82%
	B	5	5	4	14	36%
	C	0	2	4	6	67%
	Tot	90	19	15	124	
	%F	94%	26%	27%		**76%**

c)Persistence 2008		Forecasted A	B	C	Tot	%O
Observed	A	93	8	3	104	89%
	B	10	3	1	14	21%
	C	1	3	2	6	33%
	Tot	104	14	6	124	
	%F	89%	21%	33%		**79%**

Note: Case A is no episode, B alert and C pre-emergency.

It can be seen from Fig. 2.7 that the model follows the trend of the observations. However, there are several points where the observations and model diverge. The most common error observed in the forecast is the over prediction of concentrations, which often occurs the day after high concentrations are observed (e.g. June 14th, June 17th,

June 25th, July 2nd, July 4th) creating the false alarms mentioned earlier. For the seven forecasted pre-emergencies and no episode observed (Table 2.7, b), three days obey to this type of behavior and the rest is just high observed levels (over 150 μgr/m^3 in 24 hour mean) that did not make it to an episode, probably due to emission inaccuracies.

Table 2.8. Contingency table for the PM2.5 model developed (a) and for persistence (b).

a) CO PM2.5 2008		Forecasted A	B	C	D	Tot	%O
Observed	A	4	7	0	0	11	36%
	B	1	22	16	7	46	48%
	C	0	5	15	16	36	42%
	D	0	1	3	27	31	87%
	Tot	5	35	34	50	124	
	%F	80%	63%	44%	54%		**55%**
b) Persistence 2008		Forecasted A	B	C	D	Tot	%O
Observed	A	8	3	0	0	11	73%
	B	4	28	12	2	46	61%
	C	0	12	18	6	36	50%
	D	0	2	6	23	31	74%
	Tot	12	45	36	31	124	
	%F	67%	62%	50%	74%		**62%**

Note: Case A is no episode and B, C and D episodes with increasing thresholds as defined in the text.

When looking into detail on these false alarm days after a day of high concentrations, all days agree in the fact that a partial cleaning of the basin is observed. On these days, the western stations ("Pudahuel", "Cerro Navia" and "Cerrillos") show low concentrations during the night, while the rest of the central-eastern stations present high concentrations, which the model is not able to resolve and instead maintains high concentrations on the western stations (which are the critical ones) and creating the false

alarm. This behavior is usually associated with a surface wind jet that enters through the basin (observed by “El Paico” station, Fig. 2.1) and then diverges north due to topography cleaning the western stations (high wind also observed in “Pudahuel”) but never reaching the central and eastern stations, which is also not represented by the model. The reasons why the WRF simulations are not able to capture this partial cleaning of the basin could be related to potential errors in thermodynamics, inability to resolve the complex topography, inaccurate cloud representation or issues on meteorological initial and boundary conditions. The last two points could be tackled with the use of meteorological data assimilation when performing operational forecasts.

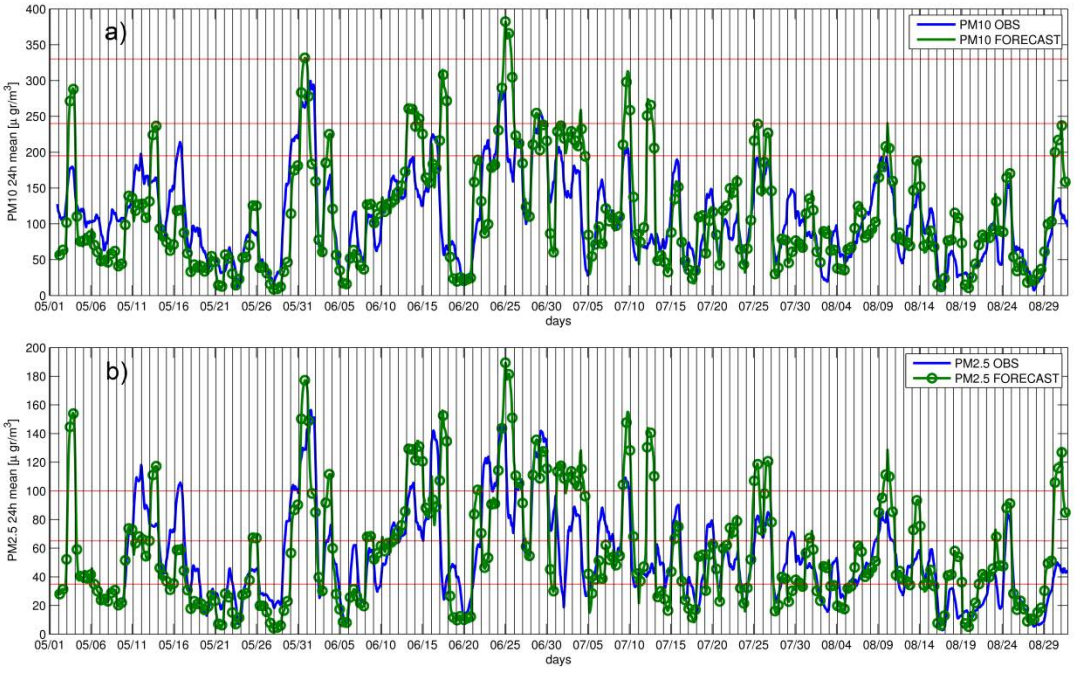

Figure 2.7. PM10 (a) and PM2.5 (b) 24-hr moving mean time series for observations and forecast in Cerro Navia station. Horizontal lines represent thresholds for determining episodes and vertical lines the start of the day in local time. Units in $\mu gr/m^3$.

Why use deterministic models on forecasting episodes?

As noted before, in Santiago de Chile, forecasting episodes is not only a way to warn people about bad air quality, but it is also used to apply emissions reduction to try to avoid bad air quality. Figure 2.8 shows the modeled contribution from emissions on different days to one hour and 24 hour mean surface values. From the one hour data it can be seen that for the period of the day where concentrations are the highest (around 0 am to 2 am) the contribution from the previous day emissions is always dominant (more than 50%). For the 24 hour average there is even influence from the emissions two days before. For example, for the time when the model is showing pre-emergency values (July 1st), the contribution from the day before is over 60% and the rest is contributed from emissions two days before. These results suggest that if measures are to be taken to prevent high concentrations, these should be focused on reducing emissions on the days before the episode happens, and even then, emissions reductions to prevent episodes should be substantial. This requires 48 hr or longer forecast periods, making deterministic models an important forecasting tool. In this study, the effect of declaring episodes by lowering emissions and thus lowering concentrations was not considered, but as these results show it is an effect that would spread over the days following the day the episode was declared. These effects can be incorporated to the model in forecast mode.

Operational feasibility of the forecasting system

The WRF configuration used is rather complex: high vertical resolution, three nested domains reaching to 2km horizontal resolution and a small time-step. However, this configuration is feasible to use in an operational setting as shown in the following. It takes ~seven hours to run a three day forecast on an eight core machine (3.33Ghz Intel Xeon), which is a relatively small machine for these applications. The run can be started with 00Z and 06Z FNL files and continued with 12Z GFS forecasts, which are all available around 12 pm Chilean local time. Then the forecasts can be ready at 19 hours in

order to support the air quality management decision at 20 hours. As more computational resources are available, this time can be reduced and GFS forecast closer to 20 hours can be used to improve the accuracy of the forecast. Also doing several cycles per day can be taken into account.

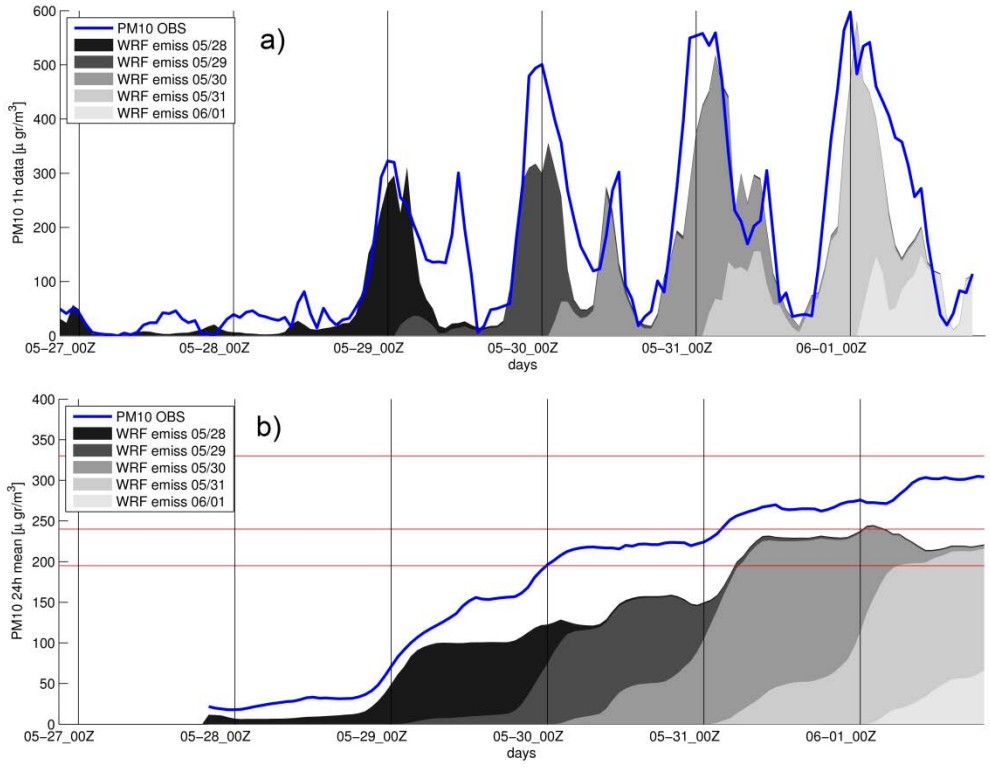

Figure 2.8. PM10 observations and model time series for one hour data and 24 hour mean for Cerro Navia station. Different tracer runs were performed for emissions on different days (in local time) showing the contribution into the total concentrations in the different gray scale colors. Horizontal lines represent thresholds for determining episodes and vertical lines the start of the day in local time.

Conclusions

A PM10 and PM2.5 forecast model was developed for the city of Santiago de Chile for use in prediction of episodes of high air pollution under stable meteorological

conditions and complex terrain. The model uses the WRF-Chem system running with CO as a tracer and doing a linear conversion to obtain PM10 and PM2.5. The linearity assumptions were checked using observation data over the monitoring stations finding correlations over 0.95. The CO to PM conversion used is station and weekend/week day dependent, as evidence shows that episodes tend to occur more frequently on weekends.

In order to obtain representative meteorology and CO concentrations several sensitivity tests were performed to find an optimum configuration for WRF-Chem. Some of the important choices regard the use of the MYNN PBL scheme (which better represented the diurnal PBL height measured with a ceilometer), no minimum thresholds on vertical diffusion, no horizontal diffusion in the most inner domain, a 2km horizontal resolution and a fine resolution in the vertical (10 m layers close to the ground, six levels below 100 m). A new emission inventory was developed in order to remove the biases from the 2000 official emissions and to add wood burning emissions temporary and spatially distributed. All these changes produced better modeling results reaching a correlation of over 0.85 in the critical stations for a period of poor air quality. Using these settings and emissions the forecast model was shown to do forecasts with similar skill as the authority decision for PM10 and to predict high pollution episodes better than persistence for both PM10 and PM2.5. Problems of false alarm forecasts appear to be related to inaccuracies on day to day emissions and to difficulties on representing a partial cleaning of the basin on days after high concentration days, which needs to be investigated further.

The need for a two or more days forecast was assessed and it was found that emissions participating in episodes correspond mainly to those from the previous days reaching roughly 100% contribution for an analyzed case. Thus in order to prevent high concentrations, which is one of the reasons why episodes are declared, episodes should be declared two or more days in advance making deterministic models probably the most adequate technique. Under this framework, it was shown that two day operational

forecasts under the settings presented are feasible. We plan to test the system operationally in the next pollution season since we understand that forecasting tools are subject to continuous improvements derived from improved models and observations, and to changing challenges.

Collaborators and funding sources

This work was carried out with the aid of a grant from the Inter-American Institute for Global Change Research (IAI) CRNII 2017which is supported by the US National Science Foundation (Grant GEO-0452325), NSF grant number 0748012, FONDECYT Iniciacion grant 11090084, and Fulbright-CONICYT scholarship number 15093810. We also acknowledge Ricardo Muñoz (Geophysics Department, University of Chile) for providing boundary layer depth estimates based on ceilometer data and two anonymous reviewers for their valuable comments.

Author contributions

This work is published in Saide *et al.* (2011). P. E. Saide, G. R. Carmichael and S. N. Spak, L Gallardo (U. de Chile), A. Osses (U. de Chile) and M. A. Mena-Carrasco (UNAB) designed the study and P. E. Saide executed it. M. Pagowski provided a data assimilation code which results were asked to be removed from the final manuscript by the reviewers. All authors contributed to the final form of the manuscript.

CHAPTER 3 EVALUATING WRF-CHEM AEROSOL INDIRECT EFFECTS IN SOUTHEAST PACIFIC MARINE STRATOCUMULUS DURING VOCALS-REX

Abstract

We evaluate a regional-scale simulation with the WRF-Chem model for the VAMOS (Variability of the American Monsoon Systems) Ocean-Cloud-Atmosphere-Land Study Regional Experiment (VOCALS-REx), which sampled the Southeast Pacific's persistent stratocumulus deck. Evaluation of VOCALS-REx ship-based and three aircraft observations focuses on analyzing how aerosol loading affects marine boundary layer (MBL) dynamics and cloud microphysics. We compare local time series and campaign averaged longitudinal gradients, and highlight differences in model simulations with (W) and without (NW) wet deposition processes. The higher aerosol loadings in the NW case produce considerable changes in MBL dynamics and cloud microphysics, in accordance with the established conceptual model of aerosol indirect effects. These include increase in cloud albedo, increase in MBL and cloud heights, drizzle suppression, increase in liquid water content, and increase in cloud lifetime. Moreover, better statistical representation of aerosol mass and number concentration improves model fidelity in reproducing observed spatial and temporal variability in cloud properties, including top and base height, droplet concentration, water content, rain rate, optical depth (COD) and liquid water path (LWP). Together, these help to quantify confidence in WRF-Chem's modeled aerosol-cloud interactions, especially in the activation parameterization, while identifying structural and parametric uncertainties including: irreversibility in rain wet removal; overestimation of marine DMS and sea salt emissions, and accelerated aqueous sulfate conversion. Our findings suggest that WRF-Chem simulates marine cloud-aerosol interactions at a level sufficient for applications in

forecasting weather and air quality and studying aerosol climate forcing, and may do so with the reliability required for policy analysis.

Introduction

Clouds play a major role in Earth's radiative balance (Ramanathan *et al.*, 1989; Cess *et al.*, 1989). However, uncertainties in the processes that affect cloud optical properties and modify this balance are still high (Solomon *et al.*, 2007). These processes are driven by the indirect climatic effects of aerosols (Lohmann and Feichter, 2005), which can modify cloud albedo (Twomey, 1991) and lifetime (Albrecht, 1989), evaporate clouds (Grassl, 1979), change thermodynamics in deep convective clouds (Andronache *et al.*, 1999), increase precipitation in ice clouds (Lohmann, 2002), and change the surface energy budget (e.g., Liepert, 2002).

Low-level marine clouds have been shown to contribute substantially to cloud radiative forcing (Ramanathan *et al.*, 1989). However, these clouds are not well represented by contemporary models (Wyant *et al.*, 2010). Previous work has shown problems in the ability of global and regional models to accurately represent marine stratocumulus clouds (Vellore *et al.*, 2007; Otkin *et al.*, 2009; Wyant *et al.*, 2010; Abel *et al.*, 2010), leading to difficulties in predicting cloud cover on an operational basis (e.g., Shah *et al.*, 2010). Some problems are thought to be related to boundary layer schemes generating insufficient vertical mixing, resulting in an unrealistically shallow cloud-topped boundary layer (Otkin and Greenwald, 2008). By comparison, Large Eddy Simulation (LES) models have been shown to more effectively describe stratocumulus clouds and their transitions (e.g., Feingold *et al.*, 1998; Khairoutdinov and Kogan, 2000; Berner *et al.*, 2011; Wang *et al.*, 2010). Efforts have been made to couple models at both scales (regional and LES), obtaining accurate representation of stratocumulus (Zhu *et al.*, 2010). However, operational use of these coupled models for numerical weather prediction (NWP) or climate studies is not yet feasible. Cloud data assimilation has been

an alternative way to improve clouds in NWP (e.g., Vellore *et al.*, 2006; Errico *et al.*, 2007; Michel and Auligné, 2010).

Uncertainties in modeling aerosol indirect effects diminish our capability to generate reliable climate projections, to evaluate policy questions and geo-engineering proposals, and to provide accurate weather and air quality predictions. Including indirect aerosol effects has been shown to improve cloud representations in global models (Lohmann, 2002), and a range of approaches in modeling them have been assessed (Ghan and Easter, 2006). On the regional scale, including aerosol indirect effects tends to impact clouds optical properties (Chapman *et al.*, 2009) and precipitation (Ntelekos *et al.*, 2009), and often produces better cloud representation by optical properties, dynamics and microphysics (Gustafson *et al.*, 2007; Yang *et al.*, 2011b). The LES scale has been able to show the effect on cloud structure by different cloud condensation nuclei (CCN) loadings, and effectively simulate the dynamics of open cells, "pockets of open cells," and closed cell marine clouds (Wang and Feingold, 2009).

Intensive measurement campaigns provide a wealth of observations that present the opportunity to evaluate models and to identify, quantify, and hopefully reduce these uncertainties. The VAMOS Ocean-Cloud-Atmosphere-Land Study Regional Experiment (VOCALS-REx, Wood *et al.*, 2011) was an international field program designed to make observations of poorly understood but critical components of the coupled climate system of the southeast Pacific on the coast of Chile and Peru. Reactive gas and aerosol observations show a marked longitudinal gradient from elevated values close to shore due to polluted conditions to cleaner remote conditions (Allen *et al.*, 2011), while cloud properties correlate to some extent with this gradient (Bretherton *et al.*, 2010). Model evaluation studies emerging from the campaign have identified difficulties in accurately representing MBL and stratocumulus clouds (Abel *et al.*, 2010; Sun *et al.*, 2010; Andrejczuk *et al.*, 2011) without considering aerosol feedbacks to meteorology. Yang *et al.* (2011b) present a comprehensive evaluation of the WRF-Chem system on a regional

scale highlighting the effects of aerosol feedbacks, showing that the inclusion of aerosol-cloud interactions typically improve model performance in simulating cloud properties.

In this work, we build upon previous regional simulations including aerosol feedbacks using the WRF-Chem model. Several modeling studies have performed sensitivity analyses of the effects of aerosol loading on cloud properties (e.g., Chen *et al.*, 2011). Starting from a base configuration, we find another configuration that better represents aerosol mass and number concentrations, and then analyze the impacts of these different aerosol loading on MBL dynamics and cloud microphysics, and compare them to observations and to the canonical conceptual model of warm cloud indirect effects. We perform an extensive evaluation of different aspects of the model representation, and identify areas for improvements and remaining problems.

Methods

For the purposes of defining representative spatial zones characterized by broadly internally similar thermodynamic aerosol and composition regimes (when averaged over the length of the VOCALS-REx campaign) we choose to use the three areas as defined by Bretherton *et al.* (2010) and Allen *et al.* (2011). These are the "coastal zone" (or "off shore", east of 75° W), and the "remote zone" (west of 80° W), with the two regions separated by a "transition zone" near the 78° W meridian (75° W–80° W).

WRF-Chem model configuration

The WRF-Chem model simulates meteorology and atmospheric constituents, as well as their interactions (Skamarock *et al.*, 2008; Grell *et al.*, 2005). We configured WRF-Chem v3.3 with a combination of model structures, parametric choices, and input data to best represent marine stratocumulus conditions, atmospheric chemistry, and secondary aerosols, with the goal of future use in meteorological and air quality forecasting.

A 12×12 km^2 horizontal resolution domain is employed, covering 91° W–65° W longitude and 40° S–12° S latitude. This choice attempts to optimize between spatial resolution, critical for representing cloud dynamics, and complete coverage of the VOCALS region of the Southeast Pacific within the limitations of computing time. The domain accounts for most major Chilean and Peruvian anthropogenic sources shown in air-mass trajectories (Chand *et al.*, 2010) to impact VOCALS-REx observations, including the Andean cordillera, and covers the entire VOCALS-REx experimental domain (to ~85° W), with a margin towards the west and north to avoid excessive boundary condition influence on meteorology and atmospheric composition. Following recommendations by Wang *et al.* (2011), a 75-level vertical resolution was chosen to reduce MBL and cloud height underestimation. The first few levels are as in Saide *et al.* (2011) with ~10m thickness, and the average vertical layer spacing between 60m and 3 km is ~60 m. In preliminary testing, this resolution produced accurate MBL and cloud heights for all longitudes, which were ~100–300m greater than the 39-level resolution used in Saide *et al.* (2011).

Model structure was configured to combine modules included in contemporary WRF-Chem public release code that best represent known aerosol, cloud, and MBL processes and their couplings. Wherever possible, the most complete representations of complex physical and chemical processes were chosen. This application requires a boundary layer closure scheme that can make use of (and maintain numerical stability at) high vertical resolution, and can accurately represent the diurnal evolution of the MBL at low wind speeds. Mellor-Yamada type schemes have generally exhibited good cloud representation under these conditions (Otkin and Greenwald, 2008; Zhu *et al.*, 2010; Rahn and Garreaud, 2010). The MYNN level 2.5 scheme (Nakanishi and Niino, 2004) was chosen since it performed well in prior applications at this resolution over Chile (Saide *et al.*, 2011). The Lin microphysics scheme (Chapman *et al.*, 2009) and Goddard short wave radiation(Chou *et al.*, 1998; Fast *et al.*, 2006) were chosen to support aerosol

direct, indirect, and semi-direct feedbacks to meteorology. Activation of aerosols from the interstitial to the cloudborne "attachment state" (Ghan and Easter, 2006) is based on a maximum supersaturation determined from a Gaussian spectrum of updraft velocities and the internally mixed aerosol properties within each aerosol size bin (Abdul-Razzak and Ghan, 2002). The updraft velocity distribution is centered in the model vertical wind component plus the subgrid vertical velocity diagnosed from vertical diffusivity. No cumulus scheme was used following the recommendation of Yang *et al.* (2011b). The RRTM longwave radiation scheme (Mlawer *et al.*, 1997) was used. Gases and aerosols were simulated using the CBMZ gas-phase chemical mechanism (Zaveri and Peters, 1999; Fast *et al.*, 2006) with dimethyl sulfide (DMS) reactions coupled to the 8-bin sectional MOSAIC (Zaveri *et al.*, 2008) aerosol module. Seawater DMS concentration was set to 2.8 nM, following the VOCA Modeling Experiment Specification (http://www.atmos.washington.edu/_mwyant/vocals/model/VOCA Model Spec.htm) and in agreement with measurements during VOCALS-REx(Hind *et al.*, 2011). DMS is transferred to the air using sea-air exchange as in Liss and Merlivat (1986).

We chose emissions and chemical boundary conditions to best resolve spatial and temporal variability in aerosols and their precursors, taking into account a complete range of natural and anthropogenic emissions sources. Continental emissions of biogenic trace gases (e.g., isoprene) were predicted hourly by the MEGAN algorithm (Guenther *et al.*, 2006), and daily biomass burning locations and fuel loadings were obtained from FIRMS MODIS fire detections (Davies *et al.*, 2009) and modeled hourly using WRF-Chem's plume rise model (Freitas *et al.*, 2006; Freitas *et al.*, 2007). Volcanic and anthropogenic emissions, including point and area sources, were taken from the VOCA inventory described in detail by Mena-Carrasco *et al.* (2012). In cases where particulate matter (PM) was not speciated, 10 %, 30% and 70% were associated to elemental carbon, organic carbon and crustal aerosol, respectively. Chemical boundary conditions are obtained from 6-hourly MOZART global simulations (Emmons *et al.*, 2010). MOZART

fields were found to overestimate near-shore concentrations, so the model was started from clean initial conditions and spun up for 6 days to avoid biasing results. MOZART sulfur dioxide (SO_2) boundary conditions in the free troposphere (FT) were found to be underestimated, so a global minimum background level of 30 ppt and a 50 ppt minimum for heights over 3.5 km were set, in agreement with flight profile measurements in the remote region (Allen *et al.*, 2011; Kazil *et al.*, 2011). Sea salt aerosol emissions were modeled following Gong *et al.* (1997), but resultant concentrations from the default scheme were found to substantially overestimate ship-based measurements from the NOAA RV Ronald H. Brown (Ron Brown). In order to avoid misleading indirect effects due to these biases, submicron emissions were reduced by a factor of 10 and supermicron emissions were reduced by a factor of 2, in line with campaign-averaged observations from the Ron Brown. Default WRF-Chem sea salt emissions do not consider sulfate coming from seawater, speciating sea salt as Na and Cl only. Wind-blown dust was not modeled, due to known high biases in WRF-Chem's online wind-blown dust emissions, concentrations, and resultant aerosol optical depth over land, and poor model representation of Andean dust composition. No organic sea emissions were considered in this study, as there was little to no evidence of these sub-micrometer particles during the campaign (Shank *et al.*, 2012). Also, no secondary organic aerosols (SOA) were modeled as the fraction of SOA to total organic aerosol is thought to be low in this region (~10 %, Kanakidou *et al.*, 2005). New particle formation is modeled by the Wexler *et al.* (1994) scheme.

WRF-Chem simulations covered the entire VOCALS-Rex campaign period, 15 October–16 November 2008, along with the extra 15 days that Ron Brown stayed in the domain (16–30 November). The model was run with an initial "chemical" spin-up period of 6 days with meteorology re-initialized from analyses at the middle of the modeling period using the previous chemical state. We found that 3–4 days of spin up are necessary to overcome the underestimated MBL height present in the National Centers for

Environmental Prediction (NCEP) Final Analysis (FNL) from GFS (Sun *et al.*, 2010), as only increasing vertical resolution is insufficient for debiasing the offshore MBL (Andrejczuk *et al.*, 2011).

As shown in the results section, aerosol wet deposition has a large influence over the modeling results. In the present version of WRF-Chem, in- and below-cloud wet removal of gases and aerosols in CBMZ-MOSAIC are modeled following Easter *et al.* (2004). This mechanism assumes that the removal processes are irreversible, and does not consider aerosol resuspension due to rain evaporation. This becomes an important issue for the Southeast Pacific during Austral spring, since most of the drizzle observed during VOCALS-REx evaporated before reaching the surface (Bretherton *et al.*, 2010), leading to a great contrast between cloud base and surface rain rates. Thus, irreversible removal of aerosol by rain might create an unrealistically strong sink, which is supported by previous modeling results (Yang *et al.*, 2011b). Kazil *et al.* (2011) implemented wet removal considering rain evaporation, but for a different modal aerosol approach and in the context of LES simulations. To assess the importance of modeled wet removal processes, we performed simulations where wet deposition was excluded, which results in higher aerosol loadings. This represents an upper limit to below cloud aerosol, and reflects the fact that low rain rates were observed at the sea surface (0.01mm/h on average) during the VOCALS campaign (Yang *et al.*, 2011a), indicating that most rain evaporated before reaching the surface (Bretherton *et al.*, 2010), suggesting nearly zero wet deposition. Thus, by turning off wet deposition the unrealistic sink of aerosol mass generated by not considering resuspension is removed. However, the effects in terms of number concentration are uncertain due to complex interactions: one droplet can collect thousands of particles by collision-coalescence but, as some have observed (Mitra *et al.*, 1992; Feingold *et al.*, 1996), only one aerosol is released after evaporation. Since rain rates increase as aerosol number concentration decrease, a cloud-scavenged ultra-clean layer can be generated which can lead to conditions of particle nucleation (Kazil *et al.*,

2011) potentially recovering the number of particles lost before. Without an aerosol module that includes reversible wet deposition, and for the sake of studying the sensitivity to different aerosol loads, both simulations were conducted for the whole period. The simulation with wet deposition turned on is hereafter referred as the base run or "W", while the simulation without wet deposition is called "NW". Since W represents large aerosol removal, while NW no aerosol removal, we hypothesize that a model with a correct wet deposition scheme should be bounded by these two states.

Observations

The observations used for comparison are provided by the VOCALS-REx airborne and marine platforms. Carbon monoxide (CO), Ozone (O_3), SO_2, DMS gases; and sulfate (SO_4), nitrate (NO_3), ammonium (NH_4) and organic carbon (OC) interstitial aerosol (from AMS: non-refractory non-sea salt) observations collected by the NSF C-130, DoE G-1, FAAM BAe-146 aircrafts and Ron Brown are thoroughly described by Allen *et al.* (2011), Kleinman *et al.* (2012), Yang *et al.* (2011a) and Hawkins *et al.* (2010), while C-130 cloud water composition measurement methods can be found in Benedict *et al.* (2012). The University of Wyoming 94 GHz cloud radar (WCR) aboard C-130 provided radar reflectivities, which were then corrected (Bretherton *et al.*, 2010) and converted to rainfall estimates using the Z-R relationship described in Comstock *et al.* (2004). This presents results consistent with Particle Measuring Systems (PMS) Two Dimensional Cloud Probe (2D-C) probe rainfall estimates during VOCALS (Bretherton *et al.*, 2010). The WCR, along with an upward-pointing lidar (WCL) provided cloud top and base height estimates from the C-130 (Bretherton *et al.*, 2010). Cloud top and base heights from Ron Brown were estimated using a millimeter-wave cloud radar (MMCR) and a Vaisala CL31 ceilometer, respectively (de Szoeke *et al.*, 2010). Capping inversion height (CIH) was estimated as the height at which the temperature was a minimum, provided the relative humidity was at least 45% (Jones *et al.*, 2011) in both Ron Brown

soundings (Wood *et al.*, 2011) and aircrafts vertical profiles. C-130 Gerber PVM-100 Probe cloud water content, PMS Cloud Droplet Probe (CDP) and Forward Scattering Spectrometer Probe (FSSP-100) cloud droplet number concentration, and PMS Passive Cavity Aerosol Spectrometer Probe (PCASP) accumulation mode aerosol number concentration observations used are described in Kazil *et al.* (2011) and Bretherton *et al.* (2010). BAe-146 cloud and accumulation mode aerosol measurements (Allen *et al.*, 2011) were performed with similar instruments as in C-130 (Droplet Measurement Technologies (DMT) CDP-100, PCASP) while G-1 (Kleinman *et al.*, 2012) used a DMT Cloud and Aerosol Sampling (CAS) probe and a PCASP, respectively. An intercomparison of the cloud microphysics probes fitted to BAe-146 and C-130 was performed on 31 October 2008 and 4 November 2008. The aircraft performed straight and level runs (of the order of 10's of km in length) through the same region of cloud approximately 5 min apart, finding that the number concentration, LWC and size distributions were similar within calibration and systematic error. However, G-1 cloud microphysics measurements showed inconsistencies compared to other probes used (Kleinman *et al.*, 2012) probably due to shattering of drizzle on CAS inlet (McFarquhar *et al.*, 2007). On the Ron Brown, total number of particles over 13 nm was measured with a TSI 3010 Condensation Particle Counter. Cloud optical depth (COD), cloud liquid water path (LWP) and cloud effective radius were obtained from MODIS-Aqua retrievals.

Performance statistics

We present box and whisker plots of longitudinal profiles at 20° S (e.g., Fig. 3.1) in order to assess model performance in a consistent manner across trace gas, aerosol, and cloud properties, and to focus evaluation on the longitudinal gradients identified in VOCALS-REx observations as the most important characteristics of aerosol and low cloud regimes in the Southeast Pacific (Allen *et al.*, 2011; Bretherton *et al.*, 2010).

Here, we introduce a measure of accuracy deduced from these plots, hereafter referred to as the Box and Whiskers (BoW) metric and summarized in Table 3.1. We define a "match" as a model (observation) median or mean falling between the two prescribed percentiles of the observation (model) distribution. The first criterion (Table 3.1, column1) uses the 25th and 75th percentiles (boxes in Fig. 3.1) and the second criterion (Table 3.1, column 2) uses the 10th and 90th percentiles (whiskers in Fig. 3.1). The third criterion (Table 3.1, column 3) is based on overlapping of the 25th and 75th (box overlapping) and 10th and 90th (whisker overlapping) percentile distributions. The net level of accuracy is determined from the best score of these three criteria, which is converted into a qualitative category: excellent, very good, good, fair and poor. Some of the advantages of the BoW method are that: it is independent of the variable being assessed; no absolute threshold of accuracy is specified for any variable; it is based on basic statistical parameters; it can easily be read from a box and whisker plot; and it transforms a quantitative measure of accuracy into a qualitative description. However, some issues could be encountered when the distributions are strongly skewed, as the mean could be found outside the inner quartile.

Statistics for cloud microphysics and aerosol number concentration were computed for aircrafts profile means instead of local point to point comparisons, since observed clouds could be in different levels than model values, generating mismatches with modeled and observed clouds both present, but at different levels. For estimating the modeled 117 nm to 3 μm PCASP aerosol number concentration, values from bins 3 to 7 (156 nm to 2.5 μm) are integrated along with 42% of the second bin (78 to 156 nm), which corresponds to the fraction over 117 nm using the logarithmic diameter.

Table 3.1. Measure of model performance using data obtained from a box and whisker plot.

	Matches in the 25th-75th percentile	Matches in the 10th-90th percentile	Overlaps
Excellent	4 or 3	-	-
Very good	2 or 1	-	-
Good	-	4 or 3	2
Fair	-	1 or 2	1
Poor	-	-	0

Notes: A "match" is defined as a model (observation) median or mean being in between the two percentiles of the observation (model) distribution. Matches ranges from 4 (perfect match) to 0 (no match). An "overlap" is defined as when modeled and observed inner quartiles (boxes) or inner deciles (whiskers) overlap. Overlaps ranges from 2 to 0. The final performance is assigned as the best of the three criteria.

Aircraft modeled and observed gases, aerosol mass, cloud heights and rain statistics were computed for one minute average values, while Ron Brown statistics were computed

for ten minute intervals. For the case of rain statistics, model results are not filtered for missing observations and vice versa as information on rain frequency can be extracted from the total sampling time in each longitude bin on the top of the box and whisker plots (e.g., Fig. 3.1). This creates minor inconsistencies; mainly in the 100m height estimates, which was not measured in sub-cloud flight legs (Bretherton *et al.*, 2010).

Results and discussion

We first focus on evaluating atmospheric concentrations of selected gases and aerosols for the base and NW simulations. Then, model performance is assessed for MBL

dynamics and cloud microphysics. Finally, spatial and temporal variability in chemical transport and cloud effects are investigated on an episodic basis.

Trace gas and aerosol evaluation

Figure 3.1 shows aircrafts flight statistics for gaseous and aerosol concentration for selected species for the MBL and free troposphere (FT). For this plot, MBL concentrations were considered for heights lower than 1200m or below cloud, and FT concentrations for heights in between 1700 and 3200m in order to avoid cloud contamination (Allen *et al.*, 2011). Trace gas data quality was assessed by intercomparison between aircrafts, obtaining 1.5 and 4 ppb as the uncertainties for CO and O_3, respectively (Allen *et al.*, 2011). As seen in Fig. 3.1, MBL CO is overestimated across the entire modeled longitudinal range with the exception of the close to the shore bin where highly polluted plumes were detected by the G-1. Measurement uncertainty is well below these differences pointing to a model bias. Neglecting these non-resolved plumes, close to shore overestimation is probably due to a lower MBL than observed (see next section), while remote zone issues are likely due to overestimation of the MBL CO MOZART boundary conditions, as these air masses often had no contact with the continent for a long time period (Allen *et al.*, 2011). However, we cannot rule out the possibility that a combination of overestimates in Central Chile anthropogenic emissions (e.g., Jorquera and Castro, 2010; Saide *et al.*, 2009a) and too much entrainment in the model could generate MBL concentrations similar to FT concentrations. The latter case is less likely, as it would have similarly affected O_3. Remote FT CO shows very good to excellent performances driven mostly by MOZART boundary conditions over the east-central Pacific. Even though MBL CO shows poor to fair performance in BoW metrics (e.g., matches only with 10^{th} and 90^{th} percentile and box/whisker overlaps), differences are no more than 15 ppb, and the observed longitudinal trend (decreasing towards remote zone) and spread (<10 pbb) are often well simulated, indicating that transport in the MBL

is resolved. The base and NW models show very small differences, attributable to changes in entrainment and MBL heights (see next section).

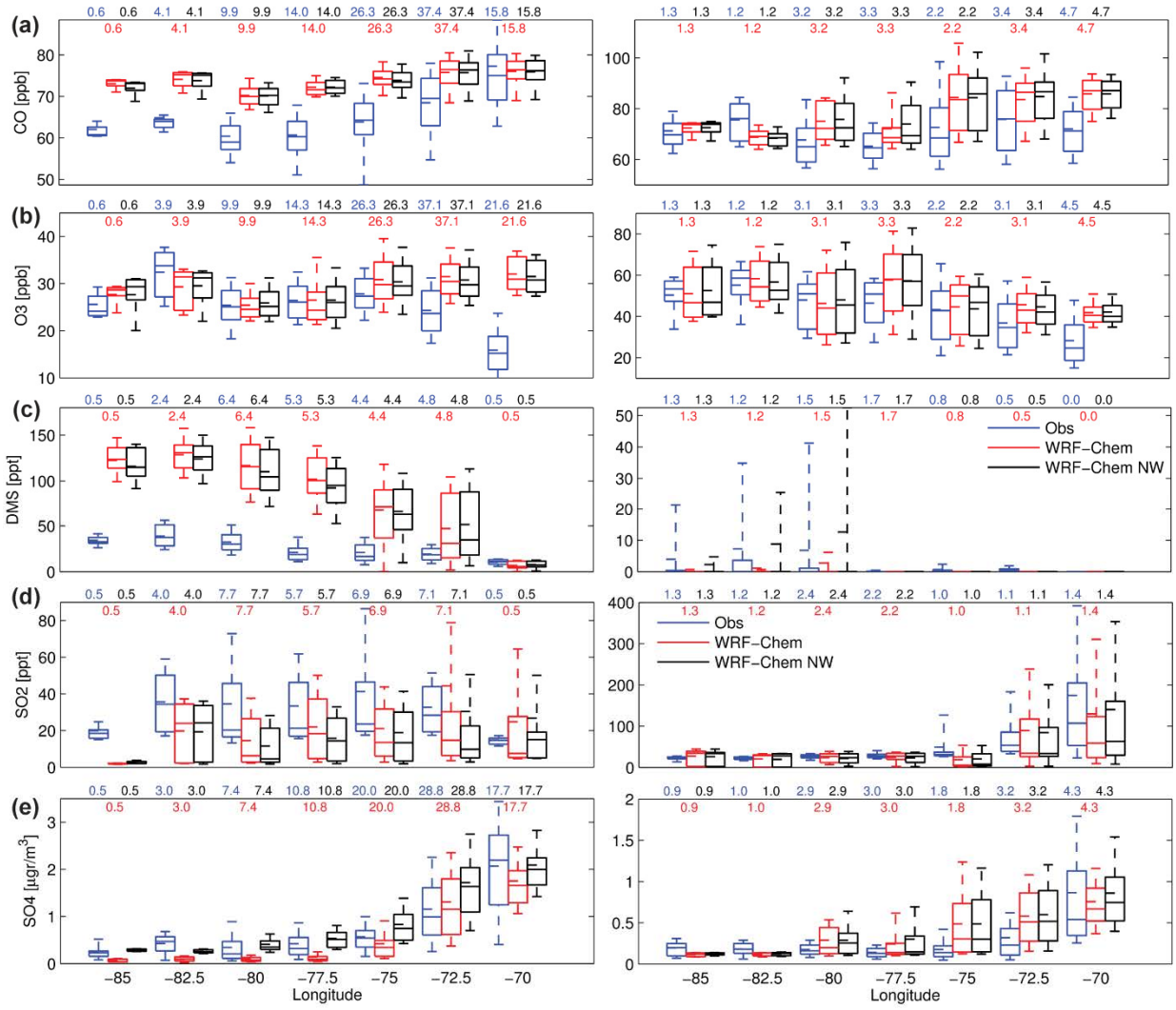

Figure 3.1. Observed and modeled statistic for selected gaseous and aerosol species gridded into 2.5 degree longitudinal zones in between 22° S and 18° S. For each zone, centre solid (dashed) lines indicate the median (mean), boxes indicate upper and lower quartiles with upper and lower decile whiskers. The sampling time in decimal hours in each longitude bin is indicated at the top. Left column and right column are for marine boundary layer (MBL) and free troposphere (FT), respectively.

Figure 3.1b shows O_3 was well simulated for both the MBL and FT, with very good to excellent BoW metrics, and with similar spread. There is no clear longitudinal trend in either the model or the observations. An important point is that, as mentioned in Allen *et al.* (2011), the model resolves the ~30 ppb difference between MBL and FT and also the higher variability in the FT. The lower O_3 in the MBL is the result of chemical destruction during the day, transport from FT during the night due to entrainment (Yang *et al.*, 2011a), and lower photolysis rates and temperatures under the cloud deck. Due to the ability of the model to correctly maintain the MBL to FT O_3 difference, we surmise that entrainment is simulated effectively. Hydroxyl radical (OH) in VOCALS MBL was estimated by Yang *et al.* (2009) from the DMS budget and found to have maximum diurnal values of $3–5\times10^6$ molecules/cm^3. WRF-Chem showed OH peaks in the lower end of this range, at ~$2.5–3.35\times10^6$ molecules/cm^3.

Statistics for gas and aerosol components of the sulfur cycle are shown in Fig. 3.1c–e. The C-130 measured FT DMS (Fig. 3.1c, right panel) was usually below the detection limit (5 ppt), as in the model. The spikes in DMS for the 75th to 90th percentile show times where the cloud top heights were >1700 m, which is better captured by NW as explained later. In general, MBL DMS has a high bias, with poor to fair BoW scores. As discussed by Yang *et al.* (2011b), this is likely related to an overestimation of DMS emissions due to overestimation of the modeled DMS ocean : atmosphere transfer velocity. Similarly to CO, and despite the emission bias, the modeled longitudinal trend is captured very well by the model. Ron Brown atmospheric DMS measurements showed higher values, in better agreement with the model but still lower. FT SO_2 is also skillfully simulated, presenting mostly excellent BoW metrics and follows the observed longitudinal trend. FT Remote zone SO_2 is mostly affected by boundary conditions, showing the importance of setting lower thresholds for influx from MOZART (see Methods section). In the MBL, the model usually exhibits very good performance, but cannot maintain the ~20 ppt lower threshold observed. When looking at the modeled SO_2

diurnal cycle, the higher values are obtained after DMS photochemical destruction, but rapidly decay to values as low as 1 ppt due to cloud processing and conversion to SO_4 aerosol. Modeled conversion appears to occur at a higher rate than observed, which is investigated later in more detail. Finally, Fig. 3.1e shows sulfate mass concentrations statistics. MBL SO_4 clearly shows the impact of wet deposition as no remote zone W and NW model distributions overlap. The observations are typically closer to the NW results, and sometimes between the two simulations. As most of the rain evaporated before reaching the sea surface, we find that the NW results are more realistic, and that any overestimation could be due to the combination of high DMS emissions rates and high SO_2 to SO_4 cloud conversion yields. In the FT, both configurations show similar results with very good to excellent BoW performances. Other species play much smaller roles in aerosol composition. The model significantly underestimates NH_4 (possibly due to emissions, which are poorly constrained in the region), estimates of NO_3 are below detection limits as observed, and accurately predicts organic carbon (not shown). Most modeled NO_3 is found in the coarser sectional bins, as it is displaced by SO_4 in fine aerosol bins due to the low NH_3 concentrations (Seinfeld and Pandis, 2006), and therefore rarely appears in aircrafts AMS observations, where aerodynamic diameter is capped at 500–700 nm. Coarser aerosol is dominated by sea-salt, where NO_3 displaces Cl creating a chloride deficit (Yang *et al.*, 2011b).

In order to further explore SO_2 to sulfate conversion processes, we compare cloud chemistry observations to the NW model (Fig. 3.2 and Table 3.2), as both models show similar cloud aerosol composition. Consistent with observations (Benedict *et al.*, 2012), model results show that bulk (summing all sizes) cloud drop ion concentrations are dominated by sea salt, followed by sulfate (Fig. 3.2a, b). Bulk sulfate concentrations are underestimated, since sulfate coming from seawater is not modeled. As shown by Table 3.2, in general the model does a good job representing the mean and variability of the ion concentrations. The most notable problems are Ca^{+2}, which is very low since no dust was

modeled, and NH_4, which is underestimated as it was in the AMS interstitial aerosol evaluation. Model pH shows the same tendency as observations, increasing towards the remote region as sulfate aerosol is more abundant close to shore (not shown). However, model pH is always under 5, while values up to 7 were observed, leading to under prediction in mean pH (Table 3.2). We found that the bulk model is extremely sensitive to chloride concentrations, as a decrease in only 5% in Cl^- (as in observations) will increase average pH by 1 and increase single values up to 2.5 pH units. This is important, as WRF-Chem uses a bulk cloud chemistry scheme (Chapman *et al.*, 2009) and small variations in Cl^- (thus in pH) can generate a shift in the dominant mechanism of SO_2 to sulfate conversion, from the roughly pH independent H_2O_2 reaction (Robbin Martin and Damschen, 1981) to the O_3 reaction which increases in rate with pH (Hoffmann and Calvert, 1985), resulting in a speeding up of the SO_2 to sulfate conversion and even further reductions in SO_2 concentrations. However, as pointed out by Yang *et al.* (2011a), most droplets nucleate from sulfate particles, so their pH will be acidic and dominated by the hydrogen peroxide reaction. This behavior for the majority of droplets is seen in modeled cloud water aerosol in the bins that dominate nucleation (Fig. 3.2c). We also see very low sea salt influence, as Na^+ percentage is low and Cl^- is diffused into the droplet from HCl gas rather than entering the droplet as sea salt. All this implies that there is clear need for sized-resolved cloud chemistry (e.g., Fahey and Pandis, 2001), and that aqueous chemistry should be considered for nucleation and accumulation modes only (Kazil *et al.*, 2011). Measurements considering the nature of the cloud condensation nuclei (CCN) composition and size should also be performed (Bator and Collett, 1997). Analyzing the H_2O_2 pathway, H_2O_2 concentrations are slightly overestimated by the model (Table 3.2), which cannot explain the SO_2 gap between model and observations. Yang *et al.* (2011a) found that to close the SO_2 budget, the Robbin Martin and Damschen (1981) H_2O_2 rate expression yielded best results, while other reaction rates were too fast to reach mass balance. We compared these rates to the McArdle and Hoffmann (1983)

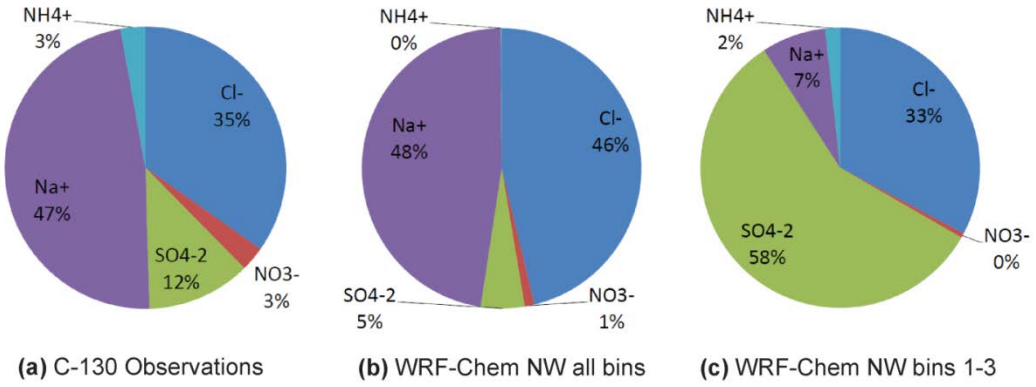

Figure 3.2. Pie charts for modeled ionic species for C-130 observations representing cloud composition (a) and the no wet deposition model (NW) using collection of wet aerosol along the flight track for all bins (b) and for bin 1, 2 and 3 (40 nm to 300 nm aerosol diameter) only (c). Units are in μN.

Table 3.2. Observed and modeled cloud chemistry statistics.

	Observation		NW model	
	Mean	Std dev	Mean	Std dev
pH	4.94	0.91	4.12	0.43
H_2O_2 (μM)	132.20	130.94	153.44	73.47
TOC (μg C/L)	2028.9	571.0	1624.6	1953.0
Cl^- (μN)	855.3	1205.0	1220.2	1450.7
NO_3^- (μN)	72.77	120.39	28.41	32.22
$SO_4^=$ (μN)	298.35	465.94	133.42	152.71
Na^+ (μN)	1204.6	2008.6	1253.3	1486.8
NH_4^+ (μN)	90.65	163.89	2.51	2.88
Ca^{2+} (μN)	128.60	203.39	0.00	0.00

Note: Values where the observations (model) were inexistent were removed from the model (observations) statistics.

rates implemented in WRF-Chem, reaching the same answer, which could explain the difference in SO_2. Another factor that influences increased SO_2 depletion is the consistent overestimation of cloud fraction, as WRF-Chem NW shows average cloud fractions of 86% on the Ron Brown track, while the MMCR on board of Ron Brown (Yang *et al.*, 2011a) showed values of 67 %.

MBL and marine Stratocumulus dynamics

Box and whisker plots for cloud base and cloud top for the VOCALS-REx period are shown in Fig. 3.3a, b. The WRF-Chem NW model shows up to 200m higher mean and median cloud top and base heights than the base model, bringing it closer to observations. The largest differences are found in the remote zone. The higher accumulation mode aerosol load obtained by NW allows for a less broken cloud deck with smaller droplet radius and less precipitation (see section Cloud microphysics), which affects the MBL energy budget by decreasing average downward shortwave radiation (SW), upward surface heat flux and top of the atmosphere (TOA) outgoing longwave radiation (LW) by 50–60W/m^2, ~3W/m^2 and 1–3W/m^2, respectively. Precipitation, SW absorption and LW cooling of clouds are the main drivers of entrainment in a cloud topped boundary layer, which in turn determines its cloud height. As shown by Pincus and Baker (1994), when number concentration of droplets increase, precipitation decreases, which increases entrainment. However, this also generates extra cloud water that produces thicker clouds that absorb more shortwave radiation (lower model downward SW), heating the layer and decreasing entrainment. Also, when clouds rise, cloud top temperature tends to decrease, decreasing LW cooling (model TOA outgoing LW decrease) and thus reducing entrainment. An overall increase in entrainment is achieved which cause cloud heights to rise (Pincus and Baker, 1994), in agreement with our results.

As aerosol loads increase for NW, the direct and semidirect effects are also expected to change. However, semidirect effects should not play an important role as BC observations (Shank *et al.*, 2012) and model results show very low concentrations. A simulation where the aerosol radiation feedbacks were turned off using the NW configuration shows small differences for cloud top pressure (<±1 %), cloud fraction (<±10 %) and water content (<±10 %), implying that indirect effects dominate under clean conditions like those observed during VOCALS-REx, where aerosol radiative effects become more important under heavily polluted conditions (Koren *et al.*, 2008).

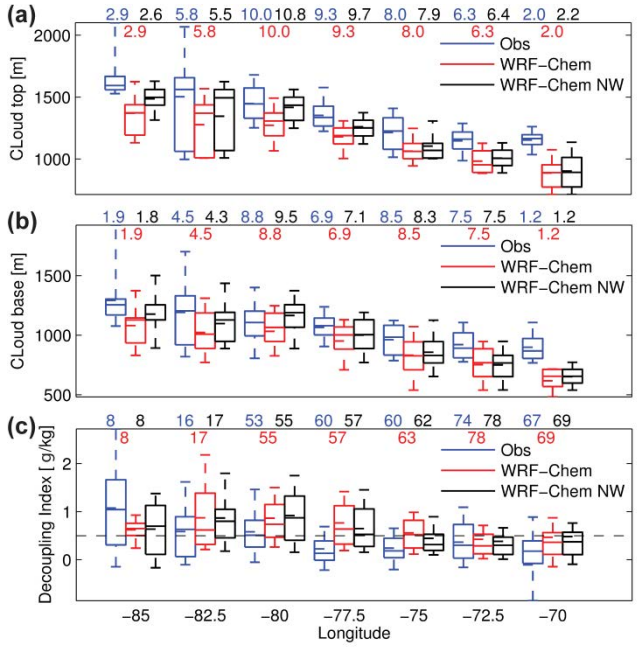

Figure 3.3. Box and whisker plots for different variables derived from aircrafts measurements as in Fig. 3.1. (a) and (b): cloud top and bottom from U. of Wyoming radar (WCR) and lidar (WCL), respectively. (c) Decoupling index, the horizontal dashed line indicates the 0.5 g/kg decoupling threshold (see explanation on the text). The numbers above each zone represent sampling time in decimal hours for (a) and (b), and number of profiles for (c).

As seen in Fig. 3.3a, b, close to shore both simulations have large cloud height negative biases (fair to good BoW), as the coarse resolution is unable to resolve the steep

topography and land-sea transition (Wang *et al.*, 2011). In the remote zone the NW heights captured well the observations (mostly excellent BoW classifications) while the base model underestimated the heights (fair to excelent BoW scores). The NW model also better represents observed temperature and water vapor profiles in the remote zone both from aircraft profiles and ship-based soundings (not shown), as the typical MBL structure approaches the observed vertical profile. Even so, there are still some periods where the model does not simulate the very high cloud heights observed in the remote zone, as depicted by the 95th extremes of the observed distribution and as seen in the Ron Brown time series in Fig. 3.4, which are responsible for the lower model means. However, these periods of poor performance appear episodic, and there are periods where WRF-Chem NW does reach the observed heights (e.g., RF03 and RF05 on Fig. 3.4). Episodic underestimation of cloud heights is thought to come from meteorological boundary condition issues, as the model is unable to represent the high clouds condition occurring over several days (e.g., 19–23 November). The model shows good agreement with observations for a range of very different conditions: a 20S/POC drift flight (RF02) with very thin clouds, two flights to 85° W (RF03 and RF05) with different longitudinal cloud trends, and a coastal pollution survey flight (RF12) capturing the latitudinal gradient in cloud height.

In order to explore the model representation of MBL dynamics in more detail, a decoupling measure was computed. Jones *et al.* (2011) showed that an effective decoupling indicator can be calculated as the difference in total water mixing ratio (q_t, water vapor plus cloud water) between two levels: 25% and 75% of the capping inversion height (CIH), considering a value below (above) 0.5 g/kg as a coupled (decoupled) MBL. Observed decoupling index and capping inversion height were obtained here from aircrafts vertical profiles following the method of Jones *et al.* (2011), and modeled values were obtained mapping the profiles and computing a modeled CIH and decoupling index. Figure 3.3c shows longitudinal statistics for all aircrafts flights. Both simulations

represent several basic aspects of the observed decoupling. The modeled decoupling index is accurately predicted everywhere (very good to excellent BoW performance) but in the transition zone, where performance is lower but still good. On average, areas west of 78° W are decoupled while areas east of 78° W are coupled both in the observations and the model, and better represented by the NW simulation. The spread of the decoupling index on each zone is also well simulated, with noticeable higher spread west to 78° W, as these zones alternate in between coupled and decoupled MBLs. Observations show a sharp longitudinal transition from coupled to decoupled MBLs, which is also represented by the model.

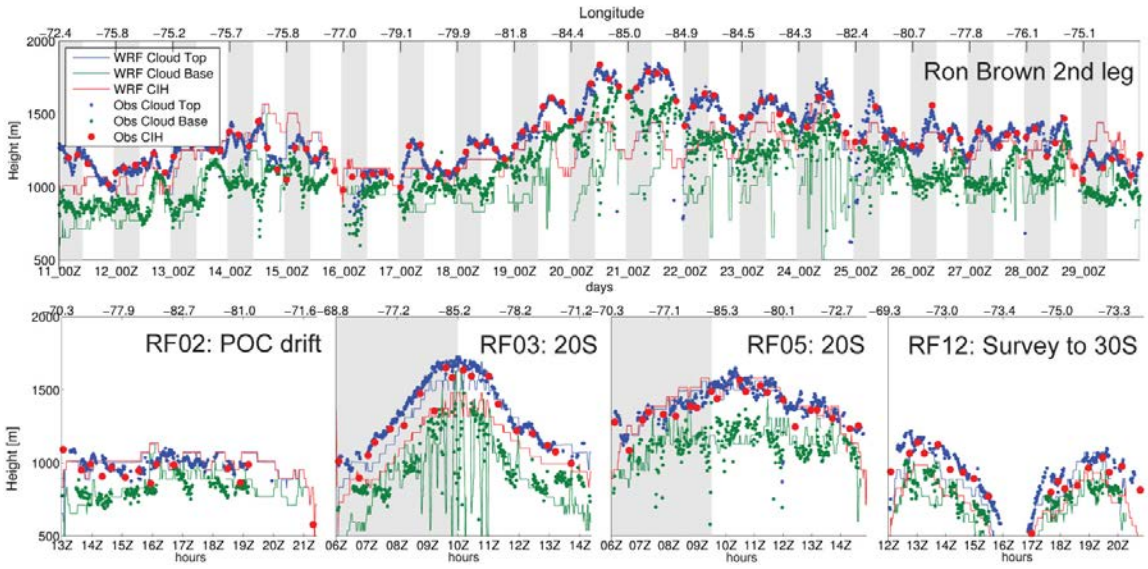

Figure 3.4. Observed and NW model cloud bottom, cloud top and capping inversion height (CIH) time series from Ron Brown (top) and four C-130 flights (bottom). Shaded areas represent night periods.

Cloud microphysics

Figure 3.5 shows statistics for cloud properties and for aerosol number concentration. Model cloud water representation is very good to excellent (in BoW

metrics) for both models (Fig. 3.5a), but the NW model typically shows higher amounts of cloud water than the base model as clouds are more permanent and thicker (consistent with the Twomey effect found by Albrecht, 1989). A clear difference is seen when analyzing number of droplets (Fig. 3.5b) where the increase in cloud albedo is more evident (Twomey, 1974) and modeled inner quartiles do not overlap over the remote region. This is a result of the difference in sub-cloud aerosol number concentration (Fig. 3.5c), where not even the modeled deciles overlap. Comparing observed and model droplet number and aerosol number concentration in the remote zone, the NW model presents excellent results while the base model is biased low (poor to good BoW scores), showing vast improvements in cloud microphysics by increasing the sub-cloud aerosol to near observed levels. We found consistency in the results, as when aerosol loads are relatively close to observations, the number of droplets also becomes closer to the observations. We thus conclude that the activation routine in WRF-Chem is consistent and reliable. The inability of NW to represent the lower end and spread of the cloud droplet and aerosol number distributions can be related to not considering wet deposition, as aerosol number is expected to decrease for intense sub-cloud rain events since a single droplet can collect a large amount of particles and release just one when evaporation occurs (Kazil *et al.*, 2011). Close to shore overestimation of droplet number concentration by both simulations may be explained by the slight overestimation of aerosol number and also by the fact that the model finds that the aerosol number concentration in the 1st bin (40 to 78 nm in diameter) is an important contributor to activated particles. The latter is not captured by the PCASP aerosol number concentrations, as it only measures aerosol diameters over 117 nm. Free troposphere aerosol number concentration (Fig. 3.5d) follows the same trend as in the MBL, with good to excellent BoW accuracy and few differences between the two simulations.

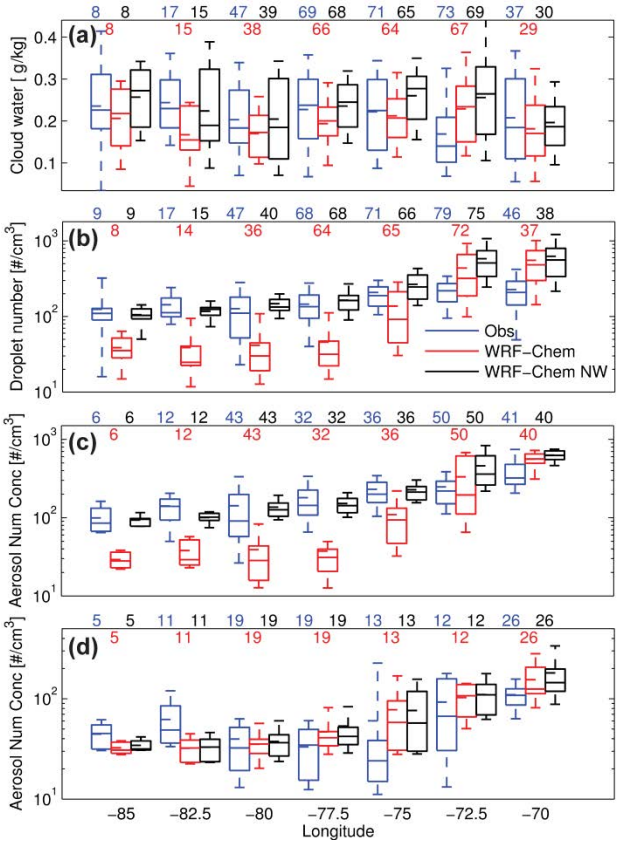

Figure 3.5. Box and whisker plots for selected cloud properties and aerosol number concentration as in Fig. 3.1. (a) Profile mean cloud water content. (b) Profile mean number of droplets concentration. (c) and (d): marine boundary layer (MBL) and free troposphere (FT) mean profile aerosol number concentration. Number of profiles is indicated at the top of each longitude bin.

Rain estimates extracted from radar reflectivities and model statistics are shown in Fig. 3.6. Focusing on the cloud top (a) and cloud base (b) plots, it can be seen that the model captures in-cloud rain stratification, showing lower mean and median values for the cloud top. WRF-Chem also represents the longitudinal gradient in rain rate (Bretherton *et al.*, 2010). The NW model tends to exhibit better agreement with observations, showing lower mean and median rainfall rates. The NW model has higher concentrations of activated particles and smaller effective droplet radius, which decrease autoconversion and suppress precipitation (Albrecht, 1989). The equilibrium reached in

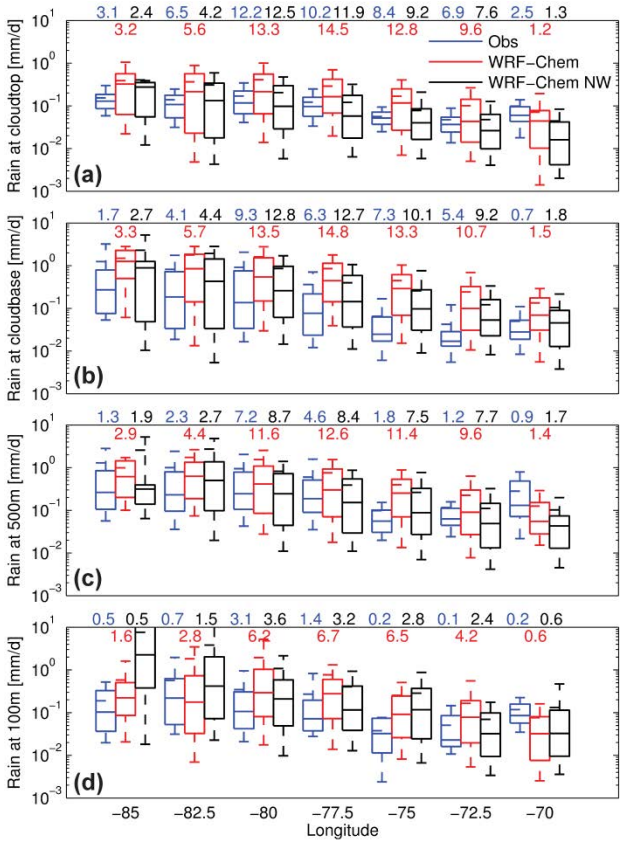

Figure 3.6. Box and whisker plots for radar derived and modeled rain at different heights as in Fig. 3.1. (a) and (b) corresponds to rain rates just below the cloud top and at the cloud base while (c) and (d) corresponds to rain rates at fixed heights of 500 and 100 m. The numbers above each zone represent sampling time in decimal hours.

the base simulation is off since as more precipitation is produced, more particles are scavenged (and not recovered after evaporation), further reducing the number of particles and leading to even more precipitation in a reinforcing feedback. Besides showing higher precipitation rates, the base run also shows higher precipitation occurrence along the flight track (sampling time on the top of each plot), while the NW results tend to agree more closely with observations. At lower altitudes (500 and 100 m), observed precipitation occurrence decreases, which is also captured by both models, with the NW model always showing lower occurrence. At 100 m, the base model shows better

agreement with remote observed rain rates and NW overestimates the mean and medium. Since the NW rain is scarcer, in agreement with observations, heavy drizzle events tend to skew the distribution. However, modeled rain range given by the outer deciles agrees with the observations.

While episodic comparisons with in-situ observations are critical, it is also important to consider model performance for regional climatology, as the model should represent monthly mean values and their spatial features. Figure 3.7 shows COD and LWP for MODIS and both WRF-Chem simulations. Model COD was computed by first computing the effective radius as in Martin *et al.* (1994) and then COD as proposed by Slingo (1989) for the 0.64–0.69 μm band, as the MODIS reference wavelength for this retrieval is 0.65 μm (King *et al.*, 2006). The base WRF-Chem model usually underestimates COD, while the NW model is closer to the observations. Several features are well represented: close to shore hotspots of COD around 17° S and 26° S, a nearshore local COD minimum around 36° S, and an increase in COD around 20° S from 80° W to 75° W. In the remote zone (83° W to 90° W), observed COD tends to fall between both models but closer to NW, for the same reasons presented before to explain episodic performance: the base model is unable to generate a thick enough cloud layer and drizzles too much, while the NW clouds do not dissipate when moving westwards, thereby increasing cloud lifetime (Albrecht, 1989). LWP path shows a different behavior, as both models underestimate MODIS LWP, probably due to a model bias in the Lin microphysics parameterization, as the Morrison scheme (Morrison and Pinto, 2005) generates higher LWP (Yang *et al.*, 2011b), as discussed further in the text. However, NW model results consistently show higher values and a better agreement with observations.

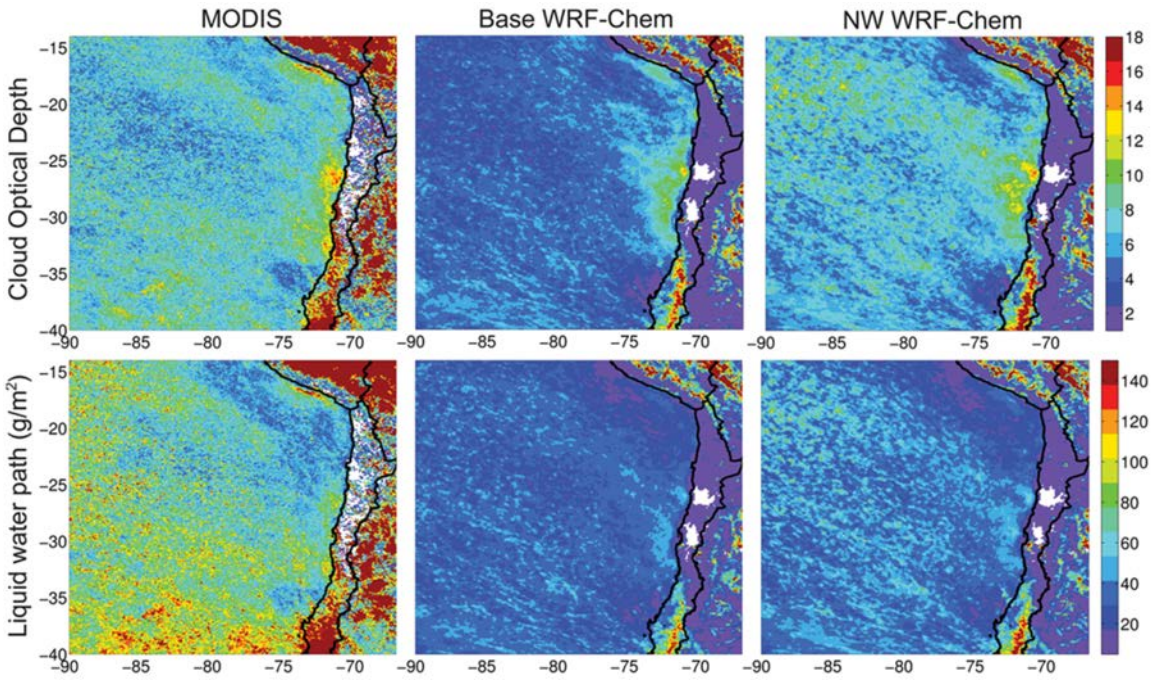

Figure 3.7. MODIS-Aqua products and model monthly averages for the VOCALS period (15 October to 16 November). First and second row show cloud optical depth (COD) and liquid water path (LWP), respectively while first, second and third columns show MODIS, the base model and the no wet deposition (NW) model, respectively.

Aerosol feedbacks and relation to sources

The Ron Brown provided a unique platform for continuous point measurements. Not only does the vessel have a much longer residence time in each regional model grid-cell than research aircraft, it also records the complete diurnal cycle at each location. One of the points where Ron Brown sampling efforts were focused was at (20° S, 75° W), where it spent approximately 8 days, 4 days on each leg of the cruise. This area was found to be affected by coastal sources (Allen *et al.*, 2011; Bretherton *et al.*, 2010; Hawkins *et al.*, 2010). To evaluate model performance and aerosol interactions, Fig. 3.8a compares total observed sulfate to the base and NW models. Observed values are closer to the NW model, but both models resolve most of the periods where SO_4 concentrations increase over 1 $\mu g/m^3$. As seen in Fig. 3.8b, the SO_4 episodes are well correlated with

aerosol number concentrations over 13 nm in diameter, a relationship also represented by the model. Observed aerosol number concentration is in the high range of the models because the lowest bin modeled is 40 nm, and does not include the 13 to 40 nm window. These sulfate episodes do not follow any diurnal pattern, and are a constant factor affecting aerosol concentrations in this zone. Model results, including prior modeling by Spak *et al.* (2010) that only included anthropogenic sulfur emissions, clearly indicate that these peaks can be attributed to continental sources, usually coming from Central Chile. As an example, Fig. 3.8c shows the evolution of second bin (78 to 156 nm in diameter) SO_4 (main contributor to aerosol number concentration) in a distinct pollution plume from the time emitted in Central Chile until it reaches the Ron Brown, 2 days after. When fresh, the maximum value of the plume is found on model level 17, around 650m above sea level. At this height, it is transported by southeasterly trades (Rahn and Garreaud, 2010) until it makes contact with the MBL, where it starts entraining and SO_2 to SO_4 conversion is enhanced in clouds. Once in the MBL, lower wind speeds result in the plume taking a longer time to reach the Ron Brown location. In the MBL, the plume receives additional SO_4 contributions from DMS, as a near-shore DMS emissions hot spot is found off central Chile (26° S-36° S) due to wind shear generated by the subtropical low-level jet (Garreaud and Muñoz, 2005; Muñoz and Garreaud, 2005). By performing a simulation without DMS initial conditions and emissions, we estimate the DMS contribution to sulfate to be from 15% to 25% in mass (which could be overestimated as shown in previous sections) by the time the plume reaches the Ron Brown location for the case analyzed, showing that these episodes are generated mainly by anthropogenic sources. The ability of these plumes to reach this zone is thought to be determined by the position of the surface pressure maximum of the Southeast Pacific Anticyclone (Spak *et al.*, 2010).

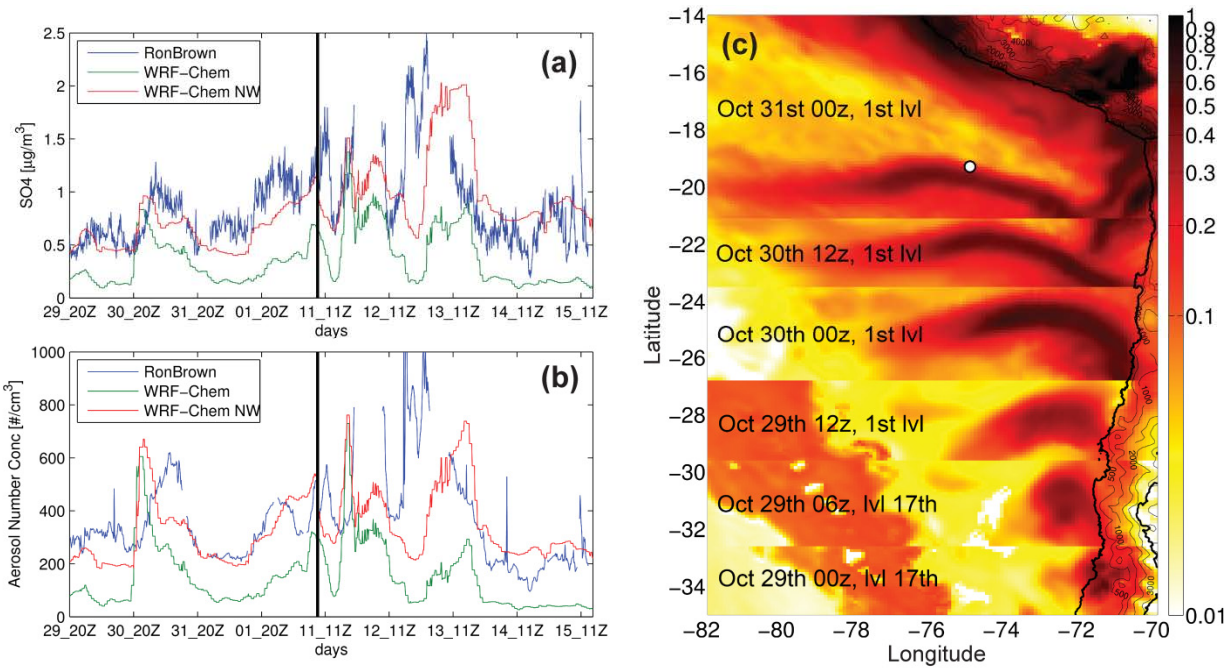

Figure 3.8. **(a)** Time series for observed and modeled SO_4. **(b)** Time series for observed and modeled aerosol number concentration for diameters over 13 nm and 40 nm respectively. Black thick lines in **(a)** and **(b)** divides both periods that Ron Brown stayed 4 days on 75° W: 29 October–1 November and 11–15 November. **(c)** Composite of NW model second bin (78–156 nm aerosol diameter) SO_4 concentration in µg/m^3. Each composite follows the same plume since it is emitted on Central Chile until it reaches Ron Brown (marked by a circle) two days after. The two most southern composites are extracted from level 17 (~670m over sea level) while the rest are extracted from the first model level. Scale is logarithmic.

Distant sources from Central Chile often have a visible footprint in SO_4 mass and aerosol number concentration over the study domain, and these enhanced aerosols participate in cloud feedbacks such as drizzle suppression. Figure 3.9 shows curtain plots of radar reflectivity (proxy for precipitation) and aerosol number concentration for C-130 RF05 flight, showing very marked and correlated longitudinal gradients both on aerosol load and precipitation for NW and observed values. The base model (W) shows the same gradient (not shown), with higher rain rates in the remote region. Bretherton *et al.* (2010) argued that lack of drizzle near the coast is not just a microphysical response to high

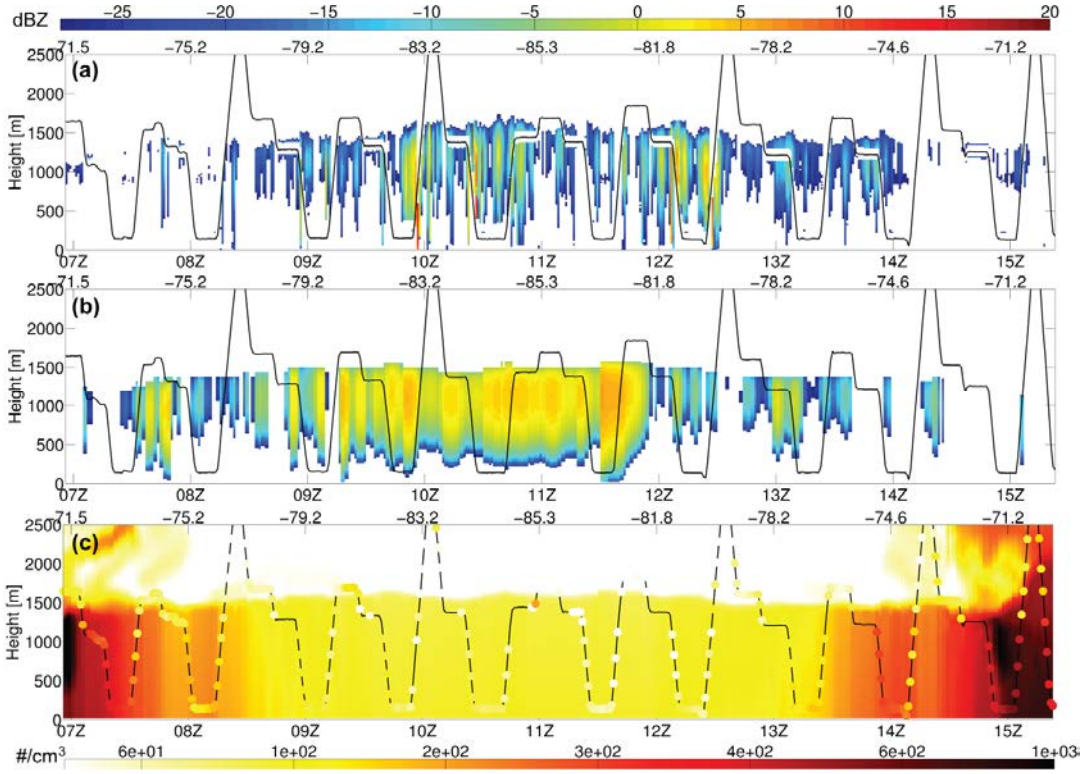

Figure 3.9. Curtain plots for radar reflectivity (Z, in dBZ) and accumulation mode aerosol number concentration (#/cm^3) for C-130 flight RF05 on 25 October. **(a)** and **(b)** shows radar observed and NW model Z while **(c)** shows NW model as the curtain and one minute average PCASP observations as colored circles. Observed Z and PCASP aerosol are 1 min averages. Mdel Z is computed according to Appendix A in Saide *et al.* (2012b). Solid lines represent flight track with the line becoming segmented on **(c)** every time there is a PCASP observation. For all panels, bottom scale is time in hours and top scale is longitude in degrees.

droplet concentrations; but other aspects such as lower LWP and thinner clouds (related to shallower and coupled MBL) can be comparably important. However, synoptic conditions present during RF05 flight were such that MBL height differences between off shore and remote zone weren't significant (cloud top and base heights differences less than 250m and 200m respectively, Fig. 3.4) and the remote region was not decoupled (no vertical gradients on aerosol concentrations inside the MBL, also verified by flight vertical profiles as in Fig. 3.3) but we still see very high precipitation gradients. Thus,

differences in aerosol load might be playing a more important role than previously thought. The enhanced aerosols also participate in cloud feedbacks visible in satellite retrievals of cloud properties. Figure 3.10a shows MODIS-Aqua cloud effective radius for an overpass on a day with a thick cloud deck, where aerosol feedbacks are more pronounced. Figure 3.10b, c show model results for effective radius and second bin sulfate surface concentrations. Model cloud effective radius clearly decreases when the MBL is dominated by high accumulation mode sulfate concentrations, following a similar shape to the plume, which can also be observed in the MODIS overpass. The scene shows two distinct plumes coming from Central Chile: an older one between 23° S and 20° S and a fresher one in between 29° S and 25° S, both showing a decrease in cloud effective radius in both model and the observations. These findings highlights the need to consider aerosol interactions and transport from far-away sources in high-resolution studies and NWP applications over the region and similar persistent coastal stratocumulus in eastern boundary tropical and subtropical areas.

Assessing differences due to model configuration

WRF-Chem is a community model with several choices of parameterizations to represent various processes (Skamarock *et al.*, 2008). These choices result in different model configurations, which can produce different predictions. For example, there are two microphysics schemes that can be used to study aerosol indirect effects in WRF-Chem v3.3: the Lin scheme (used in this study); and the Morrison scheme (Yang *et al.*, 2011b; Morrison and Pinto, 2005). Figure 3.11 shows results from a sensitivity column study where both schemes were run until reaching stable conditions as a function of number of droplets. Significant differences of over an order of magnitude are found in rain rates between both schemes. For the VOCALS-REx case of study, the Lin scheme rain rates showed good performance (Fig. 3.6), while the Morrison scheme showed under-prediction (Yang *et al.*, 2011b), in accordance with Fig. 3.11.

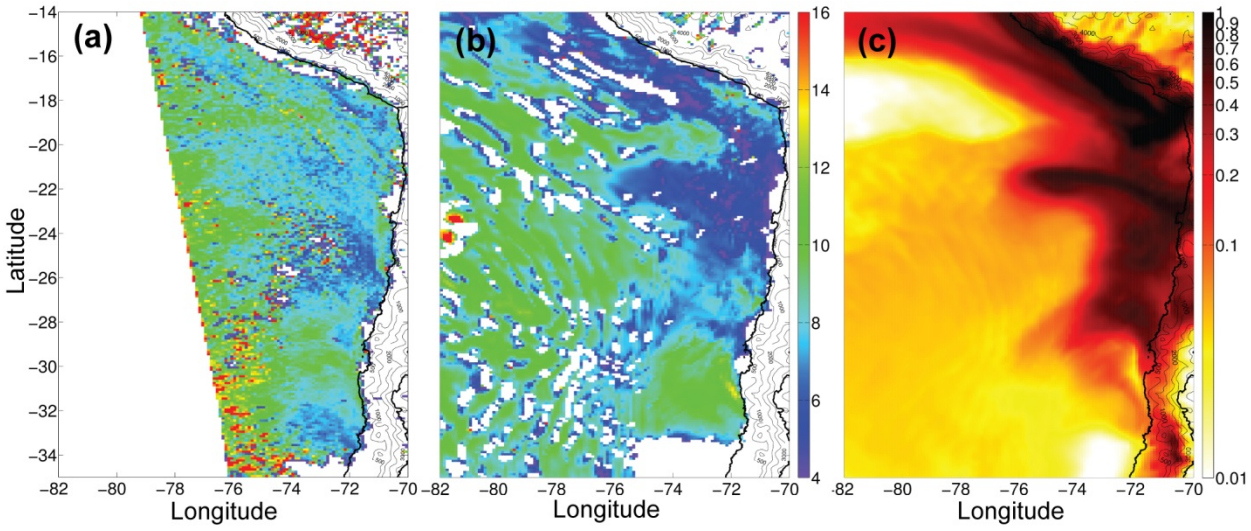

Figure 3.10. Horizontal plots of cloud effective radius (μm, a and b) and first level, second bin (78–156 nm aerosol diameter) SO_4 concentration (μg/m^3, c). (a) shows MODIS-AQUA cloud effective radius for 16 October 17:00 UTC overpass while (b) and (c) shows NW model results for the same time. Model cloud effective radius is computed for the cloud top.

The higher rain rates in our study can also explain the larger underprediction of sulfate mass and aerosol number concentration by the base model (Figs. 3.1 and 3.3) compared to the Yang *et al.* (2011b) study. We hypothesize that the main cause of the rain mismatch is the different autoconversion (cloud droplets to rain conversion) parameterization used in both schemes. The Morrison scheme uses Khairoutdinov and Kogan (2000) parameterization, which uses regressed coefficients (multiplicative and power laws) from cloud drop size spectra predicted by LES simulations, which shows a linear behavior in the log scale (Fig. 3.11a); while the Lin scheme uses Liu *et al.* (2005a) which introduces a threshold function which depends on droplet number concentration that is responsible for the curve shape and rain suppression in Fig. 3.11a. On the other hand, the Morrison scheme shows higher liquid water content (Fig. 3.11b), which is not completely explained by the lower precipitation, as LWP differences are still present

when rain rates are similar for low number of droplets. This is also coherent with the fact that Yang *et al.* (2011b) shows better agreement to MODIS LWP than our study, where this configuration under-predicts it.

Full double moment microphysics schemes (Lin scheme is double moment for cloud water only) are necessary to improve process representation in models Morrison *et al.* (2009). As autoconversion seems to be generating low performance in rain rates, we propose to implement and test the Liu *et al.* (2005a) parameterization in the Morrison scheme. The implementation has to come along with the inclusion of aerosol re-suspension due to rain evaporation on the wet deposition scheme to avoid the MBL aerosol biases seen in Figs. 3.1 and 3.3.

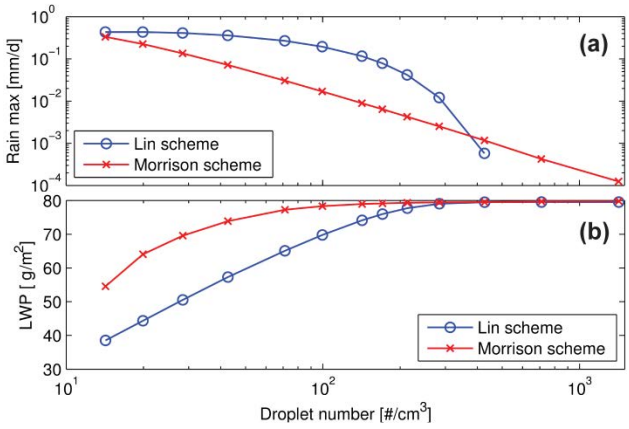

Figure 3.11. Results from column study for comparing Lin and Morrison microphysics schemes for a profile on (80° W, 20° S) at 00:00 UTC on 28 October 2008. (a) shows maximum rain rate per profile while (b) shows liquid water path (LWP) per profile. Each profile is run with a different droplet number concentration using a 12 s time step for enough time to reach stable conditions. For (a), missing points means rain rate equal to zero.

Conclusions

There is an imperative need for reducing uncertainty and improving the atmospheric models used in studies of aerosol-cloud interactions at scales needed for

NWP, air quality predictions, and policy assessments. In this context, several intensive measurement campaigns have been carried out to improve our understanding of aerosol and cloud interactions and they provide an extensive data base for use in testing and improving models. In this work we test the regional model WRF-Chem for the VOCALS-REx campaign which focused on studying the persistent stratocumulus deck on the South East Pacific, off the shore of Chile and Peru. Starting from the fact that the inclusion of aerosol cloud interactions in the model are important to represent processes in this region (Yang *et al.*, 2011b), we perform model simulations designed to address the questions: what are the effects on cloud dynamics and microphysics from changing the sub-cloud aerosol loads? And do these effects bring model results closer to observations when aerosol loads are in better agreement to measurements? To address these questions results from two model simulations, with (base) and without wet deposition (NW) were analyzed. Both runs represent an incomplete modeling picture, as the base run lacks aerosol resuspension (which is important in drizzling stratocumulus), and excluding wet deposition means neglecting a known removal process. These simulations produce significant differences in aerosol amounts, particularly in the remote zone where sulfate mass and accumulation mode aerosol number distributions do not overlap with each other and can be one order of magnitude different. Observed aerosol mass and number are usually closer to the NW results, because the model wet deposition process irreversibly removes aerosol even for evaporating rain. Little surface rain was observed during the campaign, so evaporation of drizzle drops is a likely source of sub-cloud aerosols. The increase in aerosol number in NW generate a significant difference between the models in terms of marine boundary layer (MBL) dynamics and cloud microphysics, in accordance to warm clouds aerosol indirect effects. These include an increased number of cloud droplets (Twomey, 1974) showing no overlap of the inner quartiles from the two models in the remote zone; increased MBL and cloud heights (Pincus and Baker, 1994) reaching up to 200m differences; drizzle suppression on average concentrations and on

number of detections; increased liquid water content and increased cloud lifetime (Albrecht, 1989); which helps answer the first question. MBL dynamics and cloud microphysics observed values are usually closer to NW or at least fall in between both models showing that better aerosol statistical performance lead to changes in the right direction, which helps answer the second question. This study demonstrates the capabilities of the WRF-Chem model to simulate aerosol/cloud interactions, particularly regarding the activation routine, which simulates number of droplet concentrations more accurately when sub-cloud aerosol loads more closely match observations. However, the model needs further improvements to address issues such as aerosol resuspension in rain wet removal, overestimation in oceanic DMS and sea-salt emissions, increased cloud driven SO2 to sulfate conversion and move from bulk to sectional/modal aqueous chemistry. Also, an assessment of model differences when using distinct WRF-Chem configurations shows these seem to be related to the microphysics schemes, specifically to different autoconversion parameterizations which can generate over an order of magnitude disagreement on rain rates predictions for the same conditions.

Besides performing campaign averaged comparisons, we quantified local model performance for stratocumulus properties and their hourly evolution against ship-based measurements (NOAA Ron Brown), three aircraft observations (NSF C-130, DoE G-1, FAAM BAe-146) and satellite retrievals (MODIS) using them to explain how aerosols and model processes affect system response. For instance, hourly evolution of cloud heights was evaluated showing a good model performance for the diurnal cycle and different synoptic conditions with the exception of periods where the model is not able to recover from the underestimated MBL height found on the boundary conditions. Also, an episodic study was performed showing that anthropogenic sources from Central Chile substantially changed aerosol mass and number, rain and cloud optical properties over the ocean both in modeled and observed values, showing that indirect effects might be

playing a more important role in modulating cloud properties and dynamics than stated in previous studies.

In our analysis we have attempted to perform a complete multi-platform evaluation for a regional simulation of clouds and aerosols, where we included VOCALS-REx observations which were not compared to models previously, such as decoupling state, trace gas concentrations (carbon monoxide, ozone), cloud aerosol composition, cloud water ionic balance and radar reflectivities. These are all crucial to fully quantifying regional model performance in this tightly coupled system. In order to provide quantification to this evaluation, we introduced a new metric for assessing model performance that uses box and whisker plots. This metric is independent of the variable being analyzed, thus allows doing performance cross-comparison in between different models and variables.

Together with improving model issues already mentioned, future work should be focused on continuing to validate models with aerosol and cloud interactions from measurement campaigns in other locations, as conditions for each region vary extensively. Also, several observation platforms such as close to shore flights (NERC Dornier 228 and CIRPAS Twin Otter) and inland measurements (Iquique, Paposo and Paranal sites) were not considered as the modeling was too coarse for their use (12 km^2 grid cells). Thus, finer resolution studies for the same area are needed to exploit these data (4–1 km^2 grid cells). These studies help to better quantify the uncertainties in models, that need to be considered when these models are used as tools for policy makers and for weather and air quality forecasts.

Collaborators and funding sources

We thank all people and organizations that participated in the VOCALS-REx campaign, generating and allowing us to use the complete and comprehensive data set. Special thanks to Timothy Bates, Paquita Zuidema and Ludovic Bariteau for helping

interpret and compare observational data, to William Gustafson and Jerome Fast for comments on modeling and to two anonymous reviewers for their constructive comments. Ron Brown, C-130 and G-1 measurements were obtained from the VOCALS data archive NCAR/EOL, which is sponsored by the National Science Foundation (NSF). MODIS data was obtained from the NASA Langley Research Center Atmospheric Science Data Center. Special thanks to the staff of the NCAR Research Aviation Facility for supporting the deployment of the C130 and the staff of the UWYO King Air national facility for enabling the deployment of the WCR and WCL onboard the C130 during VOCALS-REx. We also thank the UK Natural Environment Research Council (NERC) for funding the VOCALS UK contingent to the project (grant ref: NE/F019874/1) and the NERC Facility for Airborne and Atmospheric Measurment (FAAM) and Direct Flight and Avalon for operational support of the BAe-146 aircraft. This work was carried out with the aid of NSF grants 0748012 and 0745986, grant number UL1RR024979 from the National Center for Research Resources (NCRR), a part of the National Institutes of Health (NIH), FONDECYT Iniciaci´on grant 11090084, and Fulbright-CONICYT scholarship number 15093810. Its contents are solely the responsibility of the authors and do not necessarily represent the official views of the founding institutions.

Author contributions

This work is published in Saide *et al.* (2012b). P. E. Saide, S. N. Spak and G. R. Carmichael designed the study and P. E. Saide executed it. M. A. Mena-Carrasco (UNAB) contributed in the generation of the emission fields. Q. Yang (PNNL) provided feedback on model configuration and provided code for DMS emissions. The other co-authors of the paper (S. Howell, D. C. Leon, J. R. Snider, A. R. Bandy, J. L. Collett, K. B. Benedict, S. P. de Szoeke, L. N. Hawkins, G. Allen, I. Crawford, J. Crosier and S. R. Springston, see affiliations on the article) provided data measured during the VOCALS-

REx along with recommendations on how to compare measurements and model data. All authors contributed to the final form of the manuscript.

CHAPTER 4 IMPROVING AEROSOL DISTRIBUTIONS BELOW CLOUDS BY ASSIMILATING SATELLITE-RETRIEVED CLOUD DROPLET NUMBER

Abstract

Limitations in current capabilities to constrain aerosols adversely impact atmospheric simulations. Typically, aerosol burdens within models are constrained employing satellite aerosol optical properties, which are not available under cloudy conditions. Here we set the first steps to overcome the long-standing limitation that aerosols cannot be constrained using satellite remote sensing under cloudy conditions. We introduce a new data assimilation method that uses cloud droplet number (N_d) retrievals to improve predicted below-cloud aerosol mass and number concentrations. The assimilation, which uses an adjoint aerosol activation parameterization, improves agreement with independent N_d observations and with in-situ aerosol measurements below shallow cumulus clouds. The impacts of a single assimilation on aerosol and cloud forecasts extend beyond 24 hours. Unlike previous methods, this technique can directly improve predictions of near surface fine mode aerosols responsible for human health impacts and low-cloud radiative forcing. Better constrained aerosol distributions will help improve health effects studies, atmospheric emissions estimates and air quality, weather and climate predictions.

Introduction

Ambient aerosols are important air pollutants with direct impacts on human health (Pope *et al.*, 2006). They also play important roles in the Earth's weather and climate systems through their direct (Bellouin *et al.*, 2005), semi-direct (Ackerman *et al.*, 2000) and indirect effects (Lohmann and Feichter, 2005) on radiative transfer and clouds. Their role is dependent on their size, number, phase and composition distributions, which vary significantly in space and time. There remain large uncertainties in predictions of

aerosols due to uncertainties in emission estimates and in chemical and physical processes associated with their formation and removal (Mebust *et al.*, 2003; Saide *et al.*, 2012b; Yang *et al.*, 2011b; Heald *et al.*, 2010; Meskhidze *et al.*, 2011). These uncertainties in aerosol distributions lead to large uncertainties in weather and air quality predictions and in estimates of health and climate change impacts (Solomon *et al.*, 2007).

Constraining ambient aerosol distributions with current Earth observing systems is a difficult task. The most common approach is to assimilate satellite retrievals of aerosol optical depth (AOD) (Carmichael *et al.*, 2009; Benedetti *et al.*, 2009), a quantity that represents total aerosol mass and composition in the atmospheric column. The requirement of cloud-free conditions for a successful retrieval and the remaining challenges of relating AOD to aerosol mass, size and composition, limit the utility of AOD retrievals (by themselves) in constraining aerosol mass and composition (Kahn *et al.*, 2007; Redemann *et al.*, 2006). These shortcomings are particularly true in regions of persistent marine stratocumulus, such as the Southeast Pacific off the coast of Chile and Peru, where aerosol-cloud interactions are important to the energy balance (George and Wood, 2010) and limitations in current observing and modeling capabilities adversely impact regional and global weather and climate predictions (Wyant *et al.*, 2010). A typical MODIS AOD scene in this region (Figure 4.1, upper left) shows that AOD provides essentially no useful information to constrain aerosol distributions when low clouds are present (Fig. 4.2).

Aerosols play an important role in cloud formation, acting as cloud condensation nuclei (CCN), and further affect cloud macro- and micro-physical properties such as albedo (Twomey, 1991), drizzling capacity and lifetime (Albrecht, 1989), and cloud base and top heights (Pincus and Baker, 1994), among others. Despite uncertainties (Solomon *et al.*, 2007) and challenges (McFiggans *et al.*, 2006) in modeling aerosol-cloud interactions, recent studies have shown significant capabilities in predicting and explaining aerosol indirect effects in low cloud regimes (Saide *et al.*, 2012b; Yang *et al.*,

2011b; Kazil *et al.*, 2011). By building on this mechanistic understanding, observations of clouds may be used to infer aerosol physicochemical properties. This is done by using a new data assimilation technique described in the Methods section.

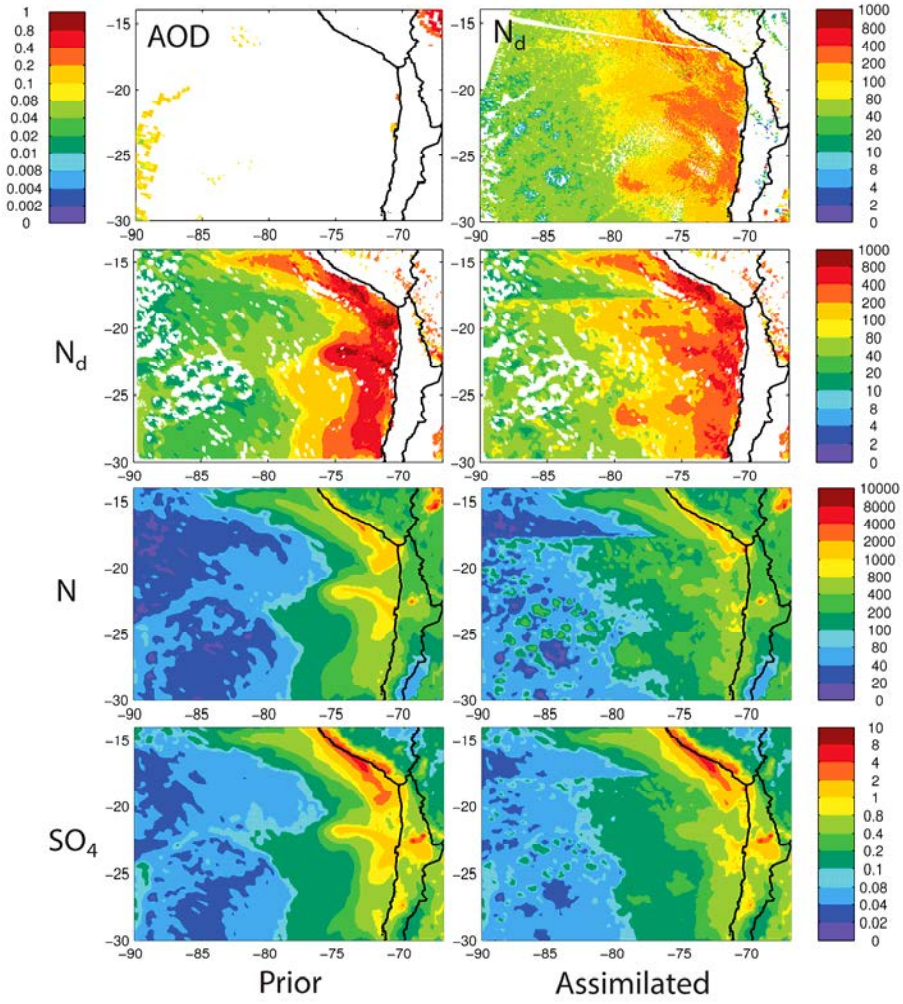

Figure 4.1. Observed and model maps for the Southeast Pacific and coastal Chile and Peru. Top row: MODIS AOD (left) and N_d (right, in #/cm^3) at Oct. 16th 2008 at 15Z overpass. Second to fourth rows show prior (left column) and assimilated (right column) results for N_{d_2} accumulation mode N (#/cm^3) and sub-micron sulfate concentrations (μg/m^3) one hour after assimilating MODIS N_d. See S1.5 for further details.

Methods

We propose a new data assimilation technique (Fig. 4.3) to improve aerosol mass (M) and number (N) distributions from satellite retrievals of cloud droplet number (N_d), and demonstrate it for a stratocumulus application, where these remote sensing products have been shown to accurately represent in-situ N_d observations (Painemal and Zuidema, 2011; Bretherton *et al.*, 2010; Painemal *et al.*, 2012). The forward model includes a vertical mixing-activation

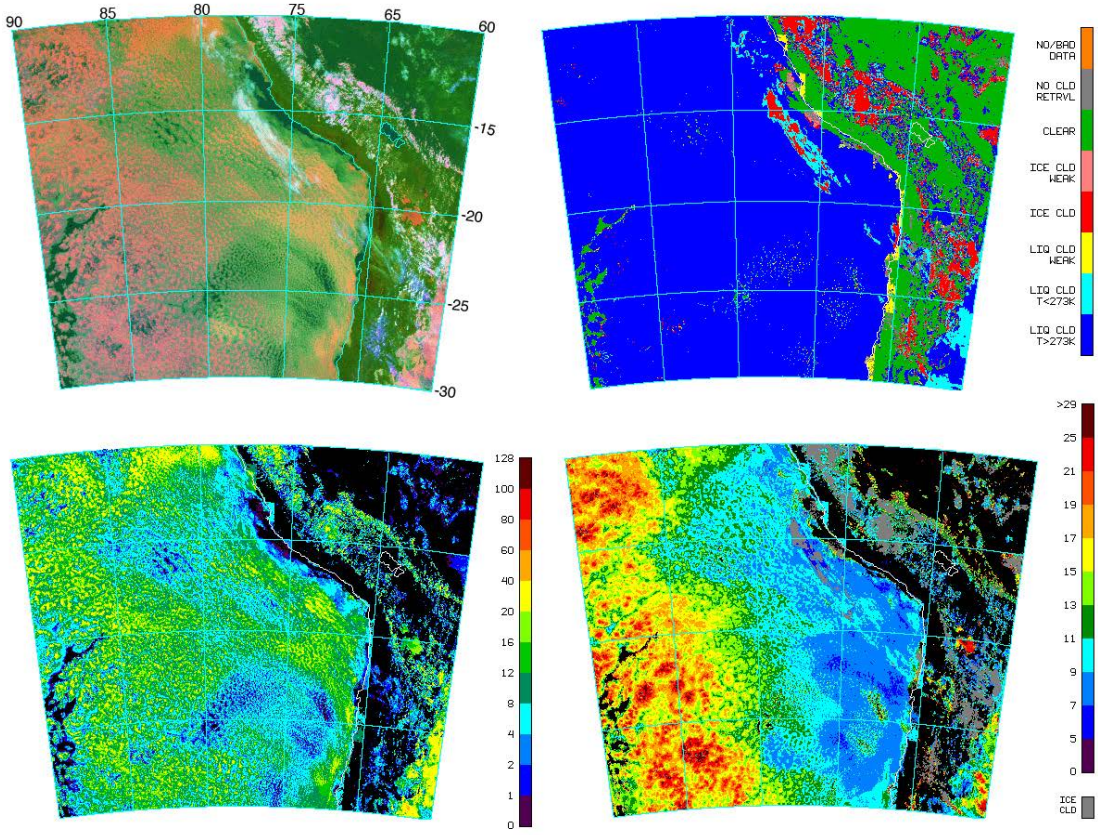

Figure 4.2. GOES10 imagery for 16 Oct 2008 at 15UTC. Clockwise from top-left corner: Multichannel RGB, Cloud phase, Cloud effective radius (μm), Cloud optical depth. Ref: http://www-angler.larc.nasa.gov

parameterization used to predict N_d from meteorological conditions and initial M (composition/size/phase resolved), N (size/phase resolved) and N_d distributions.

Sensitivities of predicted N_d derived with respect to these input variables are computed efficiently using the adjoint of the mixing-activation parameterization. These sensitivities are then utilized in a formal data assimilation framework to find the optimal model state that best fits the N_d observations considering confidence in both the observations and the initial conditions. We chose to optimize for initial N only, as it has been shown to be the most important contributor to N_d sensitivities over other variables such as vertical velocity and aerosol composition for most conditions (McFiggans *et al.*, 2006; Feingold, 2003), especially over oceans (Quaas *et al.*, 2008; Karydis *et al.*, 2012; Hegg *et al.*, 2012). This is accomplished through three-dimensional variational (3DVAR) data assimilation with a log-normal cost function and five dimensional (3D in space + size + phase) N covariances. Assimilation yields size-, phase- and space-resolved correction factors for N, which are further applied to each M composition bin (assuming the internal composition of each size/phase bin remains the same), resulting in an updated aerosol mass for each compound as well.

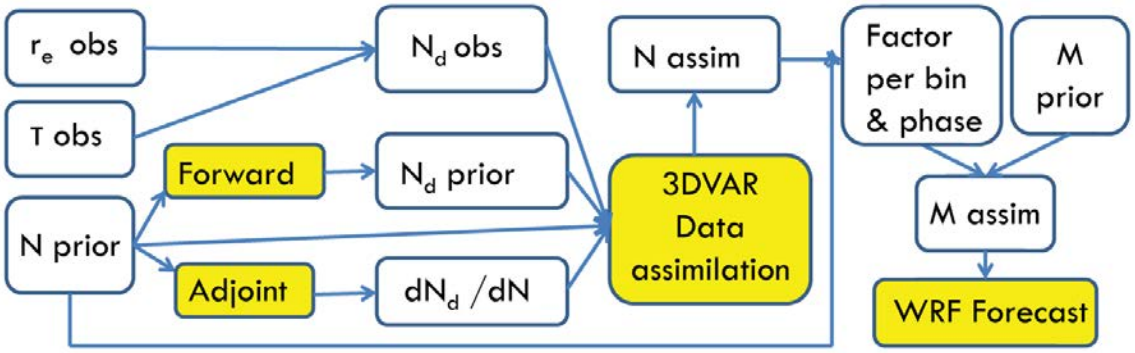

Figure 4.3. Flow diagram for droplet number concentration (N_d) data assimilation. Numerical variables are found in open boxes and code or programs are found in yellow boxes. r_e: Droplet effective radius, τ: Cloud optical depth, N: aerosol number concentration, M: Aerosol mass concentration per specie.

The following subsections further describe the observations, forward and adjoint models, assimilation technique, forecast model and experiments. Figure 4.3 presents a flow diagram describing the main variables and code used in the assimilation process and should be used as a guide when reading this section.

Observations

We use cloud optical depth (τ) and drop effective radius (r_e) observations (see examples in Fig. 4.2) to compute cloud number droplet (N_d) assuming liquid water content increases linearly with height in the cloud layer (Szczodrak *et al.*, 2001):

$$N_d = K\tau^{1/2} r_e^{-5/2}$$

with K= 1.4067x10^{-6} [$cm^{1/2}$], which generates good agreement with in-situ observations for the domain analyzed (Painemal and Zuidema, 2011; Painemal *et al.*, 2012). This equation makes the assumption that cloud profiles are adiabatic, which is a good approximation for this region. In other regions where this assumption might not be valid, other estimates that account for the sub-adiabaticity of the cloud can be used (Bennartz, 2007). Cases where τ and r_e retrievals might not be accurate should be screened out before N_d computation. An example is when a thick aerosol plume overlies the cloud. In the case of an absorbing smoke plume, r_e computed from different channels (e.g. 1.6- and 3.9-μm for GOES or METEOSAT) will start showing discrepancies, which can be used to screen them out. If a thick dust plume overlies the clouds, scattering will dominate and τ will be affected. For these cases, even an AOD of 2-3 is at the lower end of the cloud optical depth distributions (Fig. 4.2) thus the cloud signal will dominate and only optically thin clouds should be screened out. Once N_d is computed, we use nearest neighbor interpolation to place observations onto the model grid, where assimilation is performed.

Observation operator (forward and adjoint models)

The observation operator, which transforms model parameters being optimized into the observation space, is in this case the vertical mixing and activation parameterization (Chapman *et al.*, 2009) from the WRF-Chem v3.3 model (Grell *et al.*, 2005; Skamarock *et al.*, 2008). The parameterization is based on a maximum supersaturation determined from a Gaussian spectrum of updraft velocities and the internally mixed aerosol properties within each aerosol size bin (Abdul-Razzak and Ghan, 2002), and has been shown to accurately represent marine stratocumulus dynamics (Saide *et al.*, 2012b; Yang *et al.*, 2011b). Two phases are traced: dry (interstitial aerosol) and wet (activated aerosol). Starting from aerosol mass (M) and number (N) distributions and input meteorological variables, this forward model computes N_d for each model vertical layer. In order to yield a column N_d directly comparable to satellite observations, the model column value is averaged over cloud-containing grid cells, since droplet concentration tends to be relatively constant with height in these clouds (George and Wood, 2010; Bennartz, 2007). In order to compute sensitivities, the adjoint of the mix-activation and vertical averaging routines were obtained using the automatic differentiation tool TAPENADE v3.5 (Hascoët and Pascual, 2004), which successfully passed tangent linear and adjoint tests with 4 and 8 significant digits of accuracy, respectively. The adjoint provides an efficient way to compute derivatives, as sensitivities of one N_d observational pixel with respect to all parameters (N resolved in the vertical, in size and in phase) can be computed with a single run of the adjoint. Also, as the forward mix-activation parameterization is vectorized in the X and Y spatial dimension (as it is part of the WRF-Chem framework), then the adjoint inherits this characteristic so sensitivities for several columns can be computed efficiently at the same time.

Assimilation method

We choose to implement a 3DVAR method (Kalnay, 2003) modified using a Gaussian anamorphosis (Bocquet *et al.*, 2010), introducing log-normal statistics in both state (Henze *et al.*, 2008) and observation space. The use of log-normal statistics assumes errors to be of multiplicative nature, which is convenient in this case as N (parameters being improved) and N_d (observations assimilated) are always positive and they range over several orders of magnitude (10-10^4 and 10-10^3 for the study case, respectively). Thus, the functional *J* being minimized is:

$$J(N) = \frac{1}{2}\left(ln\left[\frac{H*(N-N_u)+C(N_u)}{C_{obs}}\right]\right)^t R^{-1}\left(ln\left[\frac{H*(N-N_u)+C(N_u)}{C_{obs}}\right]\right) \ldots$$
$$+\frac{E}{2}\left(ln\left[\frac{N}{N_b}\right]\right)^t B^{-1}\left(ln\left[\frac{N}{N_b}\right]\right) \qquad (1)$$

where *N* is the aerosol number field, with sub-index *b* and *u* used for background (prior) and base state for the adjoint sensitivities (*H*) computation respectively, *C(·)* is N_d concentrations from the forward operator, C_{obs} is the N_d satellite observation, *E* a regularization parameter (Henze *et al.*, 2008) and *R* and *B* the error covariance matrices for the observations and state. The minimum of *J* is found numerically using the L-BFGS-B algorithm (Zhu *et al.*, 1997). Optimization is performed using lower and upper bounds so the scaling factor applied to the background is over 0.1 and less than 10. As the aerosol activation process is highly non-linear, we implement an outer/inner loop strategy (Kleist *et al.*, 2009b) that re-computes sensitivities starting from the previous inner loop results. *B* is considered non-diagonal with five dimensional correlations: three spatial, on aerosol bins (8 sections) and on phase (dry/wet), which provides stability in the solution. Covariances between any two *i,j* gridcells are computed using an exponential decay law (Gaspari and Cohn, 1999):

$$B_{ij} = I_{ij} * e^{-\frac{Dxy_{ij}}{Lxy}} * e^{-\frac{Dz_{ij}}{Lz}} * e^{-\frac{Db_{ij}}{Lb}} * e^{-\frac{Dp_{ij}}{Lp}} \qquad (2)$$

$$I_{ij} = \begin{cases} z_i > CIH_{ij} \ or \ z_j > CIH_{ij} & 0 \\ else & 1 \end{cases} \qquad (3)$$

where Dq_{ij} represents distance between i and j on the horizontal ($q = xy$), vertical ($q = z$), size bins ($q = b$) and phase ($q = p$), with correlations lengths of $Lb = 0.5$ on size bins, $Lp = 0.5$ on phase and $Lxy = 2$ grid-cells (~25 km) on the horizontal. We use a large vertical correlation length ($Lz = 100$ levels, ~5km) to simulate good mixing in the MBL but we truncate correlations to 0 with grid-cells over the cloud layer (I_{ij} function), simulating the capping inversion height (CIH_{ij}) characteristic of this region (Bretherton *et al.*, 2010). R is considered diagonal and equal to the identity matrix meaning that the errors on the logarithmic factors of model vs. observation are the same for all observation pixels and are not correlated with each other. This is assumed for simplicity as this is the first application using this technique and can be modified for future applications propagating the uncertainties contained in the cloud optical depth and drop effective radius retrievals to N_d. E is used to weight each member of the right hand side of Eqn (1) and is chosen equal to 1, such that after assimilation similar net correction factors are found for the analysis vs prior N and modeled vs observed N_d. This combination of assumptions generates a resultant modeled N_d value in observation space directly comparable to contemporary satellite retrievals (see Fig. 4.1).

The assimilation produces an optimized N field, which is used to modify the mass and composition distributions. Comparing assimilated and prior N, multiplicative correction factors are obtained, which have the same dimension as N (number of 3D spatial grids, size bins and phases). Making the assumption that the assimilation does not change the aerosol composition within each size and phase bin, these factors are applied to each of the corresponding mass distributions (M). Then, the assimilated N and the updated M are used as initial conditions in forecast model.

Forecast model

Forecasts were performed using the WRF-Chem v3.3 model (Grell *et al.*, 2005; Skamarock *et al.*, 2008) configured specifically for this region as shown in Chapter 3.

The chemical and aerosol mechanisms used is the CBMZ gas-phase chemical mechanism (Zaveri and Peters, 1999; Fast *et al.*, 2006) coupled to the 8-bin sectional MOSAIC (Zaveri *et al.*, 2008) aerosol module. In this implementation the aerosol lower, upper and center diameter for each size bin have fixed values (Yang *et al.*, 2011b). The WRF-Chem and MOSAIC version used keeps track of nine aerosol mass composition (sulfate, nitrate, chloride, sodium, ammonium, organic and black carbon, other inorganics and aerosol water) and total number distributions. WRF-Chem is configured to include aerosol direct (Fast *et al.*, 2006) and indirect effects (Chapman *et al.*, 2009). The inclusion of indirect effects makes necessary the addition of the phase bin (wet and dry) to each of the composition and size bins. Thus, the model advects a total of (9+1)x8x2=160 aerosol variables, where only aerosol number distribution (16 variables) participates in the assimilation process and the rest (mass variables) are scaled as explained in the Methods section.

Assimilation experiments

Two types of experiments are performed: Those that assimilate MODIS N_d (Figs. 4.1 and 4.5); and those that assimilate GOES10 N_d (Fig. 4.4). The MODIS experiment consists in performing a single assimilation using data from the overpass on 16 Oct 2008 at 15Z (Fig 4.1, top-right panel). This date is chosen as it is a day with an extensive and thick stratocumulus deck and also the MODIS overpass goes right over the region of interest. The assimilation is performed in the region over 18º-34º S and 70º-90º W, over the persistent stratocumulus deck. Then, WRF-Chem forecasts are performed using prior and posterior as initial conditions. GOES10 retrievals are considered as independent data in this experiment and used for evaluation. Although highly correlated with each other, the N_d values estimated from GOES-10 are, on average, ~20% less than their MODIS counterparts because of differences in resolution and retrieval methods (Painemal *et al.*, 2012). This difference has negligible impact on the implications of the comparisons

because it does not significantly change the differences between the background and assimilation runs relative to the observations. We chose to assimilate MODIS and compare against GOES10 to use the detailed time resolution provided by GOES10 to evaluate the assimilation performance. Comparison is done by computing statistical differences between GOES10 N_d and both models (prior and posterior). Fractional error and fractional bias (Morris *et al.*, 2005) are computed over a region for each GOES10 retrieval. The regions considered are those over 18º S -30º S and 70º W-90º W during the first day (16 Oct 2008) and over 15º S -25º S and 70º W-90º W region during the second day (17 Oct 2008). Different regions are chosen for different days to account for aerosol advection. Figure 4.5 statistics are computed for 5ºx5º regions for each hour, including each satellite retrieval in the closest hour (usually two per hour).

For the second type of experiment (Fig. 4.4), we assimilate GOES10 N_d and use VOCALS-REx NCAR C-130 aerosol measurements as independent observations to evaluate the assimilation performance. In this case, GOES10 is assimilated instead of MODIS, as GOES10 enables us to choose a retrieval for assimilation that is close to the start time of each flight, so that the assimilation results can be compared to the in-situ observations. This second experiment also demonstrates that assimilation can be done using either MODIS or GOES10 data. Assimilation is performed over 18º S -30º S and 70º W-90º W and not throughout 34º S as in the MODIS assimilation because the GOES10 retrievals were only available up to 30º S. We chose 3 flights, RF11, RF12 and RF13 (Wood *et al.*, 2011), that measured the MBL during day time as the GOES10 retrieval has limited skill at night. RF11 (9 Nov. 2008) and RF12 (11 Nov. 2008) conducted coastal pollution surveys between 20º S-30º S and 72º W-75º W, while RF13 (13 Nov. 2008) sampled 20º S from 70º W to 80º W. We evaluate both forecasts (prior and posterior) against Particle Measuring Systems (PMS) Passive Cavity Aerosol Spectrometer Probe (PCASP) accumulation mode aerosol number concentration (Kazil *et al.*, 2011; Bretherton *et al.*, 2010) and Aerosol Mass Spectrometer (AMS) sub-

micrometer sulfate concentrations (Allen *et al.*, 2011). Sulfate mass was considered as a proxy for sub-micrometer aerosol mass as it dominated the hygroscopic fine aerosol mass in the MBL in this region throughout the study period (Yang *et al.*, 2011b). Statistics (Fig 4.4) are computed using flight legs within the MBL (below clouds).

Results

The assimilation procedure is demonstrated for the case of the Southeast Pacific's persistent stratocumulus deck, where in-situ aircraft observations during the VOCALS-REx field experiment (Wood *et al.*, 2011) provide independent accumulation mode aerosol mass and number concentrations (Allen *et al.*, 2011) for verification. We predict meteorology and aerosol mass (M) and number (N) distributions at the regional scale with the WRF-Chem model (Grell *et al.*, 2005; Skamarock *et al.*, 2008) configured for this area (Saide *et al.*, 2012b). Cloud optical depth and effective droplet radii retrieved from Terra MODerate-resolution Imaging Spectroradiometer (MODIS) and Geostationary Operational Environmental Satellite (GOES) imager data (Minnis *et al.*, 2008; King *et al.*, 2006) are used to compute observed N_d (Painemal and Zuidema, 2011). We perform experiments utilizing these retrievals. The impacts of assimilation of MODIS N_d on optimized modeled N_d, N and aerosol sulfate mass concentration are shown in Fig 4.1 for a day with an extensive and thick stratocumulus deck (Fig 4.1 upper right, Fig 4.2), which is a typical condition in the region (e.g. day time cloud fraction was between 70-90% during the VOCALS-REx period (Yang *et al.*, 2011b)). The background modeled N_d (prior) resolves the longitudinal gradient in the observations defined by the indirect effects due to anthropogenic pollution (Saide *et al.*, 2012b), but generally overestimates coastal amounts and underestimates remote concentrations. The assimilation produces an improved *a posteriori* modeled N_d, as shown by a 30%

fractional error reduction[(1)] and by the better resemblance of N_d assimilated fields compared to the observations (Fig. 4.1, 1st and 2nd row). Assimilation increases (decreases) N and M in places where N_d is under (over) predicted (Fig. 4.1, 3rd and 4th row), activating more (less) particles, thus reducing the error.

As the observation operator for this assimilation technique is a mixing-activation parameterization, the aerosols modified are those most active in the activation process; i.e., below cloud and accumulation mode aerosols. Coarse aerosols do participate in activation, but their sensitivities are low as their number concentrations are small. As vertical mixing is also considered, the aerosols modified are not only those in the layer immediately below clouds, but also from lower near-surface layers. The vertical extent of the impact depends on the mixing state of the atmosphere below clouds. For cloud-capped marine boundary layers (as in the stratocumulus deck studied here), depending on the decoupling state (Jones *et al.*, 2011) the aerosol constraint can extend to the sea surface. Thus, this technique can directly improve estimates of fine mode near-surface aerosol number, composition and size. For instance, sulfate dominates the hygroscopic fine aerosol mass in the marine boundary layer (MBL) in this region throughout this study period (Yang *et al.*, 2011b), and therefore receives the most constraint from assimilation (Fig. 4.1, fourth row). Species during this period found mainly in the coarser size bins like nitrate and sea salt (Yang *et al.*, 2011b) are not impacted as much, and those found in the free troposphere above the cloud layer, such as biomass burning organic aerosol (Allen *et al.*, 2011), are not affected by the assimilation.

The impact of assimilation on constraining aerosol distributions is evaluated in an experiment (see S1.5 for further details) where GOES-10 N_d was assimilated at the time when a research flight was conducted that did a longitudinal in-situ sampling of the cloud

[(1)] Fractional error of 72% and 42% are obtained between GOES-10 retrieval and prior and assimilated fields respectively at one hour after assimilation (16Z).

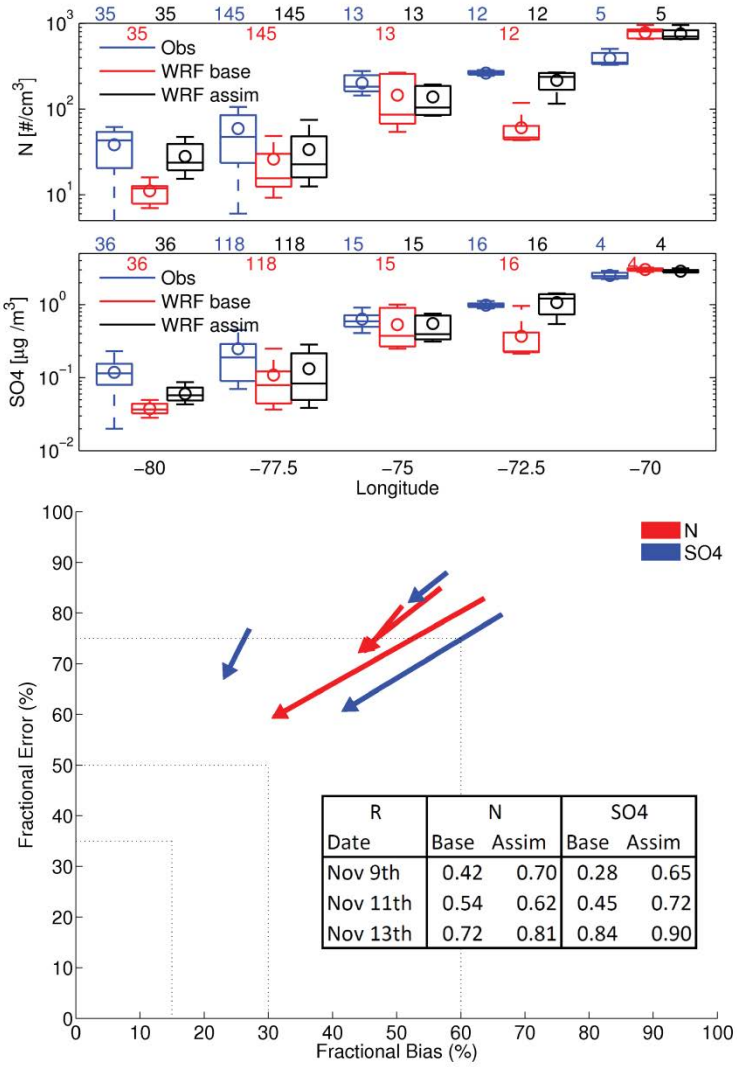

Figure 4.4. Statistical comparison between modeled and in-situ C-130 observations (Allen *et al.*, 2011) of accumulation mode aerosol number concentration and fine sulfate mass. Top panel: Longitudinal statistics as box and whisker plots for flight RF13 (13 Nov. 2008). Centre solid lines indicate the median, circles represent the mean, boxes indicate upper and lower quartiles, and whiskers show the upper and lower deciles. Number of 1-minute samples contributing to each longitudinal bin is indicated at the top. Bottom panel: "Soccer Goal" plot (Morris *et al.*, 2005) showing bias and error improvements for flights RF11 (9 Nov. 2008) , RF12 (11 Nov. 2008) and RF13. Each arrow represents N (red) and SO4 (blue) for each flight, where the arrow tail and tip represent the base and assimilated model statistics respectively. Arrows pointing towards (0,0) indicate that assimilation improves both bias and error. The embedded table shows correlation (R) between models and observations. Model and measurements are below cloud. See S1.5 for further details.

deck (Fig. 4.4, top panel). The model prior underestimates offshore aerosol mass and number, which the assimilation corrects, reducing fractional biases by 25% and 33%, respectively.

Similar assimilation experiments for two coastal pollution survey flights (Fig. 4.4, bottom panel) improved statistical performance for below cloud aerosol mass and number, reducing fractional bias and error (Morris *et al.*, 2005) and increasing spatiotemporal correlation in each case. The use of retrievals from geostationary satellites to constrain aerosols is an important advancement, as it provides a significant improvement in temporal resolution (~16 retrievals per day) compared to polar orbiting satellites that produce one retrieval per day.

An important feature of the cloud droplet number assimilation is that it results in a change in aerosols, which can impact cloud predictions forward in time over the lifetime of the aerosols throughout the region of analysis (~2 days in the MBL). To demonstrate this persistent effect of the constraint we assimilate a single retrieval of MODIS N_d and evaluate the forecast of N_d by comparing to independent hourly-resolved GOES10 N_d retrievals (Fig 4.5). One to five hours after assimilation (Fig. 4.5, 1st day) the magnitude and variability of forecast N_d over polluted and clean geographical regions are improved as seen by the enhancement in number and variability in the clean region and a decrease in mean and variability in the polluted zone, achieving a global 20-30% fractional error reduction. For the second day, model errors (Saide *et al.*, 2012b) and the transport of the aerosols out of the domain reduce the impact of the assimilated fields. However, the assimilation still has a positive impact on the forecasts that extends beyond 24 hours. . A snapshot 22 hours after assimilation (Fig. 4.5, bottom panel) shows features in the assimilation-predicted fields that resemble the observations and are not found in the prior: N_d enhancement over 100 #/cm^3 (near 20º S, 85º W) that can be traced to a plume present in the retrieval near 27º S, 79º W (Fig. 4.1); and an increase in cloud cover in the northwest of the domain that was missed in the background simulation.

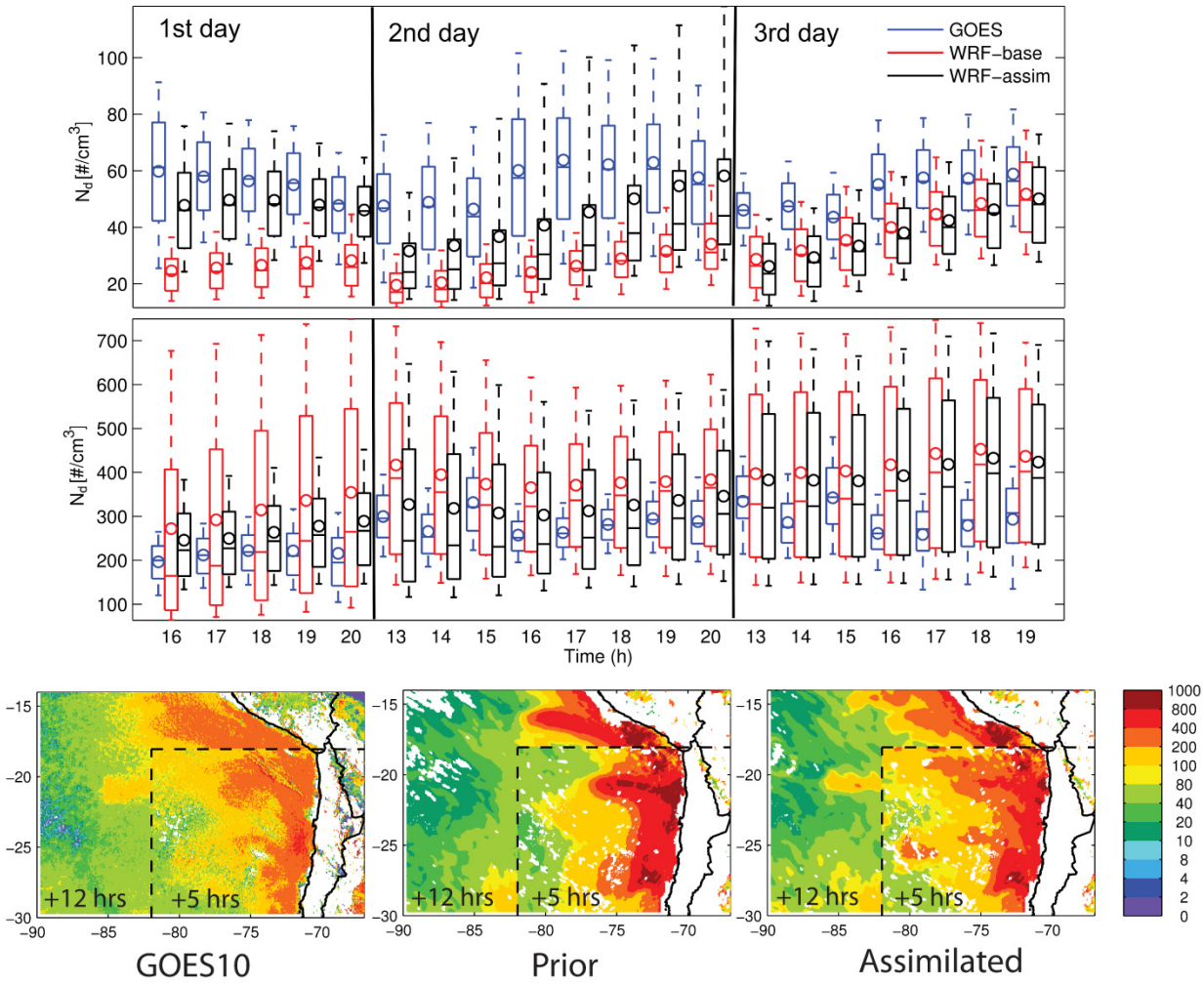

Figure 4.5. Box and whisker plots as in Fig. 4.2 for time series of GOES10 and modeled N_d statistics on 5ºx5º areas centered at 20º S,85º W (top) and 20º S,75ºW (bottom). In the assimilation, a single assimilation using MODIS N_d (Fig. 4.1, first row) is performed at 15 UTC on 16 Oct. (first day) and then the model is run as a forecast for 72 hours. Thick black vertical lines separate different consecutive days. Bottom panel: Composite maps for GOES10 observations, model prior and assimilated model N_d for 16 Oct. at 20Z (southeast box, 5 hours after assimilation) and 17 Oct. at 13Z (remainder of the map to the west and north, 22 hours after assimilation). See S1.5 for further details.

After 48 hours, the assimilated aerosol has exited the regional model domain, and only small differences between background and assimilated fields remain. This lasting influence on cloud and aerosol properties could help overcome one of the main issues in

contemporary cloud assimilation methods, where information gained in the analysis is attenuated within hours after initialization (Bauer *et al.*, 2011; Auligné *et al.*, 2011).

Discussion

The technique presented here is designed for use with single layer warm liquid cloud systems with vertically homogeneous N_d. These conditions represent low stratiform clouds, which persistently cover large regions around the world (e.g. stratocumulus decks off the west coasts of Africa, and South and North America) and are pointed out as the main players in aerosol indirect forcing (Kogan *et al.*, 1996). While this first approach to N_d assimilation does not resolve the vertical N_d gradients and ice and graupel phases that arise from convection, convective clouds are often accompanied by or form from low clouds where this technique can be applied. Beyond regions of persistent low stratocumulus, single-layer liquid cloud conditions can also be identified in model calculations and matched with instantaneous cloud retrievals on a pixel-by-pixel basis and assimilated opportunistically throughout the world, whenever and wherever they occur. The application of this technique to other regions requires further evaluation of the N_d satellite retrieval calculation. Even though global estimates of N_d can be made (Bennartz, 2007), region-specific expressions evaluated using in situ measurements can help reduce uncertainty in the retrievals (Painemal and Zuidema, 2011). In this sense, it is encouraging that for a given region, a single formula can be used across satellites and instruments (GOES imager, MODIS Aqua and Terra) with excellent performance against N_d in-situ data, remarkably better than for other retrieved cloud properties (Painemal and Zuidema, 2011; Painemal *et al.*, 2012). The activation parameterization and its assumptions represent another source of uncertainty (McFiggans *et al.*, 2006), but again, comparisons with in-situ and satellite measurements help better understand these limitations and their extent (Saide *et al.*, 2012b; Yang *et al.*, 2011b). Expanded applications of this approach (e.g., aerosol retrieval and assimilation under multi-layer,

convective, and ice clouds) may be possible, but additional research and testing is required on both retrieval and modeling sides.

Potential applications for this technique are found throughout the atmospheric sciences and beyond. When incorporating aerosol indirect feedbacks on clouds in numerical weather prediction, better aerosol predictions can further improve MBL height and cloud heights, liquid and precipitable water, precipitation rates, cloud optical properties and cloud lifetime (Saide *et al.*, 2012b). As aerosol influences on clouds have been shown to affect convective systems (Koren *et al.*, 2005), lighting (Yuan *et al.*, 2011a), tropical cyclones (Rosenfeld *et al.*, 2011a) and tornados (Rosenfeld and Bell, 2011), more accurate aerosol representation could also lead to better predictions for severe storms and hazards. In addition, better constrained fine and below-cloud aerosol distributions will help improve air quality predictions (Benedetti *et al.*, 2009) and reduce uncertainties in assessments of health and climate impacts due to aerosols (Carmichael *et al.*, 2009). The use of this technique is not limited to 3DVAR, and may be used for sensitivity analysis (Karydis *et al.*, 2012) as well as being coupled to an adjoint model for 4DVAR assimilation of aerosol state and evolution (Benedetti *et al.*, 2009) or used in inverse modeling to better estimate emission sources. In this sense, important applications include improving highly uncertain estimates of oceanic organic emissions (Heald *et al.*, 2010; Meskhidze *et al.*, 2011) and constraining anthropogenic emissions such as those occurring upwind of persistent cloud regimes (e.g. central Chile and northern California) (Saide *et al.*, 2012b) and those emitted below clouds (e.g. ship emissions). This technique is not limited to persistent stratocumulus decks, as similar aerosol feedbacks have been shown for other marine (Yuan *et al.*, 2011b) and continental (Berg *et al.*, 2011) shallow cumulus. Also, there is no limitation on aerosol composition distribution (sulfate dominates the case studied) as long as the aerosol properties participating in the activation process (e.g. hygroscopicity, solubility) are specified

correctly. These applications are currently feasible given the availability of near real-time cloud retrievals (Minnis *et al.*, 2008).

The technique can be combined with AOD assimilation to constrain aerosol distributions for mass, number, composition, and optical properties over a broader range of conditions, as AOD and N_d assimilation are complementary, employing observations that do not co-exist (e.g. there is no AOD retrieval when there are clouds and vice-versa). Using these retrievals together enables the observing system (satellites retrievals + model simulations) to "see aerosols" for a larger number of pixels in a scene, even under cloudy conditions.

Collaborators and funding sources

We would like to acknowledge insightful comments of Marc Bocquet, Elliott Campbell and 2 anonymous reviewers. This work was carried out with the aid of NSF grant 0748012, NCRR grant UL1RR024979, Fulbright-CONICYT scholarship number 15093810, the NASA MAP Program, and the DOE ASR Program. Its contents are solely the responsibility of the authors and do not necessarily represent the official views of the founding institutions.

Author contributions

This work is published in Saide *et al.* (2012a). P. Ssaide, G. Carmichael and S. Spak conceived the idea. P. Saide developed and applied the method with permanent contributions and guidance from G. Carmichael and S. Spak. P. Minnis (NASA LARC) and J.K. Ayers (SSAI) provided GOES10 satellite retrievals and contributed with insights on data usage. All authors contributed to the final form of the manuscript.

CHAPTER 5 AEROSOL OPTICAL DEPTH ASSIMILATION FOR A SIZE-RESOLVED SECTIONAL MODEL: IMPACTS OF OBSERVATIONALLY CONSTRAINED, MULTI-WAVELENGTH AND FINE MODE RETRIEVALS ON REGIONAL SCALE ANALYSES AND FORECASTS

Abstract

An aerosol optical depth (AOD) three-dimensional variational data assimilation technique is developed for the Gridpoint Statistical Interpolation (GSI) system when WRF-Chem forecasts are performed with a detailed sectional model (MOSAIC).Within GSI, forward AOD and adjoint sensitivities are performed using Mie computations from the WRF-Chem optical properties module providing consistency with the forecast. GSI tools such as recursive filters and weak constraints are used to provide correlation within aerosol size bins and upper and lower bounds for the optimization. The system is used to perform assimilation experiments with fine vertical structure and no data thinning or re-gridding on a 12 km horizontal grid over the region of California, USA, where improvements on analyses and forecasts is demonstrated. A first set of simulations is performed comparing the assimilation impacts of operational MODIS dark target retrievals to observationally constrained ones (i.e. calibrated with AERONET data), the latter ones showing higher error reductions and increased fraction of improved PM2.5 (92-96%) and AOD (100%) ground-based monitors. A second set of experiments reveals that the use of fine mode fraction AOD and ocean multi-wavelength retrievals can improve the representation of the aerosol size distribution, while assimilating only 550nm AOD retrievals produces no or at times degraded impact. While assimilation of multi-wavelength AOD shows positive impacts on all analyses performed, future work is needed to generate observationally constrained multiwavelength retrievals, which when

assimilated will generate size distributions more consistent with AERONET data and will provide better aerosol estimates.

Introduction

Atmospheric aerosols interact with society and the environment in several important ways such as producing acute health impacts, generating visibility issues and creating a substantial climate response (e.g. Ramanathan *et al.*, 2008). Thus, it is important to have accurate estimates of aerosol concentrations. However, predicting aerosols remains a challenge and models produce estimates with substantial errors and biases (Koch *et al.*, 2009; McKeen *et al.*, 2007). Current efforts to reduce the uncertainties in aerosol distributions include assimilating aerosol-related observations (e.g. Pagowski *et al.*, 2010), where one of the most commonly used observations is aerosol optical depth (AOD) from satellite retrievals. AOD has been used along with models to constrain aerosol concentrations in multiple ways: to generate AOD to surface PM2.5 conversion factors (van Donkelaar *et al.*, 2006; Liu *et al.*, 2005b); to improve model daily and monthly estimates of ground level PM2.5 (Carmichael *et al.*, 2009; Adhikary *et al.*, 2008); to correct model initial conditions to produce improved reanalysis and forecasts (Liu *et al.*, 2011; Benedetti *et al.*, 2009); and to produce better emissions estimates (Huneeus *et al.*, 2012; Heald *et al.*, 2010; Wang *et al.*, 2012; Xu *et al.*, 2013).

Among the satellites and sensors that produce AOD estimates, one of the most commonly used is the operational dark target retrieval from the Moderate Resolution Imaging Spectroradiometer (MODIS) sensor on board the Terra and Aqua platforms (Remer *et al.*, 2005), as it tends to generate accurate observations over a wide range of surfaces (Petrenko and Ichoku, 2013). However, this retrieval often shows deviations from ground measurements, and centers such as the Naval Research Laboratory (NRL) (Zhang *et al.*, 2008) and National Aeronautics and Space Administration (NASA) (GMAO, 2013) use observationally constrained retrievals (where AOD is empirically

fitted to ground sun-photometer data) in their assimilation systems. To our knowledge, the impact of assimilating operational MODIS products versus the observationally constrained ones has not been previously assessed.

MODIS AOD, as other satellite/sensor products, is reported in several wavelengths (three and seven for land and ocean retrievals, respectively) and the wavelength dependency of AOD (Angstrom Exponent) contains aerosol size information (Schuster *et al.*, 2006). However, most studies assimilate a single retrieval (usually 550nm) and there are few studies analyzing the impact of simultaneously assimilating multiple wavelengths. For instance, Schutgens *et al.* (2010) assimilated AOD and Angstrom Exponent (obtained combining multiple wavelengths) ground measurements from the Aerosol RObotic NETwork (AERONET) network to constrain a global aerosol model. AOD retrieval algorithms can also produce a fine mode fraction product. A few studies have explored the use of the fine mode fraction and total AOD simultaneously. For example, Generoso *et al.* (2007) used fine and coarse mode AOD on global data assimilation experiments using POLDER satellite measurements, as well as Huneeus *et al.* (2012), that used fine and total MODIS AOD in the context of a global emissions inversion with positive impacts including improved aerosol size distributions. There is a need to further assess the impacts of simultaneous use of these data sets in a data assimilation framework.

In this study we develop the ability of the Gridpoint Statistical Interpolation (GSI) Three dimensional variational (3DVAR) system to simultaneously assimilate various AOD products to correct Weather Research and Forecasting/Chemistry (WRF-Chem) forecasts when using the Model for Simulating Aerosol Interactions and Chemistry (MOSAIC) treatment (Zaveri *et al.*, 2008). This aerosol model is widely used in several applications, but its use in an assimilation framework is challenging due to the large number of species and size bins that need to be treated simultaneously (Li *et al.*, 2012). However, assimilation performed for aerosol treatments that have higher degrees of

freedom (i.e., multiples species and multiples size bins) may be useful when assimilating many data sources at the same time, as both the total mass and aerosol size distribution could be modified to produce a better fit to observations. The Methods section describes the method and additions introduced to GSI to effectively perform assimilation with the MOSAIC model. Then, the system is used in two experiments shown in the Results and discussion section. First, we assess the impact of assimilating operational MODIS retrievals (dark target land and ocean) versus observationally constrained products, and second, we evaluate the impact on forecasts when simultaneously assimilating multiple wavelengths and fine and total AOD compared to just assimilating total 550nm AOD. Finally, shortcomings, conclusions and future directions are presented.

Methods

Forecast model

The aerosol forecasts were performed with the Weather Research and Forecasting (WRF) version 3.4.1 regional meteorological model (Skamarock *et al.*, 2008) coupled to aerosol and chemistry (WRF-Chem) (Grell *et al.*, 2005). This is a fully coupled online model. The chemical and aerosol mechanism used is the CBMZ gas-phase chemical mechanism (Zaveri and Peters, 1999; Fast *et al.*, 2006) coupled to the 8-bin sectional MOSAIC (Zaveri *et al.*, 2008) aerosol model. MOSAIC keeps track of 8 chemical species (sulfate, nitrate, ammonium, organic carbon, black carbon, sodium, chloride and other inorganics, where dust is included) on two phases (dry/interstitial and wet/activated), that along with number concentration (on both phases), water and hysteresis water content per size bin results on a total of 160 species tracked. The model configuration is based on Chapter 3. Some of the configuration choices include a 12 km horizontal grid spacing with 72 vertical levels with ~60 m level thickness below 3km, MYNN level 2.5 planetary boundary layer (PBL) scheme (Nakanishi and Niino, 2004),

Lin microphysics (Chapman *et al.*, 2009), Goddard short wave radiation (Chou *et al.*, 1998; Fast *et al.*, 2006), and Abdul-Razzak and Ghan (2002) aerosol activation.

Emissions from different sources are treated as follows: NEI 2005 anthropogenic emissions (http://www.epa.gov/ttnchie1/net/2005inventory.html), MEGAN biogenics (Guenther *et al.*, 2006), FINN biomass burning emissions (Wiedinmyer *et al.*, 2011) coupled to an online plume-rise model (Grell *et al.*, 2011), Gong *et al.* (1997) sea salt parameterization and GOCART dust scheme (Zhao *et al.*, 2010). Meteorological and chemical boundary conditions are obtained from National Centers for Environmental Prediction (NCEP) Final Analysis (http://rda.ucar.edu/datasets/ds083.2/) and MOZART forecasts (Emmons *et al.*, 2010), respectively. MOZART uses monthly dust distributions from Community Atmosphere Model (CAM) (Mahowald *et al.*, 2006) calculations, which are also used in this study. Even though WRF-Chem has the option to include secondary organic aerosol (SOA) formation coupled to MOSAIC aerosols (Shrivastava *et al.*, 2011; Hodzic and Jimenez, 2011), this process is not included in this analysis, as the focus of this paper is the development and testing of the new assimilation system.

Assimilation system

We use the Gridpoint Statistical Interpolation (GSI) assimilation system (Wu *et al.*, 2002; Kleist *et al.*, 2009a). Even though more sophisticated assimilation schemes such as 4DVAR (Benedetti *et al.*, 2009) and Ensemble Kalman filter (Pagowski and Grell, 2012) can be used for assimilation, we chose 3DVAR as a computationally inexpensive but powerful way to demon strate AOD assimilation for the MOSAIC aerosol scheme, without having to perform an ensemble of simulations or develop the WRF-Chem adjoint. The GSI version used is based on the modifications made by Liu *et al.* (2011) and Schwartz *et al.* (2012) to assimilate AOD. However, we incorporated substantial additional modifications suited to the MOSAIC aerosol model as described in the following sub-sections.

3DVAR method

In this study we build upon work of Liu *et al.* (2011) and Schwartz *et al.* (2012). As they presented, we use the 3DVAR functional (J), but add terms to allow weak constraints:

$$J(x) = \frac{1}{2}\left(H(x) - y\right)^t R^{-1}\left(H(x) - y\right) + \frac{1}{2}\left(x - x_b\right)^t B^{-1}\left(x - x_b\right)\ldots$$

$$+ \frac{k_{uc}}{2}\left(\max\left[x - x_{uc},0\right]\right)^t K^{-1}\left(\max\left[x - x_{uc},0\right]\right) + \frac{k_{lc}}{2}\left(\max\left[x_{lc} - x,0\right]\right)^t K^{-1}\left(\max\left[x_{lc} - x,0\right]\right) \quad (1)$$

Where y represents the observation, x the control variable (e.g. the one modified during optimization), with x_b the a priori estimate and x_{uc} and x_{lc} the upper and lower constraints, H the observation operator, R, B and K the observation, background and weak constraint error covariance matrixes, and k_{uc} and k_{lc} regularization parameters to weight the weak constraint.

Liu *et al.* (2011) and Schwartz *et al.* (2012) considered as control variables three dimensional (3D) aerosol concentrations from different species and AOD as observations. In this work, we introduce new GSI options. First, we incorporate the option of using as control variables the natural logarithm (LN) of 3D aerosol concentrations. This choice naturally constrains concentrations to be positive and provides multiplicative rather than additive corrections (Henze *et al.*, 2009). In the same manner, we add the option to use the AOD natural logarithm as the observation. As both aerosol concentration and AOD are positive, it is likely that their errors are of multiplicative nature, and the use of a transformation becomes more natural as Eq. (1) implicitly assumes that the errors are normally distributed (Bocquet *et al.*, 2010). When using these logarithmic choices, the sensitivities from the observation operator have to be computed accordingly, which is achieved by using the non-log sensitivities and the chain rule of derivatives:

$$\frac{\delta \mathrm{LN}(\mathrm{AOD})}{\delta \mathrm{LN}(c)} = \frac{c}{\mathrm{AOD}} \frac{\delta AOD}{\delta c} \quad (2)$$

where *c* represents the aerosol concentrations being analyzed. By using this conversion we are able to use the same code to compute sensitivities for any choice of control variable. To avoid zero values, we set a threshold of 1e-20 for AOD and aerosol concentrations when converting to and from the LN variables.

An additional modification with respect to the control variable used in previous research is that, instead of using aerosol concentrations output by WRF-Chem (μg/kg), we multiply them by the grid-cell vertical thickness (in meters), which provides a measure of the column concentration and is proportional to aerosol mass rather than aerosol concentration. The consequences of not applying this correction are depicted by the following example. For two given grid-cells in the same column and containing the same aerosol concentrations and uncertainty, the grid with the deeper thickness will contain higher sensitivities, as the same change in concentration will generate a higher increase in AOD due to the deeper layer. This will end up in the assimilation preferentially modifying concentrations in those deeper gridcells, biasing the model. By multiplying by the thickness, we avoid the assimilation favoring changes in deeper grid-cells, which could be important in configurations with great vertical variability as the one used in this study.

Finally, instead of using as control variables all aerosol species (Liu *et al.*, 2011; Schwartz *et al.*, 2012) on all size bins, we introduce the option of using total mass per size bin as control variables, and distribute the changes within GSI considering the percentage of mass contribution of each species as a constant for each size bin. This consideration allows a reduction in the number of control variables by a factor equal to the number of species, which is eight in our case. When using this choice the system is faster, has fewer degrees of freedom and is less likely to accumulate changes on single species. Similar assumptions have been made in other AOD assimilation systems (e.g. Benedetti *et al.*, 2009) with the difference that here we can still produce changes in the total aerosol composition, as different species often dominate different size bins (Saide *et*

al., 2012a). We use the total mass per size bin as control variable for all experiments presented in this study.

The weak constraint term added in Eq. (1) constrains the control variable so the optimal solution would be within user specified bounds or close to them. The implementation is based on the relative humidity weak constrain done in GSI meteorological assimilation. K is diagonal and chosen as a scale (in the variance space) of the control variable. For simplicity we chose it equal to the diagonal of B and use the parameters k_{uc} and k_{lc} for weighting the constraint, with higher values giving a higher weight to the terms in Eq. (1), thus allowing a smaller departure of x from the target bound once it has been exceeded. x_{uc} and x_{lc} represent the desired bounds for the control variable and are calculated as multiplicative factors applied to the prior (additive in the case of LN control variable). In the experiments, x_{uc} and x_{lc} were chosen equal to 5×xb and 0.01×xb , meaning that the upper and lower bound terms are activated during minimization when x is over 5 times or below 1/100 times the background, respectively. The weights of the constraint term k_{uc} and k_{lc} were equal to 0.5 and 0.05, which were chosen experimentally by trying different values and keeping a range that both restricts x to the bounds and at the same time keeping the constraint term from becoming the largest term in the functional J. Higher weight and more constrained multiplicative bound are given for the upper constraint as we found that overly increasing concentrations (i.e. incorrectly high AOD retrieval) can excessively damage the forecasts.

Background error covariance matrix

GSI is able to approximate the convolution of a background error covariance matrix (B) by using standard deviations and vertical and horizontal correlation length scales as inputs for the use of recursive filters (Wu *et al.*, 2002; Purser *et al.*, 2003). Besides vertical and horizontal correlations, chemical and aerosol data assimilation often incorporates the use of cross-species correlation, as many of these are co-emitted or have

similar precursors (Elbern *et al.*, 2007). Since we use total mass of all species per size bin as control variable, inter-species correlation is not applicable. There is also a natural correlation for different size bins for each species that needs to be considered (e.g. Saide *et al.*, 2012a). By using recursive filters we incorporate the capacity to add correlations between aerosol size bins in GSI. Filter passes run along size bins in incremental order and are applied locally for each aerosol size distribution, in a similar way as vertical scales are applied (Wu *et al.*, 2002). For simplicity, the inter size bin correlation lengths are specified in the namelist by the user and not computed through the method described in the next paragraph. However, we do not discard this possibility for future studies. The size bin correlation length scale was chosen equal to 2 bin units, which prevents excessive accumulation of innovations on a single size bin and distributes the changes along them. The isotropic nature of one-dimensional recursive filters restricts the ability to apply different correlations scales to bins that have smaller and larger sizes than the reference one. Such anisotropic correlation would be preferred for bins located at the edges of fine and coarse distributions. We hypothesize this limitation could be partially overcome when computing the correlation with methods such as the one described next.

As in Liu *et al.* (2011) and Schwartz *et al.* (2012), we use the NMC method (Parrish and Derber, 1992) for computing the standard deviations and vertical and horizontal length scales. Depending on the choice of control variable (see 3DVAR method subsection), the same variable has to be the input to the NMC computation. For the case of LN control variables, we constrain the standard deviation to be less than or equal to one LN unit to avoid a very unconstrained system. The NMC method generally uses two forecasts (12 and 24 h or 24 and 48 h) to compute statistics. We use a long meteorological spin-up time (Saide *et al.*, 2012b), so following this strategy would consume too much computational resources. Instead, we assess uncertainties by running two continuous parallel simulations driven by different meteorology. In the case of retrospective North American experiments, this can be done using NCEP final analysis

and North American Regional Reanalysis (NARR). This method used for May 2010 yields isotropic horizontal length scales between 15 and 36 km, with smaller and higher values in the lower and upper troposphere, respectively. These are considered small values compared to global data assimilation systems, but are in the range of 1 to 3 times the horizontal grid resolution, which falls between typical ranges (Liu *et al.*, 2011). Vertical length scales vary between 1 and 6 model grid vertical level units. In general they are large near the surface due to boundary layer mixing, then decrease rapidly reaching small values around the capping inversion height, and then remain high up to ~3km where the model vertical grid gets coarser (see Forecast Model sub-section) and thus the length scales decrease down to small values.

Forward and adjoint of the Observation operator

While Liu *et al.* (2011) and Schwartz *et al.* (2012) used the Radiative Transfer Model (CRTM) (Han *et al.*, 2006) as the forward and adjoint observation operator, here we use WRF-Chem optical properties (OP) routines (Fast *et al.*, 2006). This choice provides consistency between the AOD computed for assimilation and forecast models. The WRF-Chem OP code considers an internal mixture within each aerosol size bin and uses Mie theory along with Chebyshev expansion coefficients for reducing computational time (Fast *et al.*, 2006). This code has shown skill in predicting optical properties against total column data for several regions and aerosol regimes (Yang *et al.*, 2011b; Zhang *et al.*, 2010; Chapman *et al.*, 2009; Qian *et al.*, 2010; Zhao *et al.*, 2010; Zhao *et al.*, 2012; Kalenderski *et al.*, 2013) and against in-situ data (Barnard *et al.*, 2010; Shrivastava *et al.*, 2013). The tangent linear (TL) and adjoint of this code were obtained using the automatic differentiation tool TAPENADE v 3.6 (Hascoët and Pascual, 2004). Two tests were performed to validate the code generated. First, the TL code was tested using the TL test, which consists of comparing the derivatives obtained from the code against finite differences using the forward code, obtaining better agreement as the perturbation used

was reduced, which is considered a successful test. Second, the adjoint code was tested using the adjoint test, which consists in generating derivatives with the TL code and then using them as an input for the adjoint code. In this case, a successful test is obtained when, for different perturbations, the dot product of the derivatives generated with the TL is equal to machine precision to the dot product of the adjoint derivatives and the original perturbation (Zou *et al.*, 1997), which was also accomplished.

We update aerosol water and number within the WRF-Chem OP code added to GSI, so they will be dependent on aerosol concentrations. The water uptake code is extracted from MOSAIC, which uses the activity coefficients of the electrolytes present and the Zdanovskii-Stokes-Robinson method (Zdanovskii, 1948; Stokes and Robinson, 1966). A threshold of 99% relative humidity was set for water uptake calculations and columns with clouds present are excluded from assimilation. Aerosol number is computed using aerosol concentration and diameter in each bin, assuming that the assimilation does not update diameter using the one in the prior.

Another addition to the WRF-Chem OP code added to GSI was the column AOD computation for specific MODIS wavelengths. WRF-Chem computes OP for four wavelengths: 300, 400, 600 and 999 nm. Similarly to WRF-Chem radiative transfer calculations (Fast *et al.*, 2006), interpolation/extrapolation to MODIS wavelengths is done using the Angstrom exponent from the two closest wavelengths. No modifications are needed when computing fine mode AOD, as the coarse bin mass and number are zeroed out before AOD and sensitivity computations. As the aerosol models in the MODIS algorithm use a modal approach (Remer *et al.*, 2005) while MOSAIC uses a sectional approach, it is hard to create a complete match between the two when computing the fine fraction. For simplicity, we consider fine mode as aerosols with a dry diameter equal or less than 625 nm (first 4 size bins from the 8 bins of MOSAIC), which is in agreement with the cut-off diameter of 600nm used in the standard AERONET retrieval (Dubovik and King, 2000; Dubovik *et al.*, 2000).

Observations and their errors

The observational data sets that were assimilated in the different experiments are described in the following. There was no thinning of the data to maximize data usage.

Operational MODIS level 2 retrieval

Collection 5.1 MODIS aerosol data from Aqua and Terra satellites were obtained from NASA Goddard Space Flight Center. The dark target retrieval, which is the one used, is based on Remer *et al.* (2005) and Levy *et al.* (2007). Over land, AOD (the "Corrected_Optical_Depth_Land" product) is provided in three wavelengths: 470, 550 and 660 nm. However, for AOD at 550nm lower than 0.2, the angstrom exponent used to compute the other two wavelengths is fixed (Levy *et al.*, 2007) not providing an independent measurement of size distribution. Most AOD values over land were lower than 0.2 for the period of study, thus only the 550nm retrieval was used in the assimilation. Over ocean AOD (the "Effective_Optical_Depth_Average_Ocean" product) is provided in seven wavelengths (470, 550, 660, 870, 1240, 1630 and 2130 nm) but only the ones in the range 550-1240 nm are used in the assimilation to keep the wavelengths used close to the range computed by WRF-Chem. The 470nm wavelength is not used as there is no validation presented for this wavelength over ocean (Remer *et al.*, 2005). The MODIS aerosol dataset also provides fine mode fraction, defined as fraction that the fine mode (effective radius less than 0.5 μm) (Kaufman *et al.*, 1997) contributes to the total optical thickness, which can be used to compute fine mode AOD.

When operational MODIS data are assimilated, the data are quality controlled to avoid degrading the assimilation. These controls include accepting the highest quality flag (qf=3) over land and any flag (qf=1, 2 or 3) over ocean and processing only pixels with zero cloud fraction.

NASA Neural Network Retrieval

The NASA Neural Network Retrieval (NNR) is an observationally constrained retrieval designed to generate a better fit with respect to AERONET observations, and is used operationally in the GEOS-5 (Rienecker *et al.*, 2008) aerosol assimilation system (GMAO, 2013). It uses a neural network as an alternative to linear regression to capture possible non-linear relationships. Predictors used for the ocean retrieval include level 2 multi-channel top of the atmosphere (TOA) reflectances, glint, solar and sensor angles, cloud fraction (only when it is lower than 85%, otherwise pixel is discarded) and GEOS-5 surface wind speeds. Predictors used for the Land retrievals are TOA reflectances, solar and sensor angles, cloud fraction (<85%) and climatological albedo (only if lower than 0.25). An important difference with other post-processing techniques is that it does not use any MODIS AOD retrieval as a predictor. The target used in the neural network (and in the GEOS5 assimilation system) is not directly AERONET AOD, but log(AOD+0.01), which tends to better represent a Gaussian probability distribution. The AOD at 550nm is available at the same 10km resolution of the MODIS level 2 operational retrievals (GMAO, 2013).

Naval Research Laboratory (NRL) - University of North Dakota (UND) retrieval

The NRL-UND retrieval is a value-added AOD dataset based on MODIS Level 2 aerosol products specifically designed for quantitative applications including data assimilation and model validation. The quality assurance procedures and empirical correction algorithms (to better fit AERONET data) applied to this product are described in Zhang and Reid (2006), Zhang *et al.* (2008), Shi *et al.* (2011) and Hyer *et al.* (2011). This 550nm AOD retrieval is derived from MODIS collection 5. A product gridded to 0.5 degree is produced by NASA's Land, Atmosphere Near-real-time Capability for EOS (LANCE) with product code MCDAODHD. Due to the high resolution used in this

study, the source code of this algorithm was modified to output results on a 0.05 degree grid, with a minimum of one retrieval per grid and without checking for neighbors on the output grid (no "grid buddy checking"). This method always produces a maximum of one retrieval per gridcell (as MODIS minimum grid size is ~10km) with no aggregation, being comparable in terms of possible pixels generated to the other two retrievals used (MODIS and NASA NNR). In addition, only pixels with cloud fractions equal to zero and with the highest context quality checking were processed.

Observation error

Observational errors were assumed to be the same for all data sets, even though uncertainty is usually provided for the different data sets (e.g. Shi *et al.*, 2011). This assumption was made to provide the same basis for comparing results. AOD errors over land and ocean were assumed to be equal to 0.6 and 0.2 in LN units (~60% and ~20% error, respectively). Our approach does not follow the error estimates proposed by Remer *et al.* (2005) and used by Liu *et al.* (2011) and Schwartz *et al.* (2012) (error = a + b*AOD, with a and b constants function of the type of retrieval) as in this treatment relative errors (computed as a percent of the AOD magnitude) increase as AOD is lower. In the case of operational MODIS data assimilation and when computing errors with this approach, spurious high AOD can significantly damage assimilation results as the high AOD will dominate due to the high relative error of the surrounding small AOD. In the case of applying the same relative error (our approach), the surrounding small AOD control the spike of mass incorporated in the model. These MODIS AOD artifacts are effectively erased by the post-processing techniques (NASA NNR and NRL-UND). We also found that the fixed log-space uncertainty estimates resulted in better analysis results. These improvements suggests that the uncertainty estimates used in previous research may be too high for low AOD values, or may not correctly account for reduction of random error by spatial averaging in the data assimilation system.

Study domain and experimental design

The study region is California and its surroundings, which is an area with important air pollution problems, affected by both local and distant sources (Huang *et al.*, 2010). This region has been the target of several recent measurement campaigns such as ARCTAS-CARB (Jacob *et al.*, 2010) and CALNEX/CARES (Zaveri *et al.*, 2012). The coast of California is also important since in this area a persistent stratocumulus deck is found, which means that 1) aerosol retrieval from satellite is more challenging compared with more cloud-free areas, and 2) aerosol-cloud interaction is likely to be important (Hegg *et al.*, 2012; Twohy *et al.*, 2005). The region also represents a challenge in terms of accurate meteorological and air quality predictions (Yver *et al.*, 2013; Fast *et al.*, 2012). The existence of the stratocumulus deck plus the pollution issues makes this area a good place to demonstrate the application of AOD assimilation approaches and asses its limitations.

The modeling domain is centered on the central California coast, with a domain spanning from 30 N to 47 N and from 133 W to 112 W. A large portion of the domain covers the ocean to allow a higher influence of data assimilated here and to better resolve the stratocumulus deck (Saide *et al.*, 2012b). As previously mentioned, 12 km horizontal grid spacing is used.

Results are presented for May, 2010. Simulation without data assimilation (from now on referred as "non-assimilated") start on April 26th to allow for model spin-up and run continuously until the end of May. On the assimilation experiments, analysis steps are performed every three hours with a three hour observation window, then forecasts are restarted from meteorology of the previous forecast and run for three hours. Additional simulations were performed for the first 10 days of May to assess the impact of assimilation on forecasts by performing 48 hour unconstrained simulations after each daily 21 UTC analysis. The 550nm operational MODIS AOD retrieval assimilation is considered as the "control" for all experiments, and impacts of other or additional data is

assessed. First, we evaluate the impact of assimilating observationally constrained retrievals (i.e. NASA NNR and NRL-UND) and, second, we assess the inclusion of fine mode AOD and multiple-wavelengths to the assimilation. We evaluate impacts for PM2.5, AOD and Angstrom Exponent (AE). Fractional error and fractional bias (Morris *et al.*, 2005) are computed to asses model performance against non-assimilated observations (see next paragraph). Fractional error reductions (FER) are computed subtracting fractional errors of the experiments and control assimilations. For the second set of experiments, as we assimilate multi-wavelength AOD only over ocean and fine fraction is very infrequent over land for this area and period, we focus our performance analysis on satellite data over ocean and coastal stations.

Observations from different ground monitoring networks were used as independent data to evaluate the data assimilation impacts (Fig. 5.1). Hourly PM2.5 data was obtained from U.S. Environmental Protection Agency (EPA) Air Quality System (AQS, http://www.epa.gov/ttn/airs/airsaqs/), which provides a high density of measurements over California with most sites located in urban or sub-urban areas (Pagowski and Grell, 2012). We also used data from the Interagency Monitoring of Protected Visual Environments (IMPROVE, http://vista.cira.colostate.edu/improve/, Malm *et al.* (1994)) network, which collects measurements mainly on remote regions (parks and wilderness areas), which are representative of one day and collected every 3 days. Besides total PM2.5, it also collects aerosol chemical composition measurements, from which we use sulfate, nitrate, chloride, sodium, organic carbon and black carbon. Additionally, total column AOD and Angstrom Exponent (AE) measurements were obtained from AERONET network data (Holben *et al.*, 2001). For the period of study, 10 AERONET stations had data available within the study domain (Fig. 5.1). Finally, AOD retrievals not yet assimilated are considered as independent data and compared against model forecasts. Even though we perform assimilation every 3 hours, most of the data is available in the 18 and 21 UTC cycles (due to the satellite overpass time and domain of

study), with Terra and Aqua data accumulated mainly in the 18 and 21 UTC cycles respectively. Thus, by comparing model forecasts and Aqua data one can analyze the performance of assimilation against independent satellite data for a 3 hour forecast, or a 21-hour forecast by comparing to Terra data.

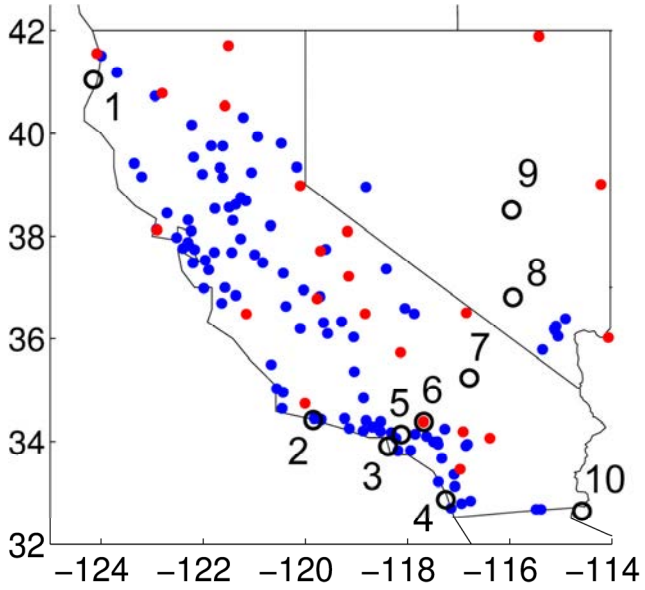

Figure 5.1. Map of ground stations used for evaluation in the study. AQS, IMPROVE and AERONET site locations are shown in blue dots, red dots and black rings, respectively. Numbers correspond to AERONET sites: 1) Trinidad Head, 2) UCSB, 3) El Segundo, 4) La Jolla, 5) Caltech, 6) Table Mountain CA, 7) Goldstone, 8) Frenchman Flat, 9) Railroad Valley, and 10) Yuma.

The validation using the three types of observations (aerosol concentration, ground AOD and satellite AOD) represent different levels of independence. The comparison against aerosol concentration observations is the true independent validation as these are not assimilated nor used for obtaining the retrievals assimilated. Comparing against AERONET AOD represents an intermediate level of independence, as even though these observations are not assimilated and have a lower level of uncertainty, they are used to tune the algorithms which compute the assimilated retrievals. Finally,

validating against satellite retrievals represents the lowest level of independence, as, even when observations from a different satellite not assimilated are compared to the forecasts, they are computed with the same algorithms as the one assimilated so they retain the same systematic biases, which are propagated into the analysis and forecast. These levels of independence must be considered when analyzing the assimilation tests performance.

Model to observation mapping is described as follows. WRF-Chem output is saved hourly and mapped to ground stations using nearest neighbor interpolation. The hourly PM2.5 WRF-Chem concentrations are used directly to compare against AQS observations. For IMPROVE stations, local time daily averages are computed. AERONET observations are averaged to hourly values which are then compared to hourly WRF-Chem output using the Angstrom Exponent for interpolation to AERONET wavelengths. Finally, both satellite retrievals and model fields are re-gridded to a fixed regular 0.2 x 0.2 degree grid where averages and performance statistics are computed.

Results and discussion

Non-assimilated model and retrievals evaluation

Figures 5.2 and 5.3 show non-assimilated model performance with respect to PM2.5 ground observations from the AQS network. In general, the model overestimates PM2.5 concentrations at most sites, with a global mean of 8.5 $\mu g/m^3$ and 14.1 $\mu g/m^3$ for observation and model, respectively. As seen in Fig. 5.2c and 5.2d, model biases tend to be more negative over northern California with biases close to zero and smaller errors in the Los Angeles area. Despite the biases, the model is able to reproduce the patterns of highest concentrations in the urban centers (Fig. 5.2) and captures the synoptic features which generate the high and low particle concentrations in the region (Fig. 5.3).

Figure 5.4 shows the non-assimilated model evaluation using the IMPROVE speciated observations. The model also overestimates PM2.5 at these sites. These high model values come from the “Other” aerosol (Fig. 5.4), which corresponds mainly (96%)

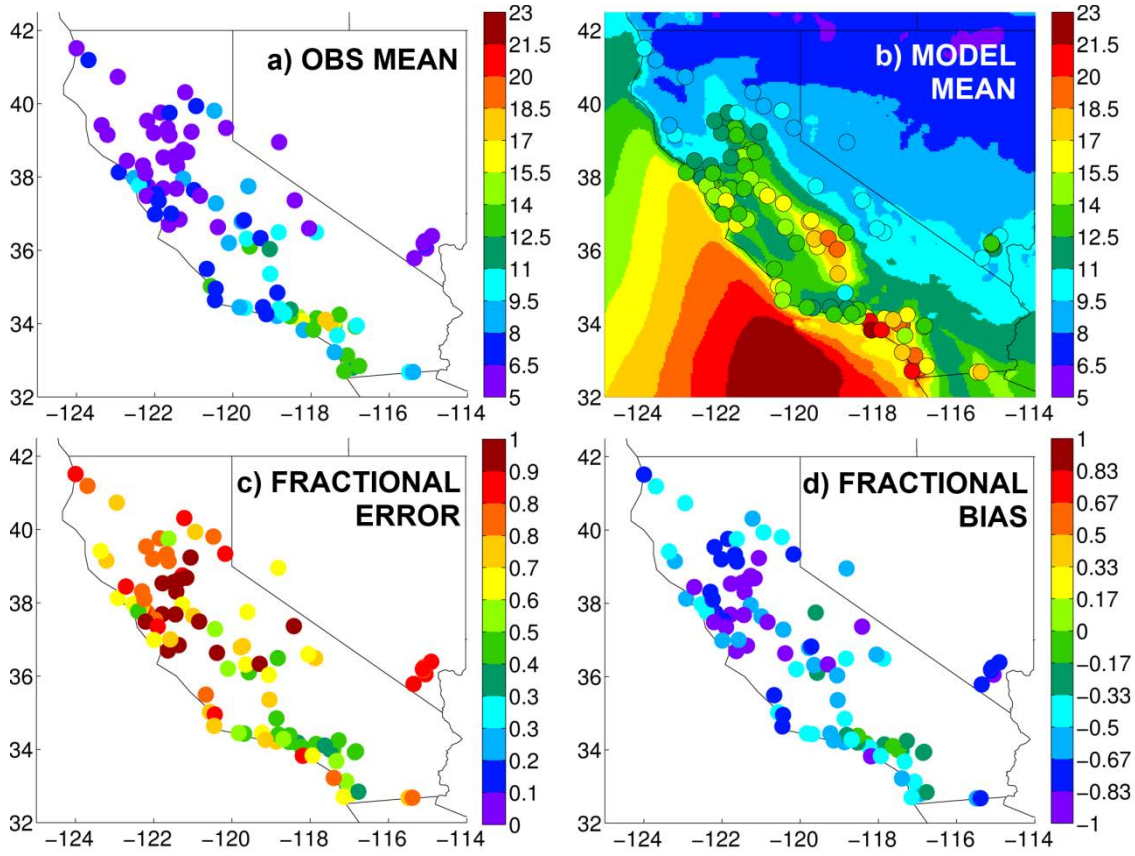

Figure 5.2. Non-assimilated model evaluation against PM2.5 monitors from AQS network over California and Nevada for May 2010. Panels show Observation mean (a), model map and model masked to observations means (b), fractional error (c) and fractional bias (d).

to the "other inorganics" (oin) specie in MOSAIC. This overestimation can be traced back to dust aerosol in the chemical boundary conditions coming predominantly from the western and northwestern boundaries. The model also shows overestimation of aerosol nitrate, sea-salt and black carbon. Sea-salt aerosol overestimation is consistent with previous work (Saide *et al.*, 2012b), which is produced by too high sea-salt emissions. The nitrate overestimation may be due to emissions, as the NO_x NEI2005 emissions have been found to be overestimated (Kim *et al.*, 2009) and they do not reflect the decreasing trend in NO_x emissions up to year 2010 (EPA, 2013a). Opposite to the general trend, organic carbon is highly underestimated by the model, which is expected as no SOA

scheme was included in the simulations. This difference is more evident as the IMPROVE network consists mostly of remote stations, leaving longer time for SOA production. Sulfate is slightly underestimated, which reflects that SO_2 emissions may be low in NEI2005. This could be the result of the NEI emissions not including shipping emissions, which is an important source in the region (Huang *et al.*, 2011).

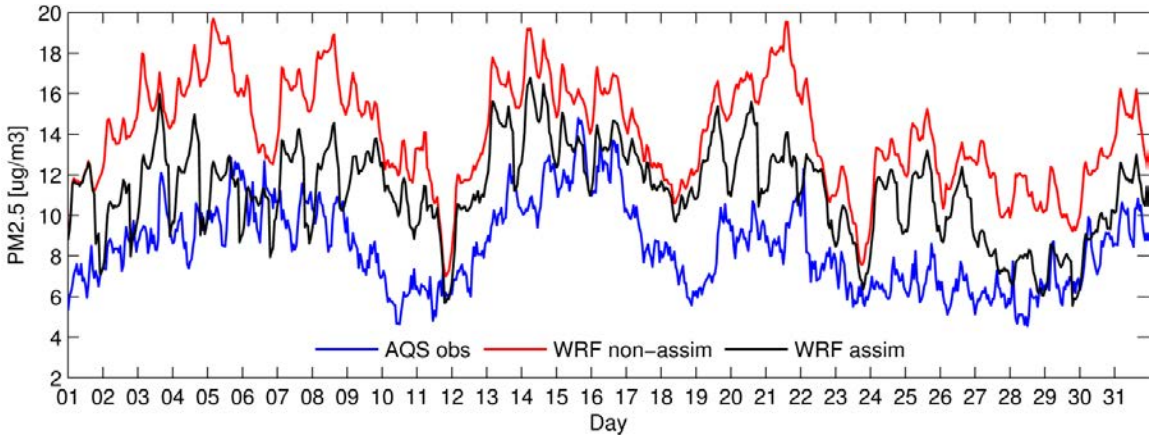

Figure 5.3. Model and observed PM2.5 time series for May 2010 over AQS sties on California and Nevada. Model simulations are the non-assimilated and assimilated using the NASA-NNR product.

As issues with local emissions are found, an emission inversion along with data assimilation could be performed as suggested by other studies (Jiang *et al.*, 2013). However, as the major problem in this study arises from the dust boundary conditions, adjusting just emissions would end up reducing them when they do not necessarily need to be reduced (e.g., case of SO_4). Thus, future studies performing data assimilation and emissions inversions, would also need to assimilate chemical boundary conditions.

Monthly mean values for the different 550nm AOD retrievals are shown in Figure 5.5 (top). Significant differences can be seen between the different retrievals. The NASA NNR and NRL-UND retrievals tend to make corrections of the same sign with respect to the operational MODIS, for example they increase AOD over coastal

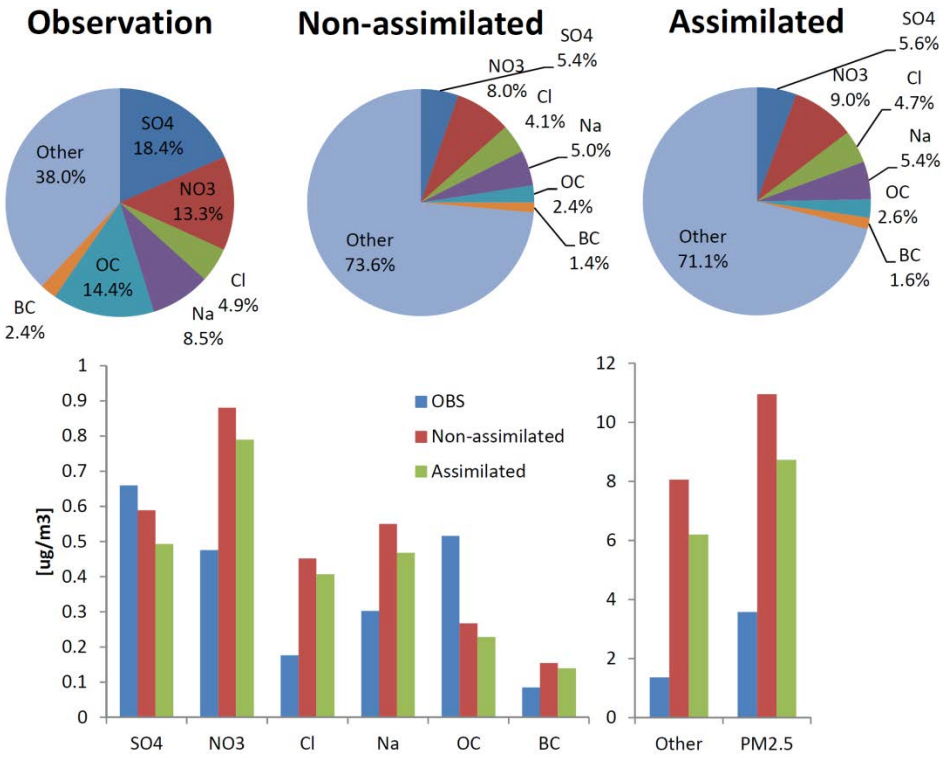

Figure 5.4. Summary of May 2010 IMPROVE observations versus non-assimilated and NASA NNR assimilated model estimates. Top figures show aerosol composition and bottom ones show mean aerosol concentration per chemical specie. Species are: sulfate (SO_4), nitrate (NO_3), chloride (Cl), sodium (Na), organic carbon (OC), black carbon (BC) and "Other", which in the observation is obtained as the mean PM2.5 minus the sum of the mean of rest of the species mentioned, and in the model as the sum of the mean of "other inorganics" (which includes dust) and ammonium species.

California, while decreasing AOD over the ocean and on the more inland territories, especially over Nevada. Both of these post processing retrievals are calibrated with the AERONET data, so this behavior is expected. However, as the algorithms and inputs are different, there are still some significant differences between both data sets. When looking at specific AERONET sites (Fig. 5.6) we can see that the post processed techniques are usually closer to the AERONET values than the operational MODIS retrieval. However, there are still persistent biases that the post-processed techniques are

not able to overcome, mainly in the area of Nevada and South-East California (Fig. 5.6f), which is also shown by the high AOD in the monthly means (Fig. 5.5) in all retrievals.

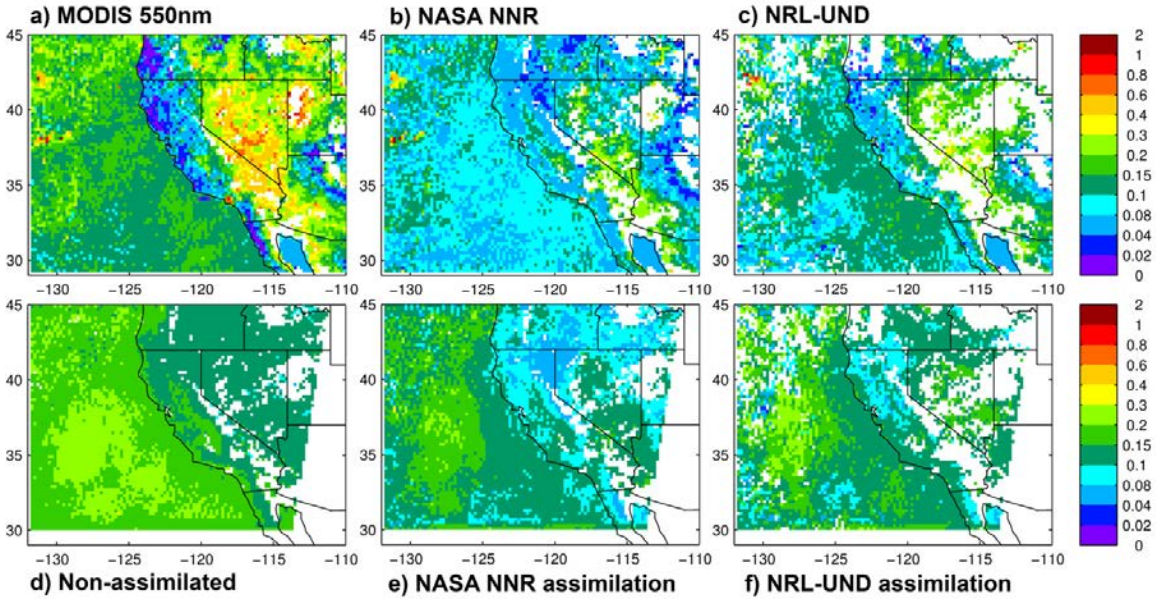

Figure 5.5. May 2010 average maps of operational MODIS Terra (a), NASA-NNR (b) and NRL-UND (c) products for the same MODIS Terra data, non-assimilated model (d) and assimilated estimates (e,f). While the non-assimilated model is masked by the NASA-NNR product, the assimilations are masked by each data ingested. MODIS data (a) is not quality controlled by cloud fraction or quality flags as done during assimilation.

Non-assimilated model monthly mean values (Fig. 5.5d) show a persistent overestimation in AOD over the ocean and over land for most of the domain. As mentioned above there appears to be a high bias in the boundary conditions associated with dust, which produces a high background AOD over the modeling domain. The non-assimilated model underestimates AOD in Nevada and South-East California, which corresponds to the area mentioned before where the retrievals show higher deviations from AERONET sites. A general overestimation is also found when comparing the non-assimilated model to AERONET stations (Fig. 5.6), so we anticipate that assimilation

should move the aerosol state towards the AERONET observations for most sites and retrievals. An interesting station to analyze is the Caltech Site (Fig. 5.6e), located in northern Los Angeles. Here, the model shows very small bias for the high AERONET AOD values, which is consistent with small errors and almost no bias found in the PM2.5 AQS comparison (Fig. 5.2, c and d). For this site, satellite retrievals do not exactly match the AERONET data, so we anticipate that assimilation will tend to degrade results in this area as errors in the retrieval are higher than model errors.

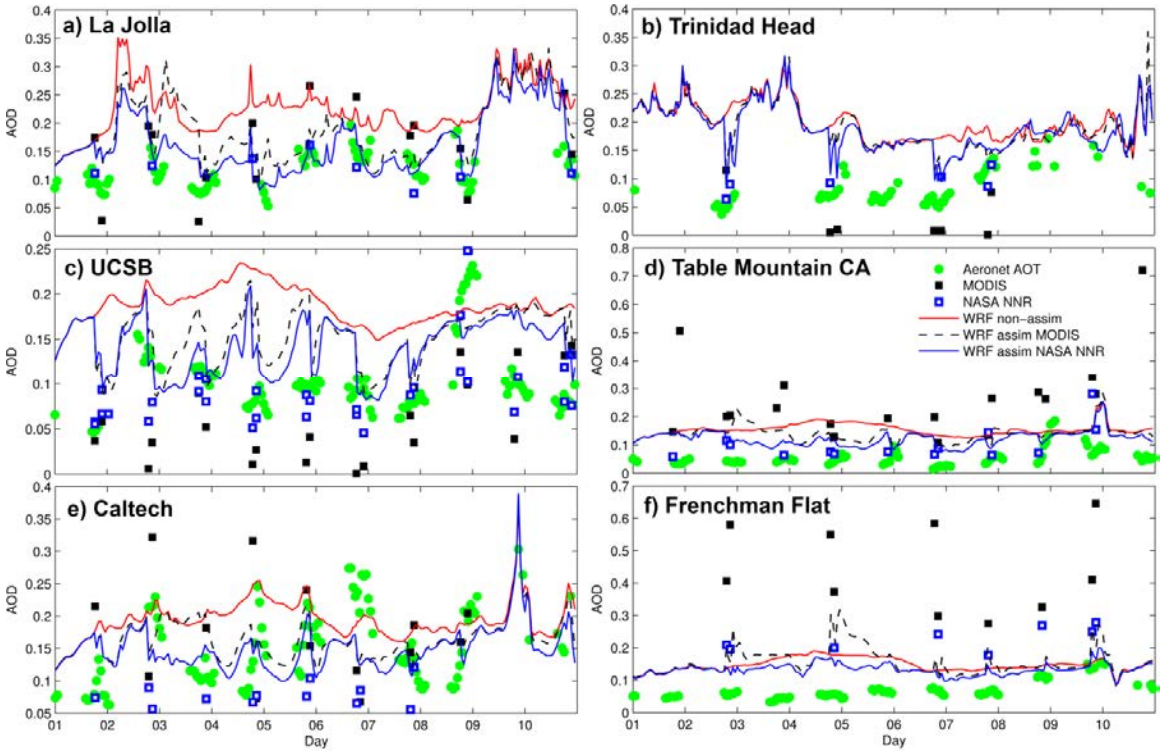

Figure 5.6. AOD time series on a selection of sites for AERONET data (500nm), operational MODIS (550nm), NASA NNR (550 nm), non-assimilated and two assimilation forecasts (500nm). MODIS shows pixels lumped from Terra and Aqua, while NASA NNR shows pixels lumped for Terra, Aqua, land and ocean retrievals. For satellite data, the closest retrieval to the site is plotted only when the distance is less than 0.2 degree. See Fig. 5.1 for AERONET sites locations.

MODIS and observationally constrained 550nm AOD

assimilation

Model AOD after assimilation is shown in Fig. 5.5 (e and f). Model estimates are closer to the observations being assimilated compared to the non-assimilated one, showing that the optimization process is working properly.

Figures 5.3, 5.4, 5.7 and 5.8 show improvements in PM2.5 after AOD assimilation. When looking at the time series of PM2.5 for the whole month (Fig. 5.3) it is seen that the bias reduction of the assimilation changes from day to day. These variations can be partially explained by the amount of data being assimilated (Fig. 5.9) which is a function of several factors including the scan pattern of the MODIS sensor, the quality control applied (the most important being the cloud fraction threshold) and post processing algorithms. For instance, the first 8 days of the month show the consecutive period with the most data available to assimilate and the largest bias reductions. One factor contributing to the correlation between the amount of assimilated data and the resulting bias reduction is the small horizontal length scale used (see Background error covariance matrix sub-section), which prevents corrections during assimilation extending too far from the observation location. Thus, more data will translate into a larger spatial coverage.

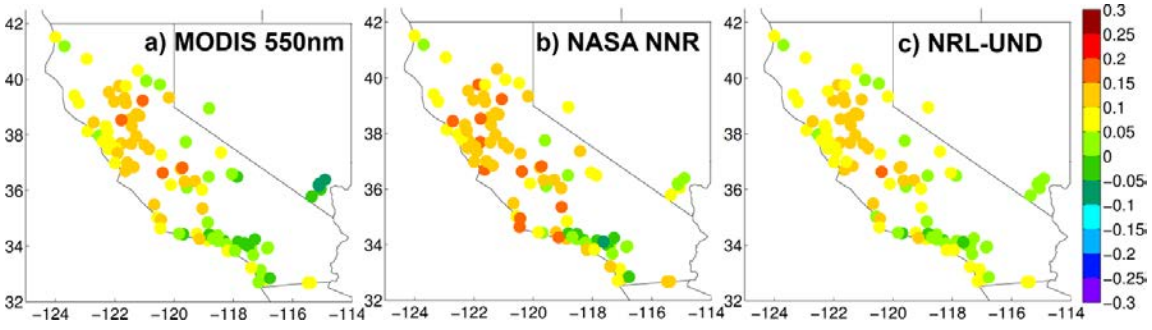

Figure 5.7. PM2.5 fractional error reductions from non-assimilated to assimilated models at AQS sites for May 2010. Positive values represent error reductions.

Results show that all assimilated retrievals reduce the fractional error (from 0.71 on the background to 0.65, 0.62 and 0.64 for MODIS, NASA NNR and NRL-UND assimilation) on a large fraction of AQS PM2.5 stations (85%, 92% and 96% for MODIS, NASA NNR and NRL-UND assimilation). Fractional error reductions (Fig. 5.7) tend to be higher in stations that originally had higher errors (Fig 5.2), like locations in northern and central California. In general, the assimilation of post-processed data (NASA NNR and NRL-UND) has better performance than the operational MODIS data. A very clear example is South Nevada, where MODIS assimilation degrades results, which is in agreement with Schwartz *et al.* (2012), while both post-processed techniques reduce the errors. As seen in figure 5.9, the NASA NNR retrieval has the highest amount of data assimilated, which is mainly due to the less restrictive quality control applied in this algorithm (e.g. cloud fraction less than 0.85 versus no cloud fraction in MODIS and NRL-UND tests). As discussed previously, having more data tends to improve assimilation performance, thus this is a factor influencing the higher error reductions of assimilating NASA NNR versus the other two retrievals. However, quality of the data is also important, which is why the post-processed techniques show a considerably higher fraction of stations with reduced errors compared to MODIS. In this dimension, the NRL-UND product is the one that shows the highest fraction of stations improved due to the more restrictive quality control applied. The assimilations tend to slightly reduce or even increase errors in the region surrounding Los Angeles (Fig. 5.7). As mentioned in the "Non-assimilated model and retrievals evaluation" sub-section, this was expected as the non-assimilated model has small error and bias in this region, both against PM2.5 and AERONET measurements. Also as this is a populated area, spatial and temporal concentration gradients are not completely resolved by the 12 km horizontal grid spacing used. This can be observed by comparing observation and model mean maps (Fig. 5.2 a and b), and by the great variability during the day at the AERONET Caltech site not entirely captured in the non-assimilated model (Fig. 5.6e).

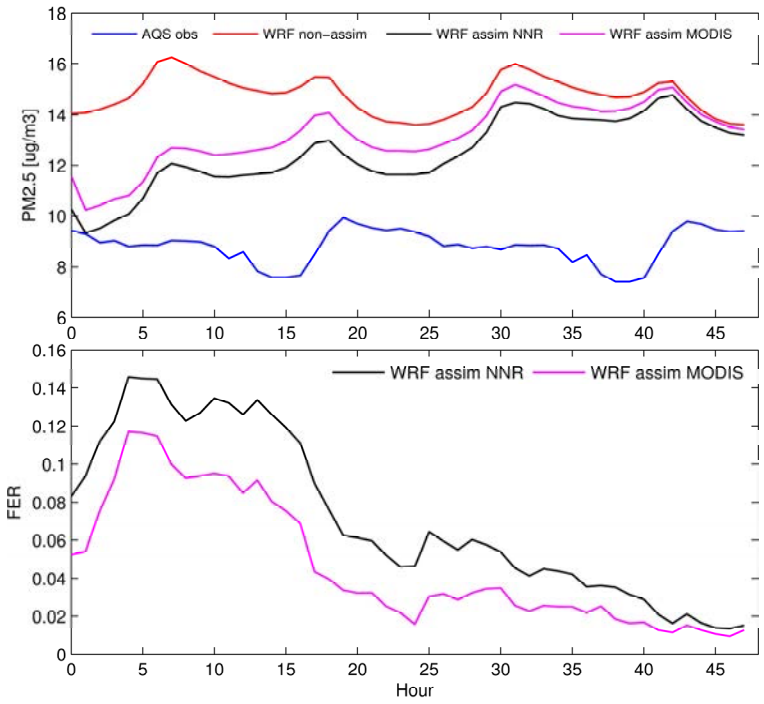

Figure 5.8. Mean PM2.5 concentrations (top) and Fractional error reductions (FER, bottom) as a function of forecast hour for all AQS stations during the first 10 days of May 2010. All 48 hour forecasts used to build the mean and FER start at 21 UTC.

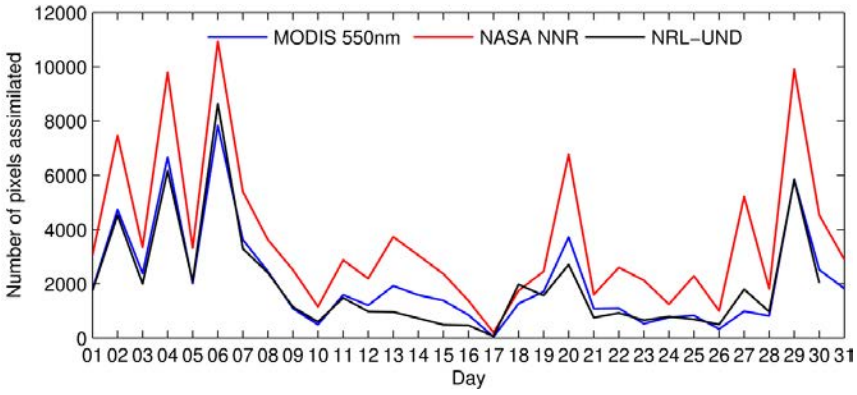

Figure 5.9. Time series of the number of pixels being assimilated for each day on May 2010 for the different 550nm AOD data sets.

The bias reduction against monitored PM2.5 can also be seen at the IMPROVE stations (Fig 5.4, bottom), with improvements in the fractional error (from 1.1 to 0.88 globally) for 100% of the stations analyzed when NASA NNR is assimilated (similar for the other two retrievals). The assimilation does not significantly change aerosol composition as only total AOD is assimilated and because a relatively long correlation length is used between size bins. Thus, the general trend is that aerosol species in the non-assimilated model that have a bias of the same sign of total PM2.5 bias will have their biases reduced in the analysis, while the bias will be increased in the opposite case. For instance, assimilated black carbon and nitrate improved while sulfate and organic carbon degraded after the assimilation tests. This behavior is similar to the one found in experiments assimilating PM2.5 observations (Pagowski and Grell, 2012).

An analysis of the impact of assimilation on forecasts starting at 21 UTC is shown in Fig. 5.8 and 5.10. When evaluating against PM2.5 AQS measurements (Fig. 5.8), as all forecasts start at the same time, the diurnal cycle modulates the bias and error reductions. For instance, the decreasing trend in fractional error on the 0-4 hour forecast follows the increase in error shown by the non-assimilated model in this portion of the diurnal cycle. PM2.5 concentrations show low bias one hour after assimilation, reaching zero values when NASA NNR retrievals are assimilated. Then, the assimilation gradually returns towards concentrations and errors found when no assimilation is performed, in agreement with previous studies (Schwartz et al., 2012). This is also seen in the AQS PM2.5 comparison, where assimilation almost never goes back to the non-assimilated model levels (Fig. 5.3) and fractional error reduction at 18:00 UTC for all stations and days in May is equal to 0.06. After 48 hours there is a slight but positive influence of assimilation for both retrievals (> 0.012 fractional error reduction). These results show that, in the context of operational air quality forecasting, AOD assimilation with the method developed here can be beneficial for improving the skill of the forecasts for the day after

the satellite overpass. As shown earlier, the NNR retrieval assimilation outperforms the MODIS 550nm assimilation for all times for both bias and fractional error.

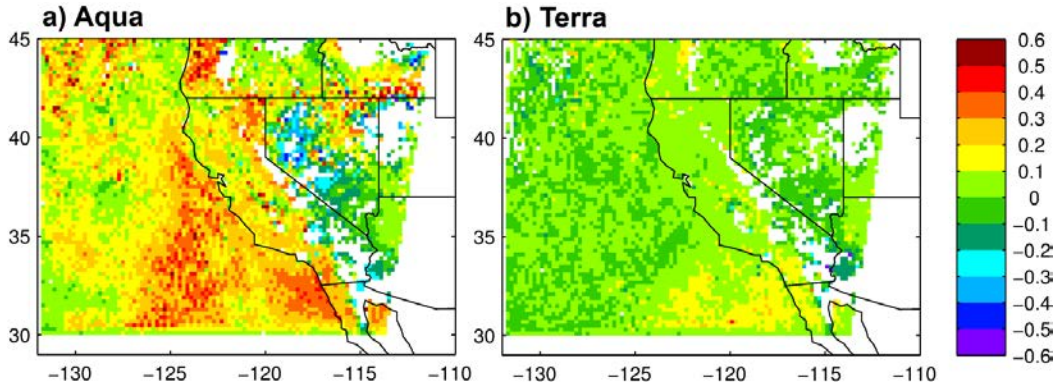

Figure 5.10. Fractional error reductions from non-assimilated to NASA NNR assimilated models computed with respect to NASA NNR Aqua (a) and Terra (b) observations. Model fields used for comparison are forecasts at 21 and 18 UTC for (a) and (b) respectively. Thus in the fractional error computation, observed data has not been assimilated yet and can be considered as independent. Thus, a) and b) are fractional error reductions for a 3 and 21 hour forecast respectively (See section "Study domain and experimental design" for more details).

Figure 5.10 shows performance evaluation for a 3 and 21 hour forecast against not yet assimilated satellite data. For the 3 hour one, assimilation shows error reductions in most of the domain, except in the Nevada and southeast California regions, where the retrievals tend to present issues (see Non-assimilated model and retrievals evaluation sub-section). Error reductions tend to be higher over ocean due to the smaller error assigned to these observations during assimilation, which allow the system to better fit the model to observations. Different errors reductions over different ocean areas are related to cloud presence from day to day, with areas with higher cloud fractions showing less error reductions. The 21 hour forecast (Fig. 5.10b) shows smaller but still significant error reductions as model errors over time bring the state closer to the non-assimilated model. Fractional error reductions are close to zero over the ocean from 125 W to the west as

after 21 hours the assimilated aerosol have already been advected away from this region, matching the error of the non-assimilated model. Over the ocean south of California there is still the presence of the assimilated aerosol and the fractional error reductions are considerable (above 0.1). Over California, error reductions are generally less than 0.1 but positive, showing that after 21 hours there is still persistence of the innovation. This is also seen in the AQS PM2.5 comparison, where assimilation almost never goes back to the non-assimilated model levels (Fig. 5.3) and fractional error reduction at 18Z for all stations and days is equal to 0.06. High error reductions over land after 21 hours (Fig. 5.10b) are found along coastal southern California and northern Mexico, which is consistent with the excellent and long-lasting performance of NASA NNR (and the other retrievals) assimilation against AERONET measurements at the La Jolla site (Fig. 5.6a). On the other hand, sites like Trinidad head (Fig. 5.6b) tend to approach the non-assimilated model more rapidly as the domain boundary is close to the site and boundary conditions blow in this direction. As NASA NNR (and NRL-UND as well, not shown) data are closer to AERONET AOD, assimilation of this data sets generally provides a closer agreement to these observations compared to the operational MODIS data assimilation (Fig. 5.6). From the 10 AERONET stations with data during May 2010, MODIS assimilation reduces fractional error in 8 of them from a global fractional error of 0.66 to 0.6, while the AERONET calibrated techniques reduce errors in all 10 stations yielding smaller fractional errors (0.54 and 0.58 for NASA NNR and NRL-UND, respectively).

Multiple wavelength and fine mode AOD assimilation

Compared to AQS and IMPROVE data, fine and total and multiple wavelength assimilations do not degrade results compared to the control 550 nm AOD assimilation, obtaining similar statistics to the ones shown in the previous section, even when results are filtered for coastal stations.

Figure 5.11 shows error reductions for a 3 hour forecast. We see that all approaches considerable reduce errors over the ocean for both wavelengths (Fig. 5.11 top and middle rows). Assimilating only 550nm AOD (control) reduces the aerosol loads, thus also reducing the 870nm AOD generating a better fit with these observations without assimilating them. Assimilating fine and total AOD generates smaller error reductions (for both 550nm and 870nm AOD) compared to only assimilating total AOD. This is probably because the additional constraint to the fine aerosol reduces the ability of the optimization to generate a closer fit to the total AOD. Another factor that could also create these results and that has been noted to generate issues (Kleidman *et al.*, 2005) is the possible mismatch in the fine and coarse mode definitions, due to different aerosol approaches used in MOSAIC and the MODIS algorithm (sectional versus modal, respectively). On the other hand and opposite to fine AOD assimilation, using multi-wavelength AOD data generates slightly better error reductions for 550 nm AOD while considerably better reductions for 870 nm AOD when compared to the control assimilation. The better fit to 870nm AOD observations is expected as the 870nm retrieval is directly being assimilated.

Figure 5.11 (bottom row) also shows error reductions for the Angstrom Exponent (AE). In general, increasing values on AE indicate finer aerosols (Schuster *et al.*, 2006). Over the ocean, the non-assimilated model tends to show very low AE compared to the observed values (not shown) which is consistent with the overestimation of dust coming from the boundaries (see Non-assimilated model and retrievals evaluation sub-section). Even though the 550nm AOD only assimilation generates a good fit to AOD observations, there is only a small change in AE, with regions where there is even an increase in the error. As this assimilation only uses one observation per column and a large correlation length between bin sizes, the assimilation tends to uniformly modify

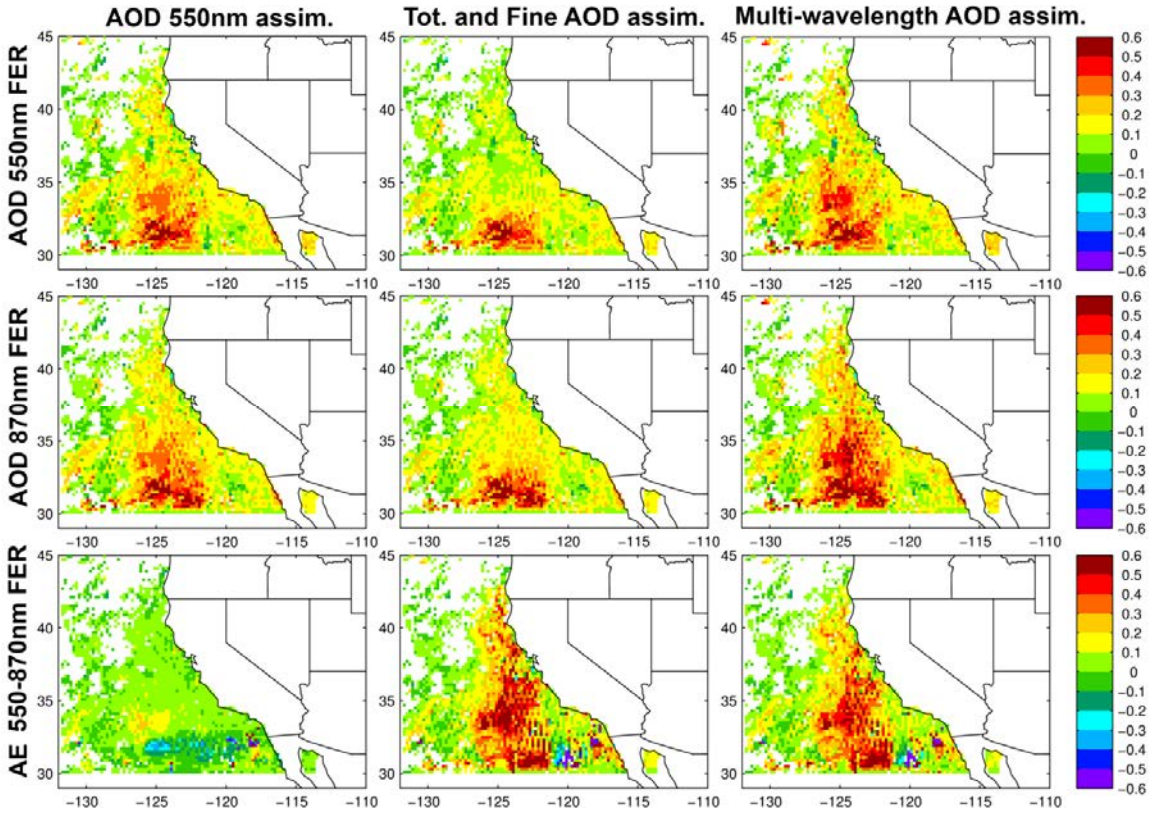

Figure 5.11. Fractional error reductions for 550 nm AOD, 870 nm AOD and 550-870nm Angstrom exponent (rows) from non-assimilated to assimilated model computed with respect to Aqua retrievals. Figures on the left column assimilate only MODIS 550nm AOD (control), on the center column assimilate both total and fine AOD at 550 nm, while the ones on the right column assimilate MODIS 550, 660, 870, and 1240nm over ocean and only 550nm over land. As described in Figure 5.10, these figures correspond to a fractional error reduction for a 3 hour forecast over May 2010.

aerosols within bin sizes, not significantly changing the size distribution and thus the AE. A completely different picture is seen for fine and total, and multi-wavelength AOD assimilations, where the use of multiple observations per column modifies the AE and in the right direction, reducing the errors in most of the domain. The fine and total AOD assimilation tends to generate slightly better AE results than the multi-wavelength AOD assimilation as the former directly modifies the fine aerosol. However, we recommend the use of the multi-wavelength over the fine and total AOD data as total AOD burdens

are much better estimated by the multi-wavelength approach, as described in the previous paragraph.

To better understand the differences between the control assimilation (550nm AOD only) versus adding additional multi-wavelength data, Fig. 5.12 shows vertical profiles of PM2.5 and aerosol number concentration 3 hours after a given assimilation. Even though the PM2.5 column is reduced for both assimilations (Fig. 5.12a), the use of multiple wavelength data selectively reduces PM2.5 in different model layers (higher reductions in the 3-8 km layer, smaller below 2km) to better fit all observations simultaneously. This can generate a shift in the AE as different size distributions are found at different heights. On the other hand, the different assimilation approaches generate opposite results for aerosol number concentrations (Fig. 5.12b), with the single and multiple wavelength cases reducing and increasing it below 5km, respectively. As explained in the previous paragraph, when assimilating 550nm AOD only, the long correlation length generates uniform modifications along bin sizes, so as the total aerosol concentration is reduced, aerosol in the small bin sizes (where aerosol number dominates) will also be reduced, not changing the overall size distribution (Fig. 5.12c). Again, multiple-wavelength AOD assimilation will selectively modify size bins to create a better fit to observations at all wavelengths, even if changes go in opposite directions between bin sizes. In the case shown, coarse and fine size bins are reducing and increasing its mass respectively, which globally reduces mass (Fig. 5.12a) but increases number (Fig. 5.12b), changing the size distribution (Fig. 5.12c). Changing aerosol number concentrations in different directions can have a great impact in this region, as these aerosols can act as cloud condensation nuclei and substantially modify cloud properties (Saide *et al.*, 2012b).

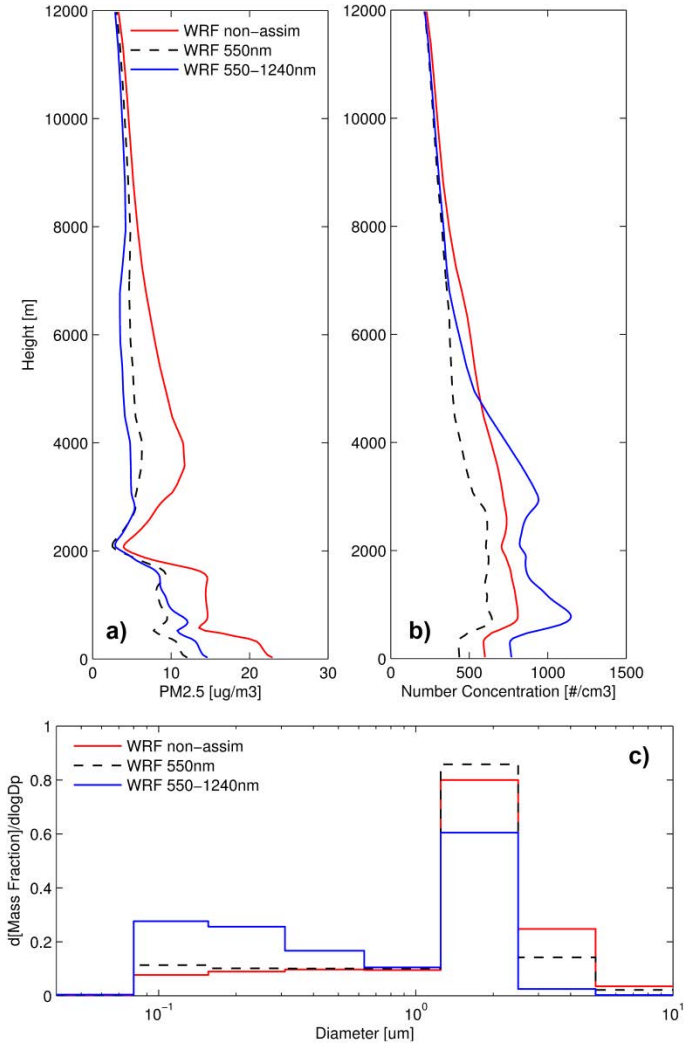

Figure 5.12. On the top, vertical profiles for PM2.5 (a) and aerosol number concentration over 80nm diameter (b), and on the bottom, mass fraction size distribution at 4km altitude (c), for forecasts on May 6th, 2010 at 21 UTC. The forecasts are the non-assimilated and two assimilated using the 550nm AOD only (control) and multiple wavelength AOD retrievals. Data assimilation was performed 3 hours before (18Z the same day). For 8 bin MOSAIC, dlogDp is 0.693.

Comparisons over coastal AERONET stations show that for periods when the single- and multi-wavelength assimilations have differences (flow towards the coast), assimilation of multi-spectral AOD tends to show slightly better performance against 870

nm AOD (Fig. 5.13, left column), but the single wavelength assimilation still shows very good skill as mentioned previously. Stronger differences can be appreciated in the AE

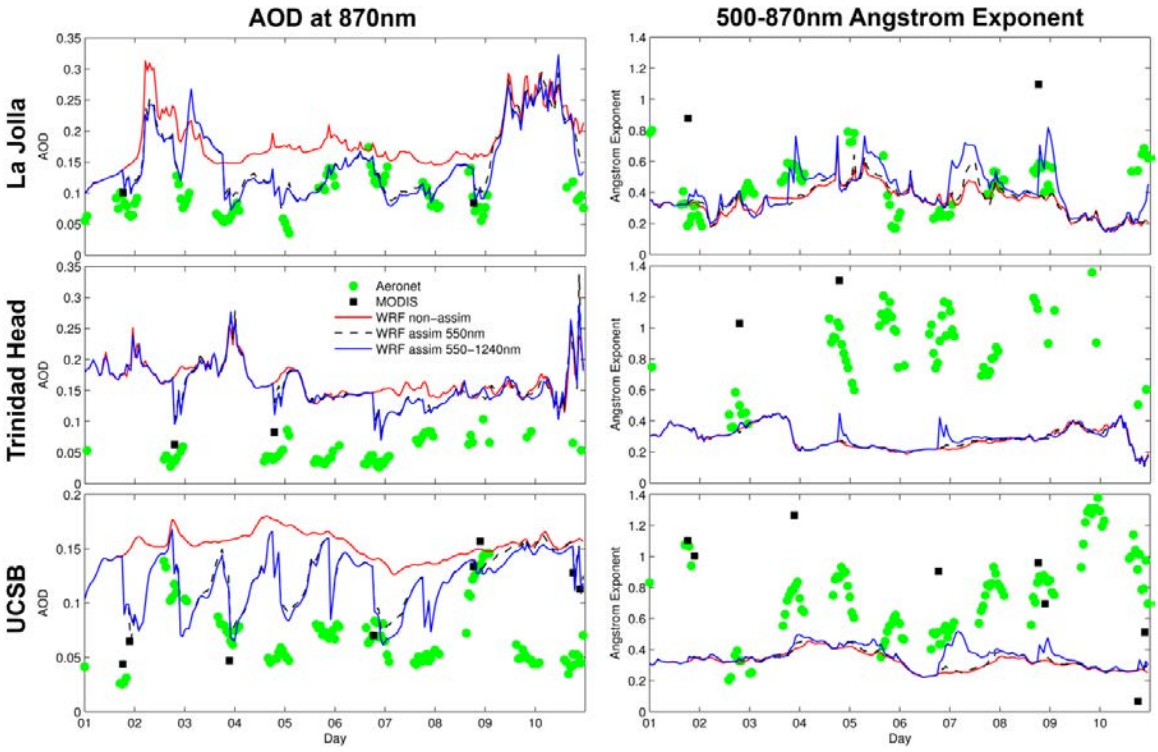

Figure 5.13. As Fig. 5.6 but for of 870nm AOD and 500-870nm Angstrom Exponent from coastal AERONET sites. The three model shown are the non-assimilated, and forecasts assimilating MODIS 550nm only and wavelengths from 550nm to 1240nm. MODIS ocean retrieval (870nm AOD and 550-870nm Angstrom Exponent) is shown when data is within 0.2 degree of the site. See Fig 5.1 for AERONET sites locations.

time series (Fig. 5.13, right column). The 550nm AOD assimilation usually follows the non-assimilated model closely while the multiple wavelength assimilation deviates from it and generally fits the observation better. The error reductions comparing to AERONET AE are not as significant as the ones shown when comparing to MODIS AE. This is probably because MODIS retrieved AE, which has yet to be validated (Remer *et al.*, 2005), is often inconsistent with AERONET AE (Fig. 5.13, right column). In this sense,

obtaining observationally constrained retrievals for multiple wavelengths AOD and AE would allow assimilations to obtain additional improvements as shown in the "MODIS and observationally constrained 550nm AOD assimilation" sub-section. Also, further work evaluating against marine AERONET stations and/or Maritime aerosol network (MAN) data (Smirnov *et al.*, 2011) is needed to substantiate these conclusions.

Conclusions

We developed the ability for the GSI system to perform AOD assimilation to correct WRF-Chem aerosol fields when simulations are done with the MOSAIC sectional aerosol model. This enables the assimilation to impact aerosol concentrations, size and composition. In doing so, we added several new capabilities to the GSI system which include: using the AOD forward and adjoint Mie computations from WRF-Chem routines making GSI results consistent with the forecasts; adding the use of logarithmic state and observations; including bounds during optimization time in the form of weak constraints; adding correlations within aerosol size bins into the background error covariance matrix by the use of GSI recursive filters; and modeling aerosol water uptake as done in MOSAIC considering atmospheric conditions and the electrolytes present. The assimilation is performed using as state variable total mass within each size bin, significantly reducing computational resources used compared to using all species in all size bins. This is all demonstrated on a 3DVAR assimilation system, but it could eventually be applied in more sophisticated frameworks such as 4DVAR or Kalman filter systems to make use their strengths over 3DVAR (e.g., Pagowski and Grell, 2012). These methods would allow performing data assimilation simultaneously with boundary conditions and emissions inversions (e.g., Elbern *et al.*, 2007), which is likely to extend aerosol improvements further on time.

This newly developed assimilation scheme was demonstrated in a regional forecast application for one month over California and its surroundings. The first set of

assimilation experiments explored the use of observationally constrained AOD retrievals (NASA NNR and NRL-UND) against using operational MODIS 550nm dark target data. All three assimilations decreased global error and biases by improving forecasts on a large fraction of PM2.5 and AOD monitoring ground stations. The assimilation of observationally constrained retrievals had consistently better performance compared to the operational MODIS data as they corrected the spatial biases and quality controlled odd retrievals, with the NASA NNR producing the higher error reductions (due to a larger amount of data) and the NRL-UND showing the higher fraction of PM2.5 stations improved (96%, due to the more restrictive quality control applied). 48 hour forecasts starting from an analysis step showed improvements on the aerosol predictions (0.15–0.015 fractional error reductions for the NASA NNR retrieval vs PM2.5), demonstrating the potential of the developed technique for air quality forecasting applications. These assimilation experiments did not change the overall aerosol composition, thus degrading model performance for single aerosol species that had an opposite bias to the global tendency. Improvements in the non-assimilated estimates are necessary to correct this issue, which could be achieved in the study case by incorporating missing SO_2 emissions and processes not modeled such as secondary organic aerosol formation.

A second set of experiments assessed the impact of assimilating fine mode and multiple-wavelength AOD. Results showed that while single wavelength assimilation did not significantly change size distributions, assimilation of additional data selectively modified aerosol at different vertical layers and changed size distributions, producing a better fit to the Angstrom Exponent (AE), an indicator of aerosol particle size distributions. The inclusion of fine AOD could not outperform the assimilation of just total AOD when comparing AOD burdens, possibly due to a mismatch between the fine mode fraction definition on model and retrieval. On the other hand, forecasts including multiple wavelengths in the assimilation further reduced errors for MODIS 550nm and 870nm AOD and simultaneously improved the 550-870nm AE. The use of multiple

wavelengths in the assimilation was also found to have positive influence on predictions at coastal AERONET sites. However, AE error reductions were not as significant as when evaluating with MODIS AE, possible due to an inaccurate performance of the MODIS against AERONET AE.

In this paper we showed the value of assimilating observationally constrained AOD and multiple wavelength data over assimilation of off-the-shelf 550nm AOD products. Future research should point towards generating observationally constrained AOD and AE for multiple wavelengths, which will bring together the best of the techniques explained in this research. We directly use MODIS resolution (10x10 km^2) in assimilation without thinning or re-gridding, showing that data assimilation on fine resolution models is feasible with positive impacts. This becomes important as newer products are available at higher resolutions (e.g. Lyapustin *et al.*, 2012; Munchak *et al.*, 2013). Even though we perform assimilations on a region densely populated by monitoring networks, we only assimilate satellite retrievals, thus this method can be applied anywhere in the world. Future work should point towards simultaneously assimilating several AOD data sets, including other observations types such as ground measurements (Schwartz *et al.*, 2012) and cloud retrievals (Saide *et al.*, 2012a). We also show that the impact of assimilation increases with the amount of data used, so further error reductions may be achieved by using AOD retrievals from geostationary satellites, provided that their quality is appropriate for data assimilation. Integration of all these datasets is likely to help in providing better aerosol estimates for a large variety of applications.

As we show that assimilation can improve estimates of surface PM2.5, this technique can be used to generate analysis with high temporal and spatial resolution for use in health assessments (e.g., Silva *et al.*, 2013). Also, the improved aerosol loads can help to better estimate aerosol climate forcing. Finally, the assimilation can be used in forecasting mode to predict air quality more accurately.

Collaborators and funding sources

We thank all WRF-Chem developers, especially Jerome Fast and Rahul Zaveri responsible for the optical properties and MOSAIC code. We thank Jochen Stutz, Pavel Ionov, Carol Bruegge, Robert Frouin, Brent Holben, Sabino Piazzolla, Ellsworth Dutton and Mark Tragesser and their staff for establishing and maintaining the 10 AERONET sites used in this investigation. MODIS data was obtained from the NASA Langley Research Center Atmospheric Science Data Center. This work was carried out with the aid of NASA grants NNX08AL05G and NNX11AI52G, grant number UL1RR024979 from the National Center for Research Resources (NCRR), a part of the National Institutes of Health (NIH), and Fulbright-CONICYT scholarship number 15093810. Its contents are solely the responsibility of the authors and do not necessarily represent the official views of the founding institutions.

Author contributions

This work is published in Saide *et al.* (2013). P. Saide and G. Carmichael designed the study and P. Saide executed it. Z. Liu, C. S. Schwartz and H. C. Lin (NCAR) provided the GSI code that does GOCART AOD assimilation which was modified by P. Saide as explained in the text. A. M. da Silva (NASA GMAO) provided the NASA NNR retrieval and E. Hyer (NRL) provided the code to process the NRL retrieval. All authors contributed to the final form of the manuscript.

CHAPTER 6 CENTRAL AMERICAN BIOMASS BURNING SMOKE CAN INCREASE TORNADO SEVERITY IN THE US

Abstract

Tornadoes in the Southeast and Central US are often accompanied by smoke from biomass burning in Central America. Numerical modeling and observations of the 27 April 2011 historical tornado outbreak show that adding smoke to an environment already conducive to severe thunderstorm development can increase the likelihood of significant tornado occurrence. Smoke leads to optical thickening of shallow clouds and soot within the smoke warms the atmosphere aloft, lowering cloud base and increasing low-level wind shear ahead of the front producing the outbreak. This mechanism can contribute to tornado modulation by aerosols, highlighting the need to incorporate aerosol interactions in severe weather forecasting.

Introduction

Smoke from Central American fires mainly related to agricultural practices is transported episodically during spring to the Southeastern, Central and Eastern US (Wang *et al.*, 2009). These events have been shown to be associated with severe weather outbreaks (Lyons *et al.*, 1998; Murray *et al.*, 2000), and updraft invigoration through suppression of the onset of warm rain (Andreae *et al.*, 2004) has been hypothesized as the mechanism by which they impact convective clouds resulting in more severe weather (Wang *et al.*, 2009). More generally, invigoration of deep convection by aerosols can increase cloudiness (Andreae *et al.*, 2004), rain (Bell *et al.*, 2008), cloud heights (Bell *et al.*, 2009b) and lighting (Yuan *et al.*, 2011b; Bell *et al.*, 2009a). In spite of evidence showing aerosol impacts on atmospheric conditions, current numerical severe weather forecast models do not include aerosol interactions due to their uncertainties (McFiggans *et al.*, 2006) and computational expense. In the case of tornado forecasting, while studies have shown impact of aerosols on tornadogenesis in idealized simulations (Snook and

Xue, 2008; Lerach *et al.*, 2008), the influences of aerosols on the parameters commonly used in tornado forecasts have not been studied, and the effects of aerosols have not been resolved in historic cases.

We analyzed the effect of Central American biomass burning on a historic severe weather outbreak that occurred during the afternoon and evening of 27 April 2011 (Doswell Iii *et al.*, 2012). This outbreak produced 122 tornados resulting in 313 deaths across the Southeastern US, with 15 tornadoes considered violent (EF 4 or 5) and 68 considered significant (EF2 or greater damage) (NOAA, 2011). The only outbreak ever recorded of a similar magnitude, which is also the last one with similar number of mortalities, occurred on 3 April 1974 (Doswell Iii *et al.*, 2012). We use a coupled aerosol, chemistry and weather model that includes aerosol effects on radiation and cloud microphysics (see Methods section) to asses if the smoke influence on the outbreak and the processes involved in it. We also outline future directions.

Methods

Modeling framework

The chemistry version of the Weather Research and Forecasting (WRF-Chem) model (Skamarock *et al.*, 2008; Grell *et al.*, 2005) version 3.4.1 was used in regional simulations of meteorology and atmospheric composition including aerosol-cloud-radiation interactions. WRF-Chem has been used extensively to characterize aerosol feedbacks in a wide variety of environments (Fast *et al.*, 2006; Chapman *et al.*, 2009; Zhao *et al.*, 2010; Zhao *et al.*, 2011; Zhao *et al.*, 2012; Gustafson *et al.*, 2007; Ntelekos *et al.*, 2009; Grell *et al.*, 2011; Saide *et al.*, 2012b; Yang *et al.*, 2011b; Yang *et al.*, 2012), while WRF (no chemistry) is used by many centers for operational weather prediction (http://wrf-model.org/plots/wrfrealtime.php), and is the basis for the NOAA/NCEP Rapid Refresh and North American Mesoscale Forecast System forecasting systems.

WRF-Chem was configured as follows. A 12km horizontal grid spacing outer domain includes the smoke source region (Fig. 6.1 and 6.2) while a nested 4km inner domain is used to explicitly resolve convection, as done by severe weather prediction centers (e.g., NOAA National Severe Storm Laboratory and WRF for Hurricanes at the NOAA National Weather Service Environmental Monitoring Center). Resolving fire emissions in the modeling domain allows the ability to isolate the effects of the resultant smoke. Vertical resolution consists of 52 levels, with the first 5 levels of ~50 m thickness, 11 and 19 levels below 1km and 3km, respectively, to a top pressure of 50 hPa. The CBMZ gas-phase chemical mechanism (Zaveri and Peters, 1999; Fast *et al.*, 2006) is coupled to the 8-bin sectional MOSAIC (Zaveri *et al.*, 2008) aerosol model. Other parameterization options include MYJ boundary layer (Janjić), NOAA land surface model (Chen and Dudhia, 2001), Goddard shortwave radiation (Chou *et al.*, 1998), which uses the Slingo (1989) scheme for computing cloud optical depth (COD), RRTMG longwave radiation (Mlawer *et al.*, 1997), Mie theory along with Chebyshev expansion coefficients for aerosol optical properties (Fast *et al.*, 2006), Morrison microphysics (Morrison *et al.*, 2009) and critical saturation aerosol activation (Abdul-Razzak and Ghan, 2002), with the last five options allowing the aerosol interactions with radiation and clouds (Fast *et al.*, 2006; Chapman *et al.*, 2009; Zhao *et al.*, 2011; Yang *et al.*, 2011b). While WRF supports a variety of microphysics schemes that can produce wide range of solutions, only two include aerosol indirect effects, with the Morrison scheme employed here currently among the most sophisticated and most capable of generating accurate clouds (Cintineo *et al.*, 2013).

The accuracy of biomass burning emissions is central to quantitative skill in modeled smoke impacts. The Quick Fire Emission Dataset (QFED) v2.0 biomass burning emissions (Darmenov and da Silva, 2013) used here deals with obscured regions and employs tunable emission coefficients adjusted using an inverse technique to improve model agreement with AOD estimates in near-real time. This empirical fitting improves

model performance. Fire emissions were coupled to the WRF-Chem online plume-rise model (Grell *et al.*, 2011). Anthropogenic emissions for the outer domain (Fig. 6.2) were computed using PREP-CHEM-SRC (Freitas *et al.*, 2011), and NEI 2005 was used for the inner domain (http://www.epa.gov/ttnchie1/net/2005inventory.html). Other emission sources include online MEGAN biogenics (Guenther *et al.*, 2012), Gong *et al.* (1997) sea salt parameterization and GOCART dust scheme (Zhao *et al.*, 2010).

The outer domain was initialized on 17 April 2011 at 00 UTC using NCEP Final Analysis (http://rda.ucar.edu/datasets/ds083.2/) and RAQMS chemical forecasts (Pierce *et al.*, 2007; Natarajan *et al.*, 2012) (both also used as lateral boundary conditions) and evolved through 00 UTC on 29 April. The long spin-up allows for the emissions and aerosol feedbacks in WRF-Chem to appear. The nested domain is initialized from and forced by the outer domain starting at 00 UTC on 26 April.

FLEXPART (Stohl *et al.*, 2005) driven by WRF-Chem (Fast and Easter, 2006) simulations including fire emissions was used to calculate back-trajectories shown in Fig. 6.1. These are initiated from the time and location of the start of violent tornado (EF4 and EF5) tracks for a period of 42 hours.

The tornado parameters, used operationally for forecasting severe weather, were computed as follows. Variables not directly provided by the model were computed using the Unified Post Processor (UPP) v2.0 (DTC, 2013), including Lifting Condensation Level height (LCL), 0-1 km convective available potential energy (CAPE), shear (0-1 and 0-6 km) and 0-1 km storm relative helicity (SRH), the later computed with the dynamic method (Bunkers *et al.*, 2000). The significant tornado parameter (STP) was then computed from these variables (Thompson *et al.*, 2003):

$$STP = \left(\frac{CAPE_{1km}}{1000}\right)\left(\frac{Shear_{6km}}{20}\right)\left(\frac{SRH_{1km}}{100}\right)\left(\frac{2000 - LCL}{1500}\right) \qquad (1)$$

WRF-Chem cloud top heights were considered as the height of the first vertical level starting from the top where total column cloud optical depth from the top to that

level was at least 0.5. This eliminates the influence of very thin cirrus often found in the model.

Observations

A suite of satellite and ground-based observations were used to compare model and observations. We used data on aerosols (AOD, plume heights, PM2.5 concentrations), clouds (optical properties, heights) and meteorological variables such as temperature, rainfall, solar radiation and wind shear. Satellites used included Terra, Aqua, GOES13 and CALIPSO, while ground-based networks included AERONET, AQS, NEXRAD, rain gauges, USRCRN, upper air soundings and NPN. These are summarized and explained in Table 6.1. In addition, CALIPSO tracks and ground-based stations are shown in Fig. 6.2.

The NOAA profiler network provides vertically resolved wind observations starting from 500m altitude, which were used to estimate shear in the 0.5-1.5km layer. For 27 April the OKOM6 station at Okolona, MS (Fig. 6.2) had valid hourly observations between 18 and 20 UTC, which yielded an average wind shear of 9.8 m/s.

The Moderate Resolution Imaging Spectroradiometer (MODIS) cloud product provided cloud top pressure. From these estimates, MODIS cloud height was obtained by interpolation to WRF-Chem pressure levels at the overpass times.

Experimental design

In order to assess the impacts of smoke, two simulations were performed with and without fire emissions. An additional simulation was performed to assess the influence of the absorption of solar radiation by black carbon (BC), where the imaginary part of the BC refractive index was set to 0 to remove BC absorption while including indirect radiative effects.

Statistics over different regions, stations, times and vertical levels and for different parameters are shown in box and whisker plots (Figs 6.3, 6.4, 6.5, 6.6, 6.9, 6.10

Table 6.1. Observational data used in the study.

Observation	**Satellite / Network**	**Instrument**	**Algorithm**	**Reference**
COD	Terra/Aqua	MODIS	-	(King *et al.*, 2006)
	GOES 13	Imager	PATMOS-x	(Pavolonis *et al.*, 2005)
Cloud top heights	GOES 13	Imager	PATMOS-x	(Pavolonis *et al.*, 2005)
	Terra/Aqua	MODIS	-	(Platnick *et al.*, 2003)
AOD	Terra/Aqua	MODIS	NASA NNR	(GMAO, 2013)
	CALIPSO	CALIOP	Feature detection, classification and extinction retrieval	(Young and Vaughan, 2009)
	AERONET	Sun photometer	SDA	(O'Neill *et al.*, 2003)
Aerosol plume height	CALIPSO	CALIOP	Feature type detection	(Young and Vaughan, 2009)
Ground PM2.5	AQS	TEOMS, FRM	-	(EPA, 2013b)
Rainfall	NEXRAD + rain gauges	Radar and rain gauges	Stage IV	(Lin and Mitchell, 2005)
Solar radiation	USRCRN	Pyranometer	-	(Diamond *et al.*, 2013)

Table 6.1. Continued.

Cloud height	Upper air	Radiosonde	-	(NOAA NWS, 2013)
Shear 0.5-1.5 km	NPN	Doppler Radar	-	(Barth *et al.*, 1994)
Tornado tracks	SPC	-	Reports and damage surveys	(SPC, 2013)

Notes: COD: Cloud optical Depth, LWP: Liquid Water Path, AOD: Aerosol Optical Depth, PM2.5: aerosol mass of sizes below 2.5 μm, AERONET: Aerosol RObotic NETwork, GOES13: Geostationary Operational Environmental Satellites number 13, CALIPSO: Cloud-Aerosol Lidar and Infrared Pathfinder Satellite Observations, AQS: Air Quality System, NEXRAD: Next-Generation Radar, USRCRN: US Regional Climate Reference Network, NPN: NOAA Profiler Network, SPC: Storm Prediction Center, MODIS: Moderate Resolution Imaging Spectroradiometer, CALIOP: Cloud-Aerosol Lidar with Orthogonal Polarization, NNR: Neural Network Retrieval, SDA: Spectral Deconvolution Algorithm.

and 6.11), with 25 and 75 percentile boxes and 10 and 90 percentile whiskers. Mean and median are indicated with a circle and horizontal line, respectively. In the case of tornado parameters, cloud properties and vertical profiles, statistics were computed over two regions, one for an area containing violent tornado tracks and smoke influence ("Stats 1" in Fig. 6.2), and another for the inflow to that region ("Stats 2" in Fig 6.2).

Results and Discussion

Modeled smoke evaluation: Plume heights, AOD and PM2.5

Smoke from Central American biomass burning was present in the boundary layer and lower free troposphere before and during the storm outbreak (Fig. 6.1 and 6.3, "Modeled smoke evaluation" sub-section), as noted in other episodes (Wang *et al.*, 2009).

Before and during the tornado outbreak, biomass burning smoke emitted in Central America was found over the Gulf of Mexico (GoM), which is supported by the high and extensive MODIS and CALIOP AOD, the great amount of fire detections surrounding the GoM, the substantially better model representation of aerosol observations when smoke emissions are included, and the lack of other sources (such as dust) coming from the boundaries (Figs. 6.1 and 3). Boundary layer air masses feeding the outbreak came primarily from the GoM (Fig. 6.1). Specifically, air masses for each of the tornadic storms originated in or near an area of biomass burning. As seen in figures 6.1 and 6.3, smoke is transported from 0-5 km in height above the GoM, impacting the boundary layer and lower troposphere over the continent.

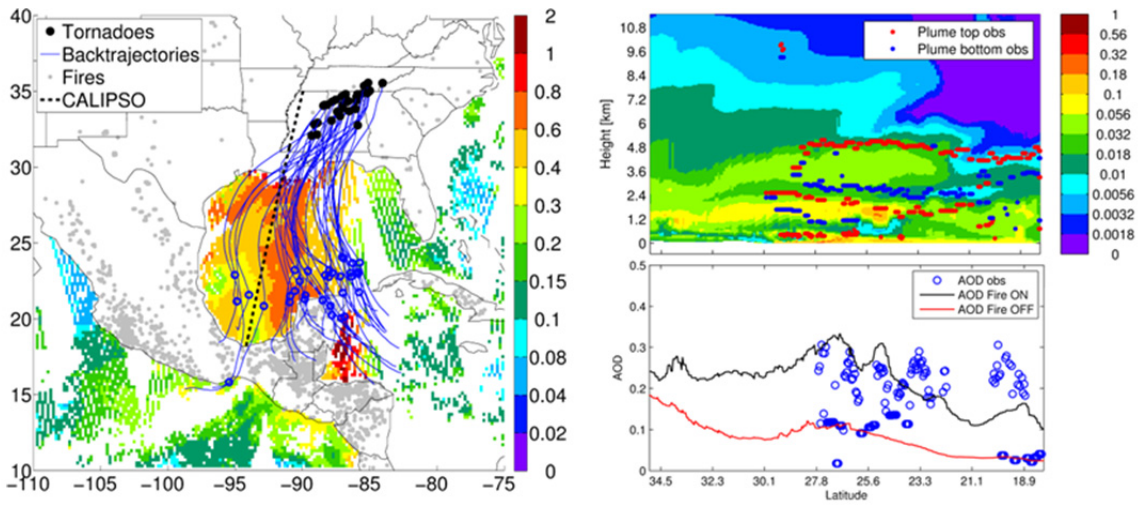

Figure 6.1. Biomass burning smoke before and during the outbreak of April 27. Left: 42 hour back trajectories from the beginning of violent tornado tracks, with circles marking 24 hours, observed AOD over ocean on 27 April, fire locations for the day before, and CALIPSO track for 26 April at 8 UTC. Right: Model extinction coefficient (1/km) profiles when including fire emissions overlaid by the smoke plumes top and bottom heights as measured by CALIOP (top), and model with and without fires and CALIOP AOD (bottom) along the CALIPSO satellite ground track. Model and observations are described in the Methods section. The area where tornadoes formed is polluted with smoke, with the model including fire emissions accurately simulating observed plume height and aerosol loads.

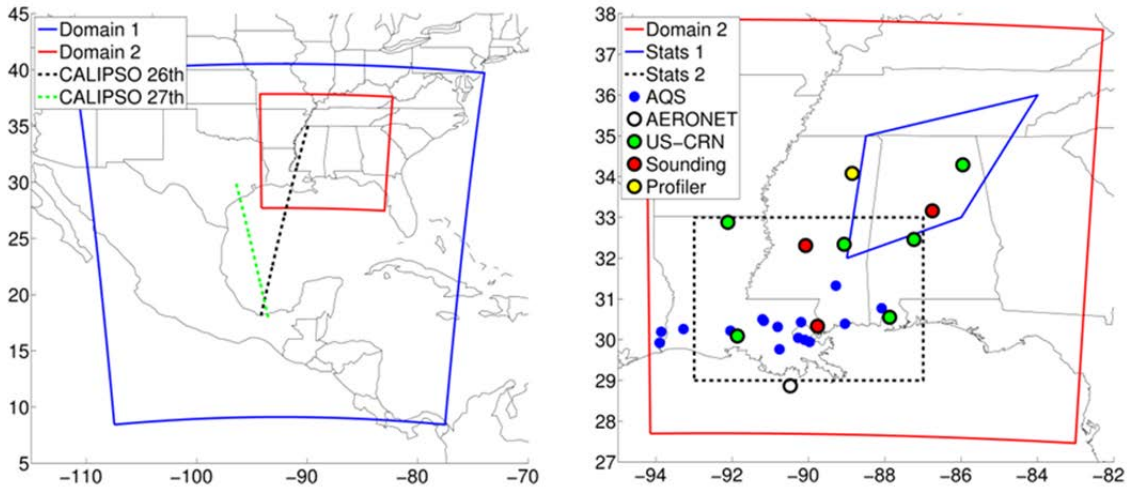

Figure 6.2. Modeling domains, analysis regions, CALIPSO tracks and observational networks. CALIPSO track overpass times are 7 UTC on 26 April and 19 UTC on 27 April. See definitions on Table 1.

On 26 April, the model containing fire emissions accurately represents all three aerosol layers vertically observed by CALIOP (Fig. 6.1), with AOD values consistent with both CALIOP and AERONET surface data (Fig. 6.3, top-right) and showing a small mean bias = 3.9 $\mu g/m^3$ with surface $PM_{2.5}$ at coastal US stations (Fig. 6.3, middle-right). On 27 April, AOD and $PM_{2.5}$ are underestimated by the model, but there is still a very clear signal of biomass burning influence as seen by the higher AOD and $PM_{2.5}$ in the model with fire emissions (Fig 6.3 left and bottom panels). For instance, on 27 April at the AERONET site, AOD from the simulation with fire emissions reaches 4.8 times the AOD without fire emissions. A closer agreement to observations could be found if MODIS AOD assimilation were performed (Saide *et al.*, 2013), but this was not included in the analysis to avoid assigning effects from total assimilated aerosol to the smoke component.

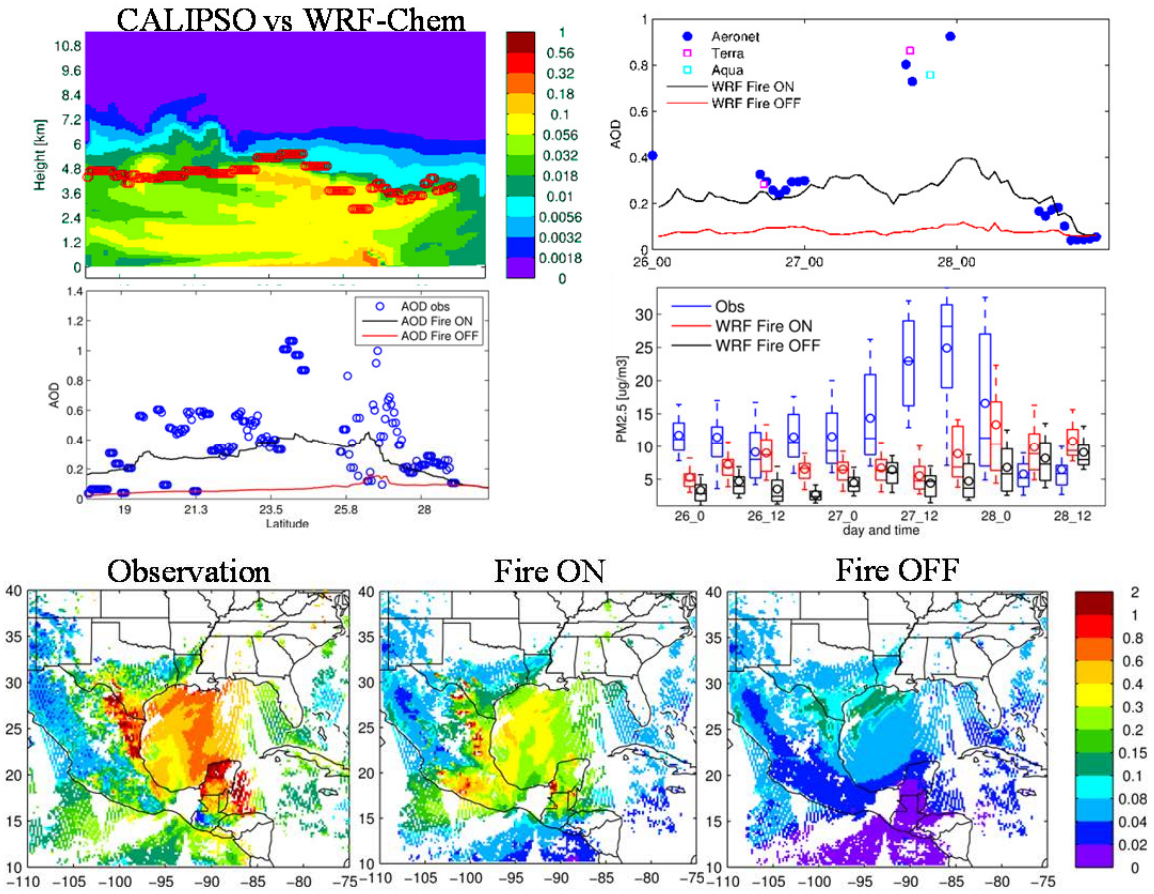

Figure 6.3. Top-Left panels: Extinction profile from the model including fire emissions overlaid by the smoke plume top height measured by CALIOP (top), and CALIPSO AOD and model estimates (bottom) for 27 April at 19 UTC. Top right panels: Time series for AOD at the WaveCIS AERONET site (top) and $PM_{2.5}$ at coastal AQS sites (bottom). Bottom panels: Average NASA NNR AOD and model estimates maps for Terra and Aqua on 27 April. See Fig. 6.2 for CALIPSO tracks and surface observation locations.

Tornado Parameters

Operational prediction centers use regional scale models to forecast the meteorological conditions (tornado parameters) that increase the likelihood of tornado occurrence and severity (Thompson *et al.*, 2003; Rasmussen and Blanchard, 1998). Simulations permitting aerosol interactions (Methods section) show that biomass burning smoke intensifies these parameters in close proximity to the tornado locations (Fig. 6.4).

In particular, the influence of smoke generates higher values of the Significant Tornado Parameter (STP) for the period of the outbreak (27 April 18 - 01 UTC mean increasing from 5.4 to 7.4). The higher STP in the simulations with fire emissions is explained mostly by the lower lifting condensation level (LCL) and the higher Storm Relative Helicity (SRH, see equation 1), as CAPE and 0-6 km shear differ by <6% and <3%, respectively, between simulations for the same period. Unlike the 0-6 km shear, the 0-1 km shear shows significant differences between simulations, with the simulation including fire emissions favoring violent tornado conditions. Wind shear in the 0-1 km layer accompanies LCL and STP as important parameters in discriminating between super-cell classes (significant-tornadic, weak-tornadic and non-tornadic) (Thompson *et al.*, 2003; Markowski *et al.*, 2003; Markowski and Richardson, 2009). Thus, the results from this case study suggest that the presence of biomass burning smoke can promote the development of conditions under which violent tornadoes, like those observed during the outbreak of April 27, are more likely to happen.

Thunderstorm invigoration

Invigoration of convection by aerosols (Andreae *et al.*, 2004) is associated with increases in precipitation (Bell *et al.*, 2008) and cloud top heights (Bell *et al.*, 2009b). We compare these two variables for simulations with and without fire emissions to investigate the possibility of convection invigoration by smoke on the April 27 outbreak. Fig 6.5 shows precipitation maps for the period of the outbreak with model values showing some skill in predictions of spatial patterns, with the tendency of underestimating accumulated precipitations rates. Both simulations miss the southern portion of the precipitation pattern (South-central Alabama, North-central Georgia), as no convective cells are generated in either simulation in this area. This region is excluded

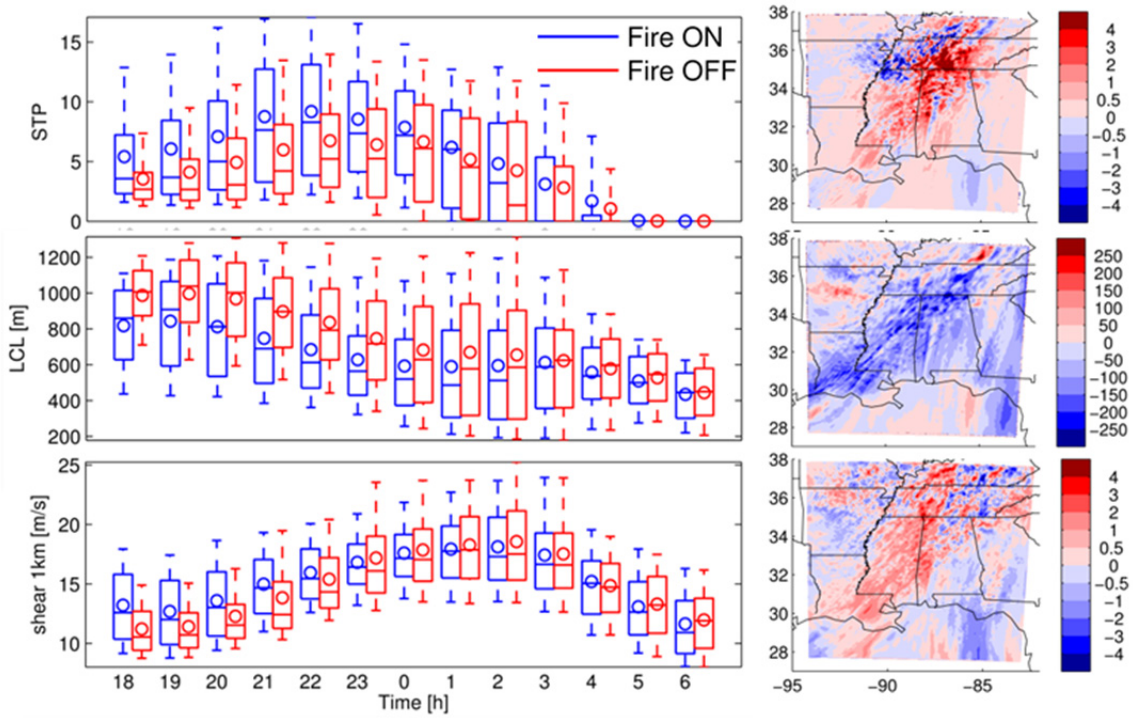

Figure 6.4. Left panels: Statistics used in tornado forecasting from WRF-Chem simulations with and without fire emissions. Statistics are computed over the outbreak area, including portions of Mississippi, Alabama, Tennessee and Georgia (see "Stats 1" in Fig 6.2). Right panels: Maps of mean differences from 18 to 01 UTC between the two simulations for the corresponding parameters on the left. Over this area and time period, most violent tornados occurred (See Fig 6.1), coincident with intensification of tornado parameters (high STP and shear, lower LCL) by smoke. Both soot absorption and aerosol indirect effects contribute to intensification.

from the "Stats 1" region of figure 6.2 where tornado parameter values were assessed. As accumulated rainfall and cloud top height statistics are also influenced by smoke (Fig 6.5), changes in the location of convective cells and precipitation patterns are found between simulations. By comparing the time series of precipitation and cloud heights for both simulations (Fig 6.5, bottom), it can be seen that, as predicted by invigoration theory, the presence of smoke delays the onset of precipitation. However, precipitation rates and cloud heights are generally higher in the simulation without smoke. We hypothesize that the system is strong enough to fully develop updrafts without smoke

particles (CAPE is usually over 1000 J/kg reaching to 3500 J/kg, see Fig. 6.6 and 6.7), and that the smoke radiative effects start playing an important role (when AOD > 0.2) in reducing convection (Rosenfeld *et al.*, 2008; Koren *et al.*, 2008), which lowers precipitation and cloud top height when smoke emissions are included. Thus we conclude that there is no model evidence that tornado occurrence or severity were enhanced by smoke invigoration of convection during this outbreak. Instead, these results point towards convection inhibition by smoke (Koren *et al.*, 2008; Rosenfeld *et al.*, 2008).

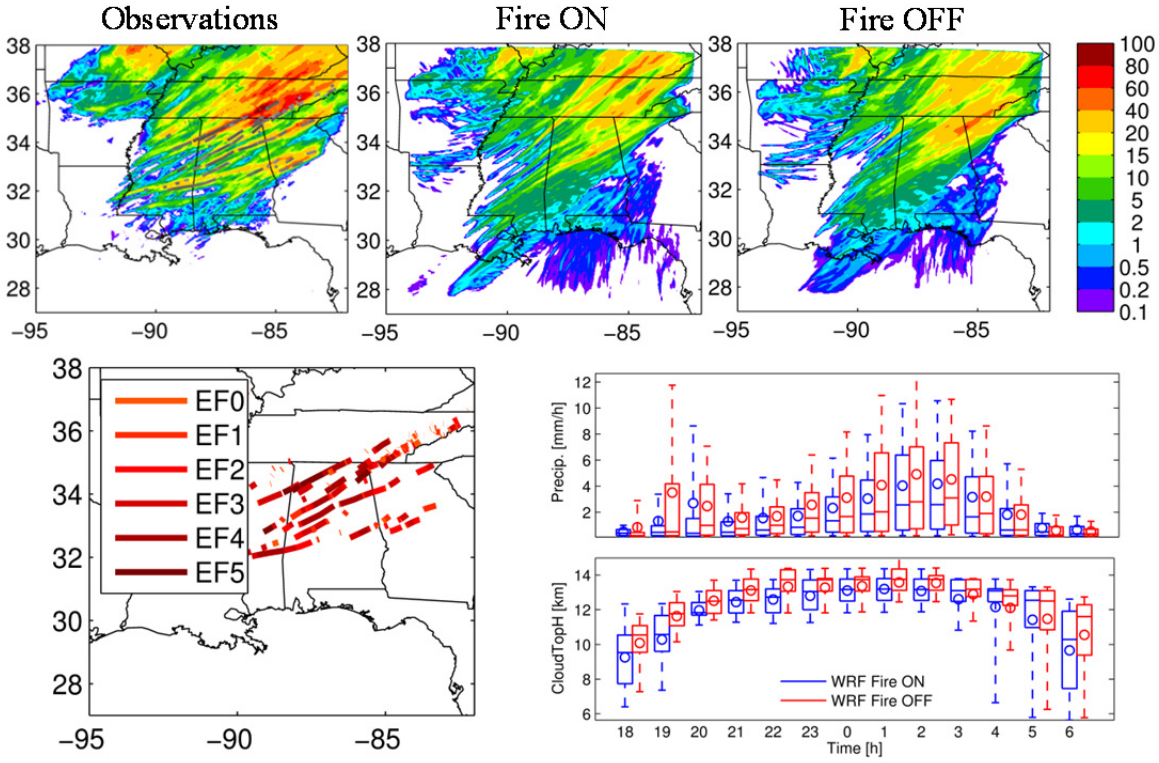

Figure 6.5. Top panels: Radar and model 12 hour accumulated precipitation (mm) valid at 6 UTC on 28 April. Bottom-left: Tornado tracks color coded by magnitude on the Enhanced Fujita (EF) Scale (84). Bottom-left panels: Model statistics for precipitation and cloud top height for the "Stats 1" area shown in Fig 6.2. Precipitation over 0.1 mm/h and cloud top heights over 5 km were considered when computing statistics.

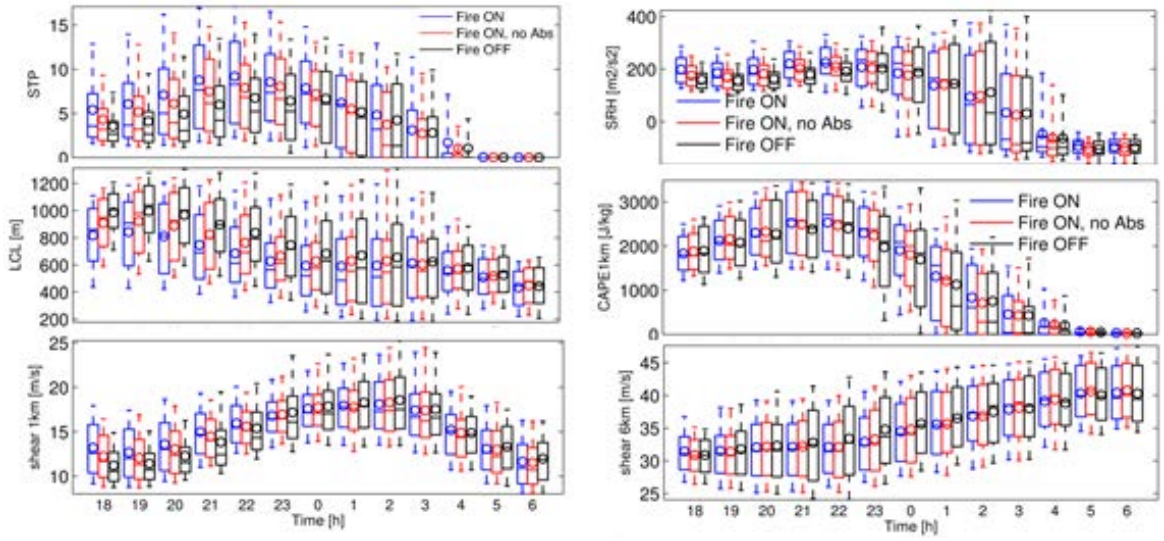

Figure 6.6. Hourly box and whisker distributions of model parameters used in tornado forecasting. The three models represent simulations with fire emissions (Fire ON), fire emissions with black carbon absorption set to 0 (Fire ON, no Abs), and no fire emissions (Fire OFF). Statistics are computed over the region "Stats 1" shown in Fig 6.2. From 18 to 01 UTC the most violent tornados occurred.

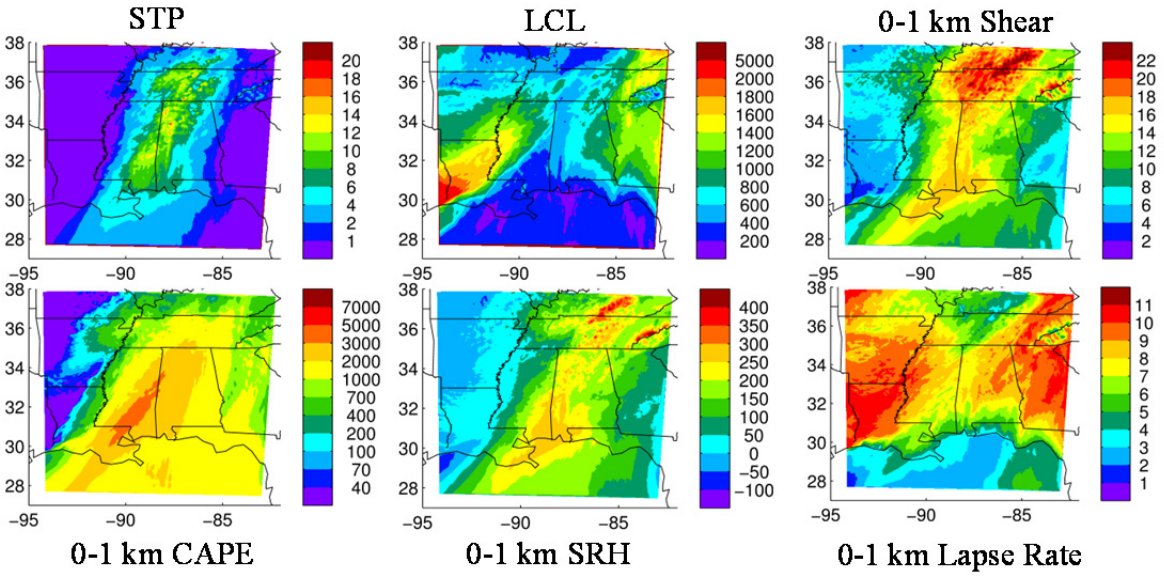

Figure 6.7. Maps of selected parameters averaged from 18 to 01 UTC for the simulation using fire emissions, which correspond to the values used when computing the differences on Fig. 6.2. Units: LCL in m, shear in m/s, CAPE in J/kg SRH in m2/s2 and Lapse Rate in C/km.

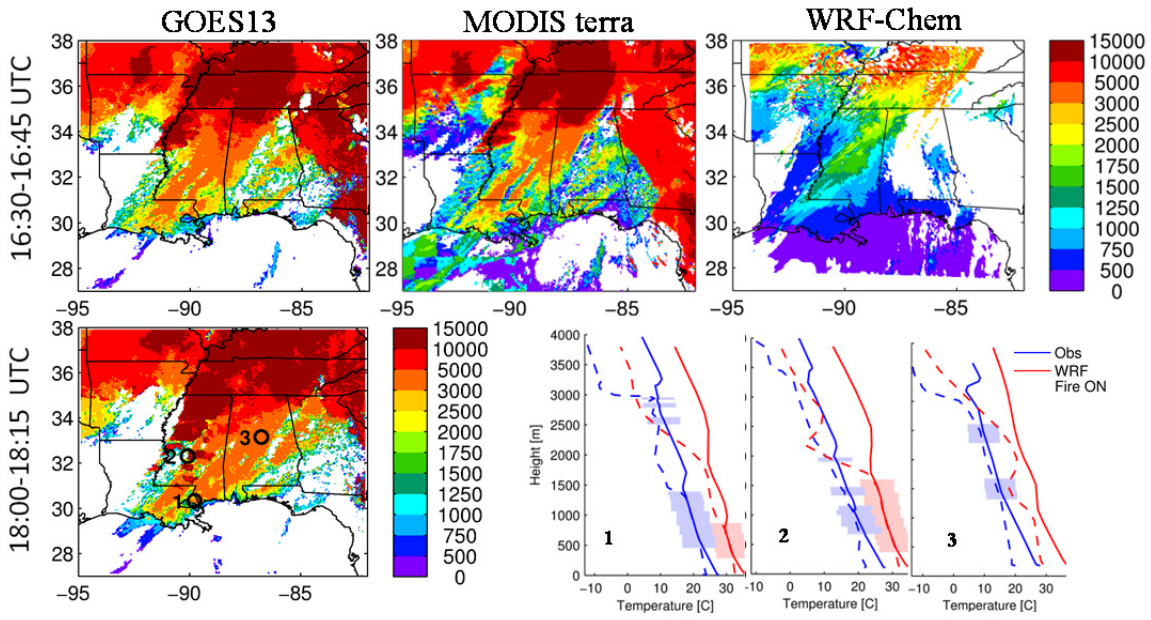

Figure 6.8. Top and bottom-left panels: Cloud top height (in m) maps for 27 April. Upper row shows GOES13, MODIS and WRF-Chem model (with fire emissions) for 16:30-16:45 UTC (Terra overpass at 16:30, GOES scan at 16:45), while the bottom panel shows GOES13 at 18:15. Bottom right panels: Temperature (T) and dew point temperature (Td) profiles for three special upper air soundings (location indicated on bottom-left map) and model (+10 C) at 18 UTC. Blue shading shows T and Td difference of less than 1.5 ºC, which represents overcast or broken cloud conditions, while red shading represents model cloud occurrence.

Shallow clouds before the outbreak

At the beginning of the outbreak (18 UTC), shallow multi-layer stratiform clouds (top heights < 3km) were observed across the region, which persisted throughout the day and followed the free troposphere flow. Fig. 6.8 shows satellite, in situ soundings and modeled cloud heights. GOES and MODIS have been found to overestimate low-level cloud height (Naud *et al.*, 2005), which is evident when comparing these values with soundings at three different locations (lower left graph of Fig. 6.8) that show cloud heights below 3km. Regardless of this positive bias, the model seems to represent fairly well the coverage and structure of shallow clouds. Even when the three modeled soundings do not show the multi-layer structure seen in the observations, the close

proximity of the temperature and dew point at two different heights (soundings 1 and 3) suggest that this structure is present in the model in nearby grid-cells. On the other hand, modeled cloud heights are found to be biased low (from ~0 to 1 km, Fig. 6.8). The model does not fully resolve the eastern side of the cloud system (over Alabama at 16:45 UTC) where broken clouds are found (Fig. 6.9, top panels). However, temperature and dew point differences in both the model and observations are small in this area (location #3 in Fig 6.8) showing that the model was close to generating local clouds.

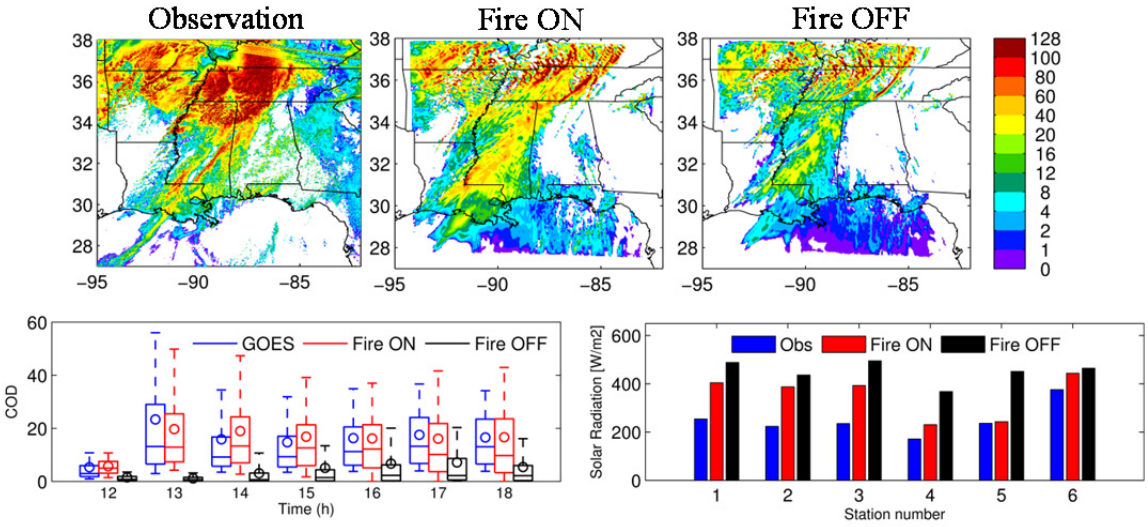

Figure 6.9. Top panels: Cloud optical depth (COD) for MODIS Terra at 16:30 UTC on 27 April (left) and simulation estimates with (middle) and without (right) fire emissions. Bottom-left: COD for GOES13 and models over the region "Stats 2" (Fig. 6.2) for a period before the outbreak. Bottom-right: Observed and modeled solar radiation between 10 and 2 UTC (local day time). Station numbers for locations indicated in Fig. 6.10.

Interactions between shallow clouds and smoke

In the absence of convection invigoration in the simulations (see "Thunderstorm invigoration" sub-section), mesoscale meteorological analysis was used to identify the driving mechanisms for tornado parameters intensification. As mentioned in the previous

subsection, clouds were present before the outbreak, which interacted with the smoke as follows. The presence of smoke increased the cloud condensation nuclei (CCN) concentration, which increased the number of cloud droplets, decreased drizzle rates and increased liquid water content through the first and second aerosol indirect effects (Twomey, 1991; Albrecht, 1989). As a result, stratiform clouds ahead of the front became optically thicker, which reduced the amount of solar radiation reaching the ground, suppressing heat fluxes from the surface, and producing more stable boundary layer conditions that reduce mixing close to the surface and generate lower LCL and higher low-level shear (Fig. 6.10). Along with increased stability, the thicker cloud layer lowers the cloud base. The smoke impacts are significant because if there were no fires, the air mass from the Gulf would have been much cleaner (see Fig. 6.3). These clouds were observed throughout the day, with GOES COD retrievals showing their persistence until the point of the outbreak both in observations and model (Fig 6.8). The shallow clouds generate a regional reduction in solar radiation reaching the ground, whose intensity is captured with excellent agreement at some stations (bias of 60 and 6.3 W/m^2 on Newton, MS [#4] and Lafayette, LA [#5] stations, respectively) only by the simulations with fire emissions (Fig. 6.10 top-right and Fig. 6.9 bottom-left). Even though clouds missing in the simulations generate overestimates of solar radiation at the eastern stations (Fairhope [#1], Gadsden [#2] and Selma [#3] stations on Alabama), the simulation with fire emissions still shows better agreement with observations (between 50 – 100 W/m^2 less bias, Fig 6.9 bottom-left). Low-level shear is also better represented when smoke is included in the simulations, with 9.8 m/s shear observed in the 0.5-1.5 km layer as compared to 8.0 and 4.1 m/s simulated with and without smoke, respectively. Thus, shallow cloud properties and atmospheric conditions are consistent with the presence and impacts of smoke.

Black carbon semi-direct effects

Soot (black carbon), responsible for 5-10% of the biomass burning smoke mass emitted, was found to play an important role in cloud dynamics. Sensitivity simulations with no soot absorption showed that it contributes 47-55% to enhancements in tornado parameters STP, LCL and shear (Fig. 6.6). In addition to cloud thickening by indirect radiative effects, soot heated the aerosol layer stabilizing the atmosphere ahead of the front (Ackerman *et al.*, 2000), thus reducing entrainment of dry air, keeping a moister boundary layer and enhancing cloud cover below the aerosol layer (Brioude *et al.*, 2009; Wilcox, 2010). These conditions produced a more stable boundary layer, lower cloud base and higher low level shear, which led to higher probability of violent tornadoes. Under the conditions of the outbreak, the impact was strong, as soot absorption above and between clouds is enhanced by the presence of multiple layers of optically thick clouds, which reflect light back to the soot layer more efficiently, producing more absorption (Haywood and Ramaswamy, 1998; Chung and Seinfeld, 2005).

As seen in Fig. 6.11, black carbon over the region feeding the outbreak is found predominantly above clouds. Previous research has found that absorption of radiation by elevated plumes of black carbon stabilizes the atmosphere below and can generate changes in clouds, with enhancements over oceanic stratocumulus and reductions over land as a general rule (Koch and Del Genio, 2010). In the case studied here we find an enhancement of continental shallow clouds (previous sub-section) and a slight suppression of convection ("Thunderstorm invigoration" sub-section) due to black carbon absorption, which is consistent with previous research as explained in the following. Shallow clouds in this study behave as oceanic stratocumulus, enhanced by a more marked inversion generated by stabilization, and not restricted by moisture, which is transported from the Gulf. Also, AOD is high enough (generally over 0.2) to produce convection inhibition rather than invigoration (Koren *et al.*, 2008). A more detailed analysis on how smoke affects vertical profiles can be found in the next sub-section.

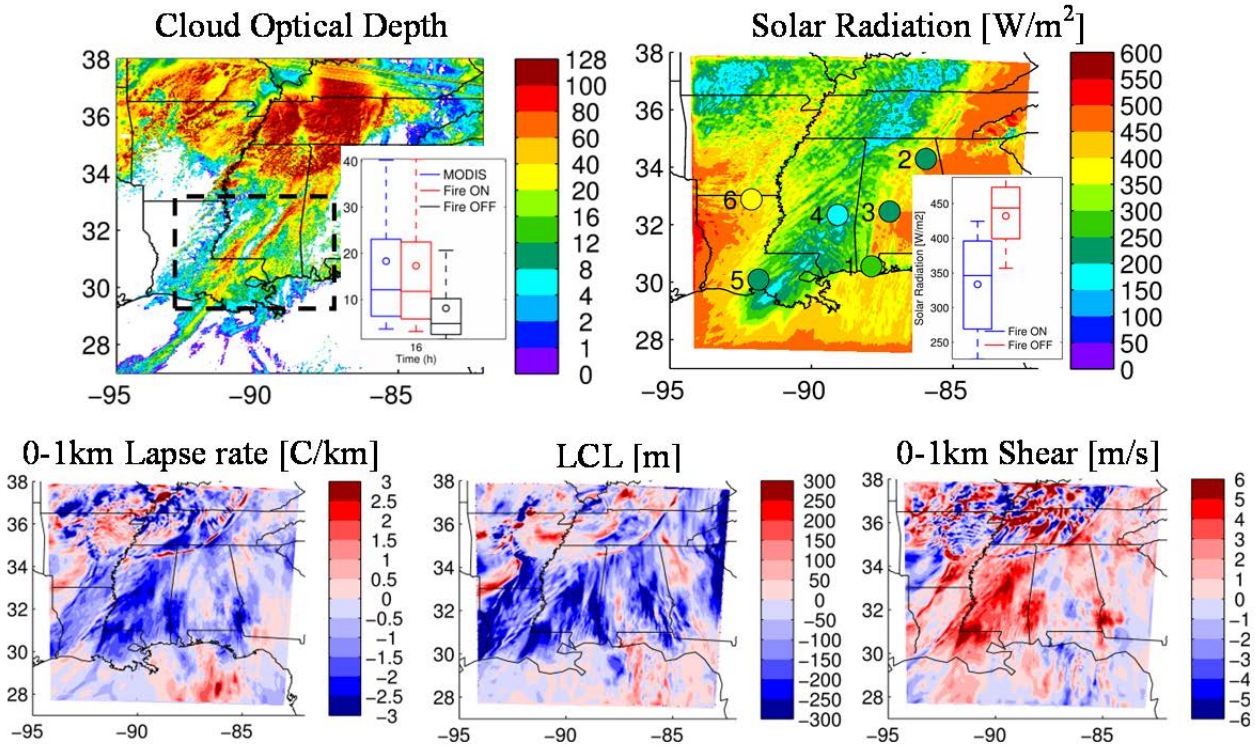

Figure 6.10. Top left panel: MODIS cloud optical depth (COD) from Terra overpass at 16:30 UTC on 27 April (~3 hours before the outbreak starts), with an insert showing observed and modeled statistics over the segmented line rectangle. Top right: Average Solar radiation for the model with fire emissions with color-coded circles showing US-CRN average observations for 27 April local daytime, with an insert showing model statistics over the same box as in COD. Bottom panels: Difference between model variables for the fire ON and fire OFF simulations at 16 UTC. The optically thicker shallow clouds lead to less solar radiation reaching the surface, which together with black carbon absorption generate a more stable boundary layer (lower lapse rate) that intensifies conditions prone to tornado generation and strengthening (lower LCL, higher 0-1 km Shear).

Smoke effects on vertical profiles

As seen in Fig. 6.11, the simulation including fire emissions shows slower wind speed at the surface, and higher wind speed above, resulting in higher shear in the 0-1 km layer. The higher shear is due to the differences in temperature, with the simulation including fires showing lower surface temperatures, and thus presenting more stable

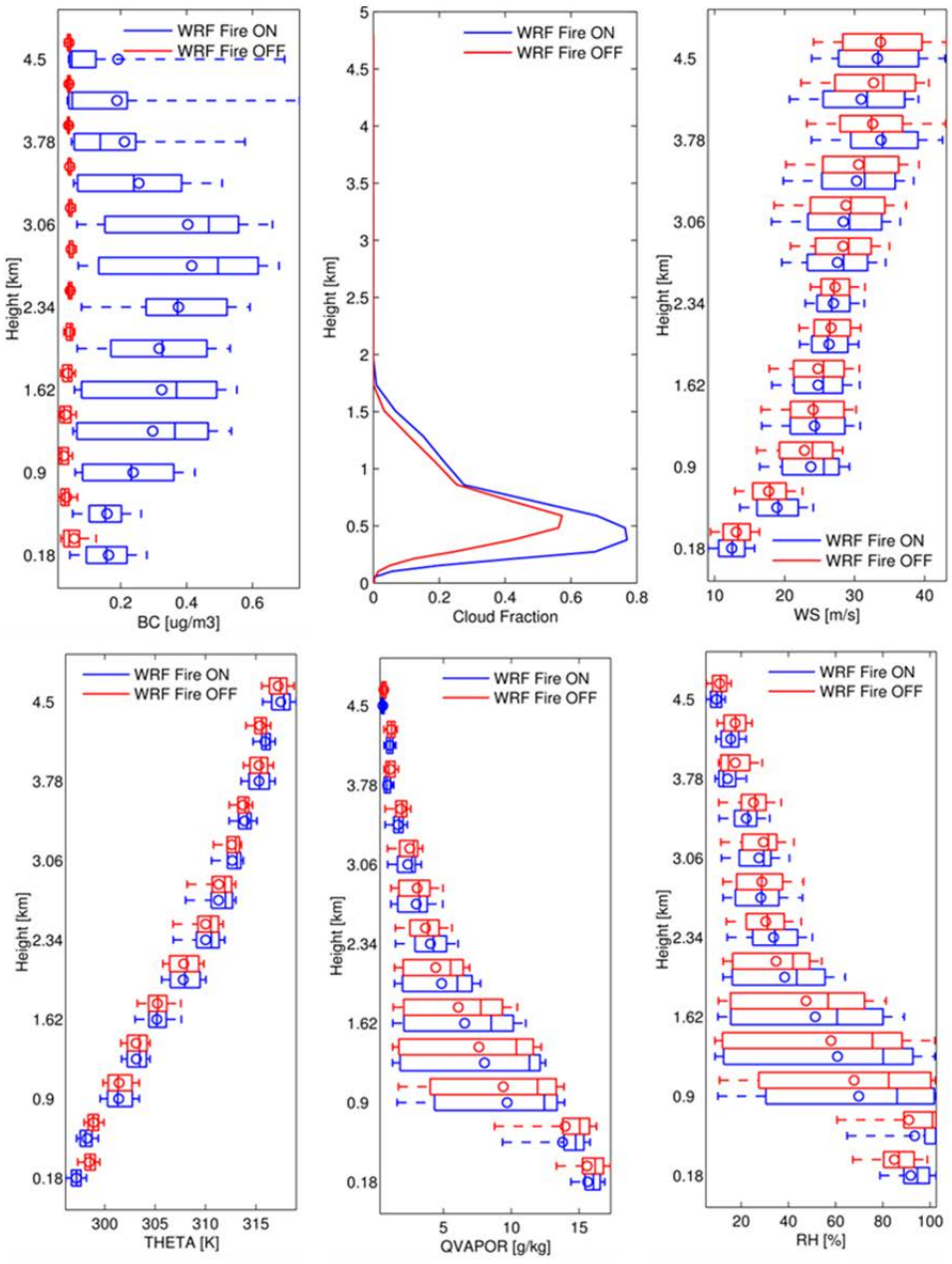

Figure 6.11. Statistics for vertical profiles at 16 UTC over the region "Stats 2" (Fig. 6.2) for simulations with and without fire emissions. Box and whisker plots are shown for soot (BC), wind speed (WS), potential temperature (THETA), water vapor (QVAPOR) and relative humidity (RH), while solid lines show mean cloud fraction.

conditions that reduce mixing and lead to sharper vertical gradients. The colder surface temperatures are due to the reduced radiation reaching the ground below optically thicker clouds and subsequent reduction in surface heat fluxes (sub-section "Interactions between shallow clouds and smoke"). Also, potential temperature in the free troposphere (above 3 km) tends to be higher when smoke is included due to black carbon absorption (previous sub-section). Water vapor is modified by two processes that happen simultaneously due to the presence of smoke. First, surface heat fluxes are reduced, less evaporation occurs, reducing water vapor near the surface (Feingold *et al.*, 2005). Second, the smoke stabilization reduces entrainment of dry air, maintaining moisture in the mixed layer and increasing water vapor near the top of the mixed layer (Brioude *et al.*, 2009; Wilcox, 2010). Overall, there is general decrease of relative humidity in the mixed layer when smoke is present, due to the moisture accumulation and the lower temperatures at the surface, which surpasses the effect of lower surface water vapor. The higher relative humidity and more stable conditions under the presence of smoke produce lower cloud base and LCL. We hypothesize the strong upper-level forcing associated with this event was able to overcome the increased low-level stability caused by the smoke and thus updrafts were not completely suppressed, as plenty of convection occurred for the simulations containing smoke (see "Thunderstorm invigoration" sub-section), and the important feature was that the increase in stability was also accompanied by a notable increase in the low-level shear and decrease in cloud base height, which are more closely associated with tornado occurrence and severity (Thompson *et al.*, 2003; Markowski *et al.*, 2003; Markowski *et al.*, 2002). This hypothesis needs to be explored in future studies.

Conclusions

This study shows that, for the case considered, the likelihood of significant tornado occurrence can increase when smoke is present and this is due to stabilization by soot and an increase in optical thickness in lower tropospheric clouds, and not due to

convection invigoration. Increased stability due to the presence of smoke (both by radiation absorption and cloud optical thickening) is likely the reason for the slight decrease in modeled convective vigor (lower cloud heights and rain rates). This stabilization occurs mostly ahead of the frontal boundary (Fig. 6.10) and leads to a lower cloud base within the region of tornado development, which is associated with higher buoyancy in the rear-flank downdraft, more likely tornadogenesis and increases in tornado intensity and longevity (Markowski *et al.*, 2002). Furthermore, increased stability produces the higher lower level shear which together with LCL offers the most promise to date in discriminating between non-tornadic and tornadic supercells (Markowski and Richardson, 2009).

Continental shallow cloud optical depths also increase in the presence of anthropogenic aerosol (Berg *et al.*, 2011; Rosenfeld, 2000). This process may contribute an additional pathway modulating the observed weekday/weekend differences in tornado occurrence that has been hypothesized to result from invigoration (Rosenfeld and Bell, 2011). Furthermore, the stronger low-level shear due to the combination of aerosol absorption and indirect radiative effects likely impact other mesoscale phenomena, including thunderstorms and derechos, and monsoonal shear dynamics. Also, the mechanism identified here shows that while aerosol warming at the synoptic scale may intensify tropical cyclones by reducing shear (Evan *et al.*, 2011), aerosols can increase severe weather by increasing low-level shear and decreasing cloud heights ahead of strong frontal systems.

The NWS vision for 2020 is to move towards a "warn-on-forecast" paradigm for hazardous convective weather (Stensrud *et al.*, 2009). A warn-on-forecast system would rely on high resolution ensemble predictions, using convection-resolving models with explicit microphysics and radar data assimilation to provide probabilistic convective scale analyses and forecasts. Our findings, along with recent studies of tropical cyclones (Dunstone *et al.*, 2013; Rosenfeld *et al.*, 2011b), show that aerosol can play an important

role in modifying severe weather conditions. Their inclusion will likely help improve the predictability of these extreme events, which can improve the timeliness and accuracy of severe weather alerts within future operational forecast systems.

Collaborators and funding sources

We thank Robert Rabin and Jack Kain for comments that helped improve the study. We also thank Bill Gibson, Alan Weidemann and their staff for establishing and maintaining the WaveCIS AERONET site used in this investigation. CALIPSO and MODIS data were obtained from the NASA Langley Research Center Atmospheric Science Data Center. This work was carried out with the aid of NASA grants NNX08AL05G and NNX11AI52G, EPA grant 83503701**,** grant number UL1RR024979 from the National Center for Research Resources (NCRR), a part of the National Institutes of Health (NIH), and Fulbright-CONICYT scholarship number 15093810. The views, opinions, and findings contained in this report are those of the author(s) and should not be construed as an official National Oceanic and Atmospheric Administration, U.S. Government and other funding institutions position, policy, or decision.

Author contributions

This work is currently under review for publication. P. Saide, G.Carmichael, S. Spak, R.B. Pierce (NOAA) and J. Otkin (U. of Wisconsin, Madison) designed the study. P. Saide executed the study with permanent guidance from G.Carmichael, S. Spak, R.B. Pierce and J. Otkin. K. Schaack (U. of Wisconsin, Madison) provided scripts for mapping boundary conditions. A. Heidinger provided GOES13 satellite retrievals. . A. da Silva (NASA GMAO) provided fire emissions and observed AOD. M. Kacenelenbogen and J. Redemann (NASA AMES) provided scripts for using CALIPSO data. All authors contributed to the final form of the manuscript.

CHAPTER 7 CHEMICAL WEATHER FORECASTS FOR FLIGHT PLANNING AND NEAR-REAL TIME ANALYSIS DURING THE SEAC4RS FIELD CAMPAIGN

Abstract

An operational forecasting system was designed, implemented and executed for The Studies of Emissions and Atmospheric Composition, Clouds and Climate Coupling by Regional Surveys (SEAC4RS) field campaign during August-September 2013. The system was based on WRF-Chem using full-chemistry and tracer forecasts and included the AOD data assimilation component developed in Chapter 5. The system was used successfully during the experiment to provide guidance for flight planning and near real time analysis. A preliminary evaluation using routine observations and measurements aboard the aircrafts deployed for the experiment showed the capabilities of the system to accurately predict aerosols from anthropogenic activities, biomass burning smoke and long-range transport dust events. The limitations of the system are highlighted and potential solutions are provided for improvement and future use in other field deployments. Overall, this study provides demonstration and feasibility of operational use of online fully coupled models.

Introduction

The Studies of Emissions and Atmospheric Composition, Clouds and Climate Coupling by Regional Surveys (SEAC4RS) was a field campaign which targeted a variety of science objectives such as understanding the role of deep convection in redistribution and evolution of pollutants, exploring aerosol-clouds-radiation interactions, studying properties and impacts of biomass burning, and acquiring data for satellite calibration/validation. The deployment was based in Ellington field airport (EFD, in Texas nearby Houston) during August and September 2013, from where 3 planes equipped with instruments were flown: The NASA DC-8, NASA ER-2 and the Learjet

(Fig 7.1). While the DC-8 objective was to sample from the boundary layer to the upper troposphere up to ~40k feet with a wide instrumental suite and over long distances (~8 hour flights), the Learjet sampled similar heights but for a shorter spatial coverage (~2 hour flights) and with in-situ aerosol-cloud targeted instruments, and the ER-2 sampled at 60k feet diving occasionally down to 45k feet for a similar spatial range as the DC-8.

Figure 7.1. The three aircrafts used for collecting dta during SEAC4RS field campaign

Due to the variety for objectives pursued by the campaign, a decision had to be made in advance to decide the location the planes were going to fly and what objectives were going to be addressed for each flight. In this sense, meteorological and atmospheric chemistry forecasting tools played an important role to give the science leaders and flight planners guidance on the conditions that might be encountered in the following days.

On the chemical forecasts side, daily briefings were prepared the day before and two days before the flights. Three groups from three institutions were in charge of the briefings preparation: National Center for Atmospheric Research (NCAR) Earth System Laboratory (NESL), NASA Global Modeling and Assimilation Office (GMAO) and The University of Iowa (UIOWA) Center for Regional and Environmental Research (CGRER). Several modeling tools from these and other groups were incorporated into the briefings, going from global predictions of aerosols (GMAO GEOS-5, Naval Research Laboratory NAAPS) and chemistry (NCAR MOZART), through full chemistry (UIOWA

WRF-Chem) and tracer (NCAR WRF-Chem) regional forecasts, up to trajectory models (FLEXPART, NCAR) analysis.

In order to provide the degree of confidence expected from the models, near real time evaluation of the forecasts was performed. This consisted in comparing the models to available observations from ground sites, satellite retrievals. Also, as they became available, data measured during the campaign was incorporated into the analysis.

In this chapter, we focus in the UIOWA forecasts description and its role on providing guidance for flight planning. Also, near real time analysis activities are shown. Even though the UIOWA model provided weather, gases and aerosol forecasts, in the following we present the aerosol component as this is the main topic of this thesis. Finally, we provide conclusions and future directions.

Methods

The UIOWA modeling system

The base of the UIOWA forecasts is the WRF-Chem online chemistry-aerosol transport model version 3.5 (Skamarock *et al.*, 2008; Grell *et al.*, 2005). The model configuration has some differences with what has been described in previous chapter to accommodate its operational use and the domain of study. WRF-Chem was configures as a single 12km horizontal grid spacing domain, which covered the Continental US (CONUS), southern Canada and north and central Mexico (Fig. 7.2). The domain was chosen to cover regions that were reachable by the aircrafts and where important processes related to the campaign objectives were happening: The domain extends over the pacific to capture stratocumulus clouds where and be able to predict smoke over them; it extends down to Mexico to capture inflow into the North American Monsoon (NAM) and Mexican pollution influence into the Gulf of Mexico; it extends to southern Canada to include Canadian biomass burning and outflow from NW US fires; and it covers the Gulf of Mexico for studies of convection and hurricanes. The 12 km resolution

was chosen as a compromise of high resolution for the large area covered and computational expenses. The vertical resolution was chosen the same as in Chapter 6. Most model parameterizations were chosen the same as in Chapter 6, with the exception of the following: The CBMZ-MOSAIC (Zaveri and Peters, 1999; Zaveri *et al.*, 2008) chemistry and aerosol models were chosen, but for a 4 sectional size bins (instead of 8); the Grell-3 parameterization (Grell and Freitas, 2013) was used for convection, convective transport, and convective wet scavenging; and resolved wet scavenging, cloud chemistry and aerosol activation was turned off. These changes allowed reducing the number of aerosol species by a factor of 4, as the configuration used in previous studies was not feasible for operational forecasts under the computational resources available.

Anthropogenic emissions were obtained from three sources. Emissions from US and Canada were obtained from NEI 2005 (http://www.epa.gov/ttnchie1/net/2005inventory.html). The Mexican emissions used are described in Mena-Carrasco *et al.* (2009) but were scaled using emission growth factors (Wolf *et al.*, 2009) from 1999 to 2012. Finally, emissions from other countries in the Caribbean and from shipping sources were computed using PREP-CHEM-SRC (Freitas *et al.*, 2011). Biomass burning emissions were obtained from two sources. From August 1st to August 13th forecasts, FINN emissions (Wiedinmyer *et al.*, 2011) were used. It was found that AOD from fires was being underestimated, while the GEOS-5 forecast were closer to the observations. Thus, Quick Fire Emission Dataset (QFED) v2.0 emissions (Darmenov and da Silva, 2013), which is the emission model used by GEOS-5, was used from August 14th forecasts until the end of the campaign. Fire emissions were downloaded daily and assumed to persist for the length of the forecast. Injection heights were computed online with the plume rise model (Grell *et al.*, 2011). Natural emissions were included through online models incorporated to WRF-Chem: MEGAN biogenic (Guenther *et al.*, 2012), Gong *et al.* (1997) sea salt and GOCART dust (Zhao *et al.*, 2010) emissions.

WRF-Chem can be configured to do simulations of full chemistry and inert tracers at the same time. This option was used to track Carbon Monoxide (CO) from US/Canadian anthropogenic emissions, Mexican anthropogenic emissions and biomass burning emissions. This was used as an efficient tool to understand the relative contribution of each source.

Meteorological initial and boundary conditions for each daily forecast were obtained from the Global Forecast System (GFS, Environmental Modeling Center, 2003), while chemical boundary conditions were obtained from MACC forecasts (Inness *et al.*, 2013; Morcrette *et al.*, 2009). Instead of initializing chemical species from MACC every day, we initialized from the previous WRF-Chem forecast.

Another important component of the UIOWA forecast was the use of satellite AOD assimilation. We used the tool developed in Chapter 5 (Saide *et al.*, 2013), assimilating the NRL-UND (Zhang *et al.*, 2008; Hyer *et al.*, 2011) retrievals. Even though this retrieval produces a lesser amount of MODIS pixels to assimilate compared to the NASA NNR retrieval (see Chapter 5), the latter was not available on time for the system to use it, while the NRL-UND code was incorporated into the system making these files available.

The system was automatically executed once daily in the following way. All the downloading and pre-processing of fire emissions and initial and boundary conditions was done in a first stage. Then, WRF-Chem simulations started at 12 UTC valid time for 3 hours. At this point (15 UTC), the latest AOD satellite data was downloaded and an assimilation step using GSI was performed. Then, a WRF-Chem restart was done and another 3 hour forecast + assimilation step were performed the same way for 18 and 21 UTC. Finally, at 21 UTC, a 78 hour forecast was performed, which added to the previous 3 hour forecasts, adds up to a 87 hour forecast starting from 12 UTC. The system was launched every day at 11:30am local time, and finished the next day around 9am, which sufficient for the planning activities one and two days before a flight.

Finally, a web interface was used to show the daily forecasts results. The NCAR Command Language (NCL, http://www.ncl.ucar.edu/) was used to produce plots, which were incorporated in a simple but efficient webpage hosted in CGRER (Fig. 7.2 and 7.3). Results were plotted for each daily forecast in the way of maps and cross-sections. Three domains and five cross-sections were plotted to cover different campaign objectives. As seen in Fig. 7.2, variables plotted were divided in 3: full chemistry, tracers and meteorology. The variables plotted corresponds to a summary of all the possible outputs WRF-Chem can provide, and were selected prior the mission using science leaders guidance. Each variable was plotted every 6 hours for the length of the forecast and for 9 pressure levels. The domains and pressure levels were agreed between the groups doing chemical forecast so all would chose the same levels and domains, to improve the ability to compare results. Another webpage was implemented to show five cross-sections, which were selected to cover ground on potential targets (Fig. 7.2 and 7.3). Besides showing each time-step, the website had the ability to show a movie by selecting different values on the start and end time steps, which allows the forecaster to better understand the transport pathways of pollution. The Mission Tools Suite (MTS, http://mts.nasa.gov/) is a system maintained by NASA Airborne Science Program, which consists in a collections of tools for aiding flight planning and operations. One of its components it's a Google Earth display where layers can be added so different geographical information can be displayed simultaneously. The UIOWA map products we incorporated into the MTS display, so the forecast products could be used for planning overlaying the planned flight tracks (see examples in the Results section), and during operations, to provide guidance or perform model validation.

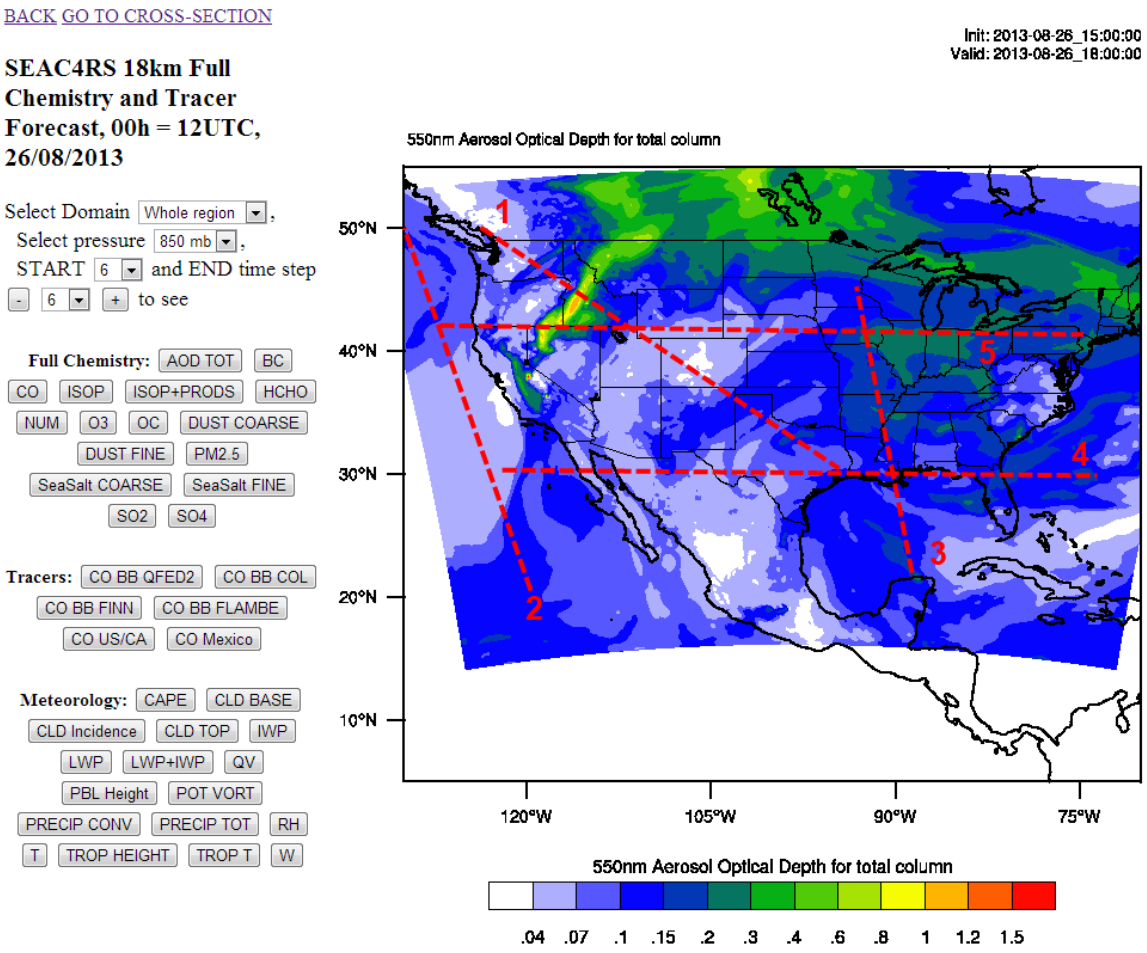

Figure 7.2. Web interface for presenting the horizontal map plots for the UIOWA model. This sample shows AOD for the whole region. Two other domains were available: the SE US region and the western US. The red segmented lines are not shown in the webpage and were added to mark the cross-sections plotted (see fig 3). This specific forecast can be access at http://bio.cgrer.uiowa.edu/SEAC4RS/wrf_fullchem_2013-08-26/pmenu.html

Besides the daily products shown in the webpage, curtain plots for a selection of variables were generated when flight plans were generated. Two days before a flight, by the end of the day, a preliminary flight plan was available, so for the chemical forecast briefing the day before a flight the curtains were presented (Fig. 7.4). Also, the curtains were updated for the new plans done that day and presented on the science meeting, which was usually held 2pm the day before a flight. Finally, the curtains were updated

with the latest forecast the day of the flight as requested by scientists going into the aircrafts to see model performance.

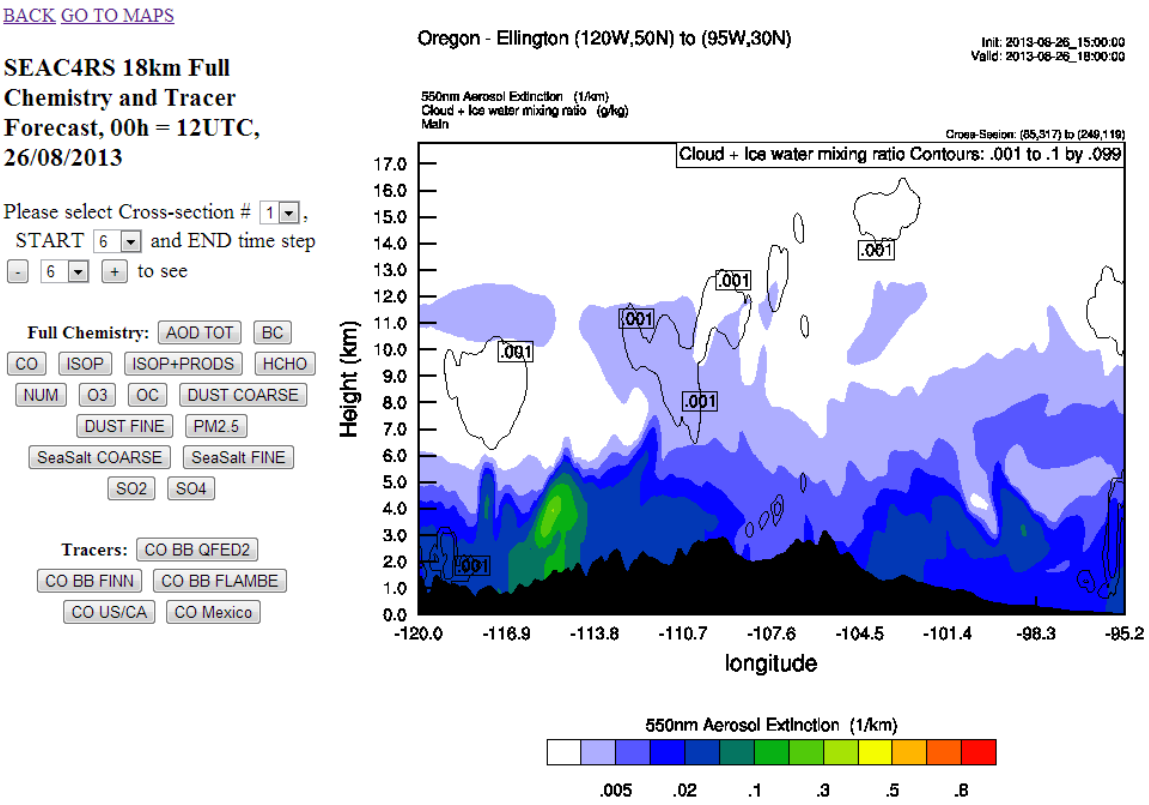

Figure 7.3. Web interface for presenting the cross-sections for the UIOWA model. Five standard cross-sections were plotted, as indicated in Fig. 7.2. The sample plot shows cross-section #1. This particular forecast can be access at http://bio.cgrer.uiowa.edu/SEAC4RS/wrf_fullchem_2013-08-26/pmenu_crossection.html

Observations

Observations incorporated into the near-real time analysis corresponds to data obtained regularly from satellite and ground based stations and also data collected during the campaign. On the satellite side, not yet assimilated MODIS AOD (Remer *et al.*, 2005) from Terra and Aqua satellite was the main product used, while the AERONET network (Holben *et al.*, 2001) was used as the ground based component. Observations collected

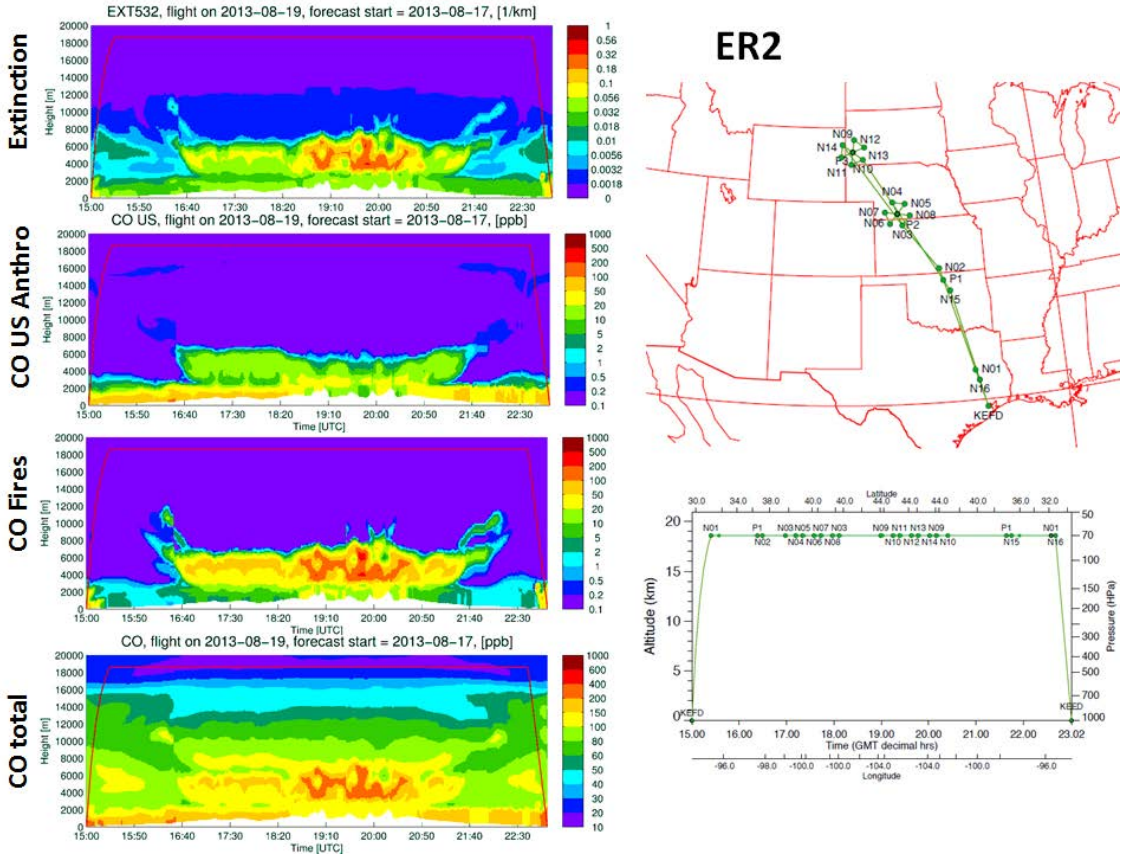

Figure 7.4. Example of a chemical forecast briefing slide for Aug 18th with the curtains for the preliminary ER-2 flight track for the flight on Aug. 19th. The flight was targeting smoke coming from NW US, which the UIOWA model was showing that it was going to encounter for most of the flight.

during the science flights correspond mainly to instruments in the DC8 aircraft are described in the following. Aerosol backscattering and extinction at 532nm was measured by the Airborne Differential Absorption Lidar -High Spectral Resolution Lidar (DIAL-HSRL) (Hair *et al.*, 2008). This data was vertically resolved and above and below the aircraft, giving information about where the different aerosol layers were located and their optical properties. Above the aircraft AOD in multiple wavelengths was measured by the Spectrometer for Sky-Scanning Sun-Tracking Atmospheric Research (4STAR) (Dunagan *et al.*, 2013), where 532nm AOD and 452-606nm Angstrom exponent were

used. In-situ measurements used for preliminary evaluation include organic carbon from a high resolution time-of-flight aerosol mass spectrometer (HR-ToF-AMS, Aerodyne Research Inc., hereinafter AMS for short; DeCarlo *et al.*, 2006) and coarse aerosol properties from NASA Langley Aerosol Research Group (LARGE) Aerodynamic Particle Sizer (APS, model TSI-3321)

Results and Discussion

Due to the different campaign objectives, the following analysis is divided by flights showing the guidance provided by the UIOWA model and forecast performance against observations.

August 6th flights

The flights on August 6th were the first science flights, were the DC-8 and ER-2 flew together. By this time the aircfrafts had not transited from Palmdale to Ellington field (EFD) yet as the instruments were assembled and tested on Palmdale, and there were mission objectives that were easier to reach from California. One of these objectives was to find biomass burning smoke over stratocumulus clouds. Large fires had been occurring on SW Oregon and the model had been predicted fires to advect over the pacific (Fig. 7.5), where a thick stratocumulus deck was also being forecasted (not shown). The model forecasts were used to place the location of the flight track putting it over the thicker smoke predicted. As seen in figure 7.5, the flight was able to measure smoke over thick clouds, confirming the model forecasts and achieving this mission objectives that was thought as one of the most difficult to achieve due to the combination of factors required achieve it. Even though the model predicted the location of the some plume accurately, it underestimated aerosol concentrations (Fig. 7.6). As pointed out in the Methods section, for the first period of the campaign the FINN fire emission were used, and comparison to data in this flight was the first evidence that FINN was underestimating aerosol emissions.

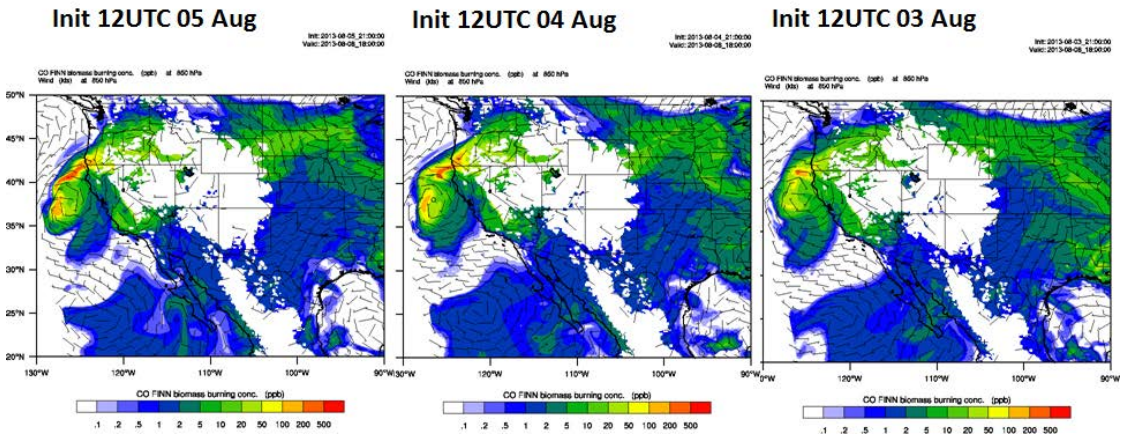

Figure 7.5. Biomass burning CO tracer at 850mb showing smoke over stratocumulus for the forecast two days before, one day before, and the same day of the 1st science flight (August 6th).

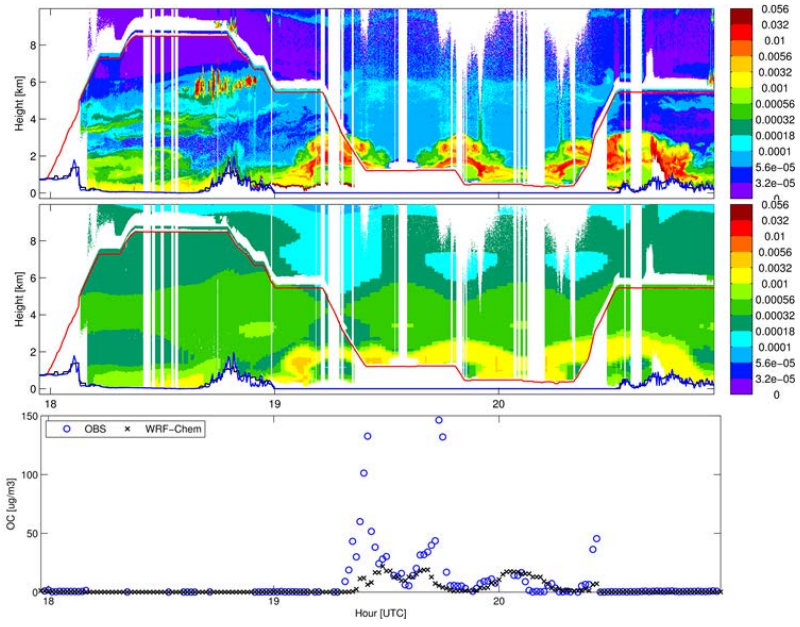

Figure 7.6. Model and observations for August 6th flight. Top and middle panels: DIAL-HSRL observations and WRF-Chem forecasts of aerosol backscatter. The red solid lines represents the plane location. Bottom panel: In-situ organic carbon measured by the AMS instrument on board of the DC-8. From 19 to 20:30 UTC the aircraft sampled smoke above stratocumulus cloud over the ocean, and after that it approached the fire location at altitude. The model is able to represent the horizontal and vertical location of the smoke, but underestimates its loads, both in backscatter and organic carbon concentrations.

August 8th flights

The August 8th flights corresponded to the transit flights of the DC-8 and ER-2 from Palmdale to EFD, which was also planned as a science flight. The flight was originally planned to sample the North American Monsoon (NAM). However, the chemical forecast models started showing an important intrusion of the Saharan dust layer into the gulf of Mexico making it all the way to SW Texas, where EFD is located. As seen in Fig 7.7, the forecast was persistently predicting this plume through the days, making it slightly more intense as the forecast approached to the day of the flight. Due to the interest in measuring aged dust making it all the way from Africa to the south US, the flight plans were changed to accommodate sampling of the dust at the end of the flight. As shown by the observations, the plume location (vertically and spatially) and intensity (against remote sensing and in-situ measurements) were captured with good skill by the model (Fig 7.7). Two factors that can explain this performance is the recent improvements in dust simulation in MACC reanalysis (A. Benedetti, ECMWF, Personal communication, May 2013) which provided accurate dust boundary conditions, and the use of AOD data assimilation, that improved the dust concentrations and corrected the location of the plume. From comparisons to an AERONET site located on the shore close to EFD, it can be seen that the dust plume was slightly underestimated an there was a shift in the exact time when the plume went inland from the gulf.

August 14th flights

The flights on August 14th were planned to primarily sample SE US chemistry. At the same time, there were strong uncontrolled fires in Idaho and the models were predicting the smoke to impact the SE region, which was confirmed by data from the Mingo AERONET site two days before the planned flight. For this reason, a secondary objective of the flights was to do radiation measurements of smoke over AERONET

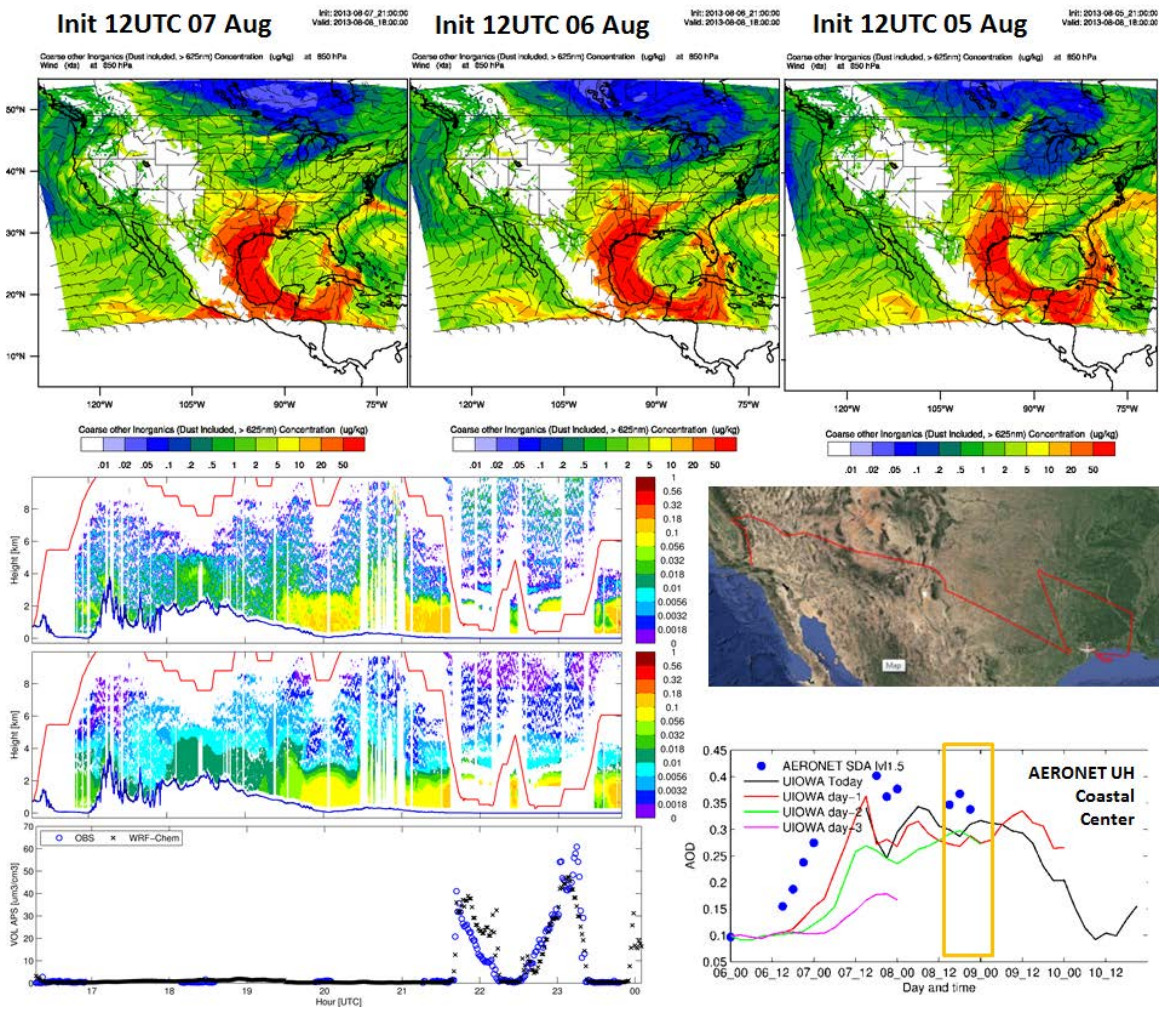

Figure 7.7. Model and observations for August 8th flight. Top panels: Dust at 850mb showing the Saharan dust layer coming inland for the forecast two days before, one day before, and the same day of the transit. Bottom-left panels: Extinction from DIAL-HSRL (top) observations and WRF-Chem forecast (middle) for the DC-8 flight the same day, along with volume concentrations of coarse aerosols (bottom). Middle-right panel: Actual DC-8 flight track. Bottom-right panel: AOD comparison for different forecasts on the Houston coastal site with the yellow rectangle marking the day of the flight.

sites, and as smoke was observed at the Mingo site in previous days, this site was selected as the target. As seen in Fig. 7.8, the UIOWA model persistently predicted that smoke influence above the boundary layer (700mb or ~3km above the ground) was going to be south of the this site. At the moment there were still uncertainties on the model

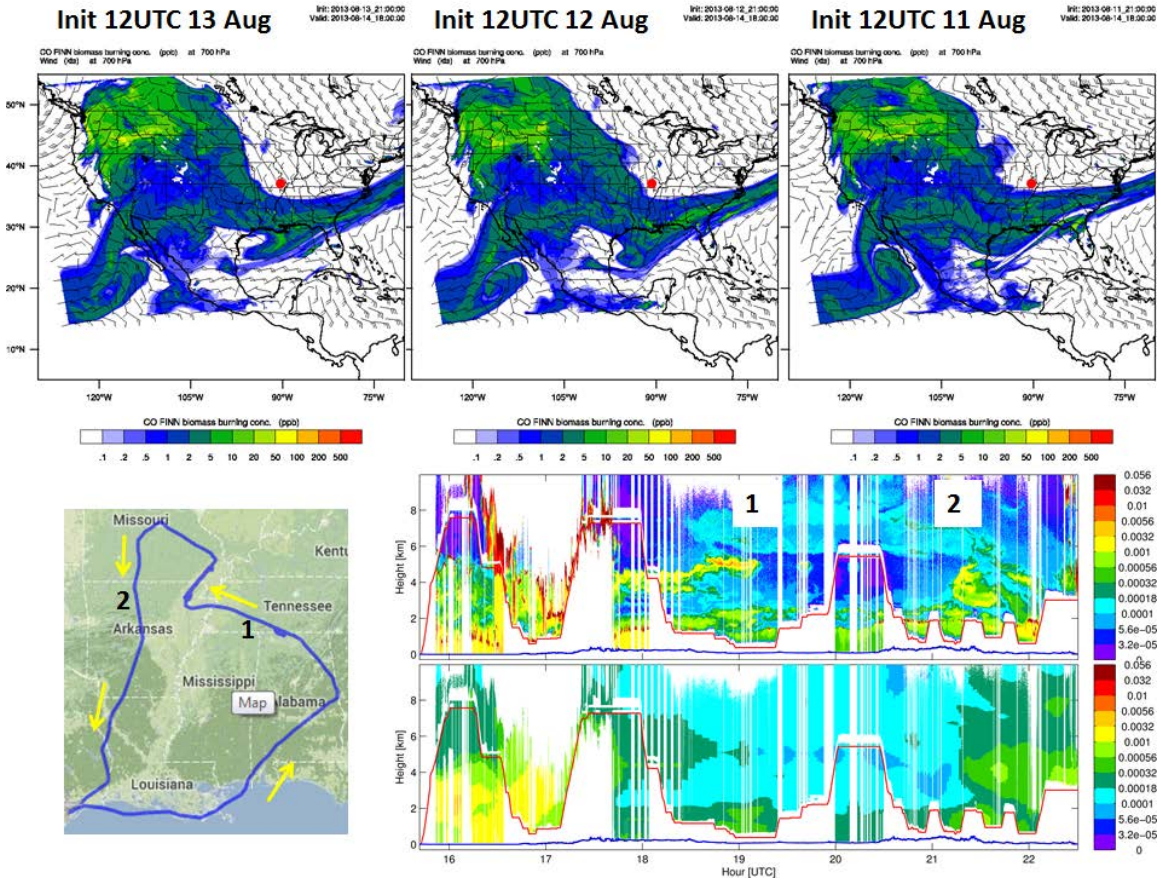

Figure 7.8. Model and observations for August 14th flight. Top panels: Biomass burning CO tracer at 700mb showing smoke transported from the Idaho fires for forecasts two days before, one day before, and the same day of the flight. The red dot represent the location of the Mingo AERONET site. Bottom-left: Actual DC-8 flight track, with arrows indicating the direction of the aircraft. Bottom-right panels: DIAL-HSRL(top) observations and WRF-Chem forecasts (bottom) of aerosol backscatter for the same flight. The numbers in the bottom panels indicate the locations with clear signal where the aircraft was no longer below the Idaho smoke plume (1) and then went back below it (2).

performance and the model had underestimated smoke concentrations, so this guidance was not considered. As shown by the data taken by the aircrafts (Fig. 7.8), the model predicted the horizontal plume location very accurately, but was low in terms of concentrations (due to low FINN fire emissions, as previously found on the Aug. 6th

flight) and did not resolved the laminar vertical structure of the plume, which could be due to model vertical resolution above the boundary layer and/or poor skill of the plume rise parameterization for this event. This outcome helped to gain confidence in the horizontal locations predicted after long-range transport and made a stronger point that fire emissions needed to be improved. Also, aerosol loads in the boundary layer on the SE US were generally underestimated by the model, which was a first indication of the potential impact of not including cloud chemistry and secondary organic production.

August 16th flights

There were two primary objectives to be accomplished during August 16th. The DC-8 and ER-2 were going to fly in formation to sample the NAM but there was also interest in sampling smoke coming from forest fires in Idaho. The center of the NAM was forecasted to be located on NW Mexico, so a strategy to sample the NAM outflow was to go to the SW US, close to the four corners region. As seen in Fig. 7.9, the model was predicting high smoke concentrations east of the Rocky mountains in Colorado, and lower concentrations on western Texas and SE California. Thus, a flight track as shown in Fig. 7.9 was designed to accomplish the two objectives, with the first part of the flight sampling the NAM, and the second the smoke over Colorado. As mentioned in the Methods section, on the August 14th forecast the QFED2 emission were used instead of FINN for biomass burning, which can be seen in the biomass burning CO in Fig. 7.9 as concentrations increased close to the fires in Idaho. As predicted by the model, the DC-8 flew over biomass burning plumes in western Texas and SE California, and was able to sample plumes of smoke south of Colorado Springs and east of the Rocky mountains with AODs around 0.4 to 0.5. The model still showed substantially lower aerosol loads than observed, probably because the new emissions did not had enough time to be transported to the sample areas. Even though there are still problems with resolving the vertical laminar structure of the smoke plumes, the vertical location of the three plumes

intercepted was represented with good skill by the model, in particular the one east of the Rockies, keeping the plume below 6km.

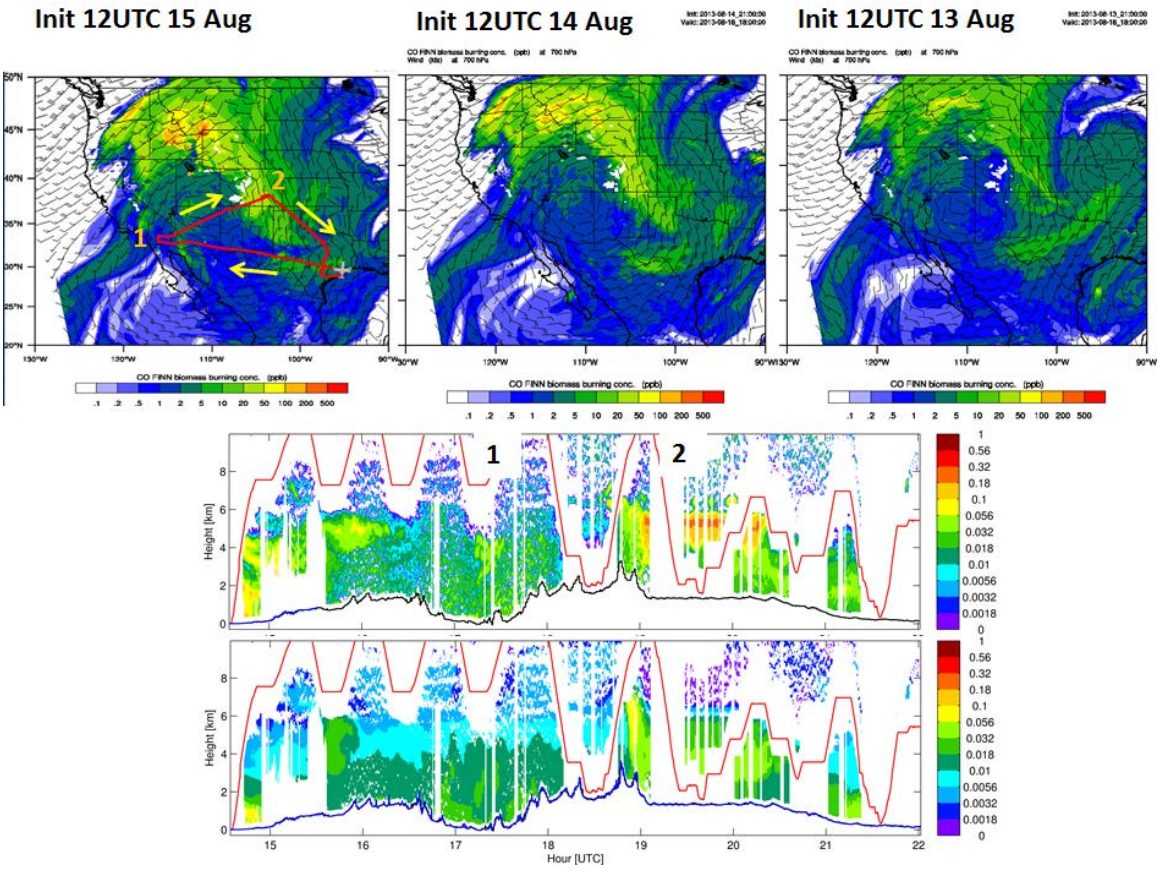

Figure 7.9. Model and observations for August 16th flight. Top panels: Biomass burning CO tracer at 700mb showing smoke transported from the Idaho fires for forecasts two days before, one day before, and the same day the flight. The actual DC-8 flight track is shown in the top-left panel, with arrows indicating the direction of the aircraft. Bottom panels: DIAL-HSRL(top) observations and WRF-Chem forecasts (bottom) of aerosol extinction for the same flight. The numbers indicate locations and times for guidance between spatial maps and curtains.

August 19th flights

At this point of the field campaign, plenty of fire plumes had been sampled but always as a secondary objective. Thus, given the persistent forest fires in the NW US,

favorable transport pathways that were bringing that smoke to the south, and a Terra overpass intercepting the smoke, it was decided to have the flight on August 19th completely dedicated to accomplish different biomass burning objectives. The model persistently predicted smoke from NW fires to advect east and then turn south towards Texas, thus the flights were planned to measure smoke all the way from Texas, going over the CART AERONET site (1 in Fig. 7.10) and then up to NE Wyoming, where DC-8 and ER-2 joint maneuvers were planned (2 in Fig. 7.10). After that, a decision was planned to be made on either keep going west or return south to do extra maneouvers. The decision was based on finding smoke thick enough over the cart site (0.3 or more), which was found, so the planes went back south and perform an extra bow-tie pattern west to the CART site (3 in Fig. 7.10). As seen in Fig. 7.10, the model still underestimates smoke loads but the new emissions bring it closer to the observations. The model has good skill representing the height of the mixed layer where smoke is confined, and has some skill when the plumes are no longer confined in this layer. On the way to the northern most point of the flight track, the flights went over two distinct smoke plumes, which, according to a MISR experimental algorithm had different optical properties even though they come from the same source (R. Kahn, personal communication, 2013). These two plumes where identified both in DC-8 measurements and in the model, and backwards trajectories using FLEX-PART (Stohl *et al.*, 2005; Fast and Easter, 2006) driven by the same WRF-Chem wind fields were obtained (Fig. 7.10). The back-trajectories show both of these airmasses went over the fire region, but with at the moment of the flight the northern airmass was ~1 day old while the southern one was ~2 days old. The different smoke age (secondary aerosol production, coagulation) can be the reason of the different optical properties found. This shows an example on the models can be valuable to interpret observations.

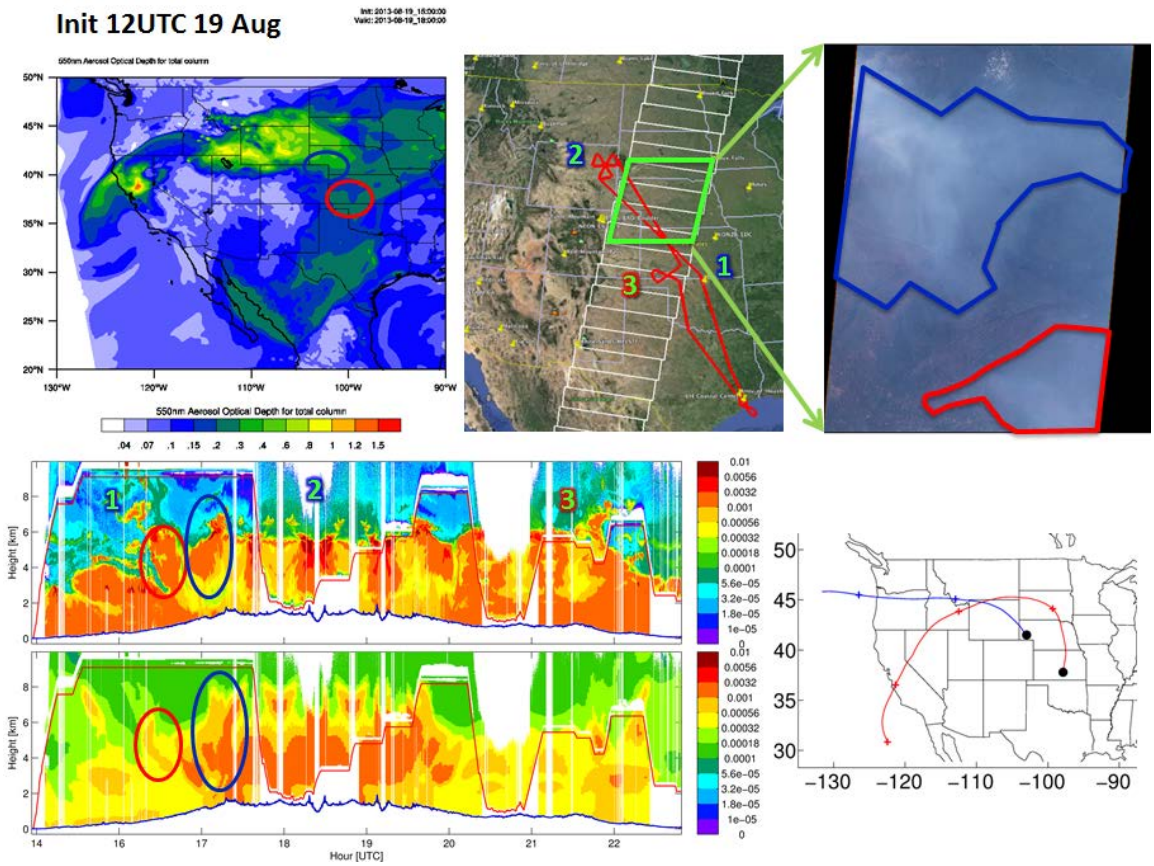

Figure 7.10. Model and observations for August 19th flight. Top-left: AOD for the forecast the day of the flight. Middle-top: ER-2 flight track with the Terra-MISR track overlaid. Top-right: Close-up over the MISR overpass true-color image showing two distinct smoke plumes. Bottom-left panels: DIAL-HSRL(top) observations and WRF-Chem forecasts (bottom) of aerosol extinction for the DC-8 flight. Bottom-right: Four days back-trajectories from the two plumes identified in the observations and on the model, which the "+" symbols representing 24 hours intervals.

August 26th and 27th flights

August 26th and 27th flights were DC-8 suitcase flights (the 1st one spend the night in Spokane) to the NW US to measure the RIM fire, a huge forest fire that affected the Yosemite national park (California) during August-September 2013. The flight on the 26th was planned to profile in the upper troposphere from EFD to the location of the fire and then to measure the plume downwind up to Idaho (Fig. 7.11). The flight on the 27th

was planned to measure plume ages of 2-4 days as it tracked the plume all the way from Idaho to Lake Winnipeg in Canada (Fig. 7.12). These ended up being very successful flights, as the plane stayed on the plume most of the time, as predicted by the model (Figs. 7.11 and 7.12).

For the August 26th flight, the model was able to predict very accurately the vertical smoke distribution containing smoke in the mixed layer for most of the flight (Fig 7.11), showing skill in the plume rise model. The model had problems on regions of the flight, especially on NW Nevada, showing very low smoke concentrations, even though close to the source smoke loads were well represented. An analysis showed that the separation of the plumes close to the RIM fire and over Idaho was due to the temporal pattern imposed in the fire emissions by the emission pre-processor. Usually, fire emissions show a strong diurnal pattern, increase emission during the hours with higher temperature. However, this event was so strong that it kept burning and emitted high aerosol loads during the night, thus generating a continuous plume as shown by the DIAL/HSRL observations and not separated as shown by the model. Away from the locations where this issue was found, the model was able to quantitatively represent remote sensing and in-situ concentrations.

On the first part of the flight on the 27th, the model concentrations seem to be lower than observed, which could be due to a slight displacement of the forecasted plume location as high AOD values are right next to the location of the flight track (Fig. 7.12). As the flight went away of the source towards Canada, model results agree much better with observations. Similarly to the August 26th flight, the vertical location of the plume were well predicted through the flight. Fig. 7.12 also shows the Angstom Exponent (AE) measured by the 4STAR instrument, which is an indicator of particle size distribution. At the beginning of the flight AE was underestimated by the model but then as older age plumes were measured better agreement was found. This underestimation can be due to not including secondary organic aerosol production in the simulations and an error in the

prescribed aerosol size distribution at the moment of emission. Coagulation and secondary aerosol production allowed the aerosol size distribution to grow and thus AE was reduced as the plume was advected east the observed AE matched the model estimates.

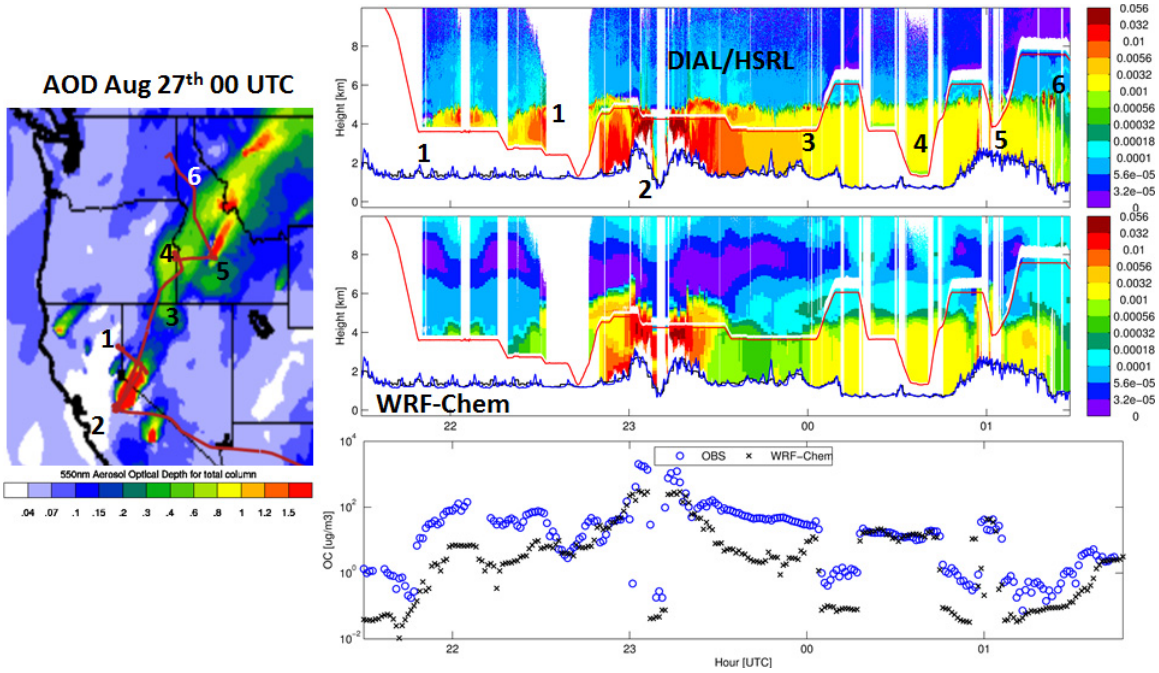

Figure 7.11. Model and observations for August 26th flight. Left panel: AOD predicted by the model one day before the flight along with the actual DC-8 flight track. Top-right panels: Backscatter from DIAL-HSRL observations and WRF-Chem forecasts for the DC8 flight the same day. Bottom-right panel: In-situ organic carbon comparison between measurements and model for the same flight.

September 6th flights

During the last week of August and the first week of September the NAM circulation prevailed over the US and by August 6th it was forecasted that it was going to decay. Due to the circulation, smoke from NE US fires was predicted to be transported following the circulation and come around impacting the SE US (Fig. 7.13). So, a flight

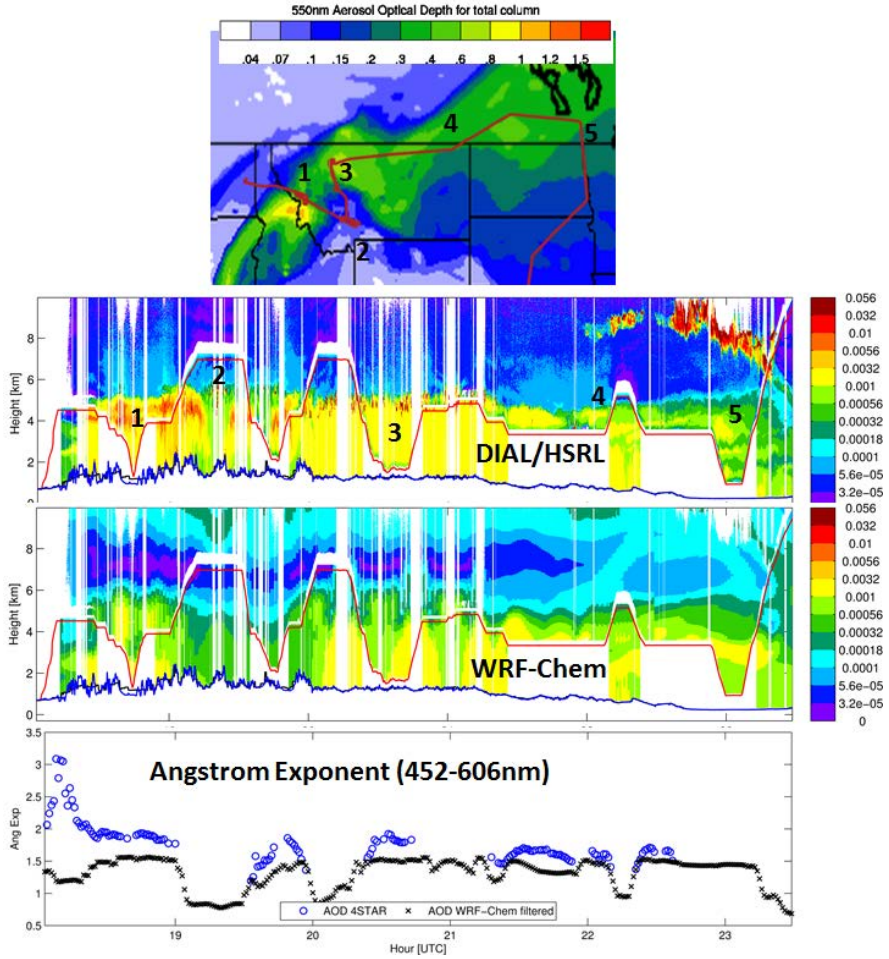

Figure 7.12. Model and observations for August 27th flight. Top panel: AOD predicted by the model one day before the flight on August 27th along with the actual DC-8 flight track. Middle panels: Backscatter from DIAL-HSRL observations and WRF-Chem forecasts for the DC8 flight the same day. Bottom panel: AOD comparison between 4STAR measurements and model for the same flight.

plan was designed to accomplish several objectives: the decaying NAM, the SE US chemistry, the isoprene hot-spot and the aged smoke from the NW US. As seen in Fig. 7.13, a thick smoke plume was found between 3-6 km altitude over the SE US with a marked clean air slot separating it from the boundary layer, just as predicted by the model. The aerosol loads in the lofted smoke plume seem to be well represented by the model, with underestimation in the boundary layer. This was persistent on the SE US

during the campaign (e.g., Aug. 14th flight) and could be related to the forecast not including aqueous chemistry (SO_4 production) and SOA production. Another important feature represented by the model is the gradient in boundary layer height, with shallow values (below 2km) for the SE US and deeper heights (up to 4km) in the Central US. When comparing to an AERONET site in the SE US (Fig. 7.13), the model forecasts were able to capture the increasing trend in aerosol loads due to the NE US smoke contribution.

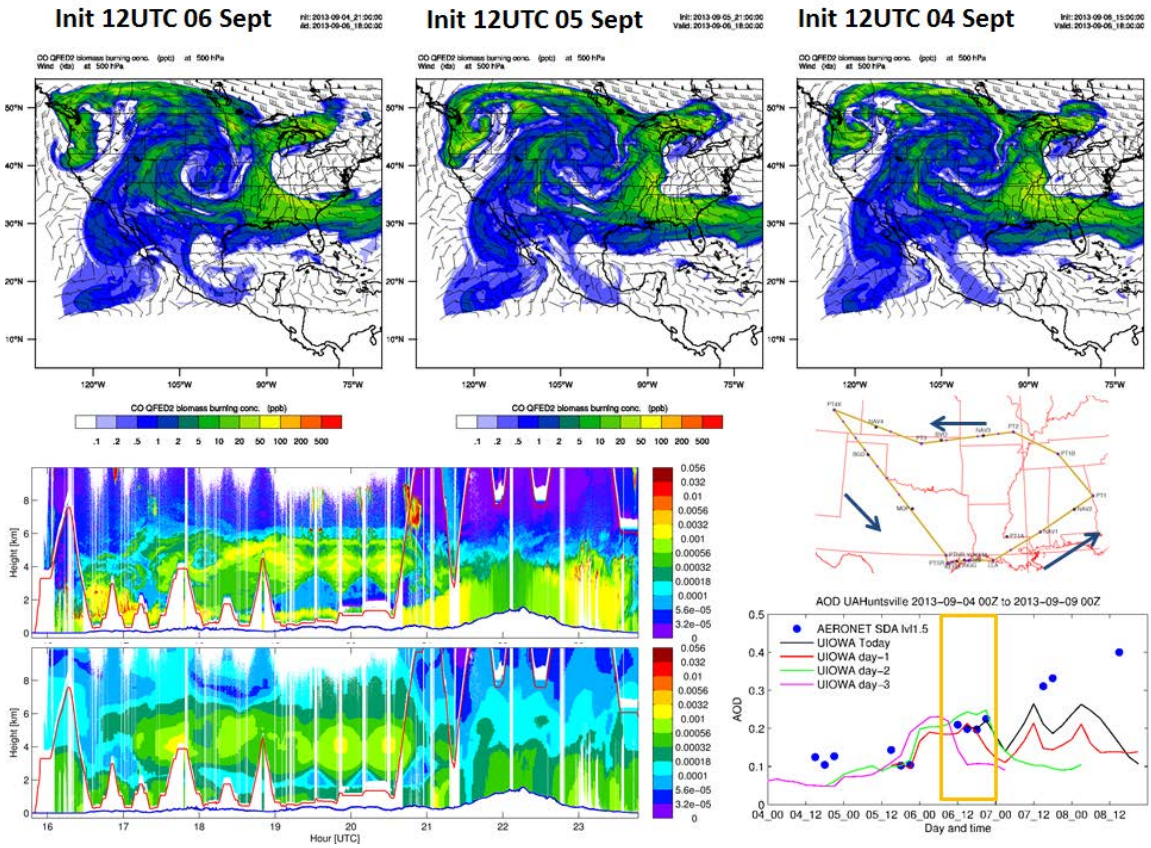

Figure 7.13. Model and observations for September 6th flight. Top panels: Smoke tracer at 500mb (~5.5 km height) showing smoke over the SE US for the forecast two days before, one day before, and the same day of the flight. Bottom-left panels: Backscattering from DIAL-HSRL (top) and WRF-Chem forecast (middle) for the DC-8 flight the same day. Middle-right panel: Planned DC-8 flight track with arrows showing the flight direction. Bottom-right panel: AOD comparison for different forecasts on the Huntsville AERONET site (northern Alabama) with the yellow rectangle marking the day of the flight.

Conclusions

The WRF-Chem model along with the GSI assimilation tool developed in Chapter 5 were used in an operational forecasting mode to provide guidance for flight planning during the SEAC4RS field experiment. The simulations were done at 12km resolution over the continental US, Mexico and Southern Canada, and included representation of key aspects to the filed campaign such as biomass burning, anthropogenic, biogenic, dust and sea-salt emissions, along with full chemistry, clouds and convection. This chapter reviewed the type of guidance given by the model for aerosol-related objectives and near real time evaluation performed to see to what extent the model guidance was accurate.

The forecasts were found to be very useful predicting several conditions which were part of the SEAC4RS objectives. One of the main uses of the model was to predict smoke locations. When predicting long-range transport of smoke, horizontal locations were predicted very accurately and were usually consistent across forecasts on different days, while vertical representation was generally correct with issues representing the laminar structure of the measured smoke plumes probably because model vertical resolution not being fine enough. Predictions of smoke close to the fire events were also accurate, with some issues often due to the prescribed diurnal cycle of the emissions and slight shift on the plumes due to inaccuracies in the wind fields. However, vertical distribution of smoke close to the sources was very well represented showing the skill on the plume rise model. Accurate prediction of smoke loads or concentrations was variable within flights, with good improvements when the emission inventory was changed from FINN to QFED2, probably because the assimilative nature of the later emissions. Some issues were found in the aerosol size distribution measured in fresh smoke, which need to be evaluated in future studies. The system was also used to forecast the location of a Saharan dust layer event which happened during the transit flight to Ellington field, which verified in the spatial and vertical placement of the plume as well as the aerosol loads found, showing the skill in the boundary conditions (MACC reanalysis) and in the

data assimilation system. The model generally represented the boundary layer and mixed layer heights with good skill, but often underestimated aerosol loads in the boundary layer, especially in the SE US, which could be due to not including processes such as cloud chemistry and secondary organic production.

These results show feasibility of running an operational forecast with an online, fully coupled chemistry and aerosol model, with results that can provide important guidance for field experiments. Future work is needed to find ways to improve model performance for the problems found. First, a simulation with a similar configuration has to be done using the analysis data as driving meteorology instead of pure forecasts to evaluate the improvement due to more accurate meteorology. Then, processes not included in the forecast (e.g., cloud chemistry, secondary organic aerosol production) or more complex representations (e.g., 8 aerosol size bins, finer vertical resolution) have to be incorporated and sensitivity simulations need to be performed to evaluate improvement on skill for addition on future studies. Also, models can be used along with observations to interpret them and better understand the processes occurring in the atmosphere and advance in science.

Collaborators and funding sources

We thank all the participants in the SEAC4RS field experiment: project managers, science leaders, flight planners, aircrafts crews and instrument groups. MODIS data were obtained from the NASA Langley Research Center Atmospheric Science Data Center. MACC forecasts were obtained from from the Jülich OWS Interface (JOIN). This work was carried out with the aid of NASA grants NNX08AL05G and NNX11AI52G, grant number UL1RR024979 from the National Center for Research Resources (NCRR), a part of the National Institutes of Health (NIH), and Fulbright-CONICYT scholarship number 15093810. Its contents are solely the responsibility of the authors and do not necessarily represent the official views of the founding institutions.

Author contributions

This work has not been published. P. Saide and G. Carmichael designed the forecasting system, while P. Saide implemented it and executed it operationally. All analyses and manuscript preparation were performed by P. Saide. Observational data was collected by the different groups participating in the SEAC4RS campaign, including DIAL-HSRL (PI: J. Hair, NASA LARC), 4STAR (PI: P. Russell, NASA Ames), AMS (PI: J. Jiménez, U. Colorado) and LARGE (PI: B. Anderson, NASA LARC). A. da Silva (NASA GMAO) and L. Emmons (NCAR) provided QFED2 and FINN biomass burning emissions, respectively.

CHAPTER 8 REGIONAL SIMULATIONS OF SMOKE OVER THE SOUTH-EAST ATLANTIC STRATOCUMULUS DECK: EVALUATION AND AEROSOL FEEDBACKS

Abstract

The southeast Atlantic is an important region to study due to the presence of a persistent stratocumulus deck and seasonal biomass burning smoke transported from the African continent, which interacts with clouds and radiation changing the meteorological conditions and radiative balance in the region. Simulations using a fully coupled and interactive weather and chemistry model are performed over the region to evaluate model performance in representing aerosol and clouds and provide an estimation of the smoke effects on the region in support of a proposed filed experiment. Modeled smoke transport from Central and South Africa shows skill in the spatial distribution and aerosol loads, but fails to represent a gap between smoke and cloud layers, which results in poor performance in long range transport of smoke. Cloud misrepresentations are found mainly close to the shore, with better model performance off-shore as long as model resolution is not coarsened. The smoke has widespread effects not only on clouds (e.g., 50 g/m2 increase in liquid water paths), but also in temperature profiles (>2 K increase) and regional meteorology. Further studies need to point towards improving model representation that will help providing more accurate forecasts and reducing uncertainties in aerosol feedbacks estimates.

Introduction

The South East Atlantic is home to one of the three permanent subtropical stratocumulus (Sc) cloud decks in the world and plays a key role in the energetic balance of the region. The physical processes governing the feedbacks between sea surface temperature (SST) and cloud properties in these Sc decks are poorly represented in climate models, as evidenced by the large model-to-model differences in cloud radiative

responses to surface temperature changes and by the large discrepancies between boundary layer cloud properties in climate models and global observations (Bony and Dufresne, 2005). The SE Atlantic Sc deck lies next to the region with the largest biomass burning emissions in the world, producing an average of ~550TgC per year (28% of global) in southern Africa (van der Werf *et al.*, 2010). In the Southern hemisphere spring (July-October), the stratocumulus deck interacts with the resulting dense layers of African biomass burning (BB) aerosols. These layers initially overlay the cloud deck or open ocean areas where they exert a direct radiative forcing. Depending on the relative location of the aerosols and the cloud deck, clouds may thicken in response to increased tropospheric stability (semi-direct effect), they may recede due to radiative burn-off (semi-direct effect), or their lifetime may be influenced by aerosol-induced changes in cloud microphysics (indirect effect) as the marine boundary layers deepens farther offshore and aerosols become mixed into the clouds. The changes in the vertical distribution of heating rates due to the presence of both clouds and aerosols affect the large scale circulation and precipitation patterns in the region, with some modeling efforts producing significant aerosol-induced surface cooling of 1-2K or more (Sakaeda *et al.*, 2011).

Satellite-based assessments of aerosol-cloud-climate interactions in the region (e.g., Wilcox, 2012) point to the need for better observations of aerosol properties and loading, and cloud fraction, albedo and liquid water path (LWP). These studies are hampered by the difficult observational environment, where clouds affect the aerosol retrievals and vice versa (Coddington *et al.*, 2010). Airborne observations are capable of separating the effects of clouds and aerosols on the radiation balance, because the airborne instruments can be located within the atmospheric column, because co-varying meteorological conditions can be measured simultaneously, and because the airborne measurements can provide meaningful constraints on the modeling of said processes.

A group of researchers, including our group, are submitting a proposal for a field campaign to analyze the smoke effects in the SE Atlantic region. This chapter shows simulations using a similar system as described in the previous chapters to evaluate model performance and to provide preliminary smoke effects on the meteorology of the region. Smoke effects have been shown previously for global models, so this is the first attempt to do so for a regional model. These results will be helpful for supporting the proposal.

Methods

Modeling system

We used WRF-Chem v3.4.1 to model aerosol and chemical transport and feedbacks to meteorology. The period simulated corresponds to the 1st week of September 2008, with 1 week of spin-up. The system has to able to resolve the stratocumulus deck (as shown in Chapter 3) and include the African biomass burning region, to be able to turn on and off emissions and see the smoke effects on clouds and meteorology, similarly as done in Chapter 6. To accomplish these two objectives, two domains with one nested within the other was used (Fig. 8.1). The outer and relatively coarse domain (36 km grid spacing) covers Central and South Africa, where the fire hotspots are found for the season being modeled and goes up to 30 W to cover the whole extent of the stratocumulus deck. The inner domain is focused on the climatological maximum of low cloud cover (Sakaeda *et al.*, 2011) and extends to capture the higher probability of finding the stratocumulus deck with a resolution fine enough to resolve it (12km grid spacing, see Chapter 3). Model vertical resolution and WRF parameterizations chosen are the same as in Chapter 3 (72 vertical levels, MYNN boundary layer, 8 size bin CBMZ-MOSAIC aerosols, radiation and microphysics for aerosol direct and indirect effects). No convective parameterization is specified as numerical instability problems arose when used, which could generate vertical transport

misrepresentation for the coarser domain. Biogenic, dust and sea-salt online emission were incorporated as in Chapter 6. Anthropogenic emissions were computed with PREP-CHEM-SRC (Freitas *et al.*, 2011) while Quick Fire Emission Dataset (QFED) v2.0 biomass burning emissions (Darmenov and da Silva, 2013) were used along with WRF-Chem plume rise model (Grell *et al.*, 2011). Meteorological and chemical boundary conditions were considered as in Chapter 3 (FNL and MOZART).

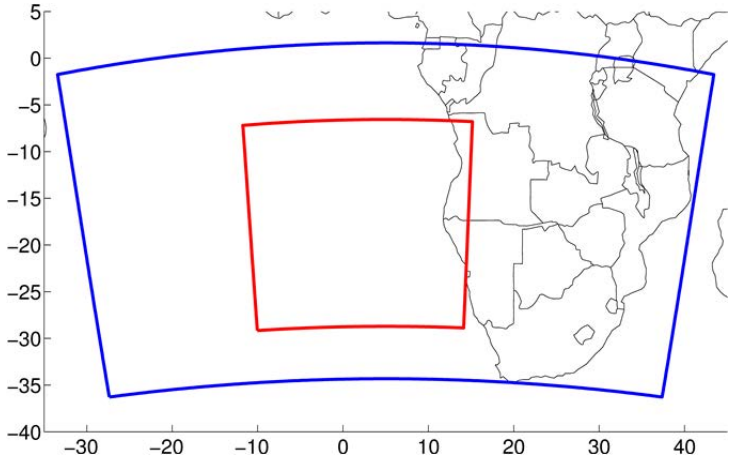

Figure 8.1. WRF-Chem modeling domains. The outer domain (blue, 36 km) contains the region with more intensibe African biomass burning, while the inner domain (red, 12km) resolved the stratocumulus deck

Observations

Measurements are limited in this region of the world, which is one of the reasons of submitting a proposal for a field experiment. MODIS aerosol optical depth (AOD) retrievals are scarce due to the persistent cloud deck. Thus, we use CALIPSO to provide extinction profiles and AOD above the clouds by using the feature type to add optical depths of aerosol layers (Young and Vaughan, 2009). Meteostat SEVIRI visible images are used to get cloud cover location. We also use ground based measurements taken on AERONET stations in Ascension Island (14 W, 7 S) off shore in the Atlantic and in Mongu (23 E, 15 S), located inland in western Zambia.

Results and discussion

Smoke evaluation

Figures 8.2 and 8.3 show a clear influence of biomass burning smoke on the aerosol loads, increasing AOD substantially. The smoke is emitted over land and is either transported east where it goes out of the domain, or is transported west were it goes over the stratocumulus deck. The main transport direction is towards the northwest, but winds can shift and advect smoke towards the west. The smoke primarily comes from the Central and South African continent, which enables us to turn on and off these emissions to evaluate the smoke effects. However, there could be other potential sources, such as smoke from Brazilian biomass burning, which is modeled on the SW of the outer domain on September 5th and 7th and have to be considered when doing this analysis. An episode of high AOD can be followed throughout the days, with the plume found on September 1st at 18 S on the African shore to the Arabian sea, then over central Africa on the 3rd, moving to the Atlantic shore on the 5th and over the ocean around 5 S on the 7th. This episode highlights the need for a long spin-up time to give enough time to the model to accumulate the smoke to better represent the high AODs.

As seen in Fig. 8.3, there is great day to day variability of smoke over the ocean, both in the smoke concentrations as in the smoke location. At the beginning of the period of study the smoke plume is confined to the NE of the inner domain, and as the days go by it spreads and covers most of the domain by September 7th. This behavior is confirmed by observations when comparing the model to CALIPSO extinction profiles in Fig. 8.4, as the south end of the plume is progressively moved to the south as days advance. Fig. 8.4 also shows that the extinction values in the smoke plumes are similar, showing some model skill on predicting smoke concentrations accurately. However, the CALIPSO profiles consistently show a gap between the smoke layer and the cloud deck, which the model is not able to represent, as the smoke sits on top of the plume for most days and

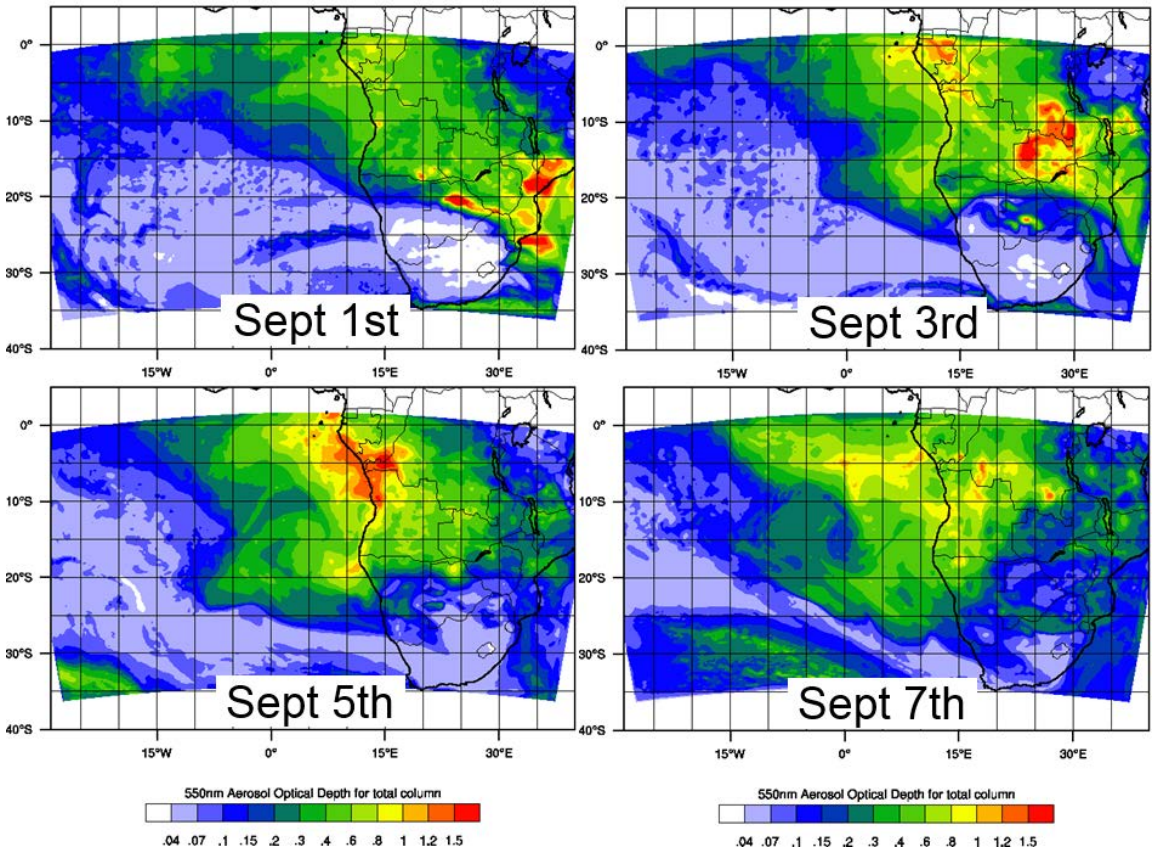

Figure 8.2. AOD maps for the outer modeling domain for 4 days at 00 UTC during the period of study.

latitudes. Opposite to these results, the smoke altitudes and separations with the boundary layer were found to be successfully represented by the model in Chapter 7. Thus, differences in model configuration could be the reason of this discrepancy, where the use of an outer domain versus using a bigger single high resolution domain (Chapter 7) and the inclusion of a convective parameterization (in Chapter 7) might be to blame. Also, we do not dismiss the possibility that the model is not able to represent the particular meteorological conditions of the region, which could be linked to the reduced amount of meteorological observations in the area to be assimilated. The physical separation between the smoke layer and the cloud deck is an important factor for the aerosol

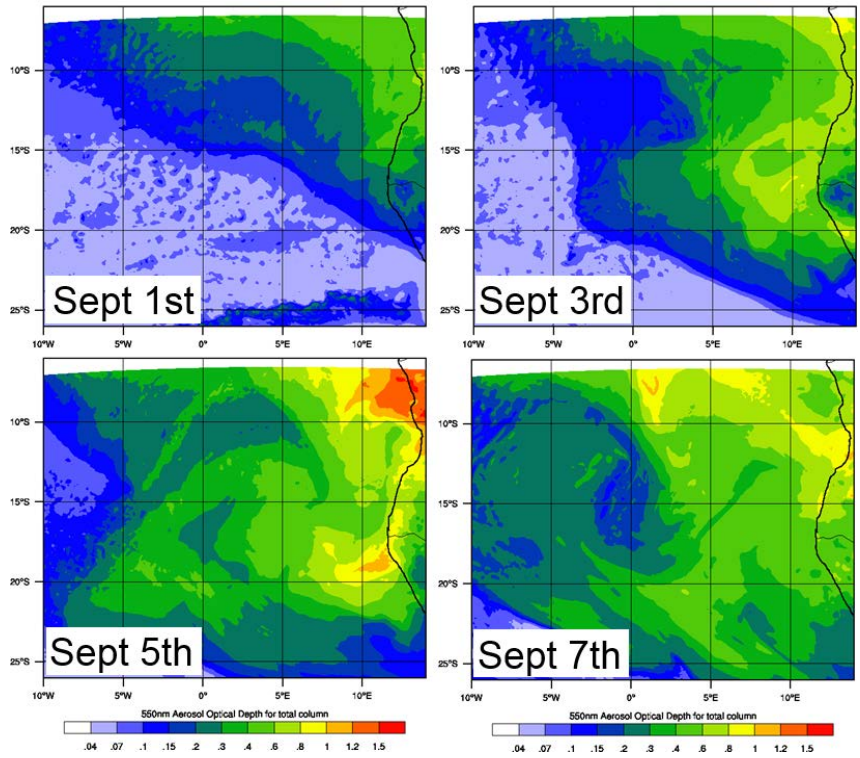

Figure 8.3. As Figure 8.2 but for the inner modeling domain.

interactions in the region (Costantino and Bréon, 2012), thus this model misrepresentation is going to increase the uncertainty of the modeled aerosol effects.

As MODIS AOD is not available over the stratocumulus deck, we use CALIPSO measurements to compute above cloud AOD (AAOD), and compare it to model estimates (Fig. 8.5). In general, the model has good representation of AAOD, underestimating and overestimating it on different days and locations. There are several aspects captured by the model, as the north to south decrease in AOD (left to right in plots on Fig. 8.5) and the increasing trend from September 1st to 7th, which is due both to the tracks being progressively to the east (Fig. 8.4) and AOD increasing as days go by (Fig. 8.3) due to higher smoke concentrations and thicker plumes (Fig. 8.4).

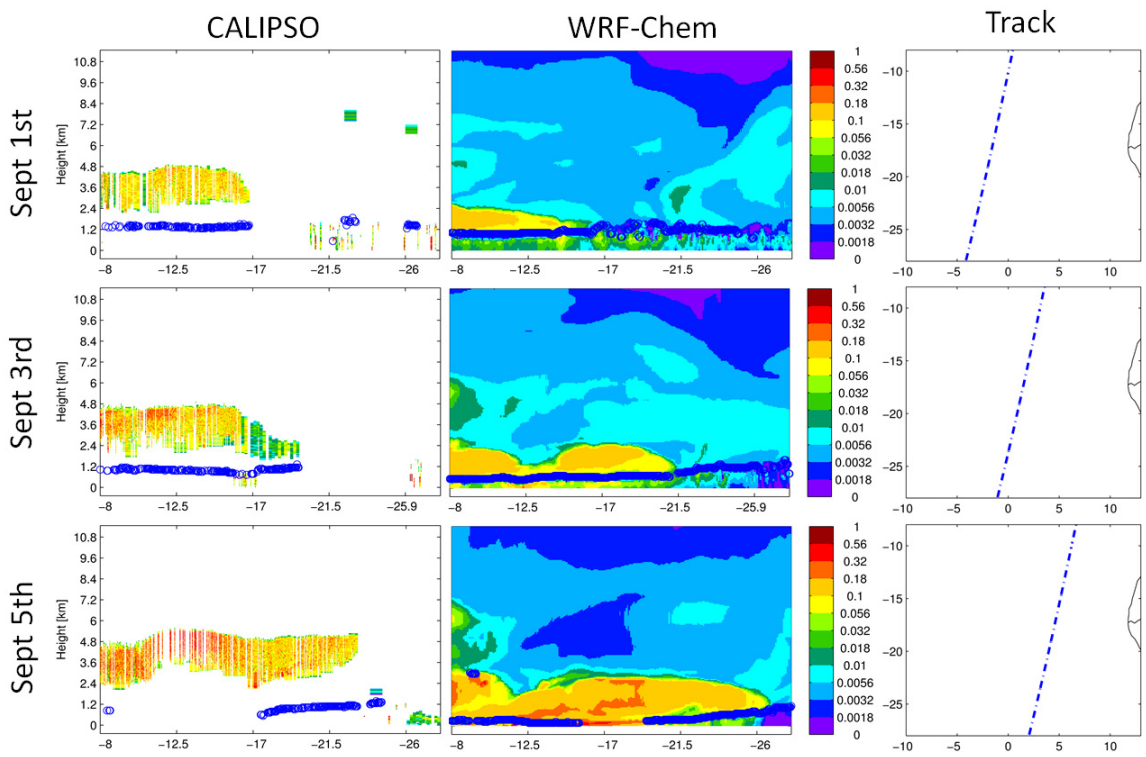

Figure 8.4. Observed (left panels) and modeled (middle panels) aerosol extinction profiles for three CALIPSO tracks (right panels) on 3 different days around 00 UTC. Blue circles represent observed and modeled cloud top. The three dates and times correspond to the first three panels in Fig. 8.3.

Model AOD can also be evaluated by comparing to AERONET stations (Fig. 8.6). The inner domain does not contain any AERONET station, which is why the evaluation is performed for the outer domain. Model performance on the Mongu site is generally good, capturing the high AOD conditions (usually above 0.5) during the period. The high AOD episode mentioned earlier is captured by the model in just 1 day (September 3rd) while is missed for August 1st and 2nd. The simulations do show an AOD maximum over the domain but not in the exact location of the AOD site, so this misrepresentation can be due to not capturing the whole spatial extent of the episode or problems in the winds that might have shifted the plume. A different picture is found for the Ascension island site, located far off-shore on the Atlantic ocean. The model is able

to represent the AOD for the first days but after that is unable to show the increasing trend and high AODs of the last 6 days of the period, showing AODs values close to

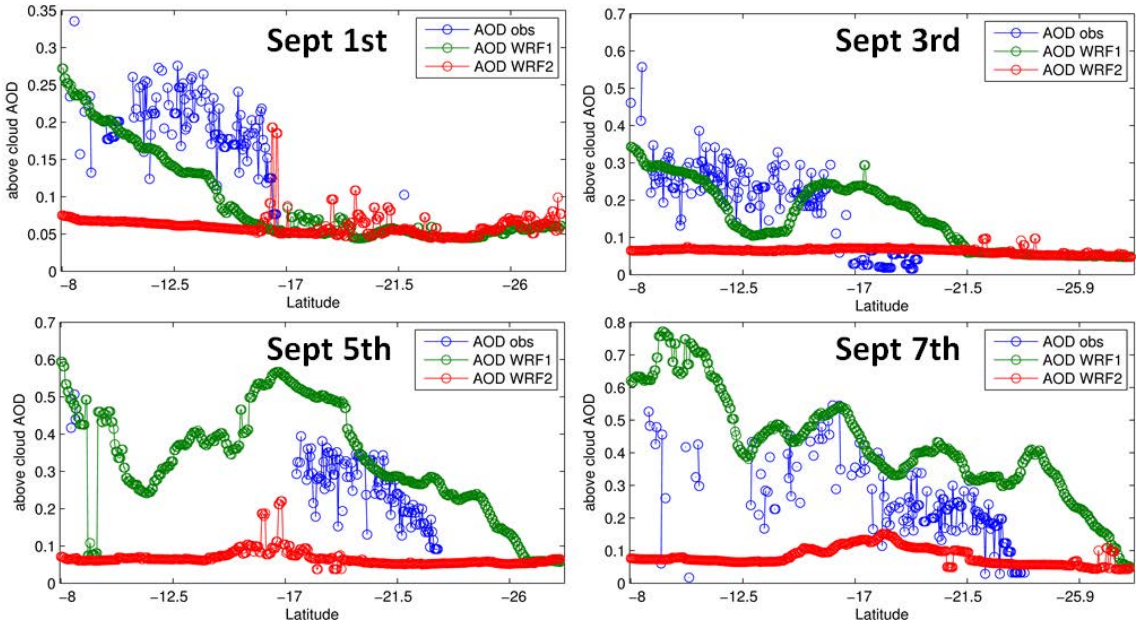

Figure 8.5. AOD above cloud estimated from CALIPSO extinction profiles and WRF-Chem for 4 days at ~ 00UTC. The WRF1 and WRF2 simulations correspond to turning on and off fire emissions, respectively. The satellite tracks of the September 1st, 3rd and 5th are shown in Fig. 8.4, while the track for Sept 7th has the same orientation as the other ones starting on 10 E and finishing on 5 E. AOD model maps for the same dates are shown in Fig. 8.3.

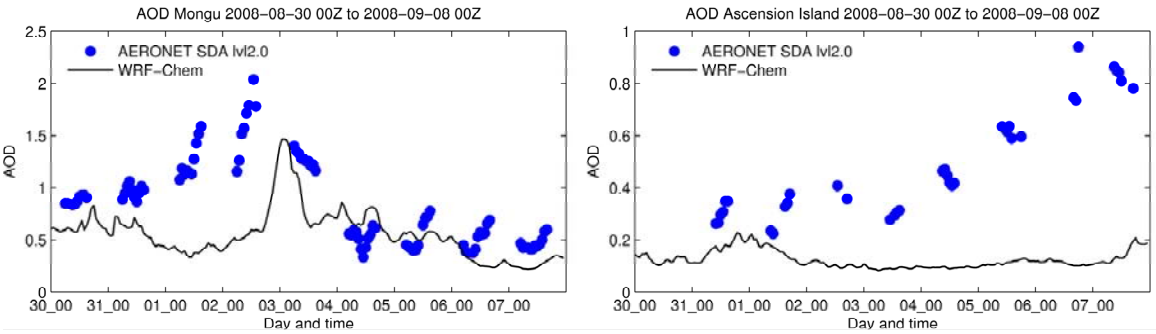

Figure 8.6. Model versus observations for Mongu (left) and Ascension Island (right) AERONET sites.

background values. This was unexpected as AAOD performance was good in locations off-shore for the inner domain. As seen in Fig. 8.2, on the site location (14 W, 7 S) for September 5th and 7th, AOD is slightly higher than background which points towards a smoke contribution but very weak. Fig. 8.7 shows profiles AOD maps for a CALIPSO overpass where the strong smoke underestimation happens on the NW region of the inner domain (up to 0.4 AOD difference), similarly as in the AERONET site. In the model, as the aerosol plume is in permanent contact with the cloud deck it starts entraining into the marine boundary layer, where is wet deposited by drizzling stratocumulus. As the smoke is transported further west, the entrainment becomes more efficient due to the more broken cloud deck. This is clear in Fig. 8.7, where the model shows a very thin layer of smoke on top of the clouds, and a polluted boundary layer. In the case of the observations, as the smoke and clouds layers are physically separated, this removal process does not happen and the smoke can be transported further, showing the high AOD at the Ascension Island station. Another factor that could be influencing the transport extent is the different wind speeds at different heights where the model and observations locate the plume. The lack of spatial extent of the smoke plume to the west is also going to influence the uncertainties in the aerosol effects on weather. However, the impact should not be small in the inner domain region, where only NW region shows this behavior.

Clouds evaluation

Another important component to evaluate is the cloud coverage and properties representation by WRF-Chem. Fig. 8.8 shows how well the model is able to represent cloud spatial distribution on the outer domain. First, there is a clear difference between the cloud fields interpolated from inner domain, which go from the coast to ~10 W, and the ones coming directly from the outer domain, with the inner domain ones showing

more wide-spread clouds. This is due to the resolution differences in the two domains highlighting the needs for fine resolution simulations. When comparing the model against

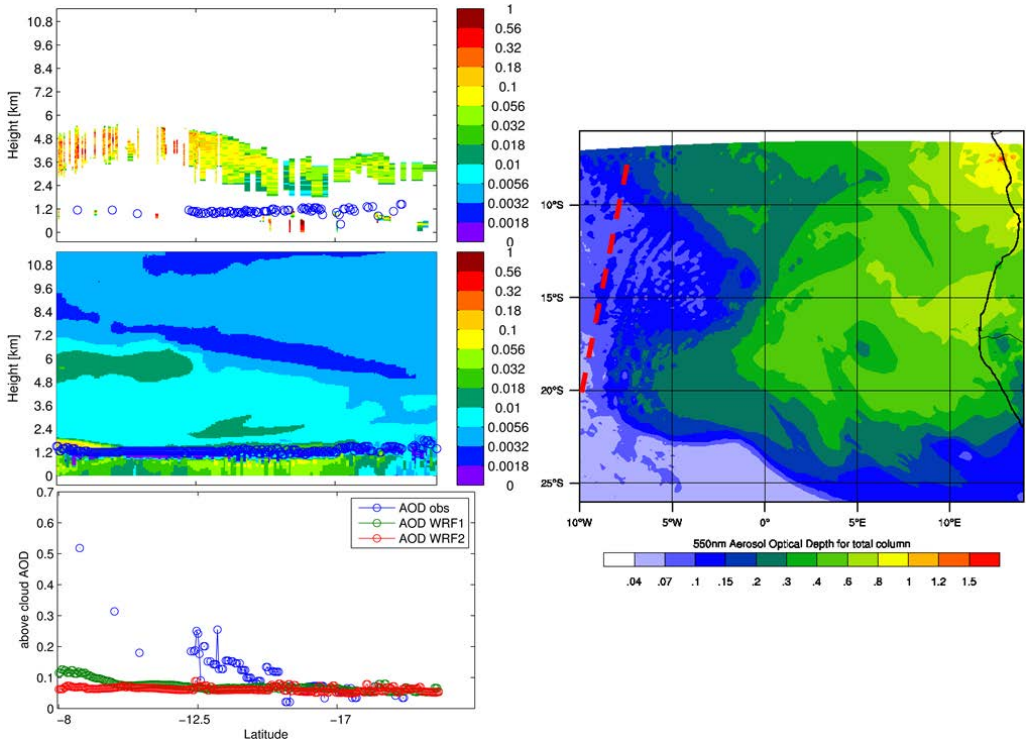

Figure 8.7. Left panels: Extinction profiles for CALIPSO (top) and WRF-Chem (middle) and above cloud AOD (bottom) for September 4th at 00UTC. Right panel: AOD for the same day and time with the CALIPSO track overlaid in red segmented line.

observed cloud distribution there is a mixed behavior. For September 1st, the model shows very good performance of the observed cloud fields, showing cloud-free region close to the shore south of 13 S and a thick cloud deck on the 5 S to 30 S region off-shore. The exception occurs west of 10 W, where the model tends to show clouds too broken compared to the observed ones, product of the coarser resolution of the outer domain. On the other hand, for September 5th, the representation is not as good. The model shows a widespread cloud free region all along the western African shore which is observed only south of 25 S. The reasons of this misrepresentation could be several. First,

as the model was initialized on August 25th, by September 5th is had been running continuously for 11 days, which could generate a larger deviation from observations. Second, this area of the world has very few meteorological soundings, with only one over the SE Atlantic on St. Helena island (5.7 W, 16 S), which is west of the region of misrepresentation. This hampers the ability of meteorological data assimilation system to constrain the region. Third, there could be problems with the model when representing the land to ocean gradients, as was also found in the SE Pacific modeling study (Chapter 3). The whole extent of the cloud deck to the west is also missed, probably to model resolution as pointed out for September 1st. The problems in representing cloud spatial coverage will add to the uncertainties when evaluating aerosol effects on climate.

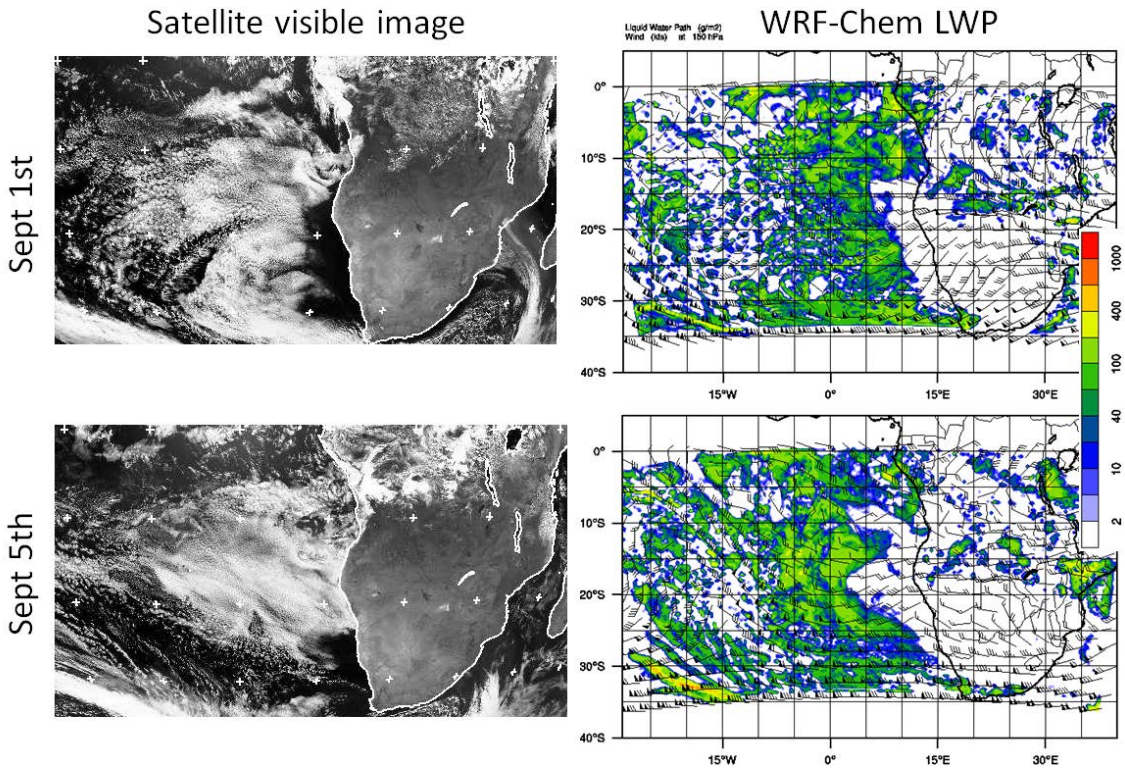

Figure 8.8. SEVIRI visible imagery (left panels) and WRF-Chem outer domain liquid water path (right panels) for two days during the period at 12 UTC. 150mb wind barbs are shown overlying the LWP.

The variability of the stratocumulus deck as seen by the model is shown in Fig. 8.9. Most of the domain but the close to shore region is covered by clouds throughout the days but the properties of the clouds vary, from broken clouds to very thick overcast clouds with a LWP up to 400 g/m2.

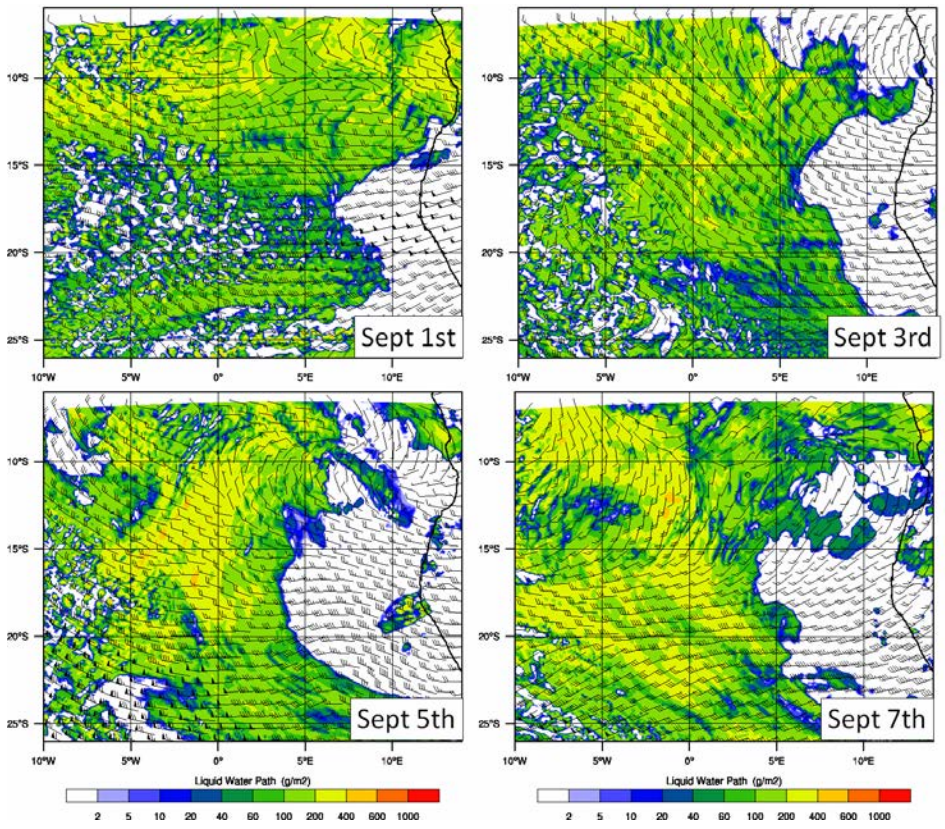

Figure 8.9. Liquid water path (LWP) maps for 4 days at 00 UTC. These days and times correspond to the ones in Fig. 8.3. 150mb wind barbs are shown overlying the LWP.

Cloud heights were evaluated using CALIPSO observations (Fig. 8.10). The model has generally good skill predicting the cloud top heights, especially in the off-shore region. The model consistently underpredicts cloud heights close to the shore, which is the same behavior found in Chapter 3 attributed to problems on resolving the land to ocean transition (Wang *et al.*, 2011). There are no enough days included in the

box and whisker plots to be able to draw definitive conclusions on longitudinal and latitudinal trends in cloud heights. However, there seems to be a tendency to shallower cloud towards the shore and increasing off-shore, which is very marked in the model.

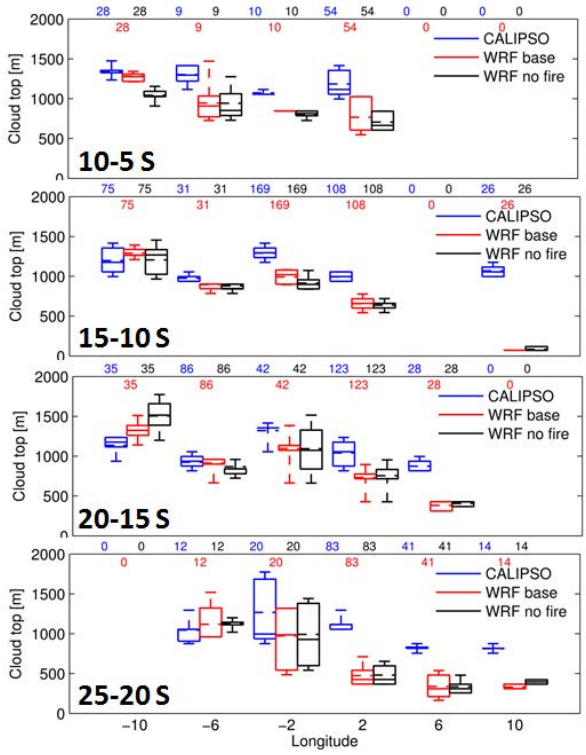

Figure 8.10. Box and whisker plots summarizing statistics of cloud top height for the September 1st to 8th period for CALIPSO measurements and inner domain WRF-Chem simulations with (base) and without (no fire) fire emissions. Different panels show statistics for different latitudinal bins, while the axes represent the longitudinal bins.

Smoke effects

Smoke from biomass burning is going to affect the meteorology over the SE Atlantic mainly by two pathways: by acting as cloud condensation nuclei (CCN) and by interacting with solar radiation. Fig. 8.11 shows strong influences of smoke on the stratocumulus deck increasing average LWP by ~50 g/m^2, which is in agreement but somewhat overestimated compared to observational studies (Wilcox, 2010, 2012). There

is a clear increase in number of droplet (Fig. 8.11), as the modeled smoke plumes were in contact with the cloud deck, which is generating part of the increase in LWP, similarly as seen in Chapter 3. The persistent physical contact which was not observed in the CALIPSO observations might be the reason of the overestimation. On the other hand, cloud heights do not follow a clear tendency, with the simulation with fire emissions showing often higher and often lower heights (Fig. 8.10), which is opposite to what was found on the Southeast Pacific stratocumulus deck (Chapter 3), where higher aerosol concentrations were increasing cloud heights. The reason of the discrepancy is the fact that an absorbing and optically thick aerosol layer sits above the cloud layer in the southeast Atlantic case.

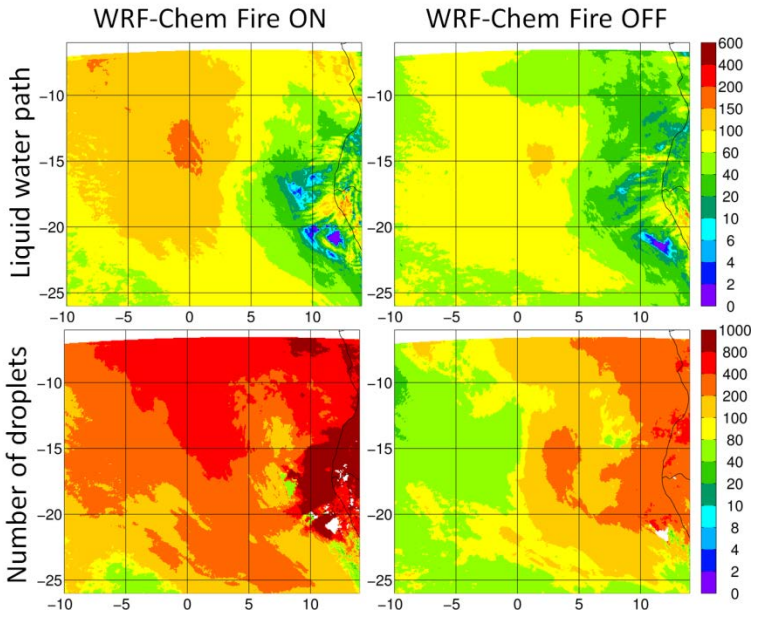

Figure 8.11. Mean liquid water path (LWP, top panels) and cloud top number of droplets (bottom panels) during September 1st to 8th 2008 for simulations with (left panels) and without (right panels) fire emissions

Figure 8.12 shows statistics for vertical profiles of a selection of variables for a region at the center of the inner domain. Clear differences are found between profiles

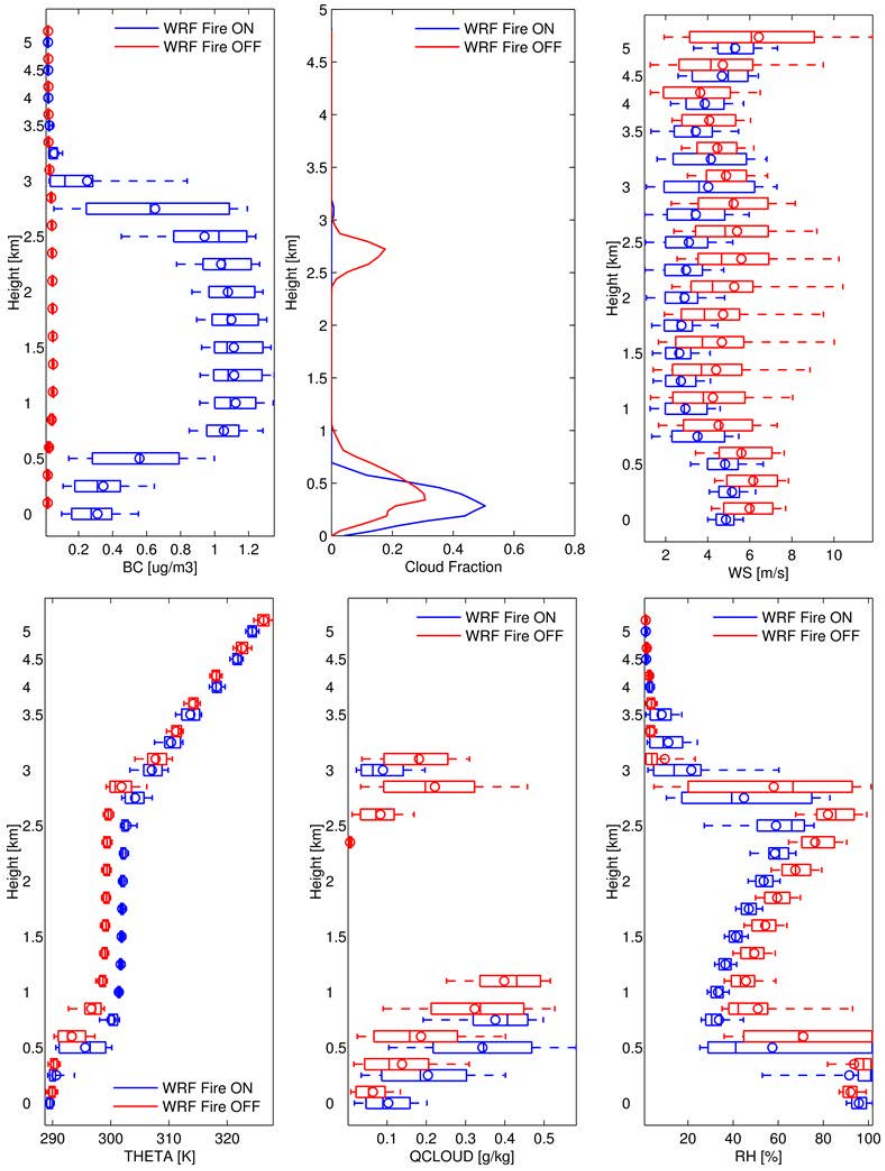

Figure 8.12. Statistics for vertical profiles at 12 UTC over the region within 0E to5E and 20S to 15S for simulations with and without fire emissions. Box and whisker plots are shown for soot (BC), wind speed (WS), potential temperature (THETA), cloud water (QCLOUD) and relative humidity (RH), while solid lines show mean cloud fraction.

from simulations with and without fire emissions. Temperature in the lower free-troposphere increases ~3 K for the day and time plotted because of soot absorption, which is of the same sign and not far of observational estimates (Wilcox, 2010). The

higher temperatures generate an intensification of the capping inversion on top of the marine boundary layer leading to several effects. First, its reduces entrainment which contains moisture in the boundary layer, increasing LWP and cloud coverage, as seen in the water content and cloud fraction vertical profiles. In the simulation with no smoke, as higher moisture and colder temperatures are found in the lower free-troposphere, relative humidity increases resulting in the formation of a second cloud layer close to 3 km reaching almost 20% cloud cover. Second, the stronger capping inversion reduces cloud height, as seen in the cloud fraction profiles, with the simulation with fire emissions showing the peak at a lower altitude. This effect counteracts the effect of deepening the boundary layer by the higher CCN, thus for the average through all cloud heights on CALIPSO overpasses ends up being balanced as stated previously (Fig. 8.10). A non-expected smoke effect is the reduction of wind-speed for all altitudes in the region where statistics were computed (Fig. 8.12), sometimes over 2 m/s on average. This point towards changes in pressure gradients due to soot heating that go beyond just local changes ad start affecting the regional meteorology.

Conclusions

A field experiment is being proposed to measure the southeast Atlantic region with the objective to improve our understanding of interactions between smoke, clouds and radiation happening here. In support to this proposal, WRF-Chem simulations were performed to evaluate the potential of the model to forecast smoke and clouds in the area, and to make a first exploration with this tool of smoke effects on clouds and climate in the region.

Large day to day variability is found in the smoke plume over the stratocumulus deck, both in the spatial locations as in the smoke loads. In the close to medium range to the coast, the model tends to represent smoke loads, spatial distribution and north-south gradients with some skill, but has problems characterizing the vertical distribution, as

persistently locates the smoke plume in physical contact with the stratocumulus deck, while observations usually show a gap between them. Since the modeled smoke plume sits on top the cloud layer, as it is transported west or north-west it entrains in the boundary layer and it is scavenged by drizzle, which generates an underestimation of smoke in the far off-shore region as this removal process does not occur in reality due to the smoke-cloud separation.

Clouds also show variations within days, mainly related to the occurrence of a clear sky region close to the shore, broken to overcast clouds conditions and changes in the water content. Model skill on representing cloud spatial patterns vary within days, with issues usually representing close to shore cloud occurrence and regions of coarse model resolution. Cloud heights are generally well represented with the exception of close to shore clouds, where model estimates are biased low, similarly to simulations over the southeast Pacific stratocumulus (Chapter 3).

Modeled smoke effects are found to be significant. Under the presence of smoke, the stratocumulus deck tends to increase its water content and cloud fractions. This is both product of increased CCN and soot absorption. Smoke radiative effects change the temperature profiles, with hotter values in the lower free-troposphere, which intensifies the capping inversion. In the case of simulation with no smoke, a weaker capping inversion allows more effective transport of moisture to the free troposphere, which together with colder temperatures can generate a second cloud layer, not obtained for simulations with smoke. Also, changes in the regional meteorology can occur due to smoke effects changing the wind intensities. While CCN effects need to be considered highly uncertain due to inability of the model to resolve the vertical smoke location, radiative effects tend to agree with observed estimates. Further studies need to be performed by trying to find a model configuration that fixes the misrepresentations found in smoke and cloud representation, which will improve our confidence in estimations of aerosol effects by models in the region.

Collaborators and funding sources

We also thank Brent Holben and their staff for establishing and maintaining the Ascension Island and Mongu AERONET sites used in this investigation. CALIPSO data were obtained from the NASA Langley Research Center Atmospheric Science Data Center.

Author contributions

This work has not been published. The study was designed by P. Saide and G. Carmichael and executed and written by P. Saide. A. da Silva (NASA GMAO) provided the QFED2 biomass burning emissions. M. Kacenelenbogen and J.Redemann (NASA AMES) provided scripts for using CALIPSO data.

CHAPTER 9 GENERAL CONCLUSSIONS AND FUTURE DIRECTIONS

Throughout the variety of studies shown in this thesis, there was always a common aspect, which is the use of the WRF-Chem system to perform predictions of different atmospheric components: gases, aerosols, clouds and meteorology in general. A recurrent subject was to advance aerosol predictions, which was achieved by a variety of strategies. These include finding the model configuration that best represented the meteorology for different modeling domains, modeling processes and sources that are important to represent aerosols and its interactions, and developing and using data assimilation techniques to observationally constrain the model state. The WRF-Chem characteristic of being a fully coupled online model provides the ability to study aerosol feedbacks into climate, which is another important component of this thesis. Due to the uncertainties on these estimates found by other studies (e.g., McFiggans *et al.*, 2006), a careful evaluation of the system is performed for each study case to better understand the limitations and effects.

Summary of results

The main finding of Chapter 2 was the feasibility to perform a high resolution forecast for complex terrain conditions to assist in the prediction of severe air quality episodes in Santiago, Chile. This system is important as it enables forecasts longer than 1 day, providing the ability to prevent episodes, rather than just warn the population. The forecasting system was transferred to the Chilean meteorological office, where it is used operationally and collaborations are under way to keep improving the system.

The ability of the WRF-Chem tool to predict observations from multiple platforms over the southeast Pacific was shown in Chapter 3. The focus of the study was the investigation of how accurate the aerosol effects on clouds are represented in the

model, finding good representation increasing our confidence in the activation parameterization used by the model.

The increased confidence in the model representation of aerosol feedbacks plus accurate retrievals of cloud properties (cloud droplet number) led to the development of a new data assimilation technique, presented in Chapter 4. The technique is shown to improve the aerosol state in regions below clouds where it was not possible with the previous methods, thus advancing science in this aspect.

Besides developing new data assimilation techniques, it is important to advance previous proven techniques, which is the basis of Chapter 5. Here, AOD assimilation is implemented for an operational data assimilation tool for the aerosol model used in this thesis, the MOSAIC model. The use of this treatment creates new possibilities of application, such as the assimilation of multiple AODs at different wavelengths with positive results. Also, advances were obtained when using observationally constrained AOD retrievals, which improved the quality of the assimilation.

As uncertainties on aerosol effects on climate are reduced other sensitivity studies can be done, including analyzing the effects of aerosols on severe weather. Chapter 6 showed a case study of an historical weather outbreak, where biomass burning smoke was found to have important effects on tornadogenesis and tornado intensity and longevity. An important finding was that simulations with smoke included were able to better represent measurements of clouds and meteorological variables, implying that including aerosol feedbacks on severe weather forecasts can likely improve predictability.

Such complex modeling systems could be regarded as unfeasible for operational forecasting. In chapter 7 we demonstrated that a system including high resolution WRF-Chem simulations and AOD data assimilation shows skill for predictions used for aiding flight planning during field experiments. A common feature is the tendency of the model to be consistent throughout the days, which is important for taking decisions on

objectives to be assessed a couple days in advance. The system was found to have good skill on qualitative aspects, like location of the plumes, and in some cases good quantitative performance.

Finally, a similar system used for the southeast Pacific is used in the southeast Atlantic to assess effects of African smoke. Preliminary evaluation showed some skill along with issues in representing key features important for resolving aerosol effects in the region, the most notable being the gap between aerosol and cloud layers. The stratocumulus environment is shown to be perturbed significantly by the smoke, but these estimates are somehow uncertain due to the misrepresentations found. This further demonstrates that each study domain is different and that an optimal model configuration needs to be found for each case.

Future directions

Even though independent studies were performed, directions where future work has to point towards often overlap. A repeated aspect has to do with model resolution, which seems to be sometimes insufficient to represent different processes, as in the cases of land to ocean transition in southeast Pacific and Atlantic stratocumulus decks, or urban scale gradients as in the AOD assimilation studies performed over California, or convective cells of smaller scales in the severe weather study. In all these cases, further studies should specify finer grid resolutions to attempt to resolve these issues, in the way that it is allowable by the computational resources. Similarly, there are cases where simulations could be improved by spatially extending the domains with finer resolutions, like the case of the Santiago forecast where the inner 2km domain could be extended up to the coast and stretch north to south to cover a larger portion of the Andes and valleys to better resolve the passing of the meteorological disturbances that generate episodes, or for the Namibian stratocumulus simulation where the inner 12km domain could cover the fire emission region to better resolve smoke transport towards the ocean. These

recommendations are based in good experiences with large and fine resolution single domains, such as the southeast Pacific and US domains for the VOCALS-REx and SEAC4RS campaigns, respectively.

The data assimilation studies showed that the modeled aerosol state can be improved significantly by using observations to constrain the system. Extensive years of experience on meteorological data assimilation have shown that simultaneously including diverse observational data sets in the process can generate further improvements. This should be the path to follow in chemical data assimilation as well, which is why our developments point towards using tools such as GSI which were originally developed for meteorological data assimilation an have these capabilities. The first example would be to complement the two techniques shown in this thesis (AOD and cloud data) to see to what extent they can complement each other. There are many examples of other data that can be incorporated to the forecasts. First, ground based data such as $PM_{2.5}$ (Schwartz *et al.*, 2012), AERONET(Schutgens *et al.*, 2010) or lidar (Wang *et al.*, 2013) networks could provide high reliability but low spatial coverage which can be complemented with the larger spatial coverage but more uncertain satellite retrievals. On the satellite side, there are a number of retrievals to be explored. One group contains other MODIS products such as Deep blue retrievals (Hsu *et al.*, 2004) which would improve biases of the dark target retrieval on bright surfaces, or above cloud AOD retrievals (Jethva *et al.*, 2013) in the case of cloudy scenes and thick aerosol layers as in the southeast Atlantic. Also, other sensors or satellite can be included in the analysis, as retrievals from other instruments (e.g., Wang *et al.*, 2012), or from other low earth orbiting (Suomi-NPP VIIRS) or geostationary satellites (Park *et al.*, 2013). Other important retrievals that could provide additional information correspond to single scattering albedo estimates, which could selectively constrain absorbing aerosol. As shown in our AOD assimilation study, all satellite retrievals should go under a correction mechanism which would improve performance. In this sense, corrected multi-wavelength retrievals should be the next step

to fully validate the incorporation of this data to the assimilation. Validation of all these techniques should include incorporation of both permanent monitoring stations and field experiment data.

The number of studies that can be performed to evaluate aerosol effects on different environments with a tool such as WRF-Chem is extensive. In the severe weather area, a more detailed case by case study needs to be performed to find tornado outbreaks that could potentially be affected by smoke or other aerosols and evaluate these effects. Also, other severe weather events need to be evaluated in the same manner. On the persistent stratocumulus deck cases (southeast and northeast Pacific, and southeast Atlantic) further studies can be performed. There are close to shore field campaign observations (e.g., VOCALS-REx, ARCTAS-CARB, CALNEX) that could be explored and used to evaluate aerosol effects with higher resolution simulations. Effects of aerosol other than smoke (e.g., anthropogenic, dust, secondary organic aerosol, absorbing organic aerosol and sea-salt) on the cloud deck properties and the marine environment can be performed to better understand the relative impact of human influences. In the same cloud deck environment, an important study would be to compare the effects of aerosols between high resolution models (as WRF-Chem) and global models, to find if there are significant differences or advantages when using regional models. This is important as climate change assessments are usually performed with global models, thus finding fundamental differences could lead to a shift in the strategy used to estimate climate change.

Final remarks

The main objective of advancing in accurate predictions of aerosol and its effects has been achieved throughout the thesis. Detailed recommendations were provided on the configuration and elements needed to achieve modeling improvements. Also, future steps on how to keep advancing have been established for other researchers to be able to use

this document as guidance. We hope this document is useful for understanding some of the capabilities of the WRF-Chem system and how diverse its applications can be.

REFERENCES

Abdul-Razzak, H., and Ghan, S. J.: A parameterization of aerosol activation 3. Sectional representation, J. Geophys. Res., 107, 4026, 10.1029/2001jd000483, 2002.

Abel, S. J., Walters, D. N., and Allen, G.: Evaluation of stratocumulus cloud prediction in the Met Office forecast model during VOCALS-REx, Atmos. Chem. Phys., 10, 10541-10559, 10.5194/acp-10-10541-2010, 2010.

Ackerman, A. S., Toon, O., Stevens, D., Heymsfield, A., Ramanathan, V., and Welton, E.: Reduction of tropical cloudiness by soot, Science, 288, 1042, 2000.

Adhikary, B., Kulkarni, S., Dallura, A., Tang, Y., Chai, T., Leung, L. R., Qian, Y., Chung, C. E., Ramanathan, V., and Carmichael, G. R.: A regional scale chemical transport modeling of Asian aerosols with data assimilation of AOD observations using optimal interpolation technique, Atmos. Environ., 42, 8600-8615, http://dx.doi.org/10.1016/j.atmosenv.2008.08.031, 2008.

Albrecht, B. A.: Aerosols, cloud microphysics, and fractional cloudiness, Science, 245, 1227, 1989.

Allen, G., Coe, H., Clarke, A., Bretherton, C., Wood, R., Abel, S., Barrett, P., Brown, P., George, R., and Freitag, S.: South East Pacific atmospheric composition and variability sampled along 20◦ S during VOCALS-REx, Atmos. Chem. Phys, 11, 5237-5262, 2011.

Andreae, M. O., Rosenfeld, D., Artaxo, P., Costa, A. A., Frank, G. P., Longo, K. M., and Silva-Dias, M. A. F.: Smoking Rain Clouds over the Amazon, Science, 303, 1337-1342, 10.1126/science.1092779, 2004.

Andrejczuk, M., Grabowski, W. W., Gadian, A., and Burton, R.: Limited-area modelling of stratocumulus over South-Eastern Pacific, Atmos. Chem. Phys. Discuss., 11, 25517-25556, 10.5194/acpd-11-25517-2011, 2011.

Andronache, C., Donner, L. J., Seman, C. J., Ramaswamy, V., and Hemler, R. S.: Atmospheric sulfur and deep convective clouds in tropical Pacific: A model study, Journal of Geophysical Research: Atmospheres, 104, 4005-4024, 10.1029/1998jd200085, 1999.

Auligné, T., Lorenc, A., Michel, Y., Montmerle, T., Jones, A., Hu, M., and Dudhia, J.: Toward a new cloud analysis and prediction system, Bull. Am. Meteorol. Soc, 92, 207-210, 2011.

Baklanov, A.: Overview of the European project FUMAPEX, Atmos. Chem. Phys., 6, 2005-2015, 10.5194/acp-6-2005-2006, 2006.

Baklanov, A., Hänninen, O., Slørdal, L. H., Kukkonen, J., Bjergene, N., Fay, B., Finardi, S., Hoe, S. C., Jantunen, M., Karppinen, A., Rasmussen, A., Skouloudis, A., Sokhi, R. S., Sørensen, J. H., and Ødegaard, V.: Integrated systems for forecasting urban meteorology, air pollution and population exposure, Atmos. Chem. Phys., 7, 855-874, 10.5194/acp-7-855-2007, 2007.

Baklanov, A., Mestayer, P. G., Clappier, A., Zilitinkevich, S., Joffre, S., Mahura, A., and Nielsen, N. W.: Towards improving the simulation of meteorological fields in urban areas through updated/advanced surface fluxes description, Atmos. Chem. Phys., 8, 523-543, 10.5194/acp-8-523-2008, 2008.

Baklanov, A.: Integrated systems of meso-meteorological and chemical transport models, Springer, 2011.

Barnard, J. C., Fast, J. D., Paredes-Miranda, G., Arnott, W. P., and Laskin, A.: Technical Note: Evaluation of the WRF-Chem "Aerosol Chemical to Aerosol Optical Properties" Module using data from the MILAGRO campaign, Atmos. Chem. Phys., 10, 7325-7340, 10.5194/acp-10-7325-2010, 2010.

Barth, M. F., Chadwick, R. B., and Kamp, D. W.: Data processing algorithms used by NOAA's wind profiler demonstration network, Annales Geophysicae, 12, 518-528, 10.1007/s00585-994-0518-1, 1994.

Bator, A., and Collett, J. L.: Cloud chemistry varies with drop size, Journal of Geophysical Research: Atmospheres, 102, 28071-28078, 10.1029/97jd02306, 1997.

Bauer, P., Ohring, G., Kummerow, C., and Auligne, T.: Assimilating satellite observations of clouds and precipitation into NWP models, Bulletin of the American Meteorological Society, 92, 25, 2011.

Bell, T. L., Rosenfeld, D., Kim, K.-M., Yoo, J.-M., Lee, M.-I., and Hahnenberger, M.: Midweek increase in U.S. summer rain and storm heights suggests air pollution invigorates rainstorms, Journal of Geophysical Research: Atmospheres, 113, D02209, 10.1029/2007jd008623, 2008.

Bell, T. L., Rosenfeld, D., and Kim, K.-M.: Weekly cycle of lightning: Evidence of storm invigoration by pollution, Geophys. Res. Lett., 36, L23805, 10.1029/2009gl040915, 2009a.

Bell, T. L., Yoo, J.-M., and Lee, M.-I.: Note on the weekly cycle of storm heights over the southeast United States, Journal of Geophysical Research: Atmospheres, 114, D15201, 10.1029/2009jd012041, 2009b.

Bellouin, N., Boucher, O., Haywood, J., and Reddy, M. S.: Global estimate of aerosol direct radiative forcing from satellite measurements, Nature, 438, 1138-1141, 2005.

Benedetti, A., Morcrette, J., Boucher, O., Dethof, A., Engelen, R., Fisher, M., Flentje, H., Huneeus, N., Jones, L., and Kaiser, J.: Aerosol analysis and forecast in the European Centre for Medium-Range Weather Forecasts Integrated Forecast System: 2. Data assimilation, J. Geophys. Res, 114, D13205, 2009.

Benedict, K. B., Lee, T., and Collett Jr, J. L.: Cloud water composition over the southeastern Pacific Ocean during the VOCALS regional experiment, Atmos. Environ., 46, 104-114, http://dx.doi.org/10.1016/j.atmosenv.2011.10.029, 2012.

Bennartz, R.: Global assessment of marine boundary layer cloud droplet number concentration from satellite, J. Geophys. Res, 112, D02201, 2007.

Berg, L. K., Berkowitz, C. M., Barnard, J. C., Senum, G., and Springston, S. R.: Observations of the first aerosol indirect effect in shallow cumuli, Geophys. Res. Lett., 38, L03809, 2011.

Berner, A. H., Bretherton, C. S., and Wood, R.: Large-eddy simulation of mesoscale dynamics and entrainment around a pocket of open cells observed in VOCALS-REx RF06, Atmos. Chem. Phys., 11, 10525-10540, 10.5194/acp-11-10525-2011, 2011.

Bocquet, M., Pires, C. A., and Wu, L.: Beyond Gaussian statistical modeling in geophysical data assimilation, Monthly Weather Review, 138, 2997-3023, 2010.

Bony, S., and Dufresne, J.-L.: Marine boundary layer clouds at the heart of tropical cloud feedback uncertainties in climate models, Geophys. Res. Lett., 32, L20806, 10.1029/2005gl023851, 2005.

Bretherton, C., Wood, R., George, R., Leon, D., Allen, G., and Zheng, X.: Southeast Pacific stratocumulus clouds, precipitation and boundary layer structure sampled along 20◦ S during VOCALS-REx, Atmos. Chem. Phys, 10, 10639-10654, 2010.

Brioude, J., Cooper, O. R., Feingold, G., Trainer, M., Freitas, S. R., Kowal, D., Ayers, J. K., Prins, E., Minnis, P., McKeen, S. A., Frost, G. J., and Hsie, E. Y.: Effect of biomass burning on marine stratocumulus clouds off the California coast, Atmos. Chem. Phys., 9, 8841-8856, 10.5194/acp-9-8841-2009, 2009.

Bunkers, M. J., Klimowski, B. A., Zeitler, J. W., Thompson, R. L., and Weisman, M. L.: Predicting Supercell Motion Using a New Hodograph Technique, Weather and Forecasting, 15, 61-79, 10.1175/1520-0434(2000)015<0061:psmuan>2.0.co;2, 2000.

Carmichael, G. R., Adhikary, B., Kulkarni, S., D'Allura, A., Tang, Y., Streets, D., Zhang, Q., Bond, T. C., Ramanathan, V., and Jamroensan, A.: Asian aerosols: current and year 2030 distributions and implications to human health and regional climate change, Environmental science & technology, 43, 5811-5817, 2009.

Cassmassi, J.: Improvement of the forecast of air quality and of the knowledge of the local meteorological conditions in the Metropolitan region, Informe final, CONAMA RM, 1999.

Cess, R. D., Potter, G. L., Blanchet, J. P., Boer, G. J., Ghan, S. J., Kiehl, J. T., Le Treut, H., Li, Z.-X., Liang, X.-Z., Mitchell, J. F. B., Morcrette, J.-J., Randall, D. A., R., R. M., Roeckner, E., Schlese, U., Slingo, A., Taylor, K. E., Washington, W. M., Wetherald, R. T., and Yagai, I.: Interpretation of Cloud-Climate Feedback as Produced by 14 Atmospheric General Circulation Models, Science, 245, 513-516, 10.1126/science.245.4917.513, 1989.

Chand, D., Hegg, D. A., Wood, R., Shaw, G. E., Wallace, D., and Covert, D. S.: Source attribution of climatically important aerosol properties measured at Paposo (Chile) during VOCALS, Atmos. Chem. Phys., 10, 10789-10801, 10.5194/acp-10-10789-2010, 2010.

Chapman, E., Gustafson Jr, W., Easter, R., Barnard, J., Ghan, S., Pekour, M., and Fast, J.: Coupling aerosol-cloud-radiative processes in the WRF-Chem model:

Investigating the radiative impact of elevated point sources, Atmos. Chem. Phys., 9, 945-964, 2009.

Chen, F., and Dudhia, J.: Coupling an advanced land surface-hydrology model with the Penn State-NCAR MM5 modeling system. Part I: Model implementation and sensitivity, Monthly Weather Review, 129, 569-585, 2001.

Chen, Y. C., Xue, L., Lebo, Z. J., Wang, H., Rasmussen, R. M., and Seinfeld, J. H.: A comprehensive numerical study of aerosol-cloud-precipitation interactions in marine stratocumulus, Atmos. Chem. Phys., 11, 9749-9769, 10.5194/acp-11-9749-2011, 2011.

Chou, M.-D., Suarez, M. J., Ho, C.-H., Yan, M. M., and Lee, K.-T.: Parameterizations for cloud overlapping and shortwave single-scattering properties for use in general circulation and cloud ensemble models, Journal of climate, 11, 202-214, 1998.

Chung, S. H., and Seinfeld, J. H.: Climate response of direct radiative forcing of anthropogenic black carbon, Journal of Geophysical Research: Atmospheres, 110, D11102, 10.1029/2004jd005441, 2005.

Cintineo, R., Otkin, J. A., Xue, M., and Kong, F.: Evaluating the Performance of Planetary Boundary Layer and Cloud Microphysical Parameterization Schemes in Convection-Permitting Ensemble Forecasts using Synthetic GOES-13 Satellite Observations, Monthly Weather Review, Under review, 2013.

Coddington, O., Pilewskie, P., Redemann, J., Platnick, S., Russell, P., Schmidt, K., Gore, W., Livingston, J., Wind, G., and Vukicevic, T.: Examining the impact of overlying aerosols on the retrieval of cloud optical properties from passive remote sensing, Journal of Geophysical Research: Atmospheres (1984–2012), 115, 2010.

Comstock, K. K., Wood, R., Yuter, S. E., and Bretherton, C. S.: Reflectivity and rain rate in and below drizzling stratocumulus, Quarterly Journal of the Royal Meteorological Society, 130, 2891-2918, 10.1256/qj.03.187, 2004.

CONAMA: Update of the Atmospheric Emission Inventories for Santiago 2005. Final Technical Report by DICTUC, January 2007, http://www.sinia.cl/1292/articles-49590_inf_final_inventario.pdf, 2007.

Corvalán, R. M., Osses, M., and Urrutia, C. M.: Hot Emission Model for Mobile Sources: Application to the Metropolitan Region of the City of Santiago, Chile, Journal of the Air & Waste Management Association, 52, 167-174, 10.1080/10473289.2002.10470774, 2002.

Costantino, L., and Bréon, F. M.: Aerosol indirect effect on warm clouds over South-East Atlantic, from co-located MODIS and CALIPSO observations, Atmos. Chem. Phys. Discuss., 12, 14197-14246, 10.5194/acpd-12-14197-2012, 2012.

Darmenov, A., and da Silva, A. M.: The Quick Fire Emissions Dataset (QFED) - Documentation of versions 2.1, 2.2 and 2.4, NASA TM-2013-104606, Vol. 32, (http://gmao.gsfc.nasa.gov/pubs/tm/), 183 pp, 2013.

Davies, D. K., Ilavajhala, S., Wong, M. M., and Justice, C. O.: Fire Information for Resource Management System: Archiving and Distributing MODIS Active Fire

Data, Geoscience and Remote Sensing, IEEE Transactions on, 47, 72-79, 10.1109/tgrs.2008.2002076, 2009.

de Szoeke, S. P., Fairall, C. W., Wolfe, D. E., Bariteau, L., and Zuidema, P.: Surface Flux Observations on the Southeastern Tropical Pacific Ocean and Attribution of SST Errors in Coupled Ocean–Atmosphere Models, Journal of climate, 23, 4152-4174, 10.1175/2010jcli3411.1, 2010.

DeCarlo, P. F., Kimmel, J. R., Trimborn, A., Northway, M. J., Jayne, J. T., Aiken, A. C., Gonin, M., Fuhrer, K., Horvath, T., Docherty, K. S., Worsnop, D. R., and Jimenez, J. L.: Field-Deployable, High-Resolution, Time-of-Flight Aerosol Mass Spectrometer, Analytical Chemistry, 78, 8281-8289, 10.1021/ac061249n, 2006.

Diamond, H. J., Karl, T. R., Palecki, M. A., Baker, C. B., Bell, J. E., Leeper, R. D., Easterling, D. R., Lawrimore, J. H., Meyers, T. P., Helfert, M. R., Goodge, G., and Thorne, P. W.: U.S. Climate Reference Network after One Decade of Operations: Status and Assessment, Bulletin of the American Meteorological Society, 94, 485-498, 10.1175/bams-d-12-00170.1, 2013.

Dobson, J. E., Coleman, P. R., Durfee, R. C., and Worley, B. A.: LandScan: a global population database for estimating populations at risk, Photogrammetric engineering and remote sensing, 66, 849-857, 2000.

Doswell Iii, C. A., Carbin, G. W., and Brooks, H. E.: The tornadoes of spring 2011 in the USA: an historical perspective, Weather, 67, 88-94, 10.1002/wea.1902, 2012.

DTC: Unified Post Processor, http://www.dtcenter.org/wrf-nmm/users/overview/upp_updates.php, 2013.

Dubovik, O., and King, M. D.: A flexible inversion algorithm for retrieval of aerosol optical properties from Sun and sky radiance measurements, Journal of Geophysical Research: Atmospheres, 105, 20673-20696, 10.1029/2000jd900282, 2000.

Dubovik, O., Smirnov, A., Holben, B. N., King, M. D., Kaufman, Y. J., Eck, T. F., and Slutsker, I.: Accuracy assessments of aerosol optical properties retrieved from Aerosol Robotic Network (AERONET) Sun and sky radiance measurements, Journal of Geophysical Research: Atmospheres, 105, 9791-9806, 10.1029/2000jd900040, 2000.

Dudhia, J.: Numerical Study of Convection Observed during the Winter Monsoon Experiment Using a Mesoscale Two-Dimensional Model, Journal of the atmospheric sciences, 46, 3077-3107, 10.1175/1520-0469(1989)046<3077:nsocod>2.0.co;2, 1989.

Dunagan, S., Johnson, R., Zavaleta, J., Russell, P., Schmid, B., Flynn, C., Redemann, J., Shinozuka, Y., Livingston, J., and Segal-Rosenhaimer, M.: Spectrometer for Sky-Scanning Sun-Tracking Atmospheric Research (4STAR): Instrument Technology, Remote Sensing, 5, 3872-3895, 2013.

Dunstone, N. J., Smith, D. M., Booth, B. B. B., Hermanson, L., and Eade, R.: Anthropogenic aerosol forcing of Atlantic tropical storms, Nature Geosci, advance online publication, 10.1038/ngeo1854

http://www.nature.com/ngeo/journal/vaop/ncurrent/abs/ngeo1854.html#supplementary-information, 2013.

Easter, R. C., Ghan, S. J., Zhang, Y., Saylor, R. D., Chapman, E. G., Laulainen, N. S., Abdul-Razzak, H., Leung, L. R., Bian, X., and Zaveri, R. A.: MIRAGE: Model description and evaluation of aerosols and trace gases, Journal of Geophysical Research: Atmospheres, 109, D20210, 10.1029/2004jd004571, 2004.

Elbern, H., Strunk, A., Schmidt, H., and Talagrand, O.: Emission rate and chemical state estimation by 4-dimensional variational inversion, Atmos. Chem. Phys., 7, 3749-3769, 10.5194/acp-7-3749-2007, 2007.

Emmons, L. K., Walters, S., Hess, P. G., Lamarque, J. F., Pfister, G. G., Fillmore, D., Granier, C., Guenther, A., Kinnison, D., Laepple, T., Orlando, J., Tie, X., Tyndall, G., Wiedinmyer, C., Baughcum, S. L., and Kloster, S.: Description and evaluation of the Model for Ozone and Related chemical Tracers, version 4 (MOZART-4), Geosci. Model Dev., 3, 43-67, 10.5194/gmd-3-43-2010, 2010.

Environmental Modeling Center: The GFS atmospheric model, NCEP Office Note, 442, 2003.

EPA: National Trends in Nitrogen Dioxide Levels, http://www.epa.gov/airtrends/nitrogen.html, 2013a.

EPA: http://www.epa.gov/ttn/airs/airsaqs/, 2013b.

Errico, R. M., Bauer, P., and Mahfouf, J.-F.: Issues Regarding the Assimilation of Cloud and Precipitation Data, Journal of the atmospheric sciences, 64, 3785-3798, 10.1175/2006jas2044.1, 2007.

Evan, A. T., Kossin, J. P., Eddy/' Chung, C., and Ramanathan, V.: Arabian Sea tropical cyclones intensified by emissions of black carbon and other aerosols, Nature, 479, 94-97, http://www.nature.com/nature/journal/v479/n7371/abs/nature10552.html#supplementary-information, 2011.

Fahey, K. M., and Pandis, S. N.: Optimizing model performance: variable size resolution in cloud chemistry modeling, Atmos. Environ., 35, 4471-4478, http://dx.doi.org/10.1016/S1352-2310(01)00224-2, 2001.

Fast, J. D., and Easter, R. C.: A Lagrangian particle dispersion model compatible with WRF, 7th Annual WRF User's Workshop, 2006, 19-22,

Fast, J. D., Gustafson Jr, W. I., Easter, R. C., Zaveri, R. A., Barnard, J. C., Chapman, E. G., Grell, G. A., and Peckham, S. E.: Evolution of ozone, particulates, and aerosol direct radiative forcing in the vicinity of Houston using a fully coupled meteorology-chemistry-aerosol model, Journal of Geophysical Research, 111, D21305, 2006.

Fast, J. D., Gustafson Jr, W. I., Berg, L. K., Shaw, W. J., Pekour, M., Shrivastava, M., Barnard, J. C., Ferrare, R. A., Hostetler, C. A., Hair, J. A., Erickson, M., Jobson, B. T., Flowers, B., Dubey, M. K., Springston, S., Pierce, R. B., Dolislager, L., Pederson, J., and Zaveri, R. A.: Transport and mixing patterns over Central

California during the carbonaceous aerosol and radiative effects study (CARES), Atmos. Chem. Phys., 12, 1759-1783, 10.5194/acp-12-1759-2012, 2012.

Fay, B., and Neunhäuserer, L.: Evaluation of high-resolution forecasts with the non-hydrostaticnumerical weather prediction model Lokalmodell for urban air pollutionepisodes in Helsinki, Oslo and Valencia, Atmos. Chem. Phys., 6, 2107-2128, 10.5194/acp-6-2107-2006, 2006.

Feingold, G., Kreidenweis, S. M., Stevens, B., and Cotton, W. R.: Numerical simulations of stratocumulus processing of cloud condensation nuclei through collision-coalescence, Journal of Geophysical Research: Atmospheres, 101, 21391-21402, 10.1029/96jd01552, 1996.

Feingold, G., Walko, R. L., Stevens, B., and Cotton, W. R.: Simulations of marine stratocumulus using a new microphysical parameterization scheme, Atmospheric Research, 47–48, 505-528, http://dx.doi.org/10.1016/S0169-8095(98)00058-1, 1998.

Feingold, G.: Modeling of the first indirect effect: Analysis of measurement requirements, Geophys. Res. Lett., 30, 1997, 2003.

Feingold, G., Jiang, H., and Harrington, J. Y.: On smoke suppression of clouds in Amazonia, Geophys. Res. Lett., 32, L02804, 10.1029/2004gl021369, 2005.

Finardi, S., De Maria, R., D'Allura, A., Cascone, C., Calori, G., and Lollobrigida, F.: A deterministic air quality forecasting system for Torino urban area, Italy, Environmental Modelling & Software, 23, 344-355, http://dx.doi.org/10.1016/j.envsoft.2007.04.001, 2008.

Freitas, S. R., Longo, K. M., and Andreae, M. O.: Impact of including the plume rise of vegetation fires in numerical simulations of associated atmospheric pollutants, Geophys. Res. Lett., 33, L17808, 10.1029/2006gl026608, 2006.

Freitas, S. R., Longo, K. M., Chatfield, R., Latham, D., Silva Dias, M. A. F., Andreae, M. O., Prins, E., Santos, J. C., Gielow, R., and Carvalho Jr, J. A.: Including the sub-grid scale plume rise of vegetation fires in low resolution atmospheric transport models, Atmos. Chem. Phys., 7, 3385-3398, 10.5194/acp-7-3385-2007, 2007.

Freitas, S. R., Longo, K. M., Alonso, M. F., Pirre, M., Marecal, V., Grell, G., Stockler, R., Mello, R. F., and Sánchez Gácita, M.: PREP-CHEM-SRC – 1.0: a preprocessor of trace gas and aerosol emission fields for regional and global atmospheric chemistry models, Geosci. Model Dev., 4, 419-433, 10.5194/gmd-4-419-2011, 2011.

Gallardo, L., Olivares, G., Langner, J., and Aarhus, B.: Coastal lows and sulfur air pollution in Central Chile, Atmos. Environ., 36, 3829-3841, http://dx.doi.org/10.1016/S1352-2310(02)00285-6, 2002.

Garreaud, R., Rutllant, J., and Fuenzalida, H.: Coastal Lows along the Subtropical West Coast of South America: Mean Structure and Evolution, Monthly Weather Review, 130, 75-88, 10.1175/1520-0493(2002)130<0075:clatsw>2.0.co;2, 2002.

Garreaud, R., and Rutllant, J.: Coastal Lows along the Subtropical West Coast of South America: Numerical Simulation of a Typical Case, Monthly Weather Review, 131, 891-908, 10.1175/1520-0493(2003)131<0891:clatsw>2.0.co;2, 2003.

Garreaud, R., and Muñoz, R. C.: The Low-Level Jet off the West Coast of Subtropical South America: Structure and Variability, Monthly Weather Review, 133, 2246-2261, 10.1175/mwr2972.1, 2005.

Gaspari, G., and Cohn, S. E.: Construction of correlation functions in two and three dimensions, Quarterly Journal of the Royal Meteorological Society, 125, 723-757, 1999.

Generoso, S., Bréon, F. M., Chevallier, F., Balkanski, Y., Schulz, M., and Bey, I.: Assimilation of POLDER aerosol optical thickness into the LMDz-INCA model: Implications for the Arctic aerosol burden, Journal of Geophysical Research: Atmospheres, 112, D02311, 10.1029/2005jd006954, 2007.

George, R., and Wood, R.: Subseasonal variability of low cloud radiative properties over the southeast Pacific Ocean, Atmos. Chem. Phys, 10, 4047-4063, 2010.

Ghan, S. J., and Easter, R. C.: Impact of cloud-borne aerosol representation on aerosol direct and indirect effects, Atmos. Chem. Phys., 6, 4163-4174, 10.5194/acp-6-4163-2006, 2006.

GMAO: http://gmao.gsfc.nasa.gov/forecasts/, 2013.

Gong, S., Barrie, L., and Blanchet, J.-P.: Modeling sea-salt aerosols in the atmosphere 1. Model development, Journal of Geophysical Research, 102, 3805-3818, 1997.

Gramsch, E., Cereceda-Balic, F., Oyola, P., and von Baer, D.: Examination of pollution trends in Santiago de Chile with cluster analysis of PM10 and Ozone data, Atmos. Environ., 40, 5464-5475, http://dx.doi.org/10.1016/j.atmosenv.2006.03.062, 2006.

Grassl, H.: Possible changes of planetary albedo due to aerosol particles, Elsevier, 1979.

Grell, G., Peckham, S. E., Schmitz, R., McKeen, S. A., Frost, G., Skamarock, W. C., and Eder, B.: Fully coupled “online” chemistry within the WRF model, Atmos. Environ., 39, 6957-6975, 10.1016/j.atmosenv.2005.04.027, 2005.

Grell, G., Freitas, S. R., Stuefer, M., and Fast, J.: Inclusion of biomass burning in WRF-Chem: impact of wildfires on weather forecasts, Atmos. Chem. Phys., 11, 5289-5303, 10.5194/acp-11-5289-2011, 2011.

Grell, G. A., and Freitas, S. R.: A scale and aerosol aware stochastic convective parameterization for weather and air quality modeling, Atmos. Chem. Phys. Discuss., 13, 23845-23893, 10.5194/acpd-13-23845-2013, 2013.

Guenther, A., Karl, T., Harley, P., Wiedinmyer, C., Palmer, P. I., and Geron, C.: Estimates of global terrestrial isoprene emissions using MEGAN (Model of Emissions of Gases and Aerosols from Nature), Atmos. Chem. Phys., 6, 3181-3210, 10.5194/acp-6-3181-2006, 2006.

Guenther, A. B., Jiang, X., Heald, C. L., Sakulyanontvittaya, T., Duhl, T., Emmons, L. K., and Wang, X.: The Model of Emissions of Gases and Aerosols from Nature

version 2.1 (MEGAN2.1): an extended and updated framework for modeling biogenic emissions, Geosci. Model Dev., 5, 1471-1492, 10.5194/gmd-5-1471-2012, 2012.

Gustafson, W. I., Chapman, E. G., Ghan, S. J., Easter, R. C., and Fast, J. D.: Impact on modeled cloud characteristics due to simplified treatment of uniform cloud condensation nuclei during NEAQS 2004, Geophys. Res. Lett., 34, L19809, 10.1029/2007gl030021, 2007.

Hair, J. W., Hostetler, C. A., Cook, A. L., Harper, D. B., Ferrare, R. A., Mack, T. L., Welch, W., Izquierdo, L. R., and Hovis, F. E.: Airborne High Spectral Resolution Lidar for profiling aerosol optical properties, Appl. Opt., 47, 6734-6752, 10.1364/ao.47.006734, 2008.

Hamdi, R., and Schayes, G.: Validation of Martilli's urban boundary layer scheme with measurements from two mid-latitude European cities, Atmos. Chem. Phys., 7, 4513-4526, 10.5194/acp-7-4513-2007, 2007.

Han, Y., van Delst, P., Liu, Q., Weng, F., Yan, B., Treadon, R., and Derber, J.: JCSDA Community Radiative Transfer Model (CRTM), Tech. Rep. 122, NOAA, 2006.

Hascoët, L., and Pascual, V.: TAPENADE 2.1 user's guide, INRIA Technical Report #0300, 2004.

Hawkins, L. N., Russell, L. M., Covert, D. S., Quinn, P. K., and Bates, T. S.: Carboxylic acids, sulfates, and organosulfates in processed continental organic aerosol over the southeast Pacific Ocean during VOCALS-REx 2008, Journal of Geophysical Research: Atmospheres, 115, D13201, 10.1029/2009jd013276, 2010.

Haywood, J. M., and Ramaswamy, V.: Global sensitivity studies of the direct radiative forcing due to anthropogenic sulfate and black carbon aerosols, Journal of Geophysical Research: Atmospheres, 103, 6043-6058, 10.1029/97jd03426, 1998.

Heald, C. L., Ridley, D. A., Kreidenweis, S. M., and Drury, E. E.: Satellite observations cap the atmospheric organic aerosol budget, Geophys. Res. Lett, 37, L24808, 2010.

Hegg, D. A., Covert, D. S., Jonsson, H. H., and Woods, R. K.: A simple relationship between cloud drop number concentration and precursor aerosol concentration for the regions of Earth's large marine stratocumulus decks, Atmos. Chem. Phys., 12, 1229-1238, 10.5194/acp-12-1229-2012, 2012.

Henze, D. K., Seinfeld, J. H., and Shindell, D. T.: Inverse modeling and mapping US air quality influences of inorganic PM2. 5 precursor emissions using the adjoint of GEOS-Chem, Atmos. Chem. Phys. Discuss., 8, 15,031-015,099, 2008.

Henze, D. K., Seinfeld, J. H., and Shindell, D. T.: Inverse modeling and mapping US air quality influences of inorganic PM2.5 precursor emissions using the adjoint of GEOS-Chem, Atmos. Chem. Phys., 9, 5877-5903, 10.5194/acp-9-5877-2009, 2009.

Hind, A. J., Rauschenberg, C. D., Johnson, J. E., Yang, M., and Matrai, P. A.: The use of algorithms to predict surface seawater dimethyl sulphide concentrations in the SE

Pacific, a region of steep gradients in primary productivity, biomass and mixed layer depth, Biogeosciences, 8, 1-16, 10.5194/bg-8-1-2011, 2011.

Hinds, W. C.: Aerosol technology: properties, behavior, and measurement of airborne particles, Wiley-interscience, 2012.

Hodzic, A., and Jimenez, J. L.: Modeling anthropogenically controlled secondary organic aerosols in a megacity: a simplified framework for global and climate models, Geosci. Model Dev., 4, 901-917, 10.5194/gmd-4-901-2011, 2011.

Hoffmann, M. R., and Calvert, J. G.: Chemical Transformation Modules for Eulerian Acid Deposition Models: Volume II, the Aqueous-phase Chemistry, Atmospheric Sciences Research Laboratory, Office of Research and Development, US Environmental Protection Agency, 1985.

Holben, B., Tanré, D., Smirnov, A., Eck, T., Slutsker, I., Abuhassan, N., Newcomb, W., Schafer, J., Chatenet, B., and Lavenu, F.: An emerging ground-based aerosol climatology: Aerosol optical depth from AERONET, Journal of Geophysical Research, 106, 12067-12012,12097, 2001.

Hong, S.-Y., Dudhia, J., and Chen, S.-H.: A Revised Approach to Ice Microphysical Processes for the Bulk Parameterization of Clouds and Precipitation, Monthly Weather Review, 132, 103-120, 10.1175/1520-0493(2004)132<0103:aratim>2.0.co;2, 2004.

Hong, S.-Y.: A new stable boundary-layer mixing scheme and its impact on the simulated East Asian summer monsoon, Quarterly Journal of the Royal Meteorological Society, 136, 1481-1496, 10.1002/qj.665, 2010.

Hsu, N. C., Si-Chee, T., King, M. D., and Herman, J. R.: Aerosol properties over bright-reflecting source regions, Geoscience and Remote Sensing, IEEE Transactions on, 42, 557-569, 10.1109/tgrs.2004.824067, 2004.

Huang, M., Carmichael, G. R., Adhikary, B., Spak, S. N., Kulkarni, S., Cheng, Y. F., Wei, C., Tang, Y., Parrish, D. D., Oltmans, S. J., D'Allura, A., Kaduwela, A., Cai, C., Weinheimer, A. J., Wong, M., Pierce, R. B., Al-Saadi, J. A., Streets, D. G., and Zhang, Q.: Impacts of transported background ozone on California air quality during the ARCTAS-CARB period – a multi-scale modeling study, Atmos. Chem. Phys., 10, 6947-6968, 10.5194/acp-10-6947-2010, 2010.

Huang, M., Carmichael, G. R., Spak, S. N., Adhikary, B., Kulkarni, S., Cheng, Y., Wei, C., Tang, Y., D'Allura, A., Wennberg, P. O., Huey, G. L., Dibb, J. E., Jimenez, J. L., Cubison, M. J., Weinheimer, A. J., Kaduwela, A., Cai, C., Wong, M., Bradley Pierce, R., Al-Saadi, J. A., Streets, D. G., and Zhang, Q.: Multi-scale modeling study of the source contributions to near-surface ozone and sulfur oxides levels over California during the ARCTAS-CARB period, Atmos. Chem. Phys., 11, 3173-3194, 10.5194/acp-11-3173-2011, 2011.

Huneeus, N., Chevallier, F., and Boucher, O.: Estimating aerosol emissions by assimilating observed aerosol optical depth in a global aerosol model, Atmos. Chem. Phys., 12, 4585-4606, 10.5194/acp-12-4585-2012, 2012.

Hyer, E. J., Reid, J. S., and Zhang, J.: An over-land aerosol optical depth data set for data assimilation by filtering, correction, and aggregation of MODIS Collection 5

optical depth retrievals, Atmos. Meas. Tech., 4, 379-408, 10.5194/amt-4-379-2011, 2011.

Inness, A., Baier, F., Benedetti, A., Bouarar, I., Chabrillat, S., Clark, H., Clerbaux, C., Coheur, P., Engelen, R. J., Errera, Q., Flemming, J., George, M., Granier, C., Hadji-Lazaro, J., Huijnen, V., Hurtmans, D., Jones, L., Kaiser, J. W., Kapsomenakis, J., Lefever, K., Leitão, J., Razinger, M., Richter, A., Schultz, M. G., Simmons, A. J., Suttie, M., Stein, O., Thépaut, J. N., Thouret, V., Vrekoussis, M., Zerefos, C., and the, M. t.: The MACC reanalysis: an 8 yr data set of atmospheric composition, Atmos. Chem. Phys., 13, 4073-4109, 10.5194/acp-13-4073-2013, 2013.

Jacob, D. J., Crawford, J. H., Maring, H., Clarke, A. D., Dibb, J. E., Emmons, L. K., Ferrare, R. A., Hostetler, C. A., Russell, P. B., Singh, H. B., Thompson, A. M., Shaw, G. E., McCauley, E., Pederson, J. R., and Fisher, J. A.: The Arctic Research of the Composition of the Troposphere from Aircraft and Satellites (ARCTAS) mission: design, execution, and first results, Atmos. Chem. Phys., 10, 5191-5212, 10.5194/acp-10-5191-2010, 2010.

Janjić, Z. I.: Nonsingular implementation of the Mellor–Yamada level 2.5 scheme in the NCEP Meso model, NCEP Office Note, No. 437, pp. 61.,

Janjić, Z. I.: Nonsingular implementation of the Mellor–Yamada level 2.5 scheme in the NCEP Meso model, NCEP office note, 437, 61, 2002.

Jethva, H., Torres, O., Remer, L. A., and Bhartia, P. K.: A Color Ratio Method for Simultaneous Retrieval of Aerosol and Cloud Optical Thickness of Above-Cloud Absorbing Aerosols From Passive Sensors: Application to MODIS Measurements, Geoscience and Remote Sensing, IEEE Transactions on, PP, 1-9, 10.1109/tgrs.2012.2230008, 2013.

Jiang, Z., Liu, Z., Wang, T., Schwartz, C. S., Lin, H.-C., and Jiang, F.: Probing into the impact of 3DVAR assimilation of surface PM10 observations over China using process analysis, Journal of Geophysical Research: Atmospheres, 118, 6738-6749, 10.1002/jgrd.50495, 2013.

Jones, C. R., Bretherton, C. S., and Leon, D.: Coupled vs. decoupled boundary layers in VOCALS-REx, Atmos. Chem. Phys., 11, 7143-7153, 10.5194/acp-11-7143-2011, 2011.

Jorquera, H., and Castro, J.: Analysis of urban pollution episodes by inverse modeling, Atmos. Environ., 44, 42-54, http://dx.doi.org/10.1016/j.atmosenv.2009.09.040, 2010.

Kahn, R. A., Garay, M. J., Nelson, D. L., Yau, K. K., Bull, M. A., Gaitley, B. J., Martonchik, J. V., and Levy, R. C.: Satellite-derived aerosol optical depth over dark water from MISR and MODIS: Comparisons with AERONET and implications for climatological studies, J. Geophys. Res, 112, D18, 2007.

Kalenderski, S., Stenchikov, G., and Zhao, C.: Modeling a typical winter-time dust event over the Arabian Peninsula and the Red Sea, Atmos. Chem. Phys., 13, 1999-2014, 10.5194/acp-13-1999-2013, 2013.

Kalnay, E.: Atmospheric modeling, data assimilation, and predictability, Cambridge Univ Pr, 2003.

Kanakidou, M., Seinfeld, J. H., Pandis, S. N., Barnes, I., Dentener, F. J., Facchini, M. C., Van Dingenen, R., Ervens, B., Nenes, A., Nielsen, C. J., Swietlicki, E., Putaud, J. P., Balkanski, Y., Fuzzi, S., Horth, J., Moortgat, G. K., Winterhalter, R., Myhre, C. E. L., Tsigaridis, K., Vignati, E., Stephanou, E. G., and Wilson, J.: Organic aerosol and global climate modelling: a review, Atmos. Chem. Phys., 5, 1053-1123, 10.5194/acp-5-1053-2005, 2005.

Kanamitsu, M., Ebisuzaki, W., Woollen, J., Yang, S.-K., Hnilo, J. J., Fiorino, M., and Potter, G. L.: NCEP–DOE AMIP-II Reanalysis (R-2), Bulletin of the American Meteorological Society, 83, 1631-1643, 10.1175/bams-83-11-1631, 2002.

Karydis, V. A., Capps, S. L., Russell, A. G., and Nenes, A.: Adjoint sensitivity of global cloud droplet number to aerosol and dynamical parameters, Atmos. Chem. Phys. Discuss., 12, 12081-12117, 10.5194/acpd-12-12081-2012, 2012.

Kaufman, Y. J., Tanré, D., Remer, L. A., Vermote, E. F., Chu, A., and Holben, B. N.: Operational remote sensing of tropospheric aerosol over land from EOS moderate resolution imaging spectroradiometer, Journal of Geophysical Research: Atmospheres, 102, 17051-17067, 10.1029/96jd03988, 1997.

Kazil, J., Wang, H., Feingold, G., Clarke, A. D., Snider, J. R., and Bandy, A. R.: Modeling chemical and aerosol processes in the transition from closed to open cells during VOCALS-REx, Atmos. Chem. Phys., 11, 7491-7514, 10.5194/acp-11-7491-2011, 2011.

Khairoutdinov, M., and Kogan, Y.: A New Cloud Physics Parameterization in a Large-Eddy Simulation Model of Marine Stratocumulus, Monthly Weather Review, 128, 229-243, 10.1175/1520-0493(2000)128<0229:ancppi>2.0.co;2, 2000.

Kim, S. W., Heckel, A., Frost, G. J., Richter, A., Gleason, J., Burrows, J. P., McKeen, S., Hsie, E. Y., Granier, C., and Trainer, M.: NO2 columns in the western United States observed from space and simulated by a regional chemistry model and their implications for NOx emissions, Journal of Geophysical Research: Atmospheres, 114, n/a-n/a, 10.1029/2008jd011343, 2009.

Kim, Y., Fu, J. S., and Miller, T. L.: Improving ozone modeling in complex terrain at a fine grid resolution: Part I – examination of analysis nudging and all PBL schemes associated with LSMs in meteorological model, Atmos. Environ., 44, 523-532, http://dx.doi.org/10.1016/j.atmosenv.2009.10.045, 2010.

King, M. D., Platnick, S., Hubanks, P. A., Arnold, G. T., Moody, E. G., Wind, G., and Wind, B.: Collection 005 change summary for the MODIS cloud optical property (06_OD) algorithm, Available: modis-atmos. gsfc. nasa. gov/C005_Changes/C005_ CloudOpticalProperties_ver311. pdf, 2006.

Kistler, R., Collins, W., Saha, S., White, G., Woollen, J., Kalnay, E., Chelliah, M., Ebisuzaki, W., Kanamitsu, M., Kousky, V., van den Dool, H., Jenne, R., and Fiorino, M.: The NCEP–NCAR 50–Year Reanalysis: Monthly Means CD–ROM and Documentation, Bulletin of the American Meteorological Society, 82, 247-267, 10.1175/1520-0477(2001)082<0247:tnnyrm>2.3.co;2, 2001.

Kleidman, R. G., O'Neill, N. T., Remer, L. A., Kaufman, Y. J., Eck, T. F., Tanré, D., Dubovik, O., and Holben, B. N.: Comparison of Moderate Resolution Imaging Spectroradiometer (MODIS) and Aerosol Robotic Network (AERONET) remote-sensing retrievals of aerosol fine mode fraction over ocean, Journal of Geophysical Research: Atmospheres, 110, D22205, 10.1029/2005jd005760, 2005.

Kleinman, L. I., Daum, P. H., Lee, Y. N., Lewis, E. R., Sedlacek Iii, A. J., Senum, G. I., Springston, S. R., Wang, J., Hubbe, J., Jayne, J., Min, Q., Yum, S. S., and Allen, G.: Aerosol concentration and size distribution measured below, in, and above cloud from the DOE G-1 during VOCALS-REx, Atmos. Chem. Phys., 12, 207-223, 10.5194/acp-12-207-2012, 2012.

Kleist, D. T., Parrish, D. F., Derber, J. C., Treadon, R., Wu, W.-S., and Lord, S.: Introduction of the GSI into the NCEP global data assimilation system, Weather and Forecasting, 24, 1691-1705, 2009a.

Kleist, D. T., Parrish, D. F., Derber, J. C., Treadon, R., Wu, W. S., and Lord, S.: Introduction of the GSI into the NCEP global data assimilation system, Weather and Forecasting, 24, 1691-1705, 2009b.

Koch, D., Schulz, M., Kinne, S., McNaughton, C., Spackman, J. R., Balkanski, Y., Bauer, S., Berntsen, T., Bond, T. C., Boucher, O., Chin, M., Clarke, A., De Luca, N., Dentener, F., Diehl, T., Dubovik, O., Easter, R., Fahey, D. W., Feichter, J., Fillmore, D., Freitag, S., Ghan, S., Ginoux, P., Gong, S., Horowitz, L., Iversen, T., Kirkev, aring, g, A., Klimont, Z., Kondo, Y., Krol, M., Liu, X., Miller, R., Montanaro, V., Moteki, N., Myhre, G., Penner, J. E., Perlwitz, J., Pitari, G., Reddy, S., Sahu, L., Sakamoto, H., Schuster, G., Schwarz, J. P., Seland, Ø., Stier, P., Takegawa, N., Takemura, T., Textor, C., van Aardenne, J. A., and Zhao, Y.: Evaluation of black carbon estimations in global aerosol models, Atmos. Chem. Phys., 9, 9001-9026, 10.5194/acp-9-9001-2009, 2009.

Koch, D., and Del Genio, A. D.: Black carbon semi-direct effects on cloud cover: review and synthesis, Atmos. Chem. Phys., 10, 7685-7696, 10.5194/acp-10-7685-2010, 2010.

Kogan, Z. N., Kogan, Y. L., and Lilly, D. K.: Evaluation of sulfate aerosols indirect effect in marine stratocumulus clouds using observation-derived cloud climatology, Geophys. Res. Lett., 23, 1937-1940, 1996.

Koren, I., Kaufman, Y. J., Rosenfeld, D., Remer, L. A., and Rudich, Y.: Aerosol invigoration and restructuring of Atlantic convective clouds, Geophys. Res. Lett, 32, L14828, 2005.

Koren, I., Martins, J. V., Remer, L. A., and Afargan, H.: Smoke invigoration versus inhibition of clouds over the Amazon, Science, 321, 946, 2008.

Lerach, D. G., Gaudet, B. J., and Cotton, W. R.: Idealized simulations of aerosol influences on tornadogenesis, Geophys. Res. Lett., 35, L23806, 10.1029/2008gl035617, 2008.

Levy, R. C., Remer, L. A., Mattoo, S., Vermote, E. F., and Kaufman, Y. J.: Second-generation operational algorithm: Retrieval of aerosol properties over land from inversion of Moderate Resolution Imaging Spectroradiometer spectral reflectance, Journal of Geophysical Research, 112, D13211, 2007.

Li, Z., Zang, Z., Li, Q. B., Chao, Y., Chen, D., Ye, Z., Liu, Y., and Liou, K. N.: A three-dimensional variational data assimilation system for multiple aerosol species with WRF/Chem and an application to PM2.5 prediction, Atmos. Chem. Phys. Discuss., 12, 13515-13552, 10.5194/acpd-12-13515-2012, 2012.

Liepert, B. G.: Observed reductions of surface solar radiation at sites in the United States and worldwide from 1961 to 1990, Geophys. Res. Lett., 29, 61-61-61-64, 10.1029/2002gl014910, 2002.

Lin, Y., and Mitchell, K. E.: The NCEP Stage II/IV hourly precipitation analyses: development and applications, Preprints, 19th Conf. on Hydrology, American Meteorological Society, San Diego, CA, 9-13 January 2005, Paper 1.2., 2005.

Liss, P., and Merlivat, L.: Air-Sea Gas Exchange Rates: Introduction and Synthesis, in: The Role of Air-Sea Exchange in Geochemical Cycling, edited by: Buat-Ménard, P., NATO ASI Series, Springer Netherlands, 113-127, 1986.

Liu, Y., Daum, P. H., and McGraw, R. L.: Size truncation effect, threshold behavior, and a new type of autoconversion parameterization, Geophys. Res. Lett., 32, L11811, 10.1029/2005gl022636, 2005a.

Liu, Y., Sarnat, J. A., Kilaru, V., Jacob, D. J., and Koutrakis, P.: Estimating Ground-Level PM2.5 in the Eastern United States Using Satellite Remote Sensing, Environmental science & technology, 39, 3269-3278, 10.1021/es049352m, 2005b.

Liu, Z., Liu, Q., Lin, H. C., Schwartz, C. S., Lee, Y. H., and Wang, T.: Three-dimensional variational assimilation of MODIS aerosol optical depth: Implementation and application to a dust storm over East Asia, Journal of Geophysical Research, 116, D23206, 2011.

Lohmann, U.: A glaciation indirect aerosol effect caused by soot aerosols, Geophys. Res. Lett., 29, 11-11-11-14, 10.1029/2001gl014357, 2002.

Lohmann, U., and Feichter, J.: Global indirect aerosol effects: a review, Atmos. Chem. Phys., 5, 715-737, 2005.

Lyapustin, A., Korkin, S., Wang, Y., Quayle, B., and Laszlo, I.: Discrimination of biomass burning smoke and clouds in MAIAC algorithm, Atmos. Chem. Phys., 12, 9679-9686, 10.5194/acp-12-9679-2012, 2012.

Lyons, W. A., Nelson, T. E., Williams, E. R., Cramer, J. A., and Turner, T. R.: Enhanced Positive Cloud-to-Ground Lightning in Thunderstorms Ingesting Smoke from Fires, Science, 282, 77-80, 10.1126/science.282.5386.77, 1998.

Mahowald, N. M., Muhs, D. R., Levis, S., Rasch, P. J., Yoshioka, M., Zender, C. S., and Luo, C.: Change in atmospheric mineral aerosols in response to climate: Last glacial period,

preindustrial, modern, and doubled carbon dioxide climates, J. Geophys. Res., 111, D10202, 2006.

Malm, W. C., Sisler, J. F., Huffman, D., Eldred, R. A., and Cahill, T. A.: Spatial and seasonal trends in particle concentration and optical extinction in the United States, Journal of Geophysical Research, 99, 1347-1370, 1994.

Markowski, P., Hannon, C., Frame, J., Lancaster, E., Pietrycha, A., Edwards, R., and Thompson, R. L.: Characteristics of Vertical Wind Profiles near Supercells Obtained from the Rapid Update Cycle, Weather and Forecasting, 18, 1262-1272, 10.1175/1520-0434(2003)018<1262:covwpn>2.0.co;2, 2003.

Markowski, P. M., Straka, J. M., and Rasmussen, E. N.: Direct Surface Thermodynamic Observations within the Rear-Flank Downdrafts of Nontornadic and Tornadic Supercells, Monthly Weather Review, 130, 1692-1721, 10.1175/1520-0493(2002)130<1692:dstowt>2.0.co;2, 2002.

Markowski, P. M., and Richardson, Y. P.: Tornadogenesis: Our current understanding, forecasting considerations, and questions to guide future research, Atmospheric Research, 93, 3-10, http://dx.doi.org/10.1016/j.atmosres.2008.09.015, 2009.

Martin, G. M., Johnson, D. W., and Spice, A.: The Measurement and Parameterization of Effective Radius of Droplets in Warm Stratocumulus Clouds, Journal of the atmospheric sciences, 51, 1823-1842, 10.1175/1520-0469(1994)051<1823:tmapoe>2.0.co;2, 1994.

McArdle, J. V., and Hoffmann, M. R.: Kinetics and mechanism of the oxidation of aquated sulfur dioxide by hydrogen peroxide at low pH, The Journal of Physical Chemistry, 87, 5425-5429, 10.1021/j150644a024, 1983.

McFarquhar, G. M., Um, J., Freer, M., Baumgardner, D., Kok, G. L., and Mace, G.: Importance of small ice crystals to cirrus properties: Observations from the Tropical Warm Pool International Cloud Experiment (TWP-ICE), Geophys. Res. Lett., 34, L13803, 10.1029/2007gl029865, 2007.

McFiggans, G., Artaxo, P., Baltensperger, U., Coe, H., Facchini, M., Feingold, G., Fuzzi, S., Gysel, M., Laaksonen, A., and Lohmann, U.: The effect of physical and chemical aerosol properties on warm cloud droplet activation, Atmos. Chem. Phys., 6, 2593-2649, 2006.

McKeen, S., Chung, S. H., Wilczak, J., Grell, G., Djalalova, I., Peckham, S., Gong, W., Bouchet, V., Moffet, R., Tang, Y., Carmichael, G. R., Mathur, R., and Yu, S.: Evaluation of several PM2.5 forecast models using data collected during the ICARTT/NEAQS 2004 field study, Journal of Geophysical Research: Atmospheres, 112, D10S20, 10.1029/2006jd007608, 2007.

Mebust, M. R., Eder, B. K., Binkowski, F. S., and Roselle, S. J.: Models-3 community multiscale air quality (CMAQ) model aerosol component 2. Model evaluation, Journal of Geophysical Research, 108, 4184, 2003.

Mena-Carrasco, M., Carmichael, G. R., Campbell, J. E., Zimmerman, D., Tang, Y., Adhikary, B., D'Allura, A., Molina, L. T., Zavala, M., García, A., Flocke, F., Campos, T., Weinheimer, A. J., Shetter, R., Apel, E., Montzka, D. D., Knapp, D. J., and Zheng, W.: Assessing the regional impacts of Mexico City emissions on air quality and chemistry, Atmos. Chem. Phys., 9, 3731-3743, 10.5194/acp-9-3731-2009, 2009.

Mena-Carrasco, M., Oliva, E., Saide, P., Spak, S. N., de la Maza, C., Osses, M., Tolvett, S., Campbell, J. E., Tsao, T. e. C.-C., and Molina, L. T.: Estimating the health benefits from natural gas use in transport and heating in Santiago, Chile, Science of The Total Environment, 429, 257-265, http://dx.doi.org/10.1016/j.scitotenv.2012.04.037, 2012.

Mena, M. A.: Improving emissions inventories in North America through systematic analysis of model performance during ICARRT and MILAGRO, dissertation, University of Iowa, http://ir.uiowa.edu/etd/153, 2007.

Meskhidze, N., Xu, J., Gantt, B., Zhang, Y., Nenes, A., Ghan, S., Liu, X., Easter, R., and Zaveri, R.: Global distribution and climate forcing of marine organic aerosol: 1. Model improvements and evaluation, Atmos. Chem. Phys, 11, 11689-11705, 2011.

Michel, Y., and Auligné, T.: Inhomogeneous Background Error Modeling and Estimation over Antarctica, Monthly Weather Review, 138, 2229-2252, 10.1175/2009mwr3139.1, 2010.

Minnis, P., Nguyen, L., Palikonda, R., Heck, P. W., Spangenberg, D. A., Doelling, D. R., Ayers, J. K., Smith Jr, W. L., Khaiyer, M. M., and Trepte, Q. Z.: Near-real time cloud retrievals from operational and research meteorological satellites, 2008, 710703,

MINSEGPRES: Actualización al Plan Prevención y Descontaminación de la

Región Metropolitana, Decreto Supremo 66, Gobierno de Chile, http://www.sinia.cl/1292/w3-article-39262.html, 2010.

Mitra, S. K., Brinkmann, J., and Pruppacher, H. R.: A wind tunnel study on the drop-to-particle conversion, Journal of Aerosol Science, 23, 245-256, http://dx.doi.org/10.1016/0021-8502(92)90326-Q, 1992.

Mlawer, E. J., Taubman, S. J., Brown, P. D., Iacono, M. J., and Clough, S. A.: Radiative transfer for inhomogeneous atmospheres: RRTM, a validated correlated-k model for the longwave, Journal of Geophysical Research: Atmospheres, 102, 16663-16682, 10.1029/97jd00237, 1997.

Morcrette, J. J., Boucher, O., Jones, L., Salmond, D., Bechtold, P., Beljaars, A., Benedetti, A., Bonet, A., Kaiser, J. W., Razinger, M., Schulz, M., Serrar, S., Simmons, A. J., Sofiev, M., Suttie, M., Tompkins, A. M., and Untch, A.: Aerosol analysis and forecast in the European Centre for Medium-Range Weather Forecasts Integrated Forecast System: Forward modeling, Journal of Geophysical Research: Atmospheres, 114, D06206, 10.1029/2008jd011235, 2009.

Morris, R. E., McNally, D. E., Tesche, T. W., Tonnesen, G., Boylan, J. W., and Brewer, P.: Preliminary evaluation of the Community Multiscale Air Quality model for 2002 over the southeastern United States, Journal of the Air & Waste Management Association, 55, 1694-1708, 2005.

Morrison, H., and Pinto, J. O.: Mesoscale Modeling of Springtime Arctic Mixed-Phase Stratiform Clouds Using a New Two-Moment Bulk Microphysics Scheme, Journal of the atmospheric sciences, 62, 3683-3704, 10.1175/jas3564.1, 2005.

Morrison, H., Thompson, G., and Tatarskii, V.: Impact of Cloud Microphysics on the Development of Trailing Stratiform Precipitation in a Simulated Squall Line: Comparison of One- and Two-Moment Schemes, Monthly Weather Review, 137, 991-1007, 10.1175/2008mwr2556.1, 2009.

Munchak, L. A., Levy, R. C., Mattoo, S., Remer, L. A., Holben, B. N., Schafer, J. S., Hostetler, C. A., and Ferrare, R. A.: MODIS 3 km aerosol product: applications over land in an urban/suburban region, Atmos. Meas. Tech. Discuss., 6, 1683-1716, 10.5194/amtd-6-1683-2013, 2013.

Muñoz, R. C., and Garreaud, R.: Dynamics of the Low-Level Jet off the West Coast of Subtropical South America, Monthly Weather Review, 133, 3661-3677, 10.1175/mwr3074.1, 2005.

Muñoz, R. C., and Undurraga, A. A.: Daytime Mixed Layer over the Santiago Basin: Description of Two Years of Observations with a Lidar Ceilometer, Journal of Applied Meteorology and Climatology, 49, 1728-1741, 10.1175/2010jamc2347.1, 2010.

Murray, N. D., Orville, R. E., and Huffines, G. R.: Effect of pollution from Central American fires on cloud-to-ground lightning in May 1998, Geophys. Res. Lett., 27, 2249-2252, 10.1029/2000gl011656, 2000.

Nakanishi, M., and Niino, H.: An improved Mellor–Yamada level-3 model with condensation physics: Its design and verification, Boundary-layer meteorology, 112, 1-31, 2004.

Natarajan, M., Pierce, R. B., Schaack, T. K., Lenzen, A. J., Al-Saadi, J. A., Soja, A. J., Charlock, T. P., Rose, F. G., Winker, D. M., and Worden, J. R.: Radiative forcing due to enhancements in tropospheric ozone and carbonaceous aerosols caused by Asian fires during spring 2008, Journal of Geophysical Research: Atmospheres, 117, D06307, 10.1029/2011jd016584, 2012.

Naud, C. M., Muller, J. P., Clothiaux, E. E., Baum, B. A., and Menzel, W. P.: Intercomparison of multiple years of MODIS, MISR and radar cloud-top heights, Ann. Geophys., 23, 2415-2424, 10.5194/angeo-23-2415-2005, 2005.

NOAA: The Historic Tornadoes of April 2011, National Oceanic and Atmospheric Administration Service Assessment. http://www.nws.noaa.gov/om/assessments/index.shtml, 2011.

NOAA NWS: http://www.ua.nws.noaa.gov/, 2013.

Ntelekos, A. A., Smith, J. A., Donner, L., Fast, J. D., Gustafson, W. I., Chapman, E. G., and Krajewski, W. F.: The effects of aerosols on intense convective precipitation in the northeastern United States, Quarterly Journal of the Royal Meteorological Society, 135, 1367-1391, 10.1002/qj.476, 2009.

O'Neill, N. T., Eck, T. F., Smirnov, A., Holben, B. N., and Thulasiraman, S.: Spectral discrimination of coarse and fine mode optical depth, Journal of Geophysical Research: Atmospheres, 108, 4559, 10.1029/2002jd002975, 2003.

Otkin, J. A., and Greenwald, T. J.: Comparison of WRF Model-Simulated and MODIS-Derived Cloud Data, Monthly Weather Review, 136, 1957-1970, 10.1175/2007mwr2293.1, 2008.

Otkin, J. A., Greenwald, T. J., Sieglaff, J., and Huang, H.-L.: Validation of a Large-Scale Simulated Brightness Temperature Dataset Using SEVIRI Satellite Observations, Journal of Applied Meteorology and Climatology, 48, 1613-1626, 10.1175/2009jamc2142.1, 2009.

Pagowski, M., Grell, G. A., McKeen, S. A., Peckham, S. E., and Devenyi, D.: Three-dimensional variational data assimilation of ozone and fine particulate matter observations: some results using the Weather Research and Forecasting—Chemistry model and Grid-point Statistical Interpolation, Quarterly Journal of the Royal Meteorological Society, 136, 2013-2024, 10.1002/qj.700, 2010.

Pagowski, M., and Grell, G. A.: Experiments with the assimilation of fine aerosols using an ensemble Kalman filter, Journal of Geophysical Research: Atmospheres, 117, D21302, 10.1029/2012jd018333, 2012.

Painemal, D., and Zuidema, P.: Assessment of MODIS cloud effective radius and optical thickness retrievals over the Southeast Pacific with VOCALS-REx in situ measurements, Journal of Geophysical Research, 116, D24206, 2011.

Painemal, D., Minnis, P., Ayers, J. K., and O'Neill, L.: GOES-10 microphysical retrievals in marine warm clouds: Multi-instrument validation and daytime cycle over the Southeast Pacific, J. Geophys. Res, In press, 2012.

Palau, J. L., Pérez-Landa, G., Diéguez, J. J., Monter, C., and Millán, M. M.: The importance of meteorological scales to forecast air pollution scenarios on coastal complex terrain, Atmos. Chem. Phys., 5, 2771-2785, 10.5194/acp-5-2771-2005, 2005.

Park, M. E., Song, C. H., Park, R. S., Lee, J., Kim, J., Lee, S., Woo, J. H., Carmichael, G. R., Eck, T. F., Holben, B. N., Lee, S. S., Song, C. K., and Hong, Y. D.: New approach to monitor transboundary particulate pollution over northeast Asia, Atmos. Chem. Phys. Discuss., 13, 15867-15905, 10.5194/acpd-13-15867-2013, 2013.

Parrish, D. F., and Derber, J. C.: The National Meteorological Center's spectral statistical-interpolation analysis system, Monthly Weather Review, 120, 1747-1763, 1992.

Pavolonis, M. J., Heidinger, A. K., and Uttal, T.: Daytime Global Cloud Typing from AVHRR and VIIRS: Algorithm Description, Validation, and Comparisons, Journal of Applied Meteorology, 44, 804-826, 10.1175/jam2236.1, 2005.

Perez, P., and Reyes, J.: Prediction of maximum of 24-h average of PM10 concentrations 30h in advance in Santiago, Chile, Atmos. Environ., 36, 4555-4561, http://dx.doi.org/10.1016/S1352-2310(02)00419-3, 2002.

Perez, P., Palacios, R., and Castillo, A.: Carbon Monoxide Concentration Forecasting in Santiago, Chile, Journal of the Air & Waste Management Association, 54, 908-913, 10.1080/10473289.2004.10470966, 2004.

Perez, P., and Reyes, J.: An integrated neural network model for PM10 forecasting, Atmos. Environ., 40, 2845-2851, http://dx.doi.org/10.1016/j.atmosenv.2006.01.010, 2006.

Perez, P., and Salini, G.: PM2.5 forecasting in a large city: Comparison of three methods, Atmos. Environ., 42, 8219-8224, http://dx.doi.org/10.1016/j.atmosenv.2008.07.035, 2008.

Petrenko, M., and Ichoku, C.: Coherent uncertainty analysis of aerosol measurements from multiple satellite sensors, Atmos. Chem. Phys. Discuss., 13, 4637-4685, 10.5194/acpd-13-4637-2013, 2013.

Pierce, R. B., Schaack, T., Al-Saadi, J. A., Fairlie, T. D., Kittaka, C., Lingenfelser, G., Natarajan, M., Olson, J., Soja, A., Zapotocny, T., Lenzen, A., Stobie, J., Johnson, D., Avery, M. A., Sachse, G. W., Thompson, A., Cohen, R., Dibb, J. E., Crawford, J., Rault, D., Martin, R., Szykman, J., and Fishman, J.: Chemical data assimilation estimates of continental U.S. ozone and nitrogen budgets during the Intercontinental Chemical Transport Experiment–North America, Journal of Geophysical Research: Atmospheres, 112, D12S21, 10.1029/2006jd007722, 2007.

Pincus, R., and Baker, M. B.: Effect of precipitation on the albedo susceptibility of clouds in the marine boundary layer, Nature, 372, 250-252, 1994.

Platnick, S., King, M. D., Ackerman, S. A., Menzel, W. P., Baum, B. A., Riedi, J. C., and Frey, R. A.: The MODIS cloud products: algorithms and examples from Terra, Geoscience and Remote Sensing, IEEE Transactions on, 41, 459-473, 10.1109/tgrs.2002.808301, 2003.

Pope, C. A., Young, B., and Dockery, D.: Health effects of fine particulate air pollution: lines that connect, Journal of the Air & Waste Management Association, 56, 709-742, 2006.

Purser, R., Wu, W., Parrish, D., and Roberts, N.: Numerical Aspects of the Application of Recursive Filters to Variational Statistical Analysis. Part I: Spatially Homogeneous and Isotropic Gaussian Covariances, Monthly Weather Review, 131, 1524-1535, 2003.

Qian, Y., Gustafson Jr, W. I., and Fast, J. D.: An investigation of the sub-grid variability of trace gases and aerosols for global climate modeling, Atmos. Chem. Phys., 10, 6917-6946, 10.5194/acp-10-6917-2010, 2010.

Quaas, J., Boucher, O., Bellouin, N., and Kinne, S.: Satellite-based estimate of the direct and indirect aerosol climate forcing, J. Geophys. Res, 113, D05204, 2008.

Rahn, D. A., and Garreaud, R.: Marine boundary layer over the subtropical southeast Pacific during VOCALS-REx – Part 1: Mean structure and diurnal cycle, Atmos. Chem. Phys., 10, 4491-4506, 10.5194/acp-10-4491-2010, 2010.

Ramanathan, V., Cess, R., Harrison, E., Minnis, P., Barkstrom, B., Ahmad, E., and Hartmann, D.: Cloud-radiative forcing and climate: Results from the Earth Radiation Budget Experiment, Science, 243, 57-63, 1989.

Ramanathan, V., and Carmichael, G.: Global and regional climate changes due to black carbon, Nature Geoscience, 1, 221-227, 2008.

Ramanathan, V., Rodhe, H., Agrawal, M., Akimoto, H., Auffhammer, M., Chopra, U., Emberson, L., Hasnain, S. I., Iyngararasan, M., and Jayaraman, A.: Atmospheric brown clouds: Regional assessment report with focus on Asia, 2008.

Rasmussen, E. N., and Blanchard, D. O.: A Baseline Climatology of Sounding-Derived Supercell and Tornado Forecast Parameters, Weather and Forecasting, 13, 1148-1164, 10.1175/1520-0434(1998)013<1148:abcosd>2.0.co;2, 1998.

Redemann, J., Zhang, Q., Schmid, B., Russell, P., Livingston, J., Jonsson, H., and Remer, L.: Assessment of MODIS-derived visible and near-IR aerosol optical properties and their spatial variability in the presence of mineral dust, Geophys. Res. Lett., 33, L18814, 2006.

Remer, L. A., Kaufman, Y., Tanré, D., Mattoo, S., Chu, D., Martins, J. V., Li, R. R., Ichoku, C., Levy, R., and Kleidman, R.: The MODIS aerosol algorithm, products, and validation, Journal of the atmospheric sciences, 62, 947-973, 2005.

Rienecker, M., Suarez, M., Todling, R., Bacmeister, J., Takacs, L., Liu, H., Gu, W., Sienkiewicz, M., Koster, R., and Gelaro, R.: The GEOS-5 data assimilation system: Documentation of versions 5.0. 1, 5.1. 0, and 5.2. 0, NASA Tech. Memo, 104606, 2008, 2008.

Robbin Martin, L., and Damschen, D. E.: Aqueous oxidation of sulfur dioxide by hydrogen peroxide at low pH, Atmospheric Environment (1967), 15, 1615-1621, http://dx.doi.org/10.1016/0004-6981(81)90146-3, 1981.

Rosenfeld, D.: Suppression of Rain and Snow by Urban and Industrial Air Pollution, Science, 287, 1793-1796, 10.1126/science.287.5459.1793, 2000.

Rosenfeld, D., Lohmann, U., Raga, G. B., O'Dowd, C. D., Kulmala, M., Fuzzi, S., Reissell, A., and Andreae, M. O.: Flood or Drought: How Do Aerosols Affect Precipitation?, Science, 321, 1309-1313, 10.1126/science.1160606, 2008.

Rosenfeld, D., and Bell, T. L.: Why do tornados and hailstorms rest on weekends?, Journal of Geophysical Research (Atmospheres), 116, 20211, 2011.

Rosenfeld, D., Clavner, M., and Nirel, R.: Pollution and dust aerosols modulating tropical cyclones intensities, Atmospheric Research, 2011a.

Rosenfeld, D., Clavner, M., and Nirel, R.: Pollution and dust aerosols modulating tropical cyclones intensities, Atmospheric Research, 102, 66-76, 10.1016/j.atmosres.2011.06.006, 2011b.

Rutllant, J., and Garreaud, R.: Meteorological air pollution potential for Santiago, Chile: Towards an objective episode forecasting, Environ Monit Assess, 34, 223-244, 10.1007/bf00554796, 1995.

Rutllant, J., and Garreaud, R.: Episodes of Strong Flow down the Western Slope of the Subtropical Andes, Monthly Weather Review, 132, 611-622, 10.1175/1520-0493(2004)132<0611:eosfdt>2.0.co;2, 2004.

Saide, P., Osses, A., Gallardo, L., and Osses, M.: Adjoint inverse modeling of a CO emission inventory at the city scale: Santiago de Chile's case, Atmos. Chem. Phys. Discuss., 9, 6325-6361, 10.5194/acpd-9-6325-2009, 2009a.

Saide, P., Zah, R., Osses, M., and Ossés de Eicker, M.: Spatial disaggregation of traffic emission inventories in large cities using simplified top–down methods, Atmos. Environ., 43, 4914-4923, http://dx.doi.org/10.1016/j.atmosenv.2009.07.013, 2009b.

Saide, P. E., Carmichael, G. R., Spak, S. N., Gallardo, L., Osses, A. E., Mena-Carrasco, M. A., and Pagowski, M.: Forecasting urban PM10 and PM2. 5 pollution episodes in very stable nocturnal conditions and complex terrain using WRF–Chem CO tracer model, Atmos. Environ., 45, 2769-2780, 2011.

Saide, P. E., Carmichael, G. R., Spak, S. N., Minnis, P., and Ayers, J. K.: Improving aerosol distributions below clouds by assimilating satellite-retrieved cloud droplet number, Proceedings of the National Academy of Sciences, 109, 11939-11943, 10.1073/pnas.1205877109, 2012a.

Saide, P. E., Spak, S. N., Carmichael, G. R., Mena-Carrasco, M. A., Yang, Q., Howell, S., Leon, D. C., Snider, J. R., Bandy, A. R., Collett, J. L., Benedict, K. B., de Szoeke, S. P., Hawkins, L. N., Allen, G., Crawford, I., Crosier, J., and Springston, S. R.: Evaluating WRF-Chem aerosol indirect effects in Southeast Pacific marine stratocumulus during VOCALS-REx, Atmos. Chem. Phys., 12, 3045-3064, 10.5194/acp-12-3045-2012, 2012b.

Saide, P. E., Carmichael, G. R., Liu, Z., Schwartz, C. S., Lin, H. C., da Silva, A. M., and Hyer, E.: Aerosol optical depth assimilation for a size-resolved sectional model: impacts of observationally constrained, multi-wavelength and fine mode retrievals on regional scale analyses and forecasts, Atmos. Chem. Phys., 13, 10425-10444, 10.5194/acp-13-10425-2013, 2013.

Sakaeda, N., Wood, R., and Rasch, P. J.: Direct and semidirect aerosol effects of southern African biomass burning aerosol, Journal of Geophysical Research: Atmospheres, 116, D12205, 10.1029/2010jd015540, 2011.

Schmitz, R.: Modelling of air pollution dispersion in Santiago de Chile, Atmos. Environ., 39, 2035-2047, http://dx.doi.org/10.1016/j.atmosenv.2004.12.033, 2005.

Schroeder, A. J., Stauffer, D. R., Seaman, N. L., Deng, A., Gibbs, A. M., Hunter, G. K., and Young, G. S.: An Automated High-Resolution, Rapidly Relocatable Meteorological Nowcasting and Prediction System, Monthly Weather Review, 134, 1237-1265, 10.1175/mwr3118.1, 2006.

Schuster, G. L., Dubovik, O., and Holben, B. N.: Angstrom exponent and bimodal aerosol size distributions, Journal of Geophysical Research, 111, D07207, 2006.

Schutgens, N. A. J., Miyoshi, T., Takemura, T., and Nakajima, T.: Applying an ensemble Kalman filter to the assimilation of AERONET observations in a global aerosol transport model, Atmos. Chem. Phys., 10, 2561-2576, 10.5194/acp-10-2561-2010, 2010.

Schwartz, C. S., Liu, Z., Lin, H. C., and McKeen, S. A.: Simultaneous three-dimensional variational assimilation of surface fine particulate matter and MODIS aerosol optical depth, Journal of Geophysical Research, 117, D13202, 2012.

Seaman, N., Gaudet, B., Zielonka, J., and Stauffer, D.: Sensitivity of Vertical Structure in the Stable Boundary Layer to Variations of the WRF Model's MELLOR-YAMADA-JANJIC Turbulence Scheme, 9th WRF Users' Workshop, Boulder, 23-27 June, http://www.mmm.ucar.edu/wrf/users/workshops/WS2009/abstracts/2B-04.pdf, 2009.

Seinfeld, J. H., and Pandis, S. N.: Atmospheric chemistry and physics: from air pollution to climate change, John Wiley & Sons, 2006.

Shah, S., Rao, B. M., Kumar, P., and Pal, P. K.: Verification of cloud cover forecast with INSAT observation over western India, J Earth Syst Sci, 119, 775-781, 10.1007/s12040-010-0062-1, 2010.

Shank, L. M., Howell, S., Clarke, A. D., Freitag, S., Brekhovskikh, V., Kapustin, V., McNaughton, C., Campos, T., and Wood, R.: Organic matter and non-refractory aerosol over the remote Southeast Pacific: oceanic and combustion sources, Atmos. Chem. Phys., 12, 557-576, 10.5194/acp-12-557-2012, 2012.

Shi, Y., Zhang, J., Reid, J. S., Holben, B., Hyer, E. J., and Curtis, C.: An analysis of the collection 5 MODIS over-ocean aerosol optical depth product for its implication in aerosol assimilation, Atmos. Chem. Phys., 11, 557-565, 10.5194/acp-11-557-2011, 2011.

Shrestha, K. L., Kondo, A., Kaga, A., and Inoue, Y.: High-resolution modeling and evaluation of ozone air quality of Osaka using MM5-CMAQ system, Journal of Environmental Sciences, 21, 782-789, http://dx.doi.org/10.1016/S1001-0742(08)62341-4, 2009.

Shrivastava, M., Fast, J., Easter, R., Gustafson Jr, W. I., Zaveri, R. A., Jimenez, J. L., Saide, P., and Hodzic, A.: Modeling organic aerosols in a megacity: comparison of simple and complex representations of the volatility basis set approach, Atmos. Chem. Phys., 11, 6639-6662, 10.5194/acp-11-6639-2011, 2011.

Shrivastava, M., Berg, L. K., Fast, J. D., Easter, R. C., Laskin, A., Chapman, E. G., Gustafson, W. I., Liu, Y., and Berkowitz, C. M.: Modeling aerosols and their interactions with shallow cumuli during the 2007 CHAPS field study, Journal of Geophysical Research: Atmospheres, 2013.

Silva, R. A., West, J. J., Zhang, Y., Anenberg, S. C., Lamarque, J.-F., Shindell, D. T., Collins, W. J., Dalsoren, S., Faluvegi, G., Folberth, G., Horowitz, L. W., Nagashima, T., Naik, V., Rumbold, S., Skeie, R., Sudo, K., Takemura, T., Bergmann, D., Cameron-Smith, P., Cionni, I., Doherty, R. M., Eyring, V., Josse, B., MacKenzie, I. A., Plummer, D., Righi, M., Stevenson, D. S., Strode, S., Szopa, S., and Zeng, G.: Global premature mortality due to anthropogenic outdoor air pollution and the contribution of past climate change, Environmental Research Letters, 8, 034005, 2013.

Skamarock, W. C., Klemp, J. B., Dudhia, J., Gill, D. O., Barker, D. M., Duda, M. G., Huang, X.-Y., Wang, W., and Powers, J. G.: A description of the Advanced Research WRF version 3, NCAR Tech. Note NCAR/TN-475+ STR, 2008.

Slingo, A.: A GCM Parameterization for the Shortwave Radiative Properties of Water Clouds, Journal of the atmospheric sciences, 46, 1419-1427, 10.1175/1520-0469(1989)046<1419:agpfts>2.0.co;2, 1989.

Smirnov, A., Holben, B. N., Giles, D. M., Slutsker, I., O'Neill, N. T., Eck, T. F., Macke, A., Croot, P., Courcoux, Y., Sakerin, S. M., Smyth, T. J., Zielinski, T., Zibordi, G., Goes, J. I., Harvey, M. J., Quinn, P. K., Nelson, N. B., Radionov, V. F., Duarte, C. M., Losno, R., Sciare, J., Voss, K. J., Kinne, S., Nalli, N. R., Joseph, E., Krishna Moorthy, K., Covert, D. S., Gulev, S. K., Milinevsky, G., Larouche, P., Belanger, S., Horne, E., Chin, M., Remer, L. A., Kahn, R. A., Reid, J. S., Schulz, M., Heald, C. L., Zhang, J., Lapina, K., Kleidman, R. G., Griesfeller, J., Gaitley, B. J., Tan, Q., and Diehl, T. L.: Maritime aerosol network as a component of AERONET – first results and comparison with global aerosol models and satellite retrievals, Atmos. Meas. Tech., 4, 583-597, 10.5194/amt-4-583-2011, 2011.

Snook, N., and Xue, M.: Effects of microphysical drop size distribution on tornadogenesis in supercell thunderstorms, Geophys. Res. Lett., 35, L24803, 10.1029/2008gl035866, 2008.

Solomon, S., Qin, D., Manning, M., Chen, Z., Marquis, M., Averyt, K., Tignor, M., and Miller, H.: Climate change 2007: the physical science basis: contribution of Working Group I to the Fourth Assessment Report of the Intergovernmental Panel on Climate Change, Cambridge Univ Pr, 2007.

Spak, S., Mena, M., and Carmichael, G.: Atmospheric transport of anthropogenic oxidized sulfur over the Southeast Pacific during VOCALS REx, CLIVAR Exchanges, 15, 20-21, 2010.

SPC: Tornado, Hail, and Wind Database available online at SPC WCM web page (http://www.spc.noaa.gov/wcm/#data), 2013.

Stensrud, D. J., Wicker, L. J., Kelleher, K. E., Xue, M., Foster, M. P., Schaefer, J. T., Schneider, R. S., Benjamin, S. G., Weygandt, S. S., Ferree, J. T., and Tuell, J. P.: Convective-Scale Warn-on-Forecast System, Bulletin of the American Meteorological Society, 90, 1487-1499, 10.1175/2009bams2795.1, 2009.

Stohl, A., Forster, C., Frank, A., Seibert, P., and Wotawa, G.: Technical note: The Lagrangian particle dispersion model FLEXPART version 6.2, Atmos. Chem. Phys., 5, 2461-2474, 10.5194/acp-5-2461-2005, 2005.

Stokes, R., and Robinson, R.: Interactions in aqueous nonelectrolyte solutions. I. Solute-solvent equilibria, The Journal of Physical Chemistry, 70, 2126-2131, 1966.

Sukoriansky, S., Galperin, B., and Perov, V.: 'Application of a New Spectral Theory of Stably Stratified Turbulence to the Atmospheric Boundary Layer over Sea Ice', Boundary-layer meteorology, 117, 231-257, 10.1007/s10546-004-6848-4, 2005.

Sun, R., Moorthi, S., Xiao, H., and Mechoso, C. R.: Simulation of low clouds in the Southeast Pacific by the NCEP GFS: sensitivity to vertical mixing, Atmos. Chem. Phys., 10, 12261-12272, 10.5194/acp-10-12261-2010, 2010.

Szczodrak, M., Austin, P. H., and Krummel, P.: Variability of optical depth and effective radius in marine stratocumulus clouds, Journal of the atmospheric sciences, 58, 2912-2926, 2001.

Thompson, R. L., Edwards, R., Hart, J. A., Elmore, K. L., and Markowski, P.: Close Proximity Soundings within Supercell Environments Obtained from the Rapid Update Cycle, Weather and Forecasting, 18, 1243-1261, 10.1175/1520-0434(2003)018<1243:cpswse>2.0.co;2, 2003.

Twohy, C. H., Petters, M. D., Snider, J. R., Stevens, B., Tahnk, W., Wetzel, M., Russell, L., and Burnet, F.: Evaluation of the aerosol indirect effect in marine stratocumulus clouds: Droplet number, size, liquid water path, and radiative impact, Journal of Geophysical Research, 110, D08203, 2005.

Twomey, S.: Pollution and the planetary albedo, Atmospheric Environment (1967), 8, 1251-1256, http://dx.doi.org/10.1016/0004-6981(74)90004-3, 1974.

Twomey, S.: Aerosols, clouds and radiation, Atmos. Environ. A-Gen., 25, 2435-2442, 1991.

van der Werf, G. R., Randerson, J. T., Giglio, L., Collatz, G. J., Mu, M., Kasibhatla, P. S., Morton, D. C., DeFries, R. S., Jin, Y., and van Leeuwen, T. T.: Global fire emissions and the contribution of deforestation, savanna, forest, agricultural, and peat fires (1997–2009), Atmos. Chem. Phys., 10, 11707-11735, 10.5194/acp-10-11707-2010, 2010.

van Donkelaar, A., Martin, R. V., and Park, R. J.: Estimating ground-level PM2. 5 using aerosol optical depth determined from satellite remote sensing, Journal of Geophysical Research, 111, D21201, 2006.

Vellore, R., Koračin, D., and Wetzel, M.: A method of improving cloud predictions for real-time weather forecasting and visualization, in: Advances in Visual Computing, Springer, 544-553, 2006.

Vellore, R., Koračin, D., Wetzel, M., Chai, S., and Wang, Q.: Challenges in Mesoscale Prediction of a Nocturnal Stratocumulus-Topped Marine Boundary Layer and Implications for Operational Forecasting, Weather and Forecasting, 22, 1101-1122, 10.1175/waf1029.1, 2007.

Wang, H., and Feingold, G.: Modeling Mesoscale Cellular Structures and Drizzle in Marine Stratocumulus. Part I: Impact of Drizzle on the Formation and Evolution of Open Cells, Journal of the atmospheric sciences, 66, 3237-3256, 10.1175/2009jas3022.1, 2009.

Wang, H., Feingold, G., Wood, R., and Kazil, J.: Modelling microphysical and meteorological controls on precipitation and cloud cellular structures in Southeast Pacific stratocumulus, Atmos. Chem. Phys., 10, 6347-6362, 10.5194/acp-10-6347-2010, 2010.

Wang, J., van den Heever, S., and Reid, J.: A conceptual model for the link between Central American biomass burning aerosols and severe weather over the south central United States, Environmental Research Letters, 4, 015003, 2009.

Wang, J., Xu, X., Henze, D. K., Zeng, J., Ji, Q., Tsay, S.-C., and Huang, J.: Top-down estimate of dust emissions through integration of MODIS and MISR aerosol retrievals with the GEOS-Chem adjoint model, Geophys. Res. Lett., 39, L08802, 10.1029/2012gl051136, 2012.

Wang, S., O'Neill, L. W., Jiang, Q., de Szoeke, S. P., Hong, X., Jin, H., Thompson, W. T., and Zheng, X.: A regional real-time forecast of marine boundary layers during VOCALS-REx, Atmos. Chem. Phys., 11, 421-437, 10.5194/acp-11-421-2011, 2011.

Wang, Y., Sartelet, K. N., Bocquet, M., and Chazette, P.: Modelling and assimilation of lidar signals over Greater Paris during the MEGAPOLI summer campaign, Atmos. Chem. Phys. Discuss., 13, 27115-27161, 10.5194/acpd-13-27115-2013, 2013.

Wexler, A. S., Lurmann, F. W., and Seinfeld, J. H.: Modelling urban and regional aerosols—I. model development, Atmos. Environ., 28, 531-546, http://dx.doi.org/10.1016/1352-2310(94)90129-5, 1994.

Wiedinmyer, C., Akagi, S. K., Yokelson, R. J., Emmons, L. K., Al-Saadi, J. A., Orlando, J. J., and Soja, A. J.: The Fire INventory from NCAR (FINN): a high resolution global model to estimate the emissions from open burning, Geosci. Model Dev., 4, 625-641, 10.5194/gmd-4-625-2011, 2011.

Wilcox, E. M.: Stratocumulus cloud thickening beneath layers of absorbing smoke aerosol, Atmos. Chem. Phys., 10, 11769-11777, 10.5194/acp-10-11769-2010, 2010.

Wilcox, E. M.: Direct and semi-direct radiative forcing of smoke aerosols over clouds, Atmos. Chem. Phys., 12, 139-149, 10.5194/acp-12-139-2012, 2012.

Wolf, M. E., Fields, P. G., Manne, G. K., Villegas, M. T. L., Bravo, V. G., Gómez, R. I., Periférico, C., Cuicuilco, C. I., and Coyoacán, D.: Developing Mexico National Emissions Inventory Projections for the Future Years of 2008, 2012, and 2030, 18th annual international emission inventory conference, US Environmental Protection Agency, Baltimore, USA, 2009,

Wood, R., Mechoso, C., Bretherton, C., Weller, R., Huebert, B., Straneo, F., Albrecht, B., Coe, H., Allen, G., and Vaughan, G.: The VAMOS Ocean-Cloud-Atmosphere-Land Study Regional Experiment (VOCALS-REx): goals, platforms, and field operations, Atmos. Chem. Phys, 11, 627-654, 2011.

Wu, W.-S., Purser, R. J., and Parrish, D. F.: Three-dimensional variational analysis with spatially inhomogeneous covariances, Monthly Weather Review, 130, 2905-2916, 2002.

Wyant, M. C., Wood, R., Bretherton, C. S., Mechoso, C. R., Bacmeister, J., Balmaseda, M. A., Barrett, B., Codron, F., Earnshaw, P., Fast, J., Hannay, C., Kaiser, J. W., Kitagawa, H., Klein, S. A., Köhler, M., Manganello, J., Pan, H. L., Sun, F., Wang, S., and Wang, Y.: The PreVOCA experiment: modeling the lower troposphere in

the Southeast Pacific, Atmos. Chem. Phys., 10, 4757-4774, 10.5194/acp-10-4757-2010, 2010.

Xu, X., Wang, J., Henze, D. K., Qu, W., and Kopacz, M.: Constraints on aerosol sources using GEOS-Chem adjoint and MODIS radiances, and evaluation with multisensor (OMI, MISR) data, Journal of Geophysical Research: Atmospheres, n/a-n/a, 10.1002/jgrd.50515, 2013.

Yang, M., Blomquist, B. W., and Huebert, B. J.: Constraining the concentration of the hydroxyl radical in a stratocumulus-topped marine boundary layer from sea-to-air eddy covariance flux measurements of dimethylsulfide, Atmos. Chem. Phys., 9, 9225-9236, 10.5194/acp-9-9225-2009, 2009.

Yang, M., Huebert, B. J., Blomquist, B. W., Howell, S. G., Shank, L. M., McNaughton, C. S., Clarke, A. D., Hawkins, L. N., Russell, L. M., Covert, D. S., Coffman, D. J., Bates, T. S., Quinn, P. K., Zagorac, N., Bandy, A. R., de Szoeke, S. P., Zuidema, P. D., Tucker, S. C., Brewer, W. A., Benedict, K. B., and Collett, J. L.: Atmospheric sulfur cycling in the southeastern Pacific – longitudinal distribution, vertical profile, and diel variability observed during VOCALS-REx, Atmos. Chem. Phys., 11, 5079-5097, 10.5194/acp-11-5079-2011, 2011a.

Yang, Q., W. I. Gustafson, J., Fast, J. D., Wang, H., Easter, R. C., Morrison, H., Lee, Y. N., Chapman, E. G., Spak, S. N., and Mena-Carrasco, M. A.: Assessing regional scale predictions of aerosols, marine stratocumulus, and their interactions during VOCALS-REx using WRF-Chem, Atmos. Chem. Phys., 11, 11951-11975, 10.5194/acp-11-11951-2011, 2011b.

Yang, Q., Gustafson Jr, W. I., Fast, J. D., Wang, H., Easter, R. C., Wang, M., Ghan, S. J., Berg, L. K., Leung, L. R., and Morrison, H.: Impact of natural and anthropogenic aerosols on stratocumulus and precipitation in the Southeast Pacific: a regional modelling study using WRF-Chem, Atmos. Chem. Phys., 12, 8777-8796, 10.5194/acp-12-8777-2012, 2012.

Young, S. A., and Vaughan, M. A.: The Retrieval of Profiles of Particulate Extinction from Cloud-Aerosol Lidar Infrared Pathfinder Satellite Observations (CALIPSO) Data: Algorithm Description, Journal of Atmospheric and Oceanic Technology, 26, 1105-1119, 10.1175/2008jtecha1221.1, 2009.

Yuan, T., Remer, L. A., Pickering, K. E., and Yu, H.: Observational evidence of aerosol enhancement of lightning activity and convective invigoration, Geophys. Res. Lett., 38, L04701, 2011a.

Yuan, T., Remer, L. A., and Yu, H.: Microphysical, macrophysical and radiative signatures of volcanic aerosols in trade wind cumulus observed by the A-Train, Atmos. Chem. Phys., 11, 7119-7132, 10.5194/acp-11-7119-2011, 2011b.

Yver, C. E., Graven, H. D., Lucas, D. D., Cameron-Smith, P. J., Keeling, R. F., and Weiss, R. F.: Evaluating transport in the WRF model along the California coast, Atmos. Chem. Phys., 13, 1837-1852, 10.5194/acp-13-1837-2013, 2013.

Zaveri, R. A., and Peters, L. K.: A new lumped structure photochemical mechanism for large-scale applications, Journal of Geophysical Research, 104, 30387-30330,30415, 1999.

Zaveri, R. A., Easter, R. C., Fast, J. D., and Peters, L. K.: Model for simulating aerosol interactions and chemistry (MOSAIC), J. Geophys. Res, 113, D13204, 2008.

Zaveri, R. A., Shaw, W. J., Cziczo, D. J., Schmid, B., Ferrare, R. A., Alexander, M. L., Alexandrov, M., Alvarez, R. J., Arnott, W. P., Atkinson, D. B., Baidar, S., Banta, R. M., Barnard, J. C., Beranek, J., Berg, L. K., Brechtel, F., Brewer, W. A., Cahill, J. F., Cairns, B., Cappa, C. D., Chand, D., China, S., Comstock, J. M., Dubey, M. K., Easter, R. C., Erickson, M. H., Fast, J. D., Floerchinger, C., Flowers, B. A., Fortner, E., Gaffney, J. S., Gilles, M. K., Gorkowski, K., Gustafson, W. I., Gyawali, M., Hair, J., Hardesty, R. M., Harworth, J. W., Herndon, S., Hiranuma, N., Hostetler, C., Hubbe, J. M., Jayne, J. T., Jeong, H., Jobson, B. T., Kassianov, E. I., Kleinman, L. I., Kluzek, C., Knighton, B., Kolesar, K. R., Kuang, C., Kubátová, A., Langford, A. O., Laskin, A., Laulainen, N., Marchbanks, R. D., Mazzoleni, C., Mei, F., Moffet, R. C., Nelson, D., Obland, M. D., Oetjen, H., Onasch, T. B., Ortega, I., Ottaviani, M., Pekour, M., Prather, K. A., Radney, J. G., Rogers, R. R., Sandberg, S. P., Sedlacek, A., Senff, C. J., Senum, G., Setyan, A., Shilling, J. E., Shrivastava, M., Song, C., Springston, S. R., Subramanian, R., Suski, K., Tomlinson, J., Volkamer, R., Wallace, H. W., Wang, J., Weickmann, A. M., Worsnop, D. R., Yu, X. Y., Zelenyuk, A., and Zhang, Q.: Overview of the 2010 Carbonaceous Aerosols and Radiative Effects Study (CARES), Atmos. Chem. Phys., 12, 7647-7687, 10.5194/acp-12-7647-2012, 2012.

Zdanovskii, A.: New methods for calculating solubilities of electrolytes in multicomponent systems, Zhur. Fiz. Kim, 22, 1475-1485, 1948.

Zhang, J., and Reid, J. S.: MODIS aerosol product analysis for data assimilation: Assessment of over-ocean level 2 aerosol optical thickness retrievals, Journal of Geophysical Research, 111, D22207, 2006.

Zhang, J., Reid, J. S., Westphal, D. L., Baker, N. L., and Hyer, E. J.: A system for operational aerosol optical depth data assimilation over global oceans, Journal of Geophysical Research, 113, D10208, 2008.

Zhang, Y., Pan, Y., Wang, K., Fast, J. D., and Grell, G. A.: WRF/Chem-MADRID: Incorporation of an aerosol module into WRF/Chem and its initial application to the TexAQS2000 episode, Journal of Geophysical Research, 115, D18202, 2010.

Zhao, C., Liu, X., Leung, L. R., Johnson, B., McFarlane, S. A., Gustafson Jr, W. I., Fast, J. D., and Easter, R.: The spatial distribution of mineral dust and its shortwave radiative forcing over North Africa: modeling sensitivities to dust emissions and aerosol size treatments, Atmos. Chem. Phys., 10, 8821-8838, 10.5194/acp-10-8821-2010, 2010.

Zhao, C., Liu, X., Ruby Leung, L., and Hagos, S.: Radiative impact of mineral dust on monsoon precipitation variability over West Africa, Atmos. Chem. Phys., 11, 1879-1893, 10.5194/acp-11-1879-2011, 2011.

Zhao, C., Liu, X., and Leung, L. R.: Impact of the Desert dust on the summer monsoon system over Southwestern North America, Atmos. Chem. Phys., 12, 3717-3731, 10.5194/acp-12-3717-2012, 2012.

Zhu, C., Byrd, R. H., Lu, P., and Nocedal, J.: Algorithm 778: L-BFGS-B: Fortran subroutines for large-scale bound-constrained optimization, ACM Transactions on Mathematical Software (TOMS), 23, 550-560, 1997.

Zhu, P., Albrecht, B. A., Ghate, V. P., and Zhu, Z.: Multiple-scale simulations of stratocumulus clouds, Journal of Geophysical Research: Atmospheres, 115, D23201, 10.1029/2010jd014400, 2010.

Zou, X., Vandenberghe, F., Pondeca, M., and Kuo, Y.-H.: Introduction to adjoint techniques and the MM5 adjoint modeling system, NCAR Technical Note, NCAR/TN-435-STR, 1997.